

Imaging from Nondedicated Satellites

ACKNOWLEDGMENTS

This report and the project it documents represents the product of a group of researchers from around the MITRE Corporation:

* Dr. Bruce Metcalf of MITRE's Optical Communications and Photonic System Group in Bedford, MA, performed the analysis and design work for the proposed focal plane array imaging instrument and provided section 2 of this report.

* Mr. Arnold Cherdak of MITRE's Center for Advanced Aviation System Development, System Engineering Division in Washington, DC, performed the Image Navigation and Registration study and provided section 3. Mr. Cherdak was also the report editor.

* Mr. E. G. Livaditis of MITRE's Weather Sensors and Systems Department in Washington, DC, performed the study of ground processing and provided section 4.

* Mr. Marvin Rosenbluth of MITRE's Weather Sensors and Systems Department in Washington, DC, performed the Deployment and Cost studies and provided section 5. Mr. Rosenbluth was the Principle Investigator for the project.

* Mr. Indar Bhatia and Mr. Alan Goldberg of MITRE's Space Projects Department provided the imager effective resolution analysis presented in Appendix B.

In addition to these primary contributors, several other MITRE staff members made contributions that must be acknowledged, including Dr. Robert T. Carlson for his insights and technical suggestions on the imager optoelectronics; Dr. Marvin D. Drake for ray tracing support; Mr. Jonathan D. Fridman for technical support in the imager design; Mr. Charles Lapinski for support in cost analysis; and Mr. Arthur Schwalb for keen insights in support of most of the activities of this project.

At several points along the way, we were privileged to have the advice and critique of several people from the government agencies that have responsibility for our nation's civilian operational remote sensing programs. Mr. W. John Hussey, Acting Deputy Assistant Administrator of the National Oceanic and Atmospheric Administration (NOAA)/National Environmental Satellite, Data, and Information Service (NESDIS) provided invaluable insights for our deployment studies and regarding the government's technical requirements. Mr. Gary Davis of NOAA/NESDIS and Mr. Thomas McGunnigal of the NOAA System Program Office provided interim review and offered important insights and advice on technical and deployment issues. Finally, Mr. Faris Kahwajy and Mr. Richard Reynolds of the NOAA/NESDIS Office of System Development offered insights and directed us to important information sources.

During the course of the project, we visited several focal plane array and system developers. These included Loral Imaging Systems, Phillips Laboratory (PL/VTPT), Santa Barbara Research Center, Amber Engineering Inc., Rockwell Science Center, and Hughes Space and Communications Group. We were impressed with their knowledge and experience, and our work benefited greatly from their critiques and useful suggestions.

Finally, the authors wish to thank several MITRE Corporation executives for their support in establishing this project: Dr. Ronald D. Haggarty, Vice President for Research and Technology; Dr. John J. Fearnside, Senior Vice President and General Manager, Director of the Center for Advanced Aviation System Development; and Dr. R. M. Harris, Vice President of the Center for Advanced Aviation System Development. We hope the results justify their support.

Arnold S. Cherdak

Editor

[Executive Summary](#)

TABLE OF CONTENTS

SECTION PAGE

1 [INTRODUCTION](#) 1-1

1.1 [Purpose](#) 1-1

1.2 [Background](#) 1-1

1.2.1 [Polar Orbiting Operational Environmental Satellite Program \(POES\)](#) 1-1

1.2.2 [Geostationary Operational Environmental Satellite \(GOES\) Program](#) 1-2

1.2.3 [GOES I-M Series](#) 1-3

1.3 [MITRE Sponsored Research \(MSR\) Initiative](#) 1-4

2 [IMAGER TECHNOLOGY AND DESIGN CONSIDERATIONS](#) 2-1

2.1 [Introduction](#) 2-1

- 2.2 [Imager Performance Goals](#) 2-2
- 2.3 [Focal Plane Array \(FPA\) Technology](#) 2-6
- 2.4 [Telescope and Array Sizes](#) 2-9
- 2.5 [Scanning](#) 2-15
- 2.6 [Radiometric Performance](#) 2-17
- 2.7 [Detector Cooling](#) 2-25
- 2.8 [Design Considerations](#) 2-27
- 2.9 [Instrument Weight and Power](#) 2-37
- 2.10 [Summary and Conclusions](#) 2-37
- 3 [IMAGE NAVIGATION AND REGISTRATION](#) 3-1
 - 3.1 [Introduction](#) 3-1
 - 3.2 [GOES I Instruments](#) 3-2
 - 3.3 [Approaches to Image Navigation and Registration](#) 3-3
 - 3.3.1 [Acquisition of Overlapping Image Frames](#) 3-6
 - 3.4 [Image Spatial Relationships](#) 3-11
 - 3.4.1 [GOES I Technology](#) 3-12
 - 3.4.2 [Array Detector Instruments](#) 3-12
 - 3.4.3 [Pixel Spread](#) 3-14
 - 3.4.4 [Image Smear](#) 3-15

3.4.5 [Field Rotation](#) 3-17

3.5 [Error Budget](#) 3-22

3.6 [Summary and Conclusions](#) 3-23

4 [GROUND-BASED PROCESSING OF FPA INSTRUMENT OUTPUT DATA](#) 4-1

4.1 [Introduction](#) 4-1

4.2 [Reference Ground Processing System](#) 4-1

4.2.1 [GOES I-M Ground Processing System](#) 4-2

4.2.2 [Spacecraft Support Subsystems](#) 4-2

4.2.3 [PG&D Subsystems](#) 4-4

4.3 [Data Reception](#) 4-5

4.4 [Calibration and Normalization](#) 4-6

4.5 [Earth Location and Gridding](#) 4-8

4.6 [Preparation for Distribution and Sector Distribution](#) 4-12

4.7 [Operating Scenarios](#) 4-13

4.8 [Summary and Conclusions](#) 4-14

5 [DEPLOYMENT](#) 5-1

5.1 [Context](#) 5-1

5.2 [Program Plan](#) 5-2

5.3 [Launch Opportunities](#) 5-4

5.3.1 [Commercial Communications Satellite Systems](#) 5-4

5.3.2 [Government Geostationary Satellite Systems](#) 5-14

5.4 [Operational Considerations](#) 5-15

5.5 [Cost Considerations](#) 5-16

5.5.1 [Projected In-Orbit Costs](#) 5-16

5.5.2 [Operating Costs](#) 5-20

5.6 [Summary and Conclusions](#) 5-21

6 [Summary of Conclusions](#) 6-1

[List of References](#) RE-1

[Appendix A](#) Blackbody Radiation A-1

[Appendix B](#) Step-Stare FPA Imager System Effective Resolution B-1

[Appendix C](#) Weighting Function For Drift and Jitter C-1

[Glossary](#) GL-1

LIST OF FIGURES

FIGURE PAGE

[2-1](#) Scanning the Field of Regard 2-1

[2-2](#) Blackbody Spectra and IR Channels 2-4

[2-3](#) Responsivity Nonuniformity of IR Sensor Arrays 2-9

[2-4](#) System Considerations 2-10

[2-5](#) Two-Telescope Imager 2-12

[2-6](#) Field of View for 30 cm f/12 Ritchey-Chretien Telescope 2-13

[2-7](#) Field of View and Array Size 2-14

[2-8](#) Redundant Arrays in the Field of View 2-14

[2-9](#) TDI Scanning 2-16

[2-10](#) Temperature Resolution 2-22

[2-11](#) Inverse Planck Function for Channel 5 2-24

[2-12](#) Quantization Noise Resolution for Channel 5 2-24

[2-13](#) Reverse Turbo-Brayton Refrigerator with Multiple Heat Loads 2-27

[2-14](#) Spectral Separation with a Grating 2-28

[2-15](#) Detectivity Tradeoff (300 degree K Scene, 2π sr FOV) 2-29

[2-16](#) Telescope Geometry 2-31

[2-17](#) First Aft Optics Design 2-32

[2-18](#) Second Aft Optics Design 2-33

[2-19](#) Cold Shield 2-35

[2-20](#) Flux Ratio and Optics Temperature 2-36

3-1 GOES: Spacecraft Dynamic Environment for INR 3-4

3-2 Spacecraft Motion Definitions 3-5

3-3 Composite of Image Frames 3-8

3-4 Effects of Spacecraft Motions on Frame Use 3-9

3-5 Spread Due to Mechanical Rates 3-16

3-6 Image Object Smear 3-18

3-7 Image Smear Due to Object Velocity 3-19

3-8 Scan Axis Directions 3-20

3-9 Frame Rotation Illustration 3-21

4-1 GOES I-M Satellite Support Subsystems 4-3

[A-1](#) Solid Angle from Blackbody to Detector Aperture A-3

[A-2](#) Blackbody Spectral Radiant Sterance A-4

[B-1](#) A Typical Spacecraft Line-of-Sight Error PSF B-4

[B-2](#) Typical Frequency Spectrum of LOS Point Spread Distribution B-5

[B-3](#) Weighting Function for Jitter and Drift B-7

[B-4](#) Normalized LOS PSD Curves B-9

[B-5](#) Modified Drift Weighting Function $G_1(a,b)$ B-10

[B-6](#) Modified Jitter Weighting Function $[1-G_1(a,b)]$ B-10

LIST OF TABLES

TABLE PAGE

[2-1](#) Imager Resolution Goals 2-3

[2-2](#) Desired (And GOES I-M) NEdT Performance Goals 2-3

[2-3](#) Photon Sterance Levels ($\text{photons/sec} \cdot \text{cm}^2 \cdot \text{sr}$) and Relative Temperature Derivatives (K^{-1}) for

the IR Channels 2-5

[2-4](#) Radiant and Photon Sterance Levels for Channel 1 2-6

[2-5](#) IR Detector Cutoff Wavelengths (um) 2-7

[2-6](#) Diffraction Limited Telescope Apertures 2-11

[2-7](#) Integration Times, TDI Dwells, and Attenuation 2-19

[2-8](#) Background-Limited Detectivities ($\text{cm} \sqrt{\text{Hz}} / \text{W}$) with f/2 Cold Shield 2-19

[2-9](#) **NEDT WITH STEP-STARE SCAN (50% BLIP FOR CHANNELS 2 AND 3, 10% FOR 4 AND 5) 2-20**

[2-10](#) **NEDT WITH TDI SCAN (50% BLIP FOR CHANNELS 2 AND 3, 10% FOR 4 AND 5) 2-21**

[2-11](#) Maximum Array Variations (percent) 2-22

[2-12](#) System Focal Lengths 2-30

3-1 Frame Edge Overlap 3-10

[3-2](#) GOES I Imager Predicted INR Performance 3-13

[5-1](#) ITU Region 2 1992 In-Orbit Communications Satellites 5-5

[5-2](#) Projected Replacement Satellites 5-11

[5-3](#) ROM Cost Summary for Commercial Host Satellite 5-17

EXECUTIVE SUMMARY

IMAGING FROM NONDEDICATED SATELLITES

INTRODUCTION

This report presents the results of a MITRE-sponsored research project that investigated the use of new technology for creating multispectral images of the earth's atmosphere and surface from geostationary orbit. The use of commercial communications satellites to carry the new-technology imaging instruments also was investigated. The research indicates that it is possible to achieve improved imaging instrument performance compared with current technology. The Geostationary Operational Environmental Satellite (GOES) system was used as a baseline for much of the work in this project since it is the primary source of earth images from geostationary orbit used by the National Weather Service (NWS) for weather warning and forecasting.

The National Oceanic and Atmospheric Administration (NOAA) implements and operates the GOES system for meteorological data collection. Each satellite provides a platform for meteorological data collection instruments whose outputs are used by the NWS and other government agencies, as well as domestic and international meteorological researchers. NOAA, through the National Aeronautics and Space Administration (NASA), has contracted for advanced versions of the GOES spacecraft, including an advanced scanning radiometer imager to provide multispectral images of the earth's atmosphere and surface. The imager for the advanced GOES I through M series spacecraft is being developed to meet performance requirements expressed in 1983 to support the NWS Modernization program. The imager design is an evolution of the imaging radiometer first launched into geostationary orbit in 1975.

In this project, MITRE assessed the technical feasibility of using advanced focal plane array (FPA) detector technology to develop an imager that would achieve NWS performance requirements for imagers for the year 2000 and beyond. In consideration of the large costs and risks associated with space-based programs, an assessment was made of the economic, institutional, and operational ramifications of carrying remote sensing instruments on geostationary satellites other than those dedicated to the meteorological mission.

Analyses were conducted of four areas associated with development of an FPA detector imager designed around state-of-the-art charge-coupled-device (CCD) detector arrays and some of the ramifications of having such an imager included in the payload of a non-dedicated satellite, such as a commercial communications satellite. The sections that follow summarize findings in each of these four areas: (1) Conceptual design for an FPA imager, (2) image navigation and registration (INR), (3) ground-based processing of FPA instrument output data, and (4) deployment opportunities and costs. The final section presents key conclusions from the four areas.

IMAGER TECHNOLOGY AND DESIGN CONSIDERATIONS

A conceptual design was developed for an FPA imaging instrument, incorporating advanced, second generation FPA detectors and mechanical cryogenic coolers. The FPA imager incorporates a 30 centimeter (cm) f/12 Ritchey-Chrétien reflector telescope with dichroic beam splitting aft optics to select visible and four infrared (IR) bands of interest. It incorporates redundant array detectors of 1024 x 512 pixels for the visible channel, 256 x 128 pixel detectors for the short-wavelength IR channel 2, and 64 x 32 pixel detectors for the medium- and long-wavelength IR channels 3-5. Corresponding earth resolutions are 0.5 km for the visible and 2 and 4 kilometers (km), respectively, for the IR channels 2 and 3-5. The proposed instrument is projected to weigh 235 lb and require 200 watts of power.

A tradeoff study of FPA scanning was conducted, in which the relative advantages of using step-stare scanning or a time delay and integration (TDI) method were weighed. TDI scanning offers improved radiometric performance, while the step-stare method provides a basis for improved INR performance as discussed below. With either approach, a full earth disc image containing 6.9×10^8 scene pixels encoded with 11 bits/pixel will result in a 50 megabits per second (Mbps) raw data rate without compression. Given sufficient downlink bandwidth, a full earth disc image can be created and transmitted to the ground every 3 minutes. This refresh rate is an order-of-magnitude improvement over the current and the planned GOES I rate of 30 minutes per image, which is governed by the imaging instrument.

The FPA imaging instrument is predicted to exceed the radiometric performance requirements expressed in 1991 by the NWS for imagers for year 2000, and to achieve the desired performance objectives for imaging beyond the 2000 requirements.

IMAGE NAVIGATION AND REGISTRATION (INR)

For the GOES I through M system, tailored to the remote sensing mission, INR is the name given to a collection of measures used to locate or assign latitude and longitude values for each pixel of an image, and to maintain absolute and mutual latitude and longitude spatial relationships within and among images. INR for the step-stare FPA imaging instrument consists of acquiring overlapping image frames covering the earth view, creating a mosaic of the frames to form an image, and providing annotation for each frame that links together the frames and provides for calibration. Studies of FPA imaging instrument INR were conducted, examining the use of step-stare scanning and contrasting it with TDI and GOES as noted above. While TDI scanning offers improved radiometric performance, the step-stare method provides a basis for improved INR performance.

The FPA instrument can capture frames of up to half a million pixels simultaneously, all pixels in a frame having fixed mutual spatial relationships. The imager allows for overlapping frames captured at very short intervals, reducing the effects of spacecraft motion while retaining spatial relationships by capturing the same image parts in adjacent frames. This provides an image of the full earth disc composed of about 1000 frames having very small error in mutual spatial relationships among frames. The frames themselves capture image areas with recognizable landmark detail used for location reference. Sufficient overlap is included to permit spacecraft motion during imaging operations to expand

and contract the overlap without losing it completely, and the frame image exposure time is short enough so that spacecraft motion has minimal effect on image quality. Through these devices, the FPA imager offers opportunities to meet and exceed current INR performance requirements.

Achieving required INR performance with a current-technology instrument requires a complex spacecraft to meet very demanding instrument pointing requirements. Onboard facilities, complex interaction with the spacecraft attitude and orbit control system, and complex ground system processing are required to deal with INR. The FPA instrument requires no complex interaction with the spacecraft other than to receive occasional commands, and to provide an output data stream and housekeeping information for transmission to earth. Furthermore, it appears technically feasible to carry an FPA instrument on a commercial communications spacecraft and produce image results that would, at a minimum, be comparable with predicted GOES I results and better with regard to the quality of image spatial relationships.

GROUND PROCESSING OF FPA INSTRUMENT OUTPUT DATA

Ground processing of FPA instrument output data is needed to provide means for assigning each individual pixel a longitude and latitude, adding geopolitical markings to the images, and providing radiometric calibration. In processing the instrument data stream, pixel values are not changed. Rather, each frame of pixels is annotated with the information needed for frame and pixel location, inclusion of geopolitical boundaries, and radiometric calibration.

Calibrated and annotated frames of FPA instrument data would be suitable for broadcast transmission to the NWS' Advanced Weather Interactive Processing System (AWIPS), currently under development, or to other systems that select satellite imagery data and resample using specialized coordinate systems. From the same broadcast transmission, image frames can be selected to form either a full earth image or a multiplicity of images for regions of interest. This means the FPA instrument can be operated in a free-running mode, with no special scanning modes or schedule interruptions for special events.

DEPLOYMENT

Based on the NASA Management Instruction, "Planning and Approval of Major Research and Development Projects" (NMI 7121.1), and a review of comparable instrument development projects, an availability date of 2003 is projected for a flight-ready FPA imaging instrument.

US domestic commercial geostationary communications satellite programs will present launch opportunities for such an instrument in the year 2003 time frame and beyond. This projection stems from the requirement to replace second-generation commercial satellites, having a 10- to 12-year mission life, in the same time frame in which an FPA instrument is anticipated.

A range of development costs for an FPA instrument and unit costs for other deliverable items have been projected based on recent contracting actions. The result, a projected range for a pro-rata share of

spacecraft and launch costs, is based on the ratio of the FPA instrument mass to the in-orbit mass of the communications payload of the commercial operator's spacecraft. Since the spacecraft operator would provide all satellite communications, command, and control services, and the government would operate the instrument payload, an estimate of annual costs for telemetry and command and data communications services also has been projected.

SUMMARY OF CONCLUSIONS

An objective of this project was to determine if an imager using FPA detector technology could be designed to provide performance that would meet the NWS requirements for imaging from geostationary orbit for the year 2000 and beyond. We also examined the potential for including such an imager in the payload of a commercial geostationary communications satellite. The limited pointing accuracy of communications satellites compared with that for satellites such as the GOES I, which are dedicated to the imaging mission, led us to explore means to compensate for pointing inaccuracies and for spacecraft motion by exploiting the imaging capabilities of the FPA instrument. We postulated ground processing concepts to achieve required INR performance given the 3 minute full-earth images provided by the FPA instrument. While many tradeoffs and options still exist, we can present our conclusions based on our work to-date. We summarize the detailed conclusions presented in sections 2 through 5 of this report as follows:

- * Second-generation FPA detector technology is the key to improved imaging from nondedicated satellites. We believe that a rapid imager is feasible and can provide the resolution and radiometric performance sought by the NWS as expressed in the NWS' GOES-N requirements [GOESN89].
- * A number of technologies now under development are important to FPA imager development. For example: IR detector arrays should be cooled to 70 degrees K or less. A passive radiative cooler to do this would be too large for an imager on a nondedicated satellite. The reverse turbo Brayton mechanical refrigerator is preferred. Mechanical refrigerator developments are well underway with lifetime goals of 10 years.
- * For step-stare scanning, the most demanding NEdT requirement is to be able to detect a 0.1 degree K temperature change in a 300 degree K scene in channels 4 and 5. This puts a 0.1 percent limit on residual FPA detector nonuniformities, which is within the state-of-the-art for FPA technology. TDI scanning offers superior radiometric performance and reduced requirements for detector production yield compared with step-stare scanning.
- * The use of FPA detectors precludes the use of image motion compensation and mirror motion compensation as defined for the GOES I system. This is due to the rigid spatial relationships among the pixels within a single frame of an image, and the consequent inability to alter the positions of individual pixels during image creation.
- * The use of overlapping image frames in the step-stare scanning method offers deterministic spatial

relationships within and among image frames to a greater degree than TDI scanning. This provides well-coregistered images using ground-based processing for assembling the frames into a whole image. While the predictor-corrector and feedback approaches to INR place the burden of image spatial relationships on the spacecraft and the imager scan system, the overlap approach uses data redundancy and ground-based image processing and results in the simplest space segment. Whole-image assembly from overlapped frames permits compensation for all spacecraft-earth relative motions.

* The proposed instrument can be operated in a free-running mode thereby precluding the need for scheduling special scanning modes or scenarios. The high resolution, improved image quality, and rapid 3 minute update rate for full-earth coverage make the resulting imagery suitable for AWIPS use and for the mesoscale observation objectives of the NWS Modernization program.

* It appears programmatically and legally feasible to deploy FPA instruments on nondedicated commercial communications spacecraft. Costs for such deployment may be less than deployment of a dedicated spacecraft. Our analysis projects cost for an operational instrument plus deployment to be in the range of \$50 to \$75 million which is at the low end of the cost range for a launch vehicle alone.

* Deployment of an instrument on a non-dedicated satellite could be done as a primary mission or as an adjunct to a primary mission. It also is possible to deploy a developmental instrument in this way to avoid risk to an operational system. Opportunities for deployment on commercial geostationary communications satellites including several Direct Broadcast Service and Mobile Subscriber Service satellites will be available in the post-2000 time frame. There appears to be little opportunity for sharing satellites with currently programmed government geostationary systems.

In the post-2000 time frame, NOAA will need advanced remote sensing technology that includes imaging from geostationary orbit. FPA technology can meet and, in some cases, exceed the performance anticipated in the GOES-N requirements for that era. Technical, programmatic, and legal issues do not appear to present barriers to lower-cost, high-quality imaging instruments to satisfy anticipated needs.

[Return to the text](#)

SECTION 1

INTRODUCTION

1.1 PURPOSE

This report documents the findings of a MITRE Sponsored Research project on "Imaging from Nondedicated Satellites." The purpose of this project was to explore the feasibility of developing an improved satellite instrument to collect visible and infrared image data from geostationary orbit, and to have such an instrument included in the payload of a satellite designed for other purposes.

1.2 BACKGROUND

The National Oceanic and Atmospheric Administration (NOAA) of the U.S. Department of Commerce (DOC) is responsible for conducting U.S. civil meteorological satellite programs. As such, it participates in the World Weather Watch (WWW) program of the World Meteorological Organization (WMO). It exchanges satellite-derived data with meteorological activities of other nations worldwide on a nondiscriminatory, no-cost basis. The National Environmental Satellite, Data, and Information Service (NESDIS), established in December, 1982, is the operations arm for NOAA satellites, providing operational control for polar orbiting and geosynchronous meteorological satellites.

1.2.1 Polar Orbiting Operational Environmental Satellite Program (POES)

The launch of the Television and Infra-Red Observation Satellite (TIROS) on April 1, 1960, ushered in the age of space meteorology. The polar orbiting meteorological satellite system has been in continuous operation since 1960, and currently has in orbit the three-axis stabilized, fourth-generation Advanced TIROS-NOAA (ATN) spacecraft of the NOAA A-J series. A follow-on series, NOAA K-N', has been programmed.

The spacecraft are launched into one of two circular, sun-synchronous, near-polar orbit-sun-synchronous in that the spacecraft precesses (rotates) eastward about the earth's polar axis 0.986 degrees per day. The precession is at the same rate and direction as the earth's average daily rotation about the sun, keeping the satellite in a constant position referenced to the sun for consistent illumination throughout the year. As a result the satellite always crosses the equator each orbit at the same local solar time.

NOAA polar orbiting spacecraft are launched into either a 450 nautical mile (nmi) altitude morning (a.m.) or a 470 nmi altitude afternoon (p.m) orbit. The orbital period is nominally 102 minutes, permitting just over 14 complete earth orbits daily. As the earth rotates each orbit, the satellite observes a different portion of the earth's surface, providing for observation and data collection on a global basis. Global data are collected by on-board remote sensing instruments, including the Advanced Very High Resolution Radiometer (AVHRR), and the High Resolution Infrared Radiation Sounder (HIRS).

The AVHRR is a scanning radiometer imager with five detectors in the visible and infrared (IR) bands for day and night imaging. The visible and the short-wavelength IR channels collect primarily reflected radiation data for observation of vegetation, clouds, lakes, shorelines, snow, and ice. The other three IR channels detect heat radiation data from which can be derived the temperature of land, water, sea surfaces, and the clouds above them. The AVHRR instrument produces image data of 1.1 kilometer (km) per pixel resolution at the subsatellite point (nadir).

The HIRS is a scanning radiation detection sounder with 20 detectors in the infrared spectrum. It detects and measures energy emitted by layers of the atmosphere to construct a vertical profile of temperatures from the earth surface to an altitude of about 40 km.

1.2.2 Geostationary Operational Environmental Satellite (GOES) Program

Geostationary satellites are launched into a 34,880 km (22,300 statute mile [mi]) circular orbit whose plane lies in the earth's equatorial plane. The circular orbital period at that altitude is 24 hours, exactly equal to the earth's rotation period, and therefore the satellite appears stationary with respect to an observer (antenna) on earth.

All GOES satellites to date have been spin-stabilized. Spin-stabilization occurs when the gyroscopic effect of spinning the cylindrical satellite body causes the satellite to retain a fixed spin axis direction. The GOES spins at 100 revolutions per minute (rpm) with respect to the subsatellite point on earth, with a despun platform containing directional antennas, rotated at the same rate but in the opposite direction. This causes the antennas and platform to appear stationary with respect to an observer (antenna) on earth.

The GOES satellite system has been in continuous operation since May 1974; GOES 7, the last of the current series of spin-stabilized GOES satellites in orbit, was launched February 1987. The GOES operating strategy is to locate one satellite at 135 degrees west longitude to cover the eastern Pacific ocean, the western contiguous 48 states, Hawaii, and the Gulf of Alaska. A second GOES satellite is located at 75 degrees west longitude to cover the eastern states, and the central and western Atlantic Ocean.

The primary instrument of the GOES satellite is the Visible and Infrared Spin Scan Radiometer (VISSR) imager, with a 40.6 centimeter (cm), Ritchey-Chrétien optical system. The VISSR is a scanning radiometer that produces a west-to-east scan line as the spin of the spacecraft causes the VISSR to view the earth. The earth view is directed to one visible and four IR detectors by means of a motor-driven scan mirror. The scan mirror steps 0.192 milliradian (mrad) from north to south between earth views to scan the full earth disc as viewed from the satellite, in 1820 steps every 26 minutes. The image resolution of the VISSR is 1 km in the visible band, 14 km in the 6.50-7.0 micron water vapor channel, and 7 km in the three other IR bands.

The configuration of the last five VISSR instruments, first launched in September 1983, incorporates an atmospheric sounding capability, sharing the telescope optics and scan mirror of the VISSR, but with 1

visible and 18 IR channels. This combined instrument is the VISSR Atmospheric Sounder (VAS).

The VAS can operate in either a multispectral imaging mode or a "dwell imaging" sounding mode. Atmospheric sounding data are obtained in the VAS dwell mode by repeatedly scanning the same earth swath. From 1 to 46 repeated views of an atmospheric column are needed to achieve an adequate signal-to-noise ratio. The dwell imaging mode enables measurements in the tropospheric temperature and moisture sounding channels to be achieved over a 35 degree latitude band in thirty minutes.

1.2.3 GOES I-M Series

A series of five advanced spacecraft, GOES I through M, is currently in the integration and test phase prior to the planned launch of GOES I in mid-1994. Spacecraft of the GOES I-M series are three-axis body stabilized, with independently operated imaging and sounding instruments.

Requirements for imager spatial resolution and registration were defined by NOAA's National Weather Service (NWS) in 1983 and are beyond the capabilities of the VAS instrument. Specifically, the NOAA I-M imager resolution requirements are for 1 km visible channel; 8 km for a 6.50-7.00 micron channel; and 4 km for the 3.80-4.00, 10.20-11.20, and 11.50-12.50 micron channels.

The imager and sounder developed for GOES I-M are adaptations by their manufacturer of the polar orbiter AVHRR and HIRS instruments. Their performance at geostationary altitudes, as contrasted with performance at the nominal 500 mile low earth orbit of the polar orbiters, has introduced difficulties in achieving image navigation and registration (INR) specifications for GOES I-M. The result has been a delay in delivery and the inclusion of significant ground processing requirements in the GOES I-M system.

The long lead time associated with realization of an operational meteorological sensor spurred an effort by NOAA to plan for GOES instrumentation beyond the lifetime of the GOES I-M program. As a result, the Advanced Mission Analysis Center of the Goddard Space Flight Center (GSFC) initiated a study in 1989 to explore concepts for meeting NOAA advanced imager requirements beyond the GOES I-M time frame. The results of this study were presented in the "GOES N Report" dated December 1991.

Performance requirements for a GOES N spacecraft were established by the NWS in May, 1989. The NWS defined the performance of the visible and IR imager specified for GOES I-M as "core requirements," which the GOES N imager must meet. NWS also defined "optional requirements," which the NWS wants seriously to explore. These optional requirements are for additional IR channels in the imager, and, more significantly, for improvement in the 4 km and 8 km spatial resolution of GOES I-M to 2 km and 4 km for GOES N.

1.3 MITRE SPONSORED RESEARCH (MSR) INITIATIVE

The Weather Sensors and Systems Department of The MITRE Corporation has been providing systems

engineering support to NESDIS since 1985, primarily in ground system design and acquisition. It supported the acquisition of the Polar Acquisition and Control Subsystem (PACS) and associated radio frequency (RF) subsystems, which became operational in July 1992. It also supported acquisition of the GOES I-M Telemetry and Command Subsystem (GIMTACS) and associated RF subsystems, and is supporting ground system testing for GOES I launch readiness.

As a result of its support for the GOES ground system effort, MITRE has been following the production of the GOES I-M imager for its impact on the ground system. Recognizing that the imager is a flying spot scanner of 1970s technology, and being aware that focal plane array (FPA) remote sensing instruments have rapidly evolved since that time, the MSR project on "Imaging from Nondedicated Satellites" was initiated with the objective of assessing the feasibility of applying FPA technology to geostationary meteorological imaging and in meeting or exceeding the GOES N imaging performance requirements.

As part of the research effort, the feasibility of having such an FPA imager integrated with the payload of other than a dedicated geostationary weather satellite was explored. Such capability could protect against interruption of imager data in the event of in-orbit or launch failures, or prolonged launch delays. A further objective of the project was to examine the institutional, technical, financial, and operational ramifications of such joint operation with government and commercial communications satellite operators.

1.4 ORGANIZATION OF THIS REPORT

This report summarizes the findings of the project in four analysis areas:

- * **IMAGER TECHNOLOGY AND DESIGN CONSIDERATIONS** (Section 2) presents background and description of proposed imaging instrument optics and detector concepts based upon new technology.
- * **IMAGE NAVIGATION AND REGISTRATION (INR)** (Section 3) presents concepts for creating useful images from the proposed imaging instrument and discusses key elements of image quality.
- * **GROUND BASED PROCESSING OF FPA INSTRUMENT OUTPUT DATA** (Section 4) presents concepts for the processing of the proposed imaging instrument output data needed to provide accurate, high-quality images.
- * **DEPLOYMENT** (Section 5) describes deployment opportunities for the proposed imager along with operational concepts and ROM costs.

Each of these sections ends with a summary and conclusions for that area. The report ends with a list of references and a glossary of acronyms and abbreviations used in the text.

1 The terms meteorological satellite, weather satellite, and environmental satellite refer to artificial earth

satellites that carry remote sensing instruments for collection of data used in weather forecasting and meteorological research, and are terms used interchangeably in this document.

[Return to the text](#)

SECTION 2

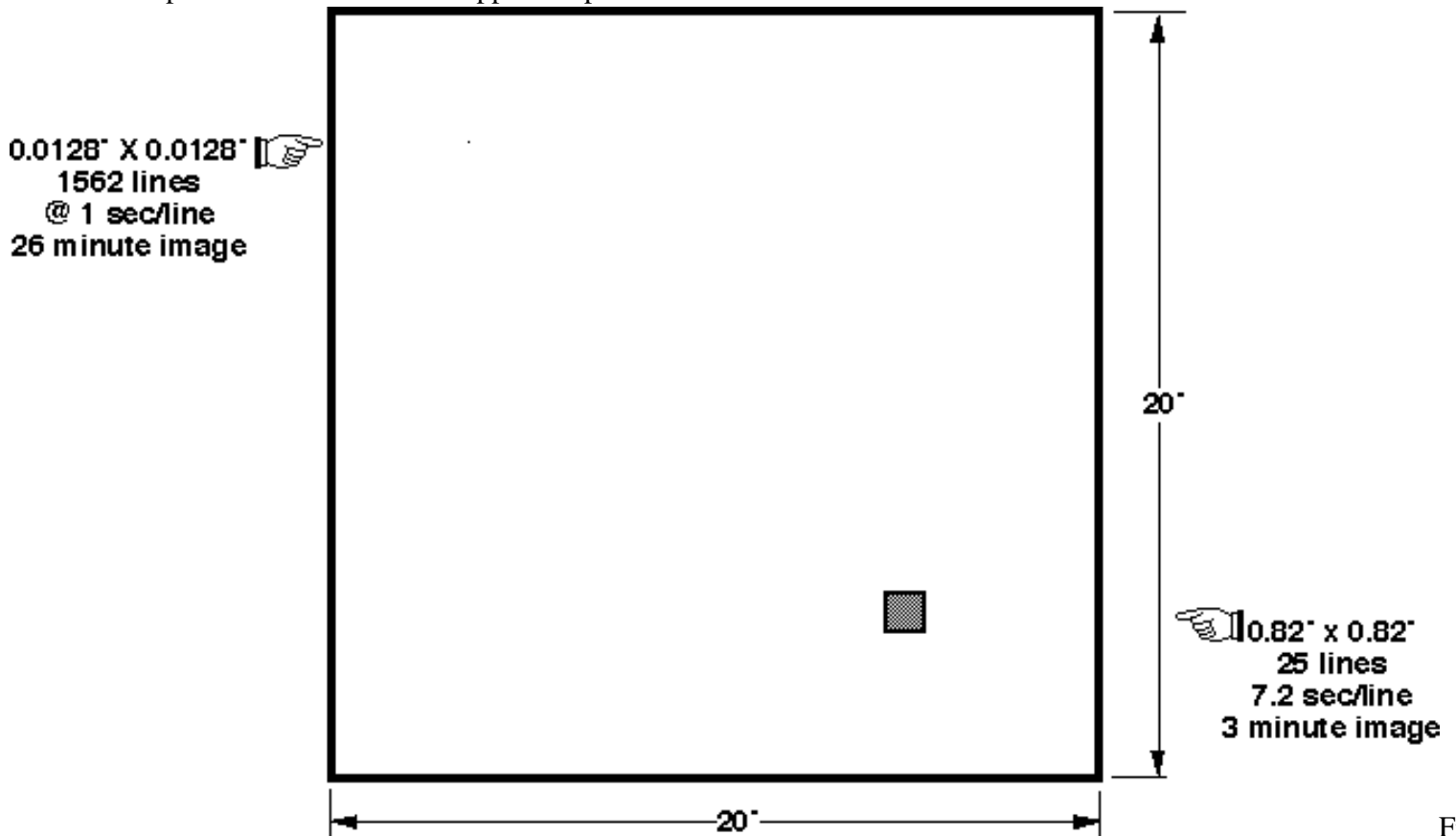
IMAGER TECHNOLOGY AND DESIGN CONSIDERATIONS

2.1 INTRODUCTION

A geostationary weather satellite orbits at an altitude of 35,800 km. The Earth's radius is 6378.4 km. The Earth disk subtends an angle of 17.3 degrees at the satellite. For scanning purposes, the field of regard (FOR) for a full disk scan is defined as 20 degrees (N/S) x 20 degrees (W/E). A 1 km length on the Earth's surface at nadir subtends an angle of 28 urad ($= 1 \text{ km}/35,800 \text{ km}$) or 1.6×10^{-3} degrees.

GOES I-M weather satellites are currently under development. The GOES I imager is based on a flying-spot-scanning technique whereby, via motion of a two-axis scan mirror, the scene's resolution areas are optically imaged onto a single pixel (or a relatively small number of pixels). The GOES I instrument images five wavelength bands with resolutions ranging from 1 km to 8 km. The 8-km-resolution channel is scanned by a single detector pixel.

The GOES I pixel is illustrated in the upper left portion of the FOR in



Figure

2-1 (Scanning the Field of Regard). The GOES I flying spot has an angular extent of 0.0128 degrees x 0.0128 degrees. There are 1562 horizontal scan lines over the FOR. The scan mirror moves horizontally at a rate of 20 degrees/sec. Therefore, a full disk image requires 1562 sec, or 26 minutes.

Imaging with detector arrays offers significant advantages over flying spot scanning. Depending on the detector material system appropriate for the desired wavelength, these arrays consist of many thousands to millions of detector pixels, along with a multiplexing and readout system. An array imager, with appropriate optics, would allow redundant arrays with a large 0.82 degree x 0.41 degree angular view. With 25 horizontal scan lines, an image can be formed in 3 minutes with a scan rate of 7.2 sec/line.

Since the scan rate is slower, the dwell time per pixel is longer, and the detectors in the array can collect more energy from the

scene. This improves signal-to-noise ratio (SNR) and noise equivalent temperature difference (NEdT) performance. Of course, detector saturation must be prevented. Alternatively, the longer dwell time can allow us to shrink (improve) the resolution area somewhat and still collect sufficient energy to meet baseline SNR and NEdT requirements. The motivation for exploring an array imager is based on faster image formation and improved resolution and radiometric performance.

We begin this section by defining performance goals for an array imager and a brief review of focal plane array technology. We then examine the impacts from wavelength, resolution, and radiometric performance requirements on telescope design and focal plane array size. Tradeoffs associated with different scanning techniques are examined. Radiometric performance estimates are made for each channel. For cooling the detector array, the size of a passive radiative cooler is estimated and the state of the art in mechanical coolers is discussed. Design issues regarding spectral separation and common focal planes are considered. A preliminary instrument design is developed.

2.2 IMAGER PERFORMANCE GOALS

Performance goals for the proposed imager are based on documented NOAA meteorological requirements [GOESN89]. There are five channels to be imaged: one visible and four infrared (IR). Wavelengths, resolution goals, and principal applications are given in [Table 2-1](#). Resolution goals for channels 1, 2, and 3 represent improvements by a factor of 2 over GOES I-M. Enhanced resolution, especially in channels 2 and 3, is considered very desirable in the requirements document.

For the visible channel (1), performance is specified in terms of SNR. An SNR of 3 is required at 0.5 percent albedo. Albedo is the ratio of solar energy reflected from a rough surface to that incident on it. The dynamic range for the visible channel extends up to 100 percent albedo.

For the IR channels, the upper end of the dynamic range for GOES I-M is 320 degrees K. An increase in dynamic range to 350 degrees K is desired. This would allow more detailed observation of extremes in surface temperatures and differential heating, and would improve the monitoring of forest fires, volcanic eruptions, and other hot spots on the Earth.

Radiometric performance for the IR channels is specified in terms of NEdT. NEdTs are specified at three scene temperatures: 200 degrees K, a typical cloud top temperature; 240 degrees K, a mid-level cloud temperature; and 300 degrees K for surface scenes. A matrix of desirable NEdTs is given in [Table 2-2](#). Core requirements, specified for GOES I-M, are shown in parentheses in Table 2-2.

Numerous benefits could be gained from the improved NEdTs. These benefits relate to the following: more accurate corrections for Earth atmosphere absorption, detection of diurnal temperature fluctuations over land and shallow waters, better tracking of the Gulf Stream, determination of coastal upwelling in response to wind changes (all of the preceding from improvements at $T = 300$ degrees K), improved mid-tropospheric moisture estimates (240 degrees K), and cloud parameter estimates for improved indicators of severe convection intensity (200 degrees K).

Blackbody spectra and the IR channels are shown in

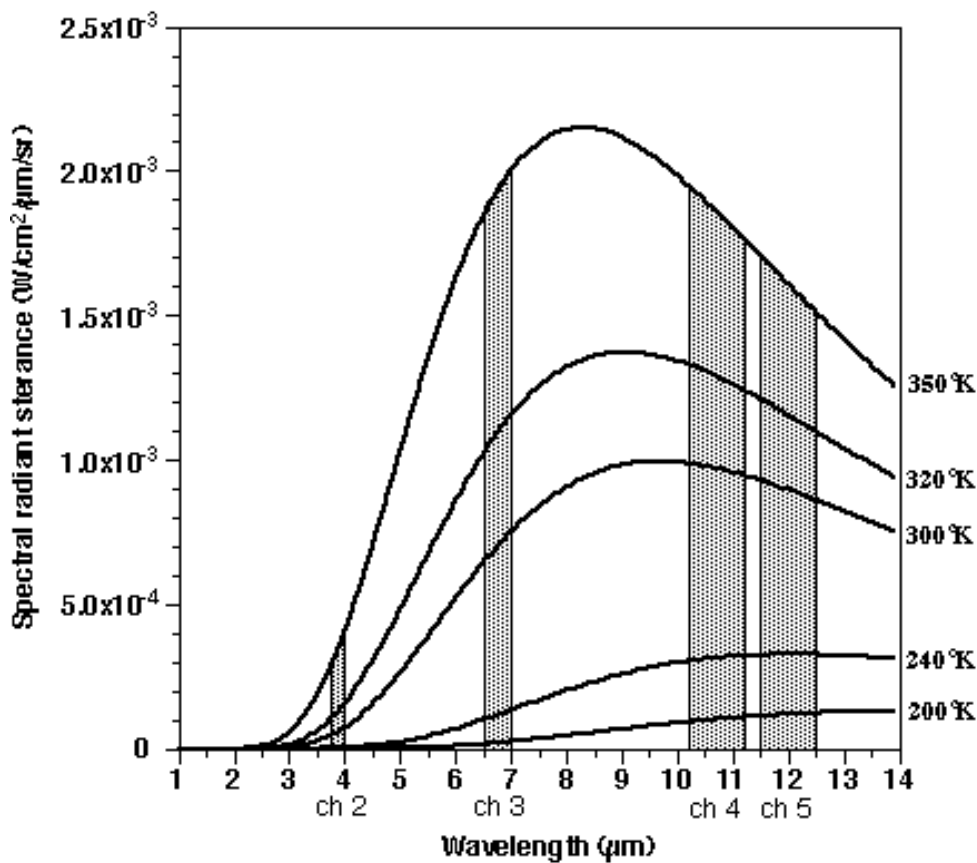


Figure 2-2 (Blackbody Spectra and IR

Channels). For the interested reader, Planck's radiation law is reviewed in Appendix A. A dynamic range increase from 320 degrees to 350 degrees K results in a thermal radiation increase of 169 percent for channel 2 (from 1.3×10^{-4} to 3.5×10^{-4} W/cm² /μm/sr). The impact from increasing dynamic range is less for the other channels. Because channel 2 lies farthest from the peak spectral wavelengths, and because it has the narrowest spectral band ($d[\lambda] = 0.2 \mu\text{m}$), it will require the longest integration time. Figure 2-2 also shows that channels 4 and 5 will have similar performance since their radiation levels are close to each other.

For each channel and temperature, we can determine the rate at which photons are emitted per unit area (of blackbody source) per unit solid angle (subtended by the detecting aperture). This normalized emission rate is called the photon sterance and has units of photons/(sec*cm²*sr). Our radiometric nomenclature is adopted from Vincent [VINCENT90]. Further discussion of this nomenclature is found in Appendix A. Photon sterance levels will be used later in our radiometric performance calculations.

For a given scene temperature, photon sterance levels for the IR channels are computed by integrating the spectral photon sterance $L_q([\lambda], T)$ over the channel wavelength bands ($[\lambda]_1$ to $[\lambda]_2$):

$$L_{q, \lambda_1, \lambda_2} = \int_{\lambda_1}^{\lambda_2} d\lambda L_q(\lambda, T) \quad \text{photons}/(\text{sec} \cdot \text{cm}^2 \cdot \text{sr})$$

Photon sterance levels, are given in Table 2-3. Also shown in parentheses in Table 2-3 is the relative temperature derivative of

the photon sterance $\frac{1}{L_{q, \lambda_1, \lambda_2}} \frac{dL_{q, \lambda_1, \lambda_2}}{dT}$. This derivative will come into play when characterizing the radiometric (NEDT) performance of the imager.

For the visible channel, we are interested in optical power levels in the range from 0.5 to 100 percent albedo. The required optical dynamic range is a factor of 200. The solar constant at the mean distance of the Earth from the sun is 0.1353 W/cm². Of this flux, 22.3 percent falls in the channel 1 wavelength band between 0.55 and 0.75 μm. At a fractional albedo, A, the

radiant sterance is $9.60 \times 10^{-3} \text{ A W}/(\text{cm}^2 \cdot \text{sr})$. With $A = 0.005$ and 1.0 , the radiant and photon sterance levels are given in [Table 2-4](#).

There are temporal requirements for synoptic (full disk) and mesoscale (U.S. sectors) applications. The core requirement is for a full disk image within 30 minutes. Any $3000 \text{ km} \times 3000 \text{ km}$ area must be imaged within five minutes, and a $1000 \text{ km} \times 1000 \text{ km}$ area must be imaged within 2 minutes. For an array imager, these temporal requirements are very liberal. Our temporal goal is for a full disk image within 3 minutes.

2.3 FOCAL PLANE ARRAY (FPA) TECHNOLOGY

Silicon image sensor arrays are appropriate for the wavelength band of channel 1. Silicon devices respond out to 1 um . Silicon arrays have been made with up to 4096×4096 pixels (e.g., Loral Fairchild CCD481 or Ford Aerospace FA4096S). Pixel sizes range from 6.8 um on edge (e.g., Kodak KAF 1400 image sensor) to more than 30 um square.

Silicon image sensor arrays employ either charge-coupled device (CCD) or charge-injection device (CID) technology. In a CCD, each photoelement has a capacitor for accumulating and storing optically generated electrons. A clocking operation shifts the charges sequentially across the capacitors. The efficiency of charge transfer can be 99.999 percent. The charges appear at an output gate at the edge of the device. In a CID, the charge under each photoelement is measured, and there is no shifting of charge. Since the charges remain stationary, a selective or random readout of individual pixels is possible. The CIDs are resistant to blooming (charge spillover from an overexposed pixel to neighboring pixels) and smearing (transfer of the overexposure effect along the array).

Image sensor array architectures may be full-frame, frame-transfer, interline, or time delay and integration:

- * With the full-frame architecture, rows of scene information (pixel charges) are shifted in parallel to a serial shift register, which subsequently shifts the row of information to the output as a serial stream of data. The process repeats until all the rows are transferred off the array.
- * In a frame-transfer architecture, there is a parallel storage array that is not light sensitive. The captured scene from the photosensitive array is rapidly transferred to the storage array. Readout from the storage array is then performed as for the full-frame architecture while the photosensitive array is integrating the next frame.
- * In an interline architecture, the photodetecting and readout functions are separated by forming isolated photosensitive regions between lines of nonsensitive (or light-shielded) parallel readout CCDs. After a scene has been integrated, the signal collected in every pixel is transferred, all at once, into the light-shielded parallel CCD.
- * Time delay and integration is a mode of processing the signal charge from the detector array that enables the integration of charge from multiple detector elements. Multiple pixel-sized images of an object are added to obtain an enhanced SNR. TDI is discussed further in connection with scene scanning tradeoffs.

There are several detector material systems for IR detection. The cutoff wavelength $[\lambda]_c$, where the spectral response on the long wavelength side is at 50 percent of peak, depends on the temperature of the detector. [Table 2-5](#), from [Norton91], shows the cutoff wavelength for several material systems at various detector temperatures.

A temperature of 190 degrees K can be achieved with a four-stage thermoelectric (TE) cooler. A temperature of 80 degrees K requires liquid nitrogen, a Joule-Thompson cryostat, or a single-stage mechanical cooler. Temperatures between 1.5 degrees K and 60 degrees K require multiple-stage mechanical coolers, or liquid neon, hydrogen, or helium.

Indium antimonide (InSb), platinum silicide (PtSi), and mercury cadmium telluride (HgCdTe) are all candidates for the wavelength range of channel 2 ($3.8\text{-}4.0 \text{ um}$), but only HgCdTe is possible for the longer-wavelength channels. The relative

concentrations of HgTe molecules with CdTe molecules can be adjusted in the growth process to form $\text{Hg}_{1-x}\text{Cd}_x\text{Te}$ and obtain a desired cutoff wavelength, larger x resulting in shorter $[\lambda]_c$. Typical uncertainties in production of long-wavelength Hg_{1-x}Cd_xTe arrays are $dx \sim \pm 0.2$ percent, corresponding to a cutoff wavelength uncertainty of $d[\lambda]_c \sim 0.5 \mu\text{m}$.

In a photovoltaic (PV) detector, there is a p-n junction. Photoelectrons created near the junction are separated by the junction and produce a voltage in proportion to the incident number of photons. With photoconductive (PC) detectors, incident photons are absorbed and produce free charge carriers. The carriers increase the electrical conductivity of the element and therefore decrease its resistivity. A bias circuit must be used with PC detectors. Advantages of PV over PC detectors include a better theoretical limit to the SNR, no biasing and therefore low power dissipation on the focal plane, high impedance for matching into a silicon CCD, and more accurately predictable responsivity ([Vincent90] and [Walter86]). PC HgCdTe technology is presently limited to linear arrays. So-called first-generation IR focal plane arrays were photoconductive and had a pair of electrical leads for every pixel; no multiplexing was involved. Second-generation PV arrays multiplex pixel signals to output ports on the readout integrated circuit (ROIC).

For IR imaging, PtSi offers the largest array sizes. Two-dimensional PtSi arrays have been made with 480×640 elements. EG&G is currently developing a monolithic-structure 512×512 PtSi array for the U.S. Air Force. Both monolithic (photodetection and readout on same substrate) and hybrid (PtSi photodetection silicon readout) arrays have been fabricated. As compared with other IR detectors, PtSi offers the advantages of large formats and excellent uniformity of response from pixel to pixel. However, the quantum efficiency of PtSi is very low--in the range of 0.1 to 1 percent. Quantum efficiency is the number of electrons generated per incident photon. Low quantum efficiencies require long integration times for low level incident radiation.

There is continuing debate in the industry on tradeoffs for selection of InSb versus HgCdTe for channel 2. The arguments center on detectivity, detector temperature, cutoff, cost, and uniformity. Some of this debate is reviewed by DeWames [DeWames92]. The detectivity of InSb is much better at 65 degrees K than at 80 degrees K; its performance is very poor above 80 degrees K. At 65 degrees K, InSb offers better (precorrected) uniformity and operability than HgCdTe. Operability is a term used to characterize the percent of pixels with detectivity and quantum efficiency greater than some acceptable level. An argument in favor of HgCdTe is that the cutoff wavelength of InSb cannot be tailored to the channel 2 application, whereas the chemistry of HgCdTe can tailor the cutoff to around $4.3 \mu\text{m}$. This would reduce noise and allow operating margin. Large array size and cost favor InSb technology. InSb arrays of 256×256 pixels have been produced, and those of 512×512 are in development. HgCdTe array sizes of 128×128 are common.

As we will see later, pixel-to-pixel uniformity is an important aspect for an imager using FPAs. Pixel-to-pixel nonuniformity is usually characterized in terms of the standard deviation of responsivity over the pixels of the array.

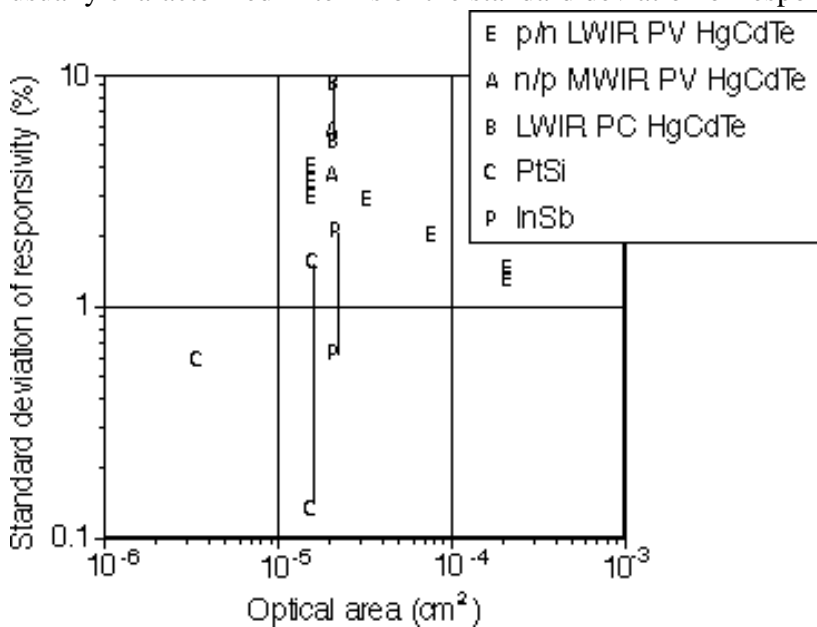


Figure 2-3 (Responsivity Nonuniformity of IR Sensor)

Arrays) [Norton91] shows response nonuniformity of IR detector material systems. PtSi is seen to approach a nonuniformity of 0.1 percent, whereas HgCdTe nonuniformity can be as high as 10 percent. InSb's nonuniformity falls in the 0.7 to 2 percent range. To reduce the effects of responsivity variations, an array must be characterized pixel-by-pixel. Correction coefficients are determined and gain values for each pixel are stored. However, even after this correction process, there are still residual variations. The residual variations result from pixel response nonlinearities. Residual variations have been reported as low as 0.01 percent.

2.4 TELESCOPE AND ARRAY SIZES

The imager requires a telescope to collect and focus energy from the Earth scene. Our study of an array imager begins with

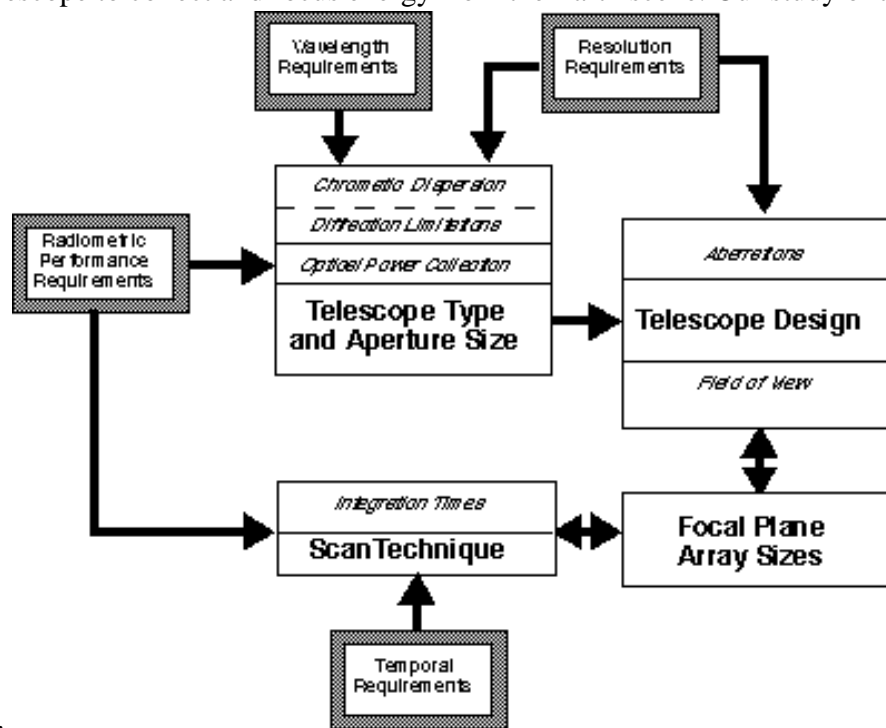


Figure 2-4 (System

telescope considerations.

Considerations) illustrates the flow of imager requirements and interaction among system aspects. The wavelength requirements impact the telescope type and aperture size through considerations of chromatic dispersion and diffraction limitations. Aperture size is also driven by radiometric performance requirements. In addition to wavelength, resolution requirements enter into determining aperture size. In the telescope design, resolution requirements set an upper limit on aberrations. This establishes the telescope's field of view (FOV), which in turn determines the maximum array sizes for the channels. Dimensions of the detector array pixels, along with resolution requirements, determine the required system focal lengths. Scan techniques are driven by temporal and radiometric performance requirements, and interact with array sizes.

Telescopes fall into the categories of reflective, refractive, and catadioptric designs. Because of the wide wavelength range required for the imager (0.55-12.5 μm), a common refractive telescope cannot be considered; chromatic aberrations would be too great. Some catadioptric telescopes, such as the Mangin mirror, Bouwers-Maksutov, and Schmidt systems, use mirrors with a refracting element to correct for spherical aberrations. Once again, the refractive element would result in severe chromatic distortion over the wide wavelength range. Other catadioptric designs use a shaped refractive meniscus to reduce chromatic aberration; however, the resulting focal plane is a curved surface.

The imager's wide wavelength requirements lead us to reflective telescope designs. The most common of the reflective designs are the two-mirror telescopes. These include the classical Cassegrain and Ritchey-Chrétien (RC) designs. In these two-mirror systems, the secondary mirror presents an obscuration to the collection of light by the primary. For our analysis, we assume a linear obscuration of $[\epsilon] = 0.25$ (0.0625 by area).

If an angular resolution $[\theta]$ is to be met with an obscured aperture, then the minimum diameter D , determined from diffraction limitations, is:

$$D \geq \frac{2\lambda x}{\pi\epsilon},$$

where x is a root of $J_1(x) - \epsilon J_1(\epsilon x) = 0$, and $J_1(x)$ is an ordinary Bessel function.

For $\epsilon = 0.25$, we found that $x = 3.59$, and the diffraction law becomes:

$$D \geq \frac{2.29\lambda}{\epsilon}.$$

Diffraction-limited apertures for the five imager channels are given in [Table 2-6](#). Channel 5 requires the largest aperture, and we henceforth assume a telescope with a 30 cm diameter aperture. Presenting an $\epsilon = 0.25$ obscuration, the diameter of the secondary mirror is 7.5 cm.

We see from [Table 2-6](#) that the diffraction-limited aperture for channel 1 is 12.3 cm for an enhanced resolution of 14 urad (0.5 km). However, if we accept the standard 28 urad (1 km) resolution, the minimum diameter is 6.1 cm. Since this diameter is smaller than the 7.5 cm obscuration of the 30 cm telescope, it allows for an interesting design of a two-telescope imager; a 30-cm reflective telescope for the IR channels and a 7.5 cm refractive telescope for the visible channel, positioned within the obscuration of the IR telescope. This design concept is illustrated in

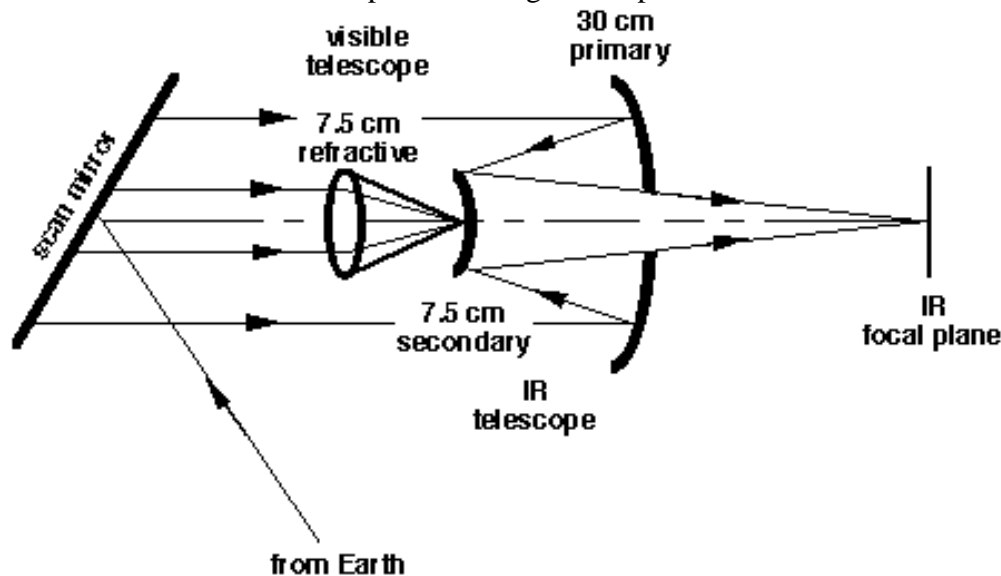


Figure 2-5 (Two-Telescope Imager). Time did

not allow us to pursue the two-telescope design, but we mention it here as a design alternative to the single-telescope system, which we analyze in detail.

Aberrations distort the focused image in a telescope. Aberrations include spherical, coma, astigmatism, and Petzval curvature. The Cassegrain telescope, with paraboloidal primary and hyperboloidal secondary mirrors, corrects for spherical aberration. The RC design has aspheric surfaces chosen to correct for both spherical and coma aberrations. Both designs have been built and flown in space. The visible and infrared spin scan radiometer (VISSR) and Hubble telescopes are RC designs. Since the RC corrects for more aberrations, and since we desire the largest FOV, we analyze the RC design.

The RC telescope suffers from astigmatism and Petzval field curvature. Aberrations are a function of the $f/\#$ of the primary mirror; the lower the $f/\#$, the worse the aberrations. However, lower primary mirror $f/\#$ s are desirable because mirror spacings are closer, the telescope is more compact, and there is more working distance behind the primary mirror before the beam comes to focus. Extra working distance for the aft optics (beamsplitters, filters, lenses, stops, etc.) is important since there are five channels to process.

The maximum full FOV is defined as twice the angle at which aberrations result in a spot diameter equal to the required

instantaneous field of view (IFOV). Astigmatism and Petzval aberrations were computed for the RC telescope according to [Wolfe89]. The magnitudes of the aberrations were added to determine a blur radius. The blur diameter divided by the focal length is the blur angle. The blur angle increases with the off-axis angle of incidence. The off-axis incidence angle was increased, and the blur angle was allowed to increase up to the IFOV for each channel. The analysis was performed as a function of primary mirror $f/\#$. The results of this analysis are shown in

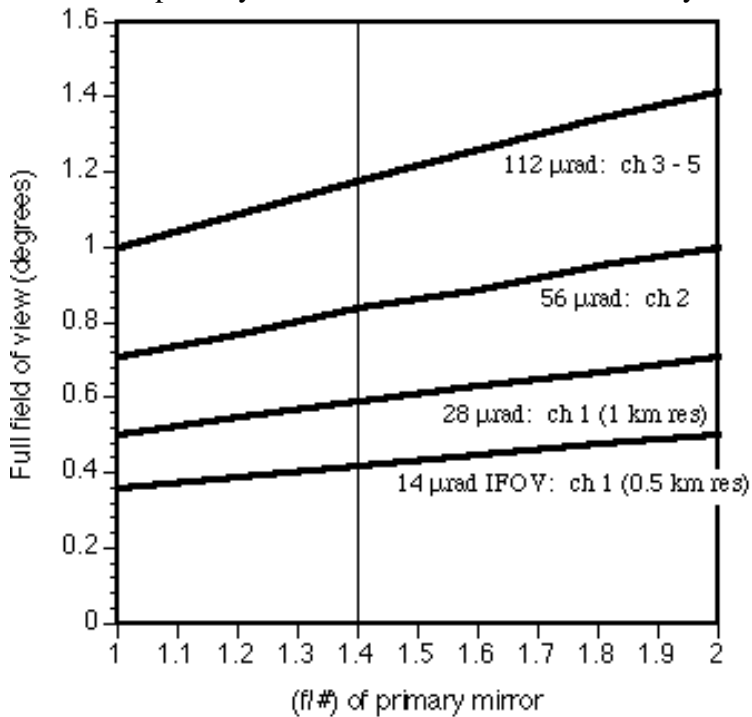


Figure 2-6 (Field of View for 30 cm $f/12$ Ritchey-Chrétien

Telescope). For an $f/1.4$ primary, the 14 urad IFOV of channel 1 limits the maximum FOV to approximately 0.42 degrees. A 28 urad IFOV, corresponding to 1 km resolution, allows a 0.59 degree FOV. The 56 urad IFOV of channel 2 allows a 0.84 degree FOV, and channels 3-5, with 112 urad resolution, allow a 1.18 degree FOV.

Channel 1 restricts the telescope FOV. Further analysis of RC telescope aberrations shows that the dominant aberration is Petzval field curvature. In effect, the focal plane is curved. A field corrector lens may be used to reduce Petzval aberration, and it is not unreasonable to assume that the correction will double the FOV from 0.42 degrees to 0.84 degrees. The field corrector lens would be required only for the optics of channel 1, not the other channels.

A square array has $N \times N$ pixels. The required FOV for an $N \times N$ array is $N(\text{IFOV})\sqrt{2}$. The factor $\sqrt{2}$ increases the diameter of the circular FOV so that it encompasses a square array (i.e., the array diagonal is the diameter of the

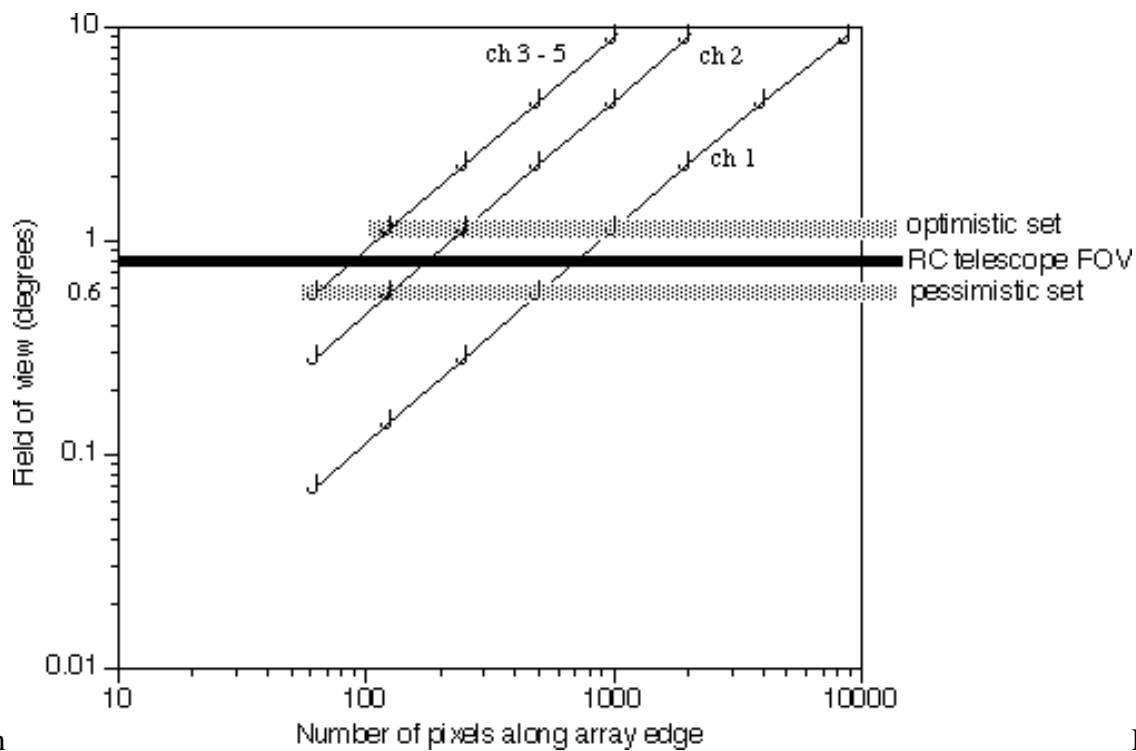
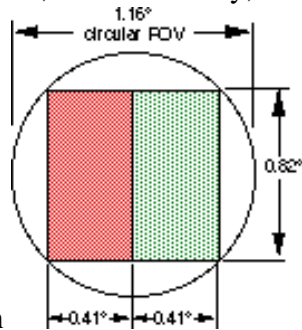


Figure 2-7

telescope's FOV). In (Field of View and Array Size), FOV is plotted against array size for the three resolutions.

For channel-to-channel coregistration, all channels must have a common FOV. The 0.84[[ring]] FOV of the 30 cm f/12 RC telescope, indicated by a dark line in [Figure 2-7](#), falls between two sets of array sizes. The optimistic set consists of a 1024 x 1024 array for channel 1, a 256 x 256 array for channel 2, and 128 x 128 arrays for channels 3-5. The optimistic set would require a telescope FOV of 1.16 degrees. The pessimistic family of array sizes is 512 x 512 for channel 1, 128 x 128 for channel 2, and 64 x 64 for channels 3-5. In our aberration analysis of the RC telescope, we added the magnitudes of the astigmatism and Petzval contributions. This is known to be a worst-case situation, so there is some justification for optimism. Furthermore, preliminary results of ray tracing analyses on an optimized RC telescope are encouraging. We are optimistic.

Redundancy is desired in spacecraft systems to avoid single points of failure. In our array size arguments, we assumed a square array. However, for redundancy, we will place two identical arrays within the FOV. Redundant rectangular arrays are



illustrated in [Figure 2-8](#) (Redundant Arrays in the Field of View). Redundancy reduces the array width by a factor of 2. The optimistic family of redundant array sizes is 1024 x 512 for channel 1, 256 x 128 for channel 2, and 128 x 64 for channels 3-5.

We assume square pixels in the array. For a channel 1 silicon array, we assume a 15 μm pixel edge. For InSb (channel 2), we assume 30 μm , and for HgCdTe (channels 3, 4, 5), 40 μm . These dimensions are typical of commercial products. The corresponding physical dimensions of the optimistic array family are 15.4 x 7.7 mm (channel 1), 7.7 x 3.8 mm (channel 2), and 5.1 x 2.6 mm (channels 3-5).

2.5 SCANNING

Before discussing scanning techniques, we need to distinguish between *scene pixels* and *detector pixels*. Scene pixels are characteristic of the object (the Earth) and are characterized by the nadir resolution or equivalent angle (IFOV). For the visible channel, the entire 20 degree x 20 degree field of regard (FOR) is divided into 6.2×10^8 scene pixels. Each of these scene pixels represents an angular IFOV of $(14 \text{ urad})^2$, corresponding to an area of $(0.5 \text{ km})^2$ at the subsatellite point (nadir). The detector array comprises a number of detector pixels. A detector pixel is a very small square area of detector material, measuring $(15 \text{ um})^2$ in the case of the visible channel. The system optics image scene pixels onto detector pixels in the focal plane.

Two methods of scanning are addressed: step-stare and time delay and integration (TDI). We first address the step-stare scan technique. The 20 degree x 20 degree FOR is to be scanned in 3 minutes. With the optimistic array set, all five arrays see the same 0.82 degree x 0.41 degree FOV. There are 1190 FOVs in the FOR. To accomplish a 180 sec scan, the FOV may dwell up to $180/1190 = 151$ milliseconds (msec). We will see later that this time interval is very long in comparison with maximum integration (exposure) times for detector arrays.

In a step-stare scan, it is desirable to overlap the FOV steps. Overlap allows consecutive FOV registration and partially compensates for any dead pixels in the detector array. Dead pixels are programmed out of the final sum. Consider the FOV of the array oriented to view 0.82 degree in the North-South direction and 0.41 degree in the West-East direction. If we require that every scene pixel (e.g., 0.5 km x 0.5 km Earth region) be viewed by four different detector pixels and their results averaged, then the 0.82 degree x 0.41 degree FOV will advance by 0.205 degrees in a west/east scan line. After completion of a scan line, the FOV will step downward (north/south direction) by 0.41 degrees. This is equivalent to a FOV measuring 0.41 degrees x 0.205 degrees stepping through the FOR. The maximum dwell in this case is 38 msec--still relatively long compared with detector saturation exposure times. Thus, even with a four-fold FOV overlap, step-stare dwell times are not limiting.

TDI is an alternative scanning technique. To illustrate TDI, we look at

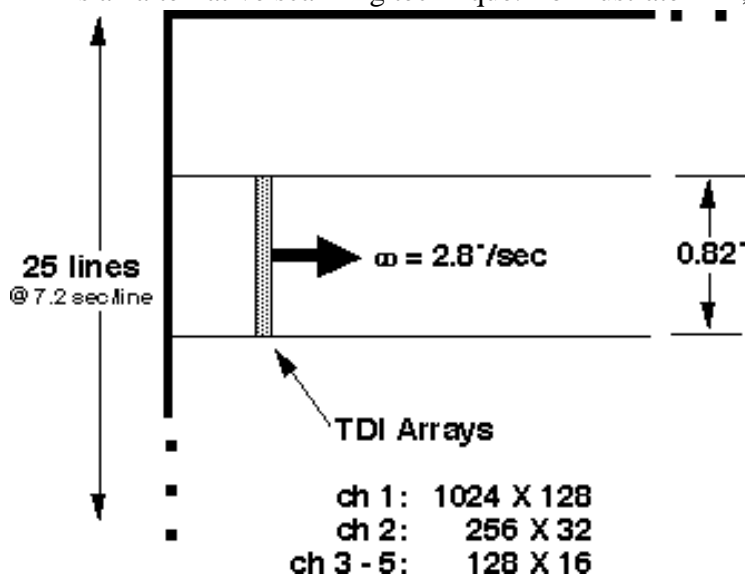


Figure 2-9 (TDI Scanning) and suppose that the 20 degree x 20 degree FOR is divided into 25 horizontal scan lines (20 degrees/0.82 degrees ~ 25). For channel 1, we use a 1024 vertical x 128 horizontal array. This array, as well as the other coregistered arrays, scans horizontally at a rate of 2.8 degrees/sec to form a 3 minute full disk image. As the array scans horizontally, each channel 1 scene pixel is seen by 128 detector pixels. The accumulated photoelectrons from the 128 pixels are added, and the final sum is read out.

As long as the detector pixels do not fill to saturation, there is an SNR performance benefit provided by the TDI scan over the step-stare approach. Essentially, this benefit arises from the coherent linear addition of signal photoelectrons to the incoherent root mean square (rms) addition of noise electrons. If there are m pixels in TDI, the SNR is improved by a factor of \sqrt{m} . Measurements have shown this improvement is valid and precise. With 128 pixels in TDI, channel 1 will have an improvement of 11.3 over the step-stare scan.

Our choice of 128 pixels in TDI for channel 1 is arbitrary. Silicon arrays have been made with 96 pixels in TDI, and 128 is not

unreasonable. [Figure 2-9](#) shows a family of TDI array sizes for all five channels. These arrays would be coregistered, simultaneously viewing the same scene area. At an angular velocity of 2.8 degrees/sec (7.2 sec/line), the maximum dwell time *per detector pixel* is 0.289 msec for channel 1, 1.156 msec for channel 2, and 2.312 msec for channels 3-5. [Figure 2-9](#) shows the TDI array scanning from left to right. At the end of this scan line, the array moves to the next scan line and moves right to left, with reversal of the charge addition process. This feature is referred to as a bidirectional TDI array. Redundant TDI arrays are easily fit within the telescope's FOV since, the TDI arrays are thinner than those portrayed in [Figure 2-8](#).

In addition to the SNR enhancement, TDI offers several other advantages over the step-stare scan. The adding/averaging process of TDI results in better pixel-to-pixel response uniformity. As will be discussed later, uniformity is very important for array imagers. Inoperable or dead pixels may be deselected in a TDI array. Furthermore, the redundancy inherent in the TDI array lessens production yield requirements, and therefore reduces development risk and cost. All focal plane vendors and sensor system developers contacted during the course of this effort were advocates of TDI. Further arguments on the TDI/step-stare tradeoff, from a navigation/registration perspective, are found elsewhere in this document.

Whether a TDI or step-stare scan is employed, we can estimate the downlink data rate from the satellite to a ground station. The data rate is found by determining the total number of scene pixels, encoding each pixel in a data word, and then transmitting the resulting data load within a specified (3 minute) interval. The total number of scene pixels is 6.9×10^8 . Later, we will see that radiometric goals require encoding with 11 bits/pixel, and on top of this we allow a 20 percent overhead. The resulting data load is 9.1×10^9 bits (b). If this data load is sent within 3 minutes, the data rate is on the order of 50 megabits per second (Mbps). However, data compression could result in a reduced data rate. Therefore, with compression the downlink would require a data rate well within transponder capability that would be employed on a nondedicated communications satellite.

2.6 RADIOMETRIC PERFORMANCE

The dwell times determined in the previous section are an upper bound on detector integration times. The integration time is determined by the upper end of the instrument's dynamic range, and detector characteristics such as quantum efficiency and electron well capacity. These parameters depend on the detector material system, pixel size, and maximum radiation level from the scene. Integration times will vary considerably over the five channels.

Maximum IR radiation levels are at a scene temperature of 350 degrees K. [Table 2-3](#) provides the 350 degrees K photon sterance levels, $L_{\lambda, \lambda_1, \lambda_2}$. The resolution areas, Ares, of the blackbody sources are $(2 \text{ km})^2$ for channel 2 and $(4 \text{ km})^2$ for channels 3-5. The 30 cm optical aperture of the telescope subtends a solid angle of $[\Omega] = 5.5 \times 10^{-17} \text{ sr}$, and we assume that the transmission of the optical system (fore and aft optics) is $[\tau] = 0.25$. The integration time is often defined as the time to fill the electron well to half capacity (0.5w). This leaves a little reserve to prevent the possibility of saturation. The integration time is:

$$t_{\text{int}} = \frac{0.5w}{L_{\lambda, \lambda_1, \lambda_2} A_{\text{res}} \Omega \tau}$$

The quantum efficiency of the detector is $[\eta]$. We use $[\eta] = 0.55$ for both InSb and HgCdTe, but $[\eta] = 0.0042$ for the PtSi channel 2 alternative. Well capacities, taken from the technical literature on commercial array products, are $w = 1.6 \times 10^7$ e- for InSb, 4.0×10^7 e- for HgCdTe, and 1.7×10^5 e- for PtSi.

The integration times work out to 19 msec for channel 2 with InSb, 0.5 msec for channel 3, and 0.165 msec for channels 4 and 5. If PtSi were used for channel 2, the integration time would increase to 26 msec. Clearly, channel 2 paces the system because of its longer integration time. The other channels must be shuttered or attenuated to balance the integration times.

The integration times all fall well within the maximum dwell times for the overlapping step-stare scan with optimistic array sizes. However, for the TDI scan, we previously found that the maximum dwell times *per detector pixel* were 1.16 msec for

channel 2, and 2.32 msec for channels 3-5. The implication is that with a 3 minute TDI scan, the integration time of channel 2 will be limited by the mechanics of the scan. This may be offset by the SNR enhancement provided by TDI. The impact on channel 2's radiometric performance from this limited integration time is examined later.

The per pixel integration time for the visible channel 1 is based on the characteristics of a commercially available 1024 x 96 TDI array. In this array, the TDI process works on the bucket brigade principle. Each pixel in TDI accepts the accumulated charge from the previous pixels and adds to this charge during its own integration time. The charge is then passed along to the next pixel. The specified saturation exposure pertains to the total integration time (i.e., the sum of all the TDI exposures).

The saturation exposure for channel 1 is determined at 100 percent albedo, which is $9.60 \times 10^{-3} \text{ W}/(\text{cm}^2 \cdot \text{sr})$ (see [Table 2-4](#)). With the previous assumptions for solid angle, transmission, and with a resolution area of $(0.5 \text{ km})^2$, the maximum incident optical power level is 330 pW. The channel 1 integration time is determined from the specified saturation exposure and pixel area as:

$$t_{\text{int}} = \frac{E_{\text{sat}} A_{\text{pixel}}}{P_{\text{max}}} = \frac{(1.3 \times 10^{-9} \text{ J}/\text{cm}^2)(1.24 \times 10^{-5} \text{ cm}^2)}{330 \times 10^{-12} \text{ W}} = 4.9 \text{ } \mu\text{sec}$$

This per pixel integration time is for each of the 96 pixels in TDI. The total time for all 96 integrations is 470 usec. Scaling the integration time to our case of 128 pixels in TDI, the channel 1 per pixel integration time is $t_{\text{int}} = 3.7 \text{ usec}$.

Except for channel 2, the mechanical dwell times exceed the pixel integration times. To avoid saturation of the other channels, they may be attenuated to balance the exposures. An appropriate attenuation factor is found from the ratio of integration time to dwell time. Attenuation factors for exposure balancing are given in [Table 2-7](#). With exposure balancing, all detectors integrate for their full mechanical TDI dwell time. For all channels, the total TDI integration time is 37 msec (= $128 \times 289 \text{ usec}$ = $32 \times 1156 \text{ usec}$ = $16 \times 2312 \text{ usec}$).

At 0.5 percent albedo, the optical power collected by the telescope aperture for channel 1 is 6.4 pW. With an aft optics transmission of $[\tau]_o = 0.25$ and a neutral density filter with $[\tau]_{\text{nd}} = 0.013$ for exposure balancing, the detector collects $P_{\text{min}} = 21 \text{ nW}$. With 128 pixels in TDI, the SNR is:

$$\text{SNR} = \frac{128 R P_{\text{min}} t_{\text{dwell}}}{V_{\text{noise}} A_{\text{pixel}}} = 1200$$

where the responsivity is $400 \text{ V} \cdot \text{cm}^2/\text{uJ}$, and the specified rms noise voltage is $V_{\text{noise}} = 0.2 \text{ mV}$. A SNR of 1200 at 0.5 percent albedo greatly exceeds the required value.

For IR photon detectors, a well-known figure of merit is the detectivity, D^* . D^* is the reciprocal of the detector's noise equivalent power. It is used in determining the detector's NEdT performance. There is a theoretical limit to D^* based on the detector's cutoff wavelength, $[\lambda]_c$ and quantum efficiency, $[\eta]$, and the background photon flux, Q , seen by the detector. For a photovoltaic detector, the theoretical limit is:

$$D^* = \frac{\lambda_c}{2 h c} \sqrt{\frac{2 \eta}{Q}} = 3.56 \times 10^{18} \lambda_c \sqrt{\frac{\eta}{Q}} \quad (\text{cm} \cdot \sqrt{\text{Hz}} / \text{W})$$

where $[\lambda]_c$ is in microns, and Q is in photons/(sec \cdot cm 2). This is called the background-limited (BLIP) D^* . Depending on the cutoff wavelength and detector temperature, state-of-the-art IR detectors can approach the theoretical limit to D^* .

The smaller the background flux Q , the better the detectivity. For our application, Q is limited spectrally by channel bandpass

filters. Additionally, Q can be limited spatially with a cold shield or cold stop. The cold shield, specified by its f/# or cone angle, prevents radiation from IR sources at angles greater than the cone angle. For our computations, we use an f/2 cold shield. The cold cone has a 29 degree full angle and reduces background flux by a factor of 16, thereby improving D* by a factor of 4.

Theoretical D* values were computed for each material system ([eta] = 0.55 for InSb and HgCdTe; [eta] = 0.0042 for PtSi) and each channel at the scene temperatures of interest. The resulting BLIP D*s are given in [Table 2-8](#).

Several FPA vendors claimed that for the lower-wavelength channels (2 and 3), a 50 percent BLIP D* could be expected; however, for the longer-wavelength channels (4 and 5) only 10 percent BLIP could be expected. We followed their suggestions for the computation of NEdT performance. NEdT can be evaluated in terms of system parameters as:

$$\text{NE}\Delta T = \frac{\lambda_c \sqrt{A_{\text{det}}}}{hc \tau \left(\frac{dL_{q,\lambda_1,\lambda_2}}{dT} \right) A_{\text{res}} \Omega D' \sqrt{t_{\text{int}}}}$$

[Table 2-9](#) shows NEdTs computed for the step-stare scan with 50 percent BLIP detection assumed for channels 3 and 4, and 10 percent BLIP for channels 4 and 5. Values in parentheses do not meet the GOES N desired NEdT performance levels of [Table 2-2](#); the majority of cases fall in this category.

Improvements in NEdT performance are attained with TDI scanning. The improvement reduces the NEdT by a factor of $[\sqrt[m]]{m}$, where $m = 32$ for channel 2, and $m = 16$ for channels 3-5. NEdTs for a TDI scan are shown in [Table 2-10](#). It is important to note that we have not assumed bucket-brigade-style charge-passing pixels as we did for the visible channel. Rather, we have assumed here that the charge is removed from each pixel after it is exposed. The charges are then added in a higher electron-well capacity CCD. This assumption means that the *per pixel* integration time for TDI is the same as the step-stare integration time tint. The total TDI integration time is therefore mt_{int} . This assumption allows us to divide the step-stare NEdT values by $[\sqrt[m]]{m}$ without worrying about overexposure.² We discussed this assumption with array developers, they considered it to be a reasonable assumption.

The TDI calculations show that all desired NEdT performance goals are met or exceeded except for the case of using a PtSi detector array. Its low quantum efficiency and detectivity result in very poor performance. PtSi is therefore considered no further.

The NEdT calculations were performed under the tacit assumption of perfect response uniformity from pixel to pixel in the array. Of course, nothing is perfect, and there will be some level of nonuniformity. Nonuniformities take the form of variations in quantum efficiency from pixel to pixel, response nonlinearities, and variations in offset (response under conditions of no light). In attempting to measure small temperature differences over the array, response nonuniformities will appear as noise. Characterization and correction of the array and frequent calibration will help. However, there will still be *residual* nonuniformity. Our next step is to determine a bound for residual nonuniformity. This bound depends on the NEdT.

The inverse Planck function is used in ground processing to determine the temperature from the estimated number of photons collected by the imager from the scene resolution area.

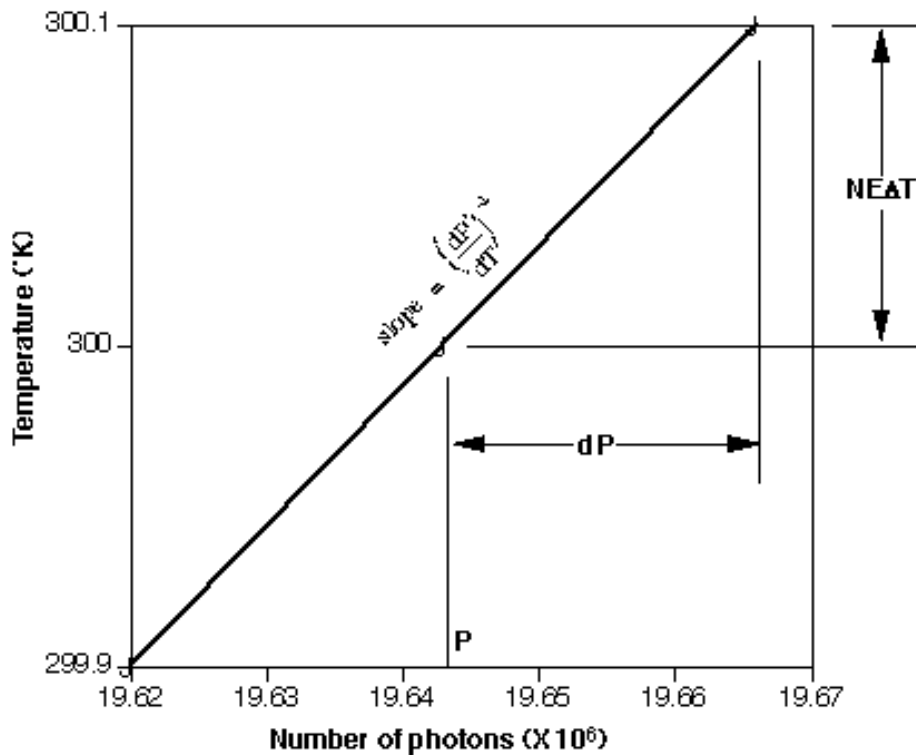


Figure 2-10 (Temperature Resolution) shows the

inverse Planck function for channel 5 around 300 degrees K. The abscissa is the number of photons, P , collected during the 165 usec integration time, and the ordinate is the corresponding temperature as determined by the inverse Planck function. The desired 0.1 degree NEdT is indicated. If residual nonuniformities result in a pixel-to-pixel variation, dP , in the estimated received number of photons, then to achieve a specified NEdT, the relative variation must be bounded by:

$$\frac{dP}{P} \leq \frac{NE\Delta T}{P} \left(\frac{dP}{dT} \right)$$

P and $\frac{dP}{dT}$ are the Planck function and its derivative. Thus the NEdT sets a bound on residual array nonuniformities. We determined the maximum residual nonuniformities for all channels and their specified scene temperatures. The results are given in [Table 2-11](#). The most demanding requirements are imposed by channels 4 and 5 at the scene temperature of 300 degrees K. To achieve the GOES N desired 0.1 degree NEdT, a residual array nonuniformity of less than 0.1 percent is required. Experimental residual nonuniformities as low as 0.012 percent [GOESN91] have been reported. Other developers have reported TDI arrays with 0.1 percent nonuniformity. The requirement is therefore within the state of the art.

The TDI scan provides a better uniformity characteristic than the step-stare scan. By summing m pixels in TDI, the standard deviation is reduced by a factor of $[\text{radical}]m$. This further amplifies the arguments favoring the TDI scan.

Another impact levied by the NEdT requirement, along with the extended dynamic range, lies in encoding of the pixel samples. Specifically, the number of bits used to encode each sample is determined from these performance requirements. An insufficient number of bits will result in quantization noise greater than the desired NEdT. We use the worst case of channel 5 for this analysis.

At the maximum temperature of 350 degrees K, the spectral photon exitance (see Appendix A) from a blackbody at $[\lambda]$ = 12 μm is $Q_{\text{max}} = 3 \times 10^{17}$ photons/(sec*cm² * μm). The electrical output of an ideal photodetector is proportional to the input photon flux. If there are N bits for encoding, there are 2^N levels (bins) into which the detector's output is quantized. If the flux range from 0 to Q_{max} is divided equally into 2^N levels, then the flux increment dQ is:

$$\Delta Q = \frac{Q_{\text{max}}}{2^{\frac{N}{2}}}$$

With $N = 10$ bits for encoding (as is used in GOES I-M), the flux increment is $dQ = 2.9 \times 10^{14}$ photons/(sec*cm²*μm). A plot of the inverse Planck function for channel 5 in increments of dQ is given in

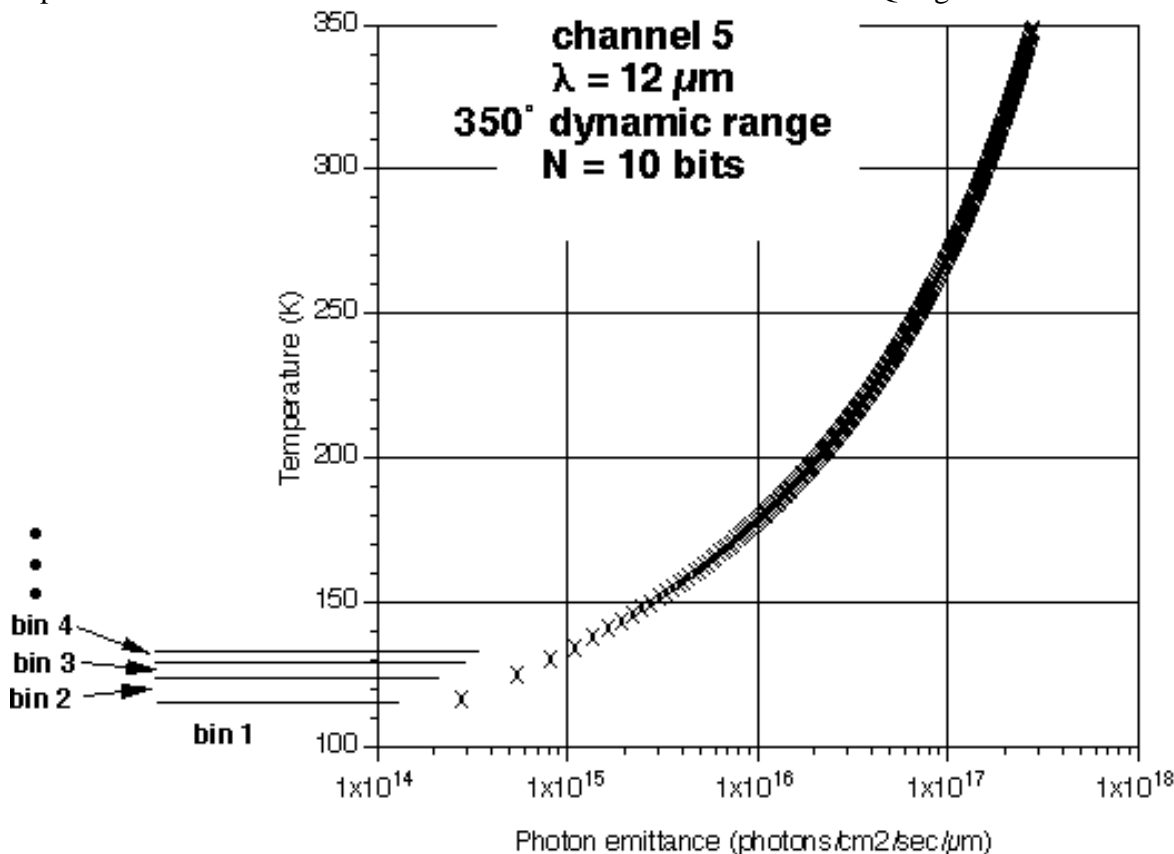


Figure 2-11 (Inverse Planck

Function for Channel 5). Detection of flux values in the range of 0 to dQ is in the first bin. The corresponding temperature is 116 degrees K. Any scene temperatures up to 116 degrees K are quantized to this first bin. The next dot up the curve is at $T = 124.3$ degrees K at twice the unit flux $2dQ$. Any scene temperature between 116 degrees K and 124.3 degrees K is quantized in the second bin. The resolution rapidly improves with temperature since the inverse Planck function becomes very steep. Resolution is defined here as the difference in temperature levels separated by unit flux steps dQ .

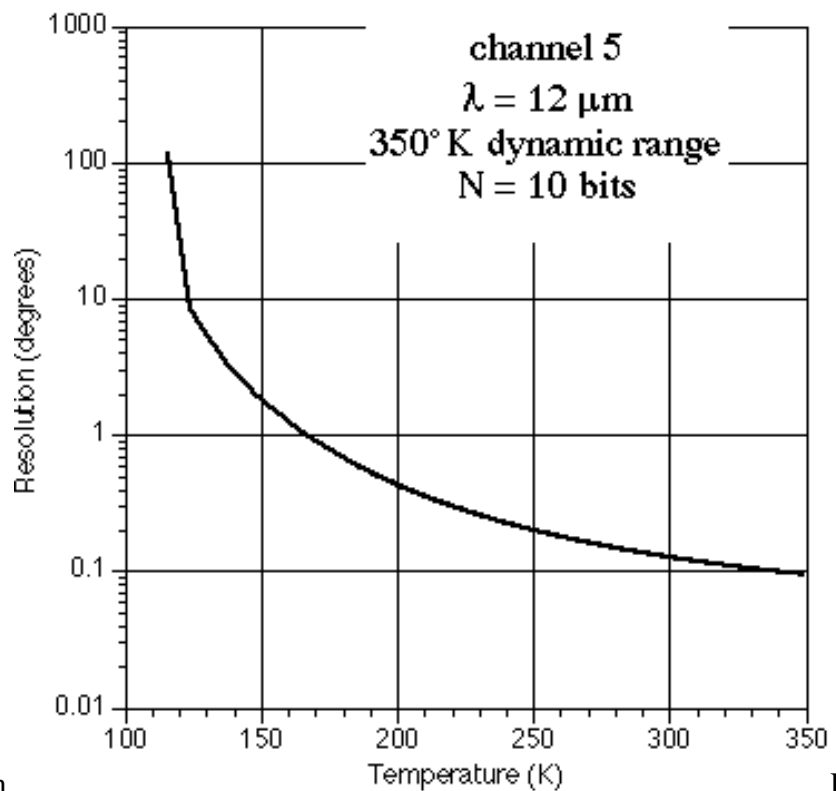


Figure 2-12

Resolution as a function of temperature is seen in (Quantization Noise Resolution for Channel 5). At 200 degrees K, the resolution is 0.44 degrees, which is within the desired 0.5 degree specification. Similarly, at 240 degrees K, the resolution is 0.23 degrees, which is within the 0.3 degree specification. However, at 300 degrees K, the resolution is 0.13 degrees and is worse than the desired 0.1 degree specification. In this case, quantization noise is larger than the desired NEdT. Encoding with more than 10 bits will decrease quantization noise and improve resolution. We found that with 11 bits, the quantization noise allows a resolution of less than 0.07 degrees on a 300 degree K scene, and 12 bits are necessary to resolve better than 0.05 degrees.

2.7 DETECTOR COOLING

To approach background limited detection, the IR detector arrays must be cooled. The maximum detector temperature for BLIP operation is a function of cutoff wavelength and background flux levels: the longer the cutoff wavelength, the colder the detector must be. The cutoff wavelength for channel 5 is at 13.5 μm , one micron above the upper end of its optical passband. With an $f/2$ cold stop, a scene at 200 degrees K gives a background flux of 5.7×10^{15} photons/(sec*cm²). Using IR Handbook nomographs, [WOLFE89] we found the maximum detector temperature for BLIP operation to be 80-85 degrees K. However, this is a theoretical maximum, and all focal plane array developers we contacted emphasized the importance of operating at 65-70 degrees K. In addition to cooling the IR detector arrays, the cold shields and aft optics of the imager system must be cooled, though not necessarily to the temperature of the detector arrays.

A passive radiative cooler radiates heat into cold space. The *ideal* radiative cooler radiates a flux, Q , from its area, A , at temperature T according to Stefan-Boltzmann's law:

$$\frac{Q}{A} = \sigma T^4,$$

with $[\sigma] = 5.67 \times 10^{-8} \text{ W}/(\text{m}^2 \cdot \text{K}^4)$. If we estimate a minimum heat load of $Q = 1 \text{ W}$ for array dissipation and parasitic heat creeping through support structures, and require the radiative cooler surface at a temperature of $T = 60$ K to provide a temperature difference between the arrays and the radiator for heat to flow through a reasonably sized thermal link, then the minimum area of the radiator is found to be $A = 1.4 \text{ m}^2$ or 1.2 m on edge. This is a large radiator and would, in practice, probably be larger because of less-than-ideal conditions. In fact, a doubling of the radiator area might be expected in practice. This large radiating surface must be thermally isolated from the platform on which it is mounted, and shielded from

sunshine and Earthshine. Shielding of such a large surface may be very difficult to achieve on a nondedicated spacecraft. We therefore turn our attention to mechanical coolers.

Two mechanical coolers that show promise of long-lifetime operation are the Stirling engine and the reverse turbo-Brayton refrigerator. Both of these refrigerators have been designed for 10-year operating lifetimes. The Stirling engine for British Aerospace was originally designed by Oxford University and Rutherford Appleton Laboratory. The Stirling cooler consists of three components: a compressor, a displacer, and electronics. The detector is cooled by thermal contact with a *cold finger*. This cooler can supply 0.8 W of cooling capacity at 80 degrees K with a power consumption of 35 W. The mass of the refrigerator is 8.4 kilograms (kg) (18.5 pounds). In 1992, the Stirling cooler was flying on the Improved Stratospheric and Mesospheric Sounder (ISAMS) experiment on the NASA Upper Atmosphere Research Satellite (UARS), and on the European Remote Sensing (ERS-1) Satellite. Stirling coolers are being built in the United States by TRW, Creare Inc., Hughes, Lockheed, and Ball Aerospace. TRW has developed and tested a miniature Stirling engine capable of 0.25 milliwatt (mW) cooling at 65 degrees K with a power input of 18 W.

Creare Inc. is developing a 65 degree K Stirling cooler with a 2 W capacity, with a 60 W input power and a target mass of 14 kg (31 pounds). The cooler is designed for a 10 year lifetime with 95 percent reliability. The Ball Aerospace Stirling cooler can provide 0.8 to 3 W of cooling capacity at 80 degrees K, with a power consumption of 60 W. Its mass is 12 kg (26.4 pounds), and is also designed for a 10 year lifetime.

The reverse turbo-Brayton refrigerator, also under development by Creare, works by compressing and expanding neon gas through tiny turbines. The compressor turbine rotates at 300,000 revolutions per minute (rpm), and the turbo-expander spins at 600,000 rpm. After the refrigerator starts and the turbines lift off, the turbine rotor is suspended on gas bearings, and there are no touching parts to wear out. The most likely failure mechanism is the three-phase motor that spins the turbines. Other factors that could affect reliability are particle jamming (e.g., impurities in the neon gas) and material mismatches. The lifetime goal is 10 years. The cooler is being designed to deliver 5 W of cooling at 65 degrees K, with a power consumption of 200 W (specific power = 40W/W). The mass of the cooler is 13.7 kg (30 pounds).

The reverse turbo-Brayton refrigerator is preferred over the Stirling engine for our imager application. One reason is that piston movements of the Stirling engine impart some level of vibration to the host spacecraft, whereas with the Brayton, virtually no vibration is imparted to the mounting structure. The second reason is that the Stirling refrigerator is basically designed to handle only a single load at the end of its cold finger. In our multiple-array application, several Stirling engines would be required, and several more when redundancy is considered. The turbo-Brayton, however, can service multiple loads at multiple locations. Our imager will have as many as four IR arrays, cold shields, and optics to be cooled, and the turbo-

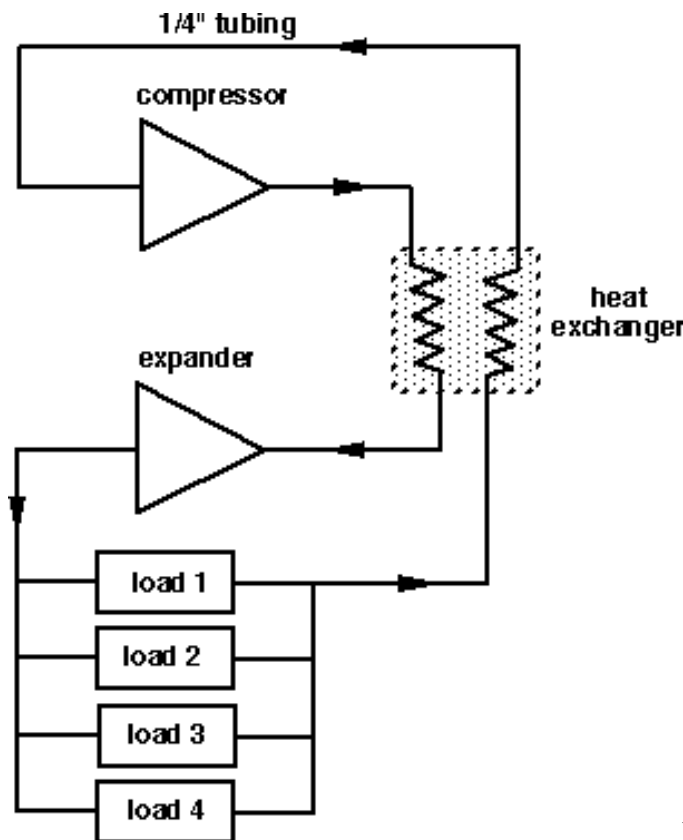


Figure 2-13 (Reverse Turbo-

Brayton Refrigerator with Multiple Heat Loads) is a schematic of the components of a turbo-Brayton refrigerator, with multiple loads being cooled in parallel. The neon gas flows through 1/4" tubing. Refrigerator plumbing lines may be routed to various array and aft optics locations.

A typical lifetime design goal specification is a 95 percent chance of operation after a period of 10 years. Thus the probability of failure of a single refrigerator is $p = 0.05$ after 10 years of operation. With a redundant compressor, expander, and motor, the probability of failure is $p^2 = 0.0025$ or 0.25 percent. A redundant compressor and expander system would be valved into the plumbing of the primary system.

Technical risk lies in the lifetime of the mechanical coolers. Design goal lifetimes may be quoted at 10 years, but there are no flight test data over this long period of time. The turbo-Brayton refrigerator is still under development. A brassboard model now exists, and an engineering development model (EDM) is to be completed by the end of the third quarter 1993. The EDM will then be subjected to laboratory testing and parametric mapping. The current development schedule calls for protoflight hardware to be constructed by early 1995. Low-rate initial production (LRIP) refrigerators, if funded, would be available in the 1996/7 time frame.

2.8 DESIGN CONSIDERATIONS

The fore optics consist of the scan mirror and telescope. The aft optics reside behind the primary mirror of the telescope. The functions of the aft optics are to separate the collected radiation into the spectral channels, prevent stray radiation by stopping and filtering the beams, and focus the beams on the focal plane detector arrays.

Approaches to spectral separation of the beam include dispersion by a prism, diffraction with a grating, and optical filtering. The benefit of spectral separation with a prism or grating is less loss than an approach using beamsplitters. Several filters (dichroic beamsplitters) in series add to the loss of the system. Another advantage of a prism/grating separation over the full IR band of interest (3.8-12.5 μm) is that it would provide the hook for adding additional spectral channels desired for GOES N. With the series beamsplitter approach, adding extra channels would radically alter the optical layout and add to insertion losses. With a grating or prism, the separation is done over the full band, and it is a matter of component spacings to collect and focus the wavelengths of interest. The concept of spectral separation with a grating over the full IR band of the imager is

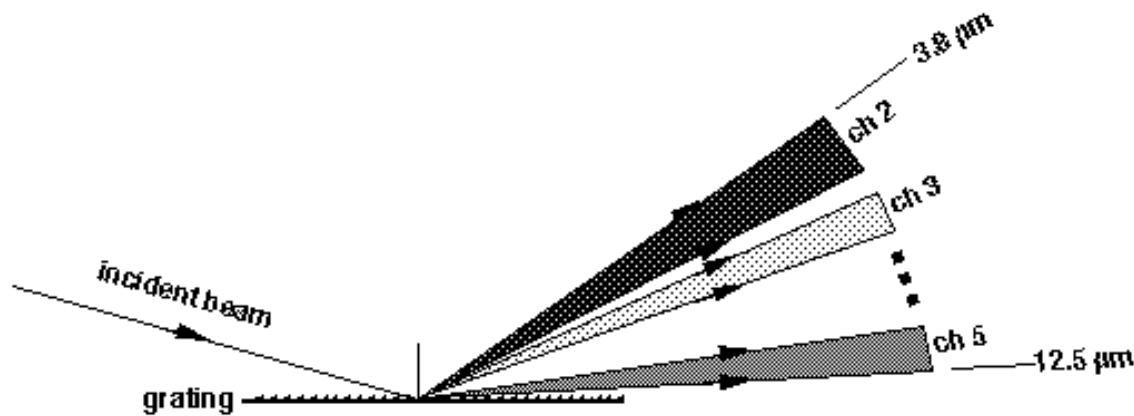


Figure 2-14 (Spectral

illustrated in Separation with a Grating). The concept is similar with a prism.

A recent study [GOESN91] suggests an approach that avoids beamsplitters. It describes a common extended focal plane providing enhanced channel-to-channel co-registration. However, no method is suggested as to how the beam is to be spectrally separated.

A potential problem with the grating or prism is that the passband of both channels 4 and 5 is 1 μm wide, and the upper edge of channel 4 (11.2 μm) is only 0.3 μm from the lower edge of channel 5 (11.5 μm). The diffraction (or dispersion) required to separate these channel edges and also to work over the full 3.8 μm -12.5 μm spectrum could result in a very complicated aft optics system, possibly more complex than that of the beamsplitter approach. The grating/prism approach needs further analysis.

Another imager instrument design issue is the use of a common FPA for multiple channels. Let us examine the radiometric performance penalty for a common array. Suppose that all four IR channels are to be detected with a common focal plane detector array. The only possible material system is HgCdTe, and the cutoff wavelength must be around 13.5 μm , 1 μm above

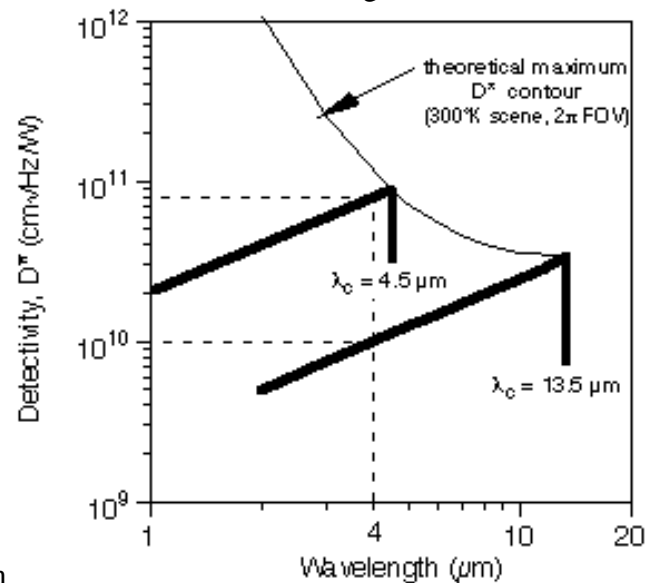


Figure 2-15

the upper band edge of channel 5. The thin-line curve in (Detectivity Tradeoff (300 degrees K Scene, 2π sr FOV)) shows the well-known contour for the theoretical maximum detectivity with a 300 degree K background flux. The detector FOV is 2π sr. For a cutoff wavelength λ_c , the contour gives the maximum achievable D^* for an HgCdTe detector ($\eta = 0.55$). The theoretical detectivity curves for two detector arrays are shown with thick lines--one with the required 13.5 μm cutoff and the other for an array with a 4.5 μm cutoff.

We wish to compare the degraded performance of channel 2 detected with a 13.5- μm -cutoff common array against the performance of a system with an array optimized for channel 2 (i.e., with $\lambda_c = 4.5$ μm). The penalty at 4.0 μm , projected with dashed lines in [Figure 2-15](#), is a factor of 8 in detectivity. The detectivity of the optimized 4.5 μm cutoff

detector at 4 μm is $8 \times 10^{10} \text{ cm} \sqrt{\text{Hz/W}}$, whereas if the 13.5- μm -cutoff common array is used, the detectivity is $1 \times 10^{10} \text{ cm} \sqrt{\text{Hz/W}}$. Furthermore, since array developers were consistent in estimating 10 percent BLIP for long-wavelength IR detectors and 50 percent BLIP for short-wavelength IR detectors, the degradation factor is multiplied by a factor of 5. The estimated D^* degradation is therefore on the order of a factor of 40. It follows that NEdT performance will suffer by a factor of 40. The feasibility of a common array for all four IR channels is therefore questionable.

In our discussions with detector array developers and imaging system houses, the possibility of using a single HgCdTe array for channels 4 and 5 was suggested. The possibility of using an InSb array for both the visible channel and the 3.8-4.0 μm IR channel was also discussed. A tradeoff similar to that illustrated in [Figure 2-15](#) may be performed on the case of combining channels 4 and 5; only a small penalty is expected. These two-channel combination cases need further analysis. Here we proceed under the assumption of four separate IR detector arrays.

We now focus on a specific optical implementation for the imager. It is a preliminary design and is not optimized. Its purpose is to identify optical parameters (lens spacings, surface curvatures, focal lengths, etc.) to a point where analysis of optical performance (e.g. spot size, transmission) can be carried out by ray-trace simulation. This analysis would be used to determine problems and optimize performance. Such analysis was beyond the resources available for this effort, but should be performed in the event of a follow-on effort. We assume a system with five FPAs, and therefore five separate optical paths.

If a detector pixel is square with an edge length h , and an IFOV is to be focused within the pixel, then the required system focal length, f , is:

$$f = \frac{h}{\text{IFOV}},$$

where the system consists of the combination of fore and aft optics.

The required IFOVs and assumed pixel sizes, shown in [Table 2-12](#), determine the necessary focal lengths for the various optical paths of the system.

The focal length of the RC telescope is $f_T = 360 \text{ cm}$. For each channel, a lens system must be placed between the telescope and the detector array. The system focal length, f , is approximated from the thin lens equation:

$$\frac{1}{f} = \frac{1}{f_T} + \frac{1}{f_L} - \frac{f_T - x}{f_T f_L},$$

where x is the location of the principal point of the lens system measured from the focal point of the telescope. To determine the appropriate lens focal lengths, we solve this expression for f_L in terms of f_T and f . The required lens focal lengths are determined from:

$$f_L = \frac{fx}{f_T - f} = \frac{x}{\left(\frac{360}{f}\right) - 1}$$

(x, f in cm).

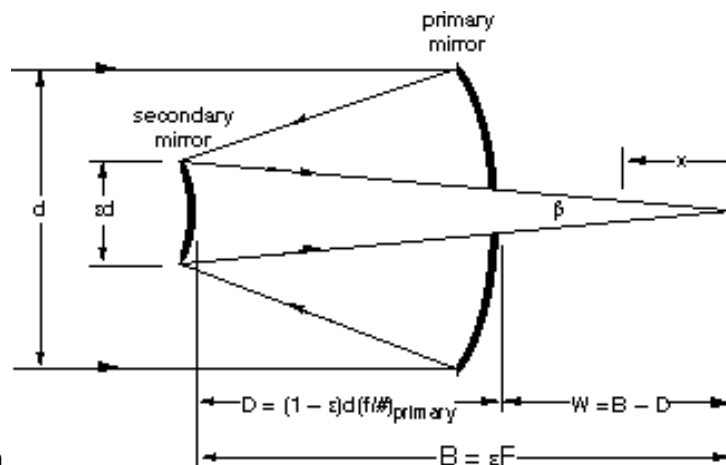


Figure 2-16 (Telescope Geometry), and the coordinate x is shown. For the $f/12$, $d = 30$ cm, $f/1.4$ primary RC telescope under consideration, the telescope parameters are:

focal length $f_T = 360$ cm

obscuration $[\epsilon] = 0.25$

beam angle $[\beta] = 4.77$ degrees

mirror spacing $D = 31.5$ cm

back focal length $B = 90$ cm

working distance $W = 58.5$ cm (behind primary, before focus).

The range of the coordinate x is up to $W = 58.5$ cm.

Our design uses a series of dichroic beamsplitters for spectral separation of the five channels. The diameter of the telescope beam as it just emerges behind the primary mirror is 4.88 cm. We use a series of 45 degree-oriented beamsplitters, each being the diagonal of a 6 cm x 6 cm x 6 cm cube. Our first aft optics design is illustrated in

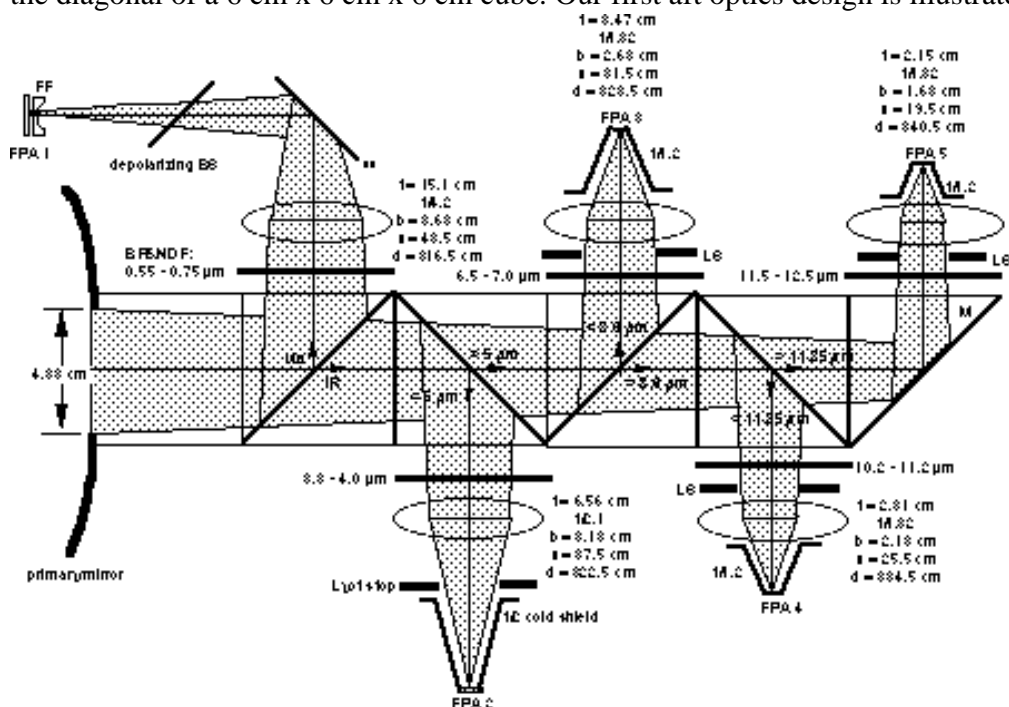


Figure 2-17 (First Aft Optics Design). Lens

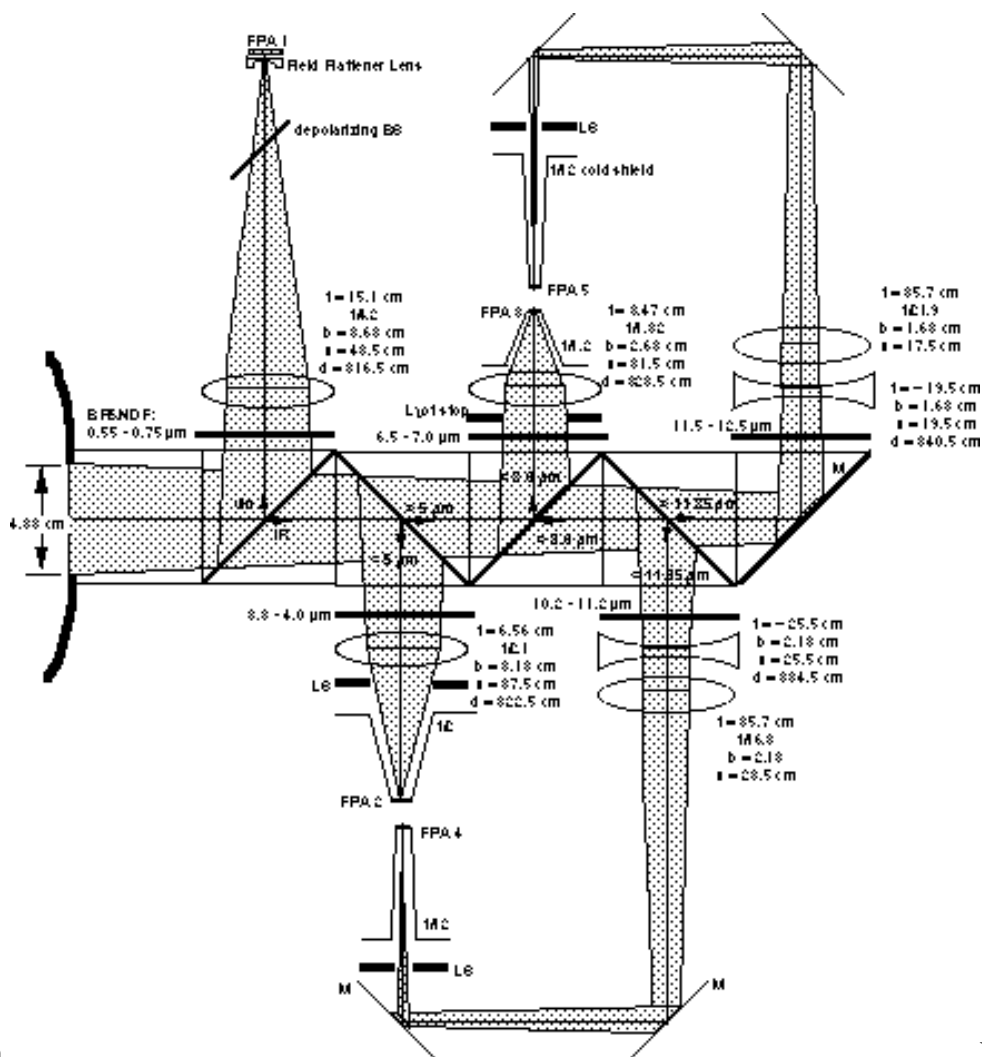
positions, beam diameters, focal lengths, and operating f/numbers are shown for each lens.

The first dichroic beamsplitter in the optics train splits the visible from the IR channels. The visible channel 1 is filtered and attenuated by an optical bandpass filter and neutral density filter (BP&NDF). The total attenuation of the BP&NDF was given in [Table 2-7](#). The visible beam is then focused by an f/4.2, 15.1 cm lens onto the visible detector array. The beam is depolarized by a beamsplitter and corrected for the telescope's Petzval curvature by a field flattener lens.

The second beamsplitter in line separates the IR spectrum at 5 μm . Channel 2 is split off, filtered and attenuated, and focused by an f/2.1, 6.56 cm lens. The FOV of the channel 2 detector array is limited by an f/2 cold shield. A Lyot stop images the entrance pupil and prevents stray light from reaching the detector array.

Channels 3, 4, and 5 are split off in sequence and then focused with f/1.32 lenses. Their cold shields have been set at f/1.2. We previously computed detectivities and NEDTs based on an f/2 cold shield; however, this optics design requires a wider-angle f/1.2 cold cone. The improvement factor at f/2 was a factor of 4, whereas with an f/1.2, we only obtain an improvement of 2.6. The net result is that the D*s and NEDTs are degraded by a factor of 1.5 from the values we computed earlier.

Notice that the focal lengths of channel 3, 4, and 5 relay lenses are short. Each beam focuses quickly after its lens. This is undesirable because these infrared beams cannot be folded, with mirrors, to a common location for cooling. Cooling would be more efficient if the detectors were in close proximity. The beamsplitter orientations could be rotated to get the detector arrays closer together. Imagine, for example, that the beamsplitters and following optics for channels 2 and 4 were rotated 90 degrees, so that the detector arrays came out of the page. Still, the short focal lengths prevent a common cold area.



A second aft optics design is illustrated in [Figure 2-18 \(Second Aft Optics Design\)](#). Here we have altered the optics of channels 4 and 5. These beams are collimated by negative

lenses and then focused by a positive lens with the proper focal length. This allows long high f/number beams, which can be redirected by folding mirrors. Channels 3 and 5 are in close proximity, as are channels 2 and 4. The beams of channels 4 and 5 have f/numbers of f/16.8 and f/21.9, respectively, allowing a smaller-angle cold cones. [Figure 2-18](#) shows an f/12 cold stop. An f/12 cold stop has a theoretical improvement factor of 24; however, in practice the factor is typically limited to less than 4.

The design of [Figure 2-18](#) could be further modified to bring all IR arrays in close proximity. For example, a third aft optics design could collimate and refocus channels 3, 4, and 5. These beams could then be manipulated in three-dimensional space and all brought close to the focus of channel 2.

With any of these aft optics designs, a detailed ray trace simulation of the optics should be performed. In particular, the impact from the required wide FOV should be examined. A potential aberration problem in any of these designs relates to angular magnification resulting from Lagrange's optical invariant. The beam diameter at the lenses for channel 5 is on the order of $b = 1.6$ cm. The system demagnification is $m = -30 \text{ cm} / 1.6 \text{ cm} = -18.75$. The magnitude 18.75 is also the angular magnification. Incident angles as great as 0.6 degrees (i.e., half the FOV for an optimistic array set) will be multiplied to 11.25 degrees. These large angles could cause problems since aberrations increase as angles depart from paraxial.

In previous calculations, we made an assumption of an aft optics transmission of $[\tau] = 0.25$. Let us now estimate the transmission for the design of [Figure 2-18](#). We base this estimate on the worst case with channel 5. Not shown in [Figure 2-18](#) are the scan mirror and the secondary mirrors of the RC telescope. Desired radiation from the Earth first reflects from the scan mirror, then from the two mirrors of the telescope. The telescope's secondary mirror presents a 6.25 percent area (25 percent linear) obscuration of the primary mirror aperture. The radiation then passes through four dichroic beamsplitters, reflects from a mirror, passes through the 11.5-12.5 μm bandpass filter and two lenses, reflects from two folding mirrors, and comes to focus on the detector array.

The following terms and assumed values are defined:

r_m = mirror reflectivity = 0.98

t_o = transmission through 6.25 percent area obscured aperture = 0.94

t_1 = transmission at air/lens interface of lens = 0.90 (antireflection coatings are assumed $t = 1 - \left(\frac{n-1}{n+1}\right)^2$)

t_2 = transmission through dichroic beamsplitter/bandpass filter = 0.8

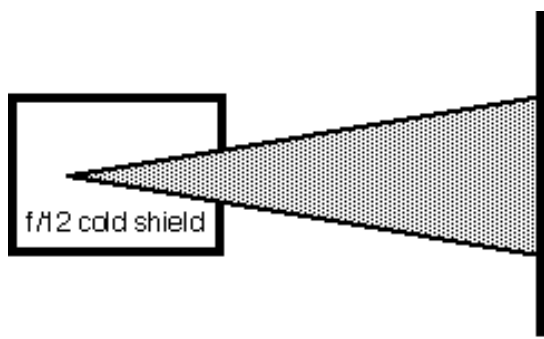
In total, the beam passes through the obscuration, 6 mirrors, 5 dichroic beamsplitters/filters, and 4 air/lens material interfaces--16 events in total. The optical transmission of the system is then:

$$\tau = t_o^6 t_m^5 t_2^4 t_1^4 = 0.18.$$

The sum of the exponents in the above expression totals 16. This 18 percent transmission is somewhat less than the 25 percent value assumed in earlier radiometric performance computations.

The optics in front of the IR detector arrays may be considered as a graybody with some emissivity, $[\epsilon]$. Depending on their temperature, these optical elements (filters, lenses, mirrors) will radiate, and some amount of this radiation will find its way to the detector array and introduce noise. If these optics are cooled, the noise will be reduced.

A simplified model for estimating the required aft optics temperature is illustrated in



graybody Figure 2-19 (Cold Shield). The detector's FOV is limited by an f/12 cold stop.

The aft optics are represented by a graybody of emissivity ϵ . We will compute the photon flux emitted from the aft optics graybody (within the f/12 cone) and compare it with the flux collected from the Earth scene.

On the detector, the noise flux from the graybody is:

$$\Phi_{\text{noise}} = \frac{\epsilon A_{\text{det}}}{1 + 4(f/\#)^2} \int_{11.5 \mu\text{m}}^{125 \mu\text{m}} d\lambda \frac{M_{\text{q},T}}{\pi} \quad (\text{photons/sec}),$$

where M_{q} is at the temperature T of the aft optics. The signal flux collected from the Earth scene is given by:

$$\tau = t_o t_m^6 t_z^5 t_1^4 = 0.18.$$

For a worst case, we have taken the Earth scene at 200 degrees K.

We now examine the flux ratio $\Phi_{\text{signal}}/\Phi_{\text{noise}}$ in terms of the aft optics temperature. This is plotted in

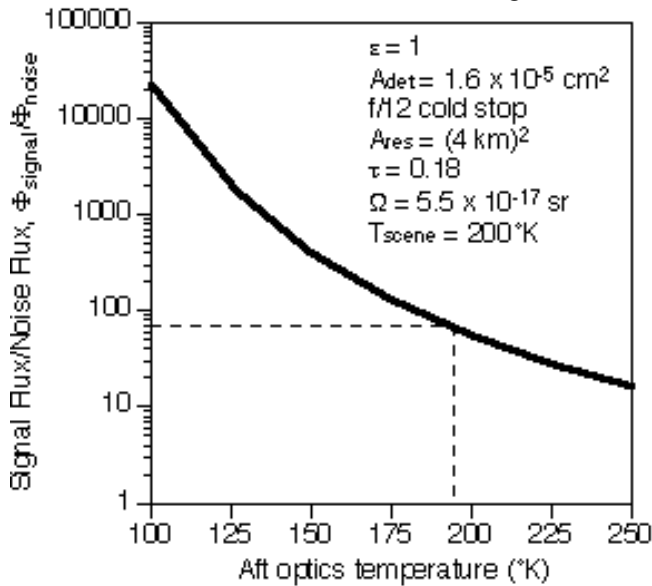


Figure 2-20 (Flux Ratio and Optics Temperature) for a worst-case aft optics emissivity of unity ($\epsilon = 1$).

An operating point on this curve can be established from NEdT requirements. We define:

$$L = \frac{\int_{11.5 \mu\text{m}}^{125 \mu\text{m}} d\lambda \frac{M_{\text{q}}}{\pi}}{11.5 \mu\text{m}}.$$

For a $T = 200$ degree K scene, [Table 2-3](#) gives the ratio:

$$\frac{1}{L} \frac{dL}{dT} = 0.03 / ^\circ K$$

With a required NEdT of 0.5 degrees, a minimum flux ratio of 67 is found from:

$$\frac{L}{\frac{dL}{dT} (NEdT)} = \frac{L}{\Delta L} = 67$$

In other words, for a 200 degree K scene, the signal level L is 67 times the differential signal dL corresponding to a scene temperature change of NEdT = 0.5 degrees. If the noise flux from aft optics radiation is greater than 1/67th of the signal flux level, a 0.5 degree scene temperature change will be hidden. The flux ratio must be greater than 67. This operating point is indicated in the graph of [Figure 2-20](#). The optics temperature must be less than 190 degrees K. However, this may be too stringent since Figure 2-20 is based on the assumption of an emissivity of unity. If the emissivity of the optics were $\epsilon = 0.5$, the flux ratio would double and the aft optics temperature would be between 200 and 225 degrees K.

2.9 Instrument weight and power

The total weight of the GOES I imager is 267 pounds. This represents the combined weight for the sensor assembly, electronics module, and power supply module. An itemized component weight breakdown for the GOES I subsystems was not available. Our best estimate for the weight of our array imager is 80 to 100 percent of the GOES I imager: 214 to 267 pounds, including the mechanical cooler. Because of the long-wavelength resolution requirement, the telescope size and the weight of the array imager will be comparable to those of the GOES I telescope. The weight of the turbo-Brayton refrigerator, discussed earlier, is 30 pounds. With redundant compressor/expander turbines and motors, the cooling system would weigh 40-45 pounds. We believe this would be heavier than the three-stage aluminum-beryllium radiative cooler used on GOES I.

Weight savings might be achieved with new mirror materials such as silicon carbide instead of the ultra low expansion (ULE) glass used on the GOES I telescope. Furthermore, weight reduction might be achieved with graphite epoxy as a lighter weight structural alternative to INVAR. Another area where weight savings might be realized is in the use of application-specific integrated circuits (ASICs) for the electronics and control modules.

Because of the mechanical cooler, the electrical power requirement for our array imager will undoubtedly exceed that of the GOES I instrument. The GOES I average power consumption is 120.5 W. The specific power of the turbo-Brayton cooler is 40 W/W. For an estimated heat load of 1-2 W to cool the detector and aft optics, an additional 40 - 80 W of power would be required. The required power estimate is therefore in the range of 160 - 200 W.

2.10 SUMMARY AND CONCLUSIONS

The above discussion can be summarized in the following conclusions:

- * Second-generation FPA technology is the key to rapid imaging from a nondedicated satellite. We believe a rapid imager is feasible and can provide the enhanced resolution and radiometric performance sought by the National Weather Service.
- * The wavelength and resolution requirements for the long-wavelength channel 5 dictate the size of the imager. Diffraction limitations require an optical aperture 30 cm in diameter.
- * The wide wavelength range of the imager leads to reflective telescope designs.
- * Rapid imaging with a large FPA requires a telescope with a wide FOV. Of the common two-mirror telescope designs, the RC system offers the widest FOV.

- * The resolution of channel 1 limits the telescope's FOV, which in turn limits usable array sizes. We found that redundant TDI-architecture arrays of sizes 1024 x 128 (channel 1), 256 x 32 (channel 2), and 128 x 16 (channels 3-5) require an FOV of 1.16 degrees. The RC telescope cannot provide this wide FOV for channel 1 because of Petzval field curvature aberrations. A field flattener lens may be used to counter the Petzval aberrations.
- * To meet the desired requirements for a 350 degree K dynamic range and 0.1 degree NEdT at 300 degreesK, 11-bit encoding is required.
- * The low flux from imaging channel 2 temporally paces the system. The other channels must be attenuated to balance integration times.
- * The material PtSi does not meet the desired NEdT performance level within the 3 minute scan time. There is continuing debate on the use of InSb versus HgCdTe for the 3.8-4.0 um band.
- * TDI scanning offers certain advantages over step-stare scanning. These advantages include superior radiometric performance and reduced yield requirements which translate to lower production risk and cost.
- * The most demanding NEdT requirement is to be able to detect a 0.1 degree temperature change in a 300 degree K scene in the wavelength bands of channels 4 and 5. This requirement puts a 0.1 percent limit on residual array nonuniformities. This level of uniformity is within the state of the art.
- * The IR detector arrays should be cooled to 70 degrees K or less. The aft optics should be cooled to less than 225 degrees K.
- * A passive radiative cooler will be too large for an imager on a nondedicated satellite. The reverse turbo-Brayton mechanical refrigerator is preferred over the Stirling refrigerator because of the multipoint and multiload nature of the imager. Mechanical refrigerator developments are well under way, with lifetime goals of 10 years.
- * The concept of imaging all four IR channels with a single detector array would compromise NEdT performance by a factor of 40. However, combining two channels on a common array appears feasible.
- * We developed a preliminary optical instrument design. This design is conservative in the sense that it uses an array per channel instead of common arrays for multiple channels, and it uses a train of beamsplitters to spectrally separate the channels instead of a single optical element (prism or grating). The design defines basic optical parameters for input to an optical ray tracing program. Ray tracing could reveal problems that would suggest design modifications. This process would be used to verify the feasibility of rapid imaging with second-generation FPA technology.
- * We estimate that the weight of the imager will be in the range of 210 to 270 pounds. Weight savings, relative to the 267 pound GOES I imager, might be realized by use of ASICs for the electronics module, silicon carbide for the telescope, and graphite epoxy for structural supports. The power requirement is estimated in the range of 160 - 200 W. This is more than the 120.5 W GOES I power requirement because of our use of mechanical, rather than radiative, cooling.

We identified several areas where further analysis would be required to arrive at an optimum instrument design. Time and resources prevented us from delving into the following areas:

- * A two-telescope design with a refractive telescope for the visible channel residing in the obscuration of a reflective IR telescope. The field-of-view constraint could be reduced, and larger arrays (faster imaging) might be possible. The resolution of the visible channel would be 1 km.
- * Ray tracing, discussed earlier, to verify the feasibility of the optimistic versus pessimistic families of array sizes. Aberrations of the total system would be modeled.

- * The issue of calibrating the detector arrays, which we did not examine in our preliminary design. Calibration at two or more temperatures would be required to meet the desired radiometric performance.
- * Performance tradeoffs of InSb versus HgCdTe for the channel 2 array.
- * Spectral separation with a grating or prism instead of beamsplitters. Using diffraction/dispersion to spectrally separate the channels offers the potential advantage of superior channel-to-channel coregistration. It also provides the hook for adding additional spectral channels.
- * Combining channels on a common FPA, for example, combining channels 1 and 2 on a single InSb array, and combining channels 4 and 5 on a single HgCdTe array. Coregistration benefits may result.

1 The 20 degrees x 20 degrees FOR contains 6.2×10^8 channel 1 pixels (14 urad square); 3.9×10^7 channel 2 pixels (56 urad square); and 9.7×10^6 pixels (112 urad square) each for channels 3-5. The total number of pixels is 6.9×10^8 ; 90 percent of the pixels are for channel 1.

2 To alleviate the well capacity saturation problem in bucket-brigade TDI, one array developer suggested the possibility of grading the well capacities so that they become progressively larger in the direction of the bucket brigade. However, there may be a problem with graded well capacities in a bidirectional TDI array, where the brigade must pass electrons in both directions.

3 Note that antireflection coating of germanium lenses is very important. For a wavelength of 12 μm , the index of refraction of germanium is $n = 4$. Transmission at an air/material interface at normal incidence is:

$$t=1-[(n-1)/(n+1)]^2.$$

For an uncoated air/germanium interface, the transmission is only 0.64. This would reduce the system transmission to $[[\tau]] = 0.046$.

Table 2-1. Imager Resolution Goals

Ch.	Spectral Range	Spatial/Angular Resolution	Applications
1	0.55-0.75 μm	0.5 km/14 urad	Weather monitoring, severe storm detection, cloud mapping, snow cover
2	3.8-4.0 μm	2 km/56 urad	Nighttime cloud detection, water vapor estimates

3	6.5-7.0 um	4 km/112 urad	Jet stream location, mid-tropospheric circulations
4	10.2-11.2 um	4 km/112 urad	Surveillance of convective storms, low-level moisture, surface temperatures, winds, soil moisture
5	11.5-12.5 um	4 km/112 urad	Low-level water vapor, surface temperature

Table 2-2. Desired (and GOES I-M) NEdT Performance Goals

Ch.	200 degrees K Cloud Tops	240 degrees K Mid-level Cloud	300 degrees K Surface
2	--	< 1.00 degrees (1.4 degrees)	
3	0.7 degrees	0.3 degrees (1.0 degrees)	--
4	0.5 degrees	0.3 degrees	0.1 degrees
	(1.4 degrees)		(0.35 degrees)
5	0.5 degrees	0.3 degrees	0.1 degrees (0.35 degrees)

Table 2-3. Photon Sterance Levels (photons/(sec*cm⁽²⁾*sr)) and Relative Temperature Derivatives (K⁽⁻¹⁾) for the IR Channels

Ch.	T = 200 degrees K	240 degrees K	300 degrees K	350 degrees K
2	--	1.11 x 10 ⁽¹³⁾ (0.064)	2.39 x 10 ⁽¹⁴⁾ (0.041)	1.38 x 10 ⁽¹⁵⁾ (0.030)
3	3.42 x 10 ⁽¹⁴⁾ (0.053)	2.02 x 10 ⁽¹⁵⁾ (0.037)	3.28 x 10 ⁽¹⁶⁾ (0.017)	--
4	5.50 x 10 ⁽¹⁵⁾ (0.034)	1.69 x 10 ⁽¹⁶⁾ (0.023)	5.22 x 10 ⁽¹⁶⁾ (0.015)	1.00 x 10 ⁽¹⁷⁾ (0.011)
5	7.21 x 10 ⁽¹⁵⁾ (0.030)	1.97 x 10 ⁽¹⁶⁾ (0.021)	5.41 x 10 ⁽¹⁶⁾ (0.014)	9.71 x 10 ⁽¹⁶⁾ (0.010)

Table 2-4. Radiant and Photon Sterance Levels for Channel 1

Percent Albedo	Radiant Sterance	Photon Sterance @ $[\lambda] = 0.65 \text{ um}$
(photons/(sec*cm ⁽²⁾ *sr))	(W/(cm ⁽²⁾ *sr))	
0.5%	4.8 x 10 ⁽⁻⁵⁾	1.57 x 10 ⁽¹⁴⁾
100%	9.60 x 10 ⁽⁻³⁾	3.14 x 10 ⁽¹⁶⁾

Table 2-5. IR Detector Cutoff Wavelengths (um)

Detector	300 degrees K	190 degrees K	80 degrees K	60-1.5 degrees K
----------	---------------	---------------	--------------	------------------

		Uncooled	TE Cooled	Mechanically Cooled
InSb	--	6.1	5.5	5.0
PtSi	--	--	4.8	--
PV HgCdTe	1-3	1-5	3-12	10-16
PC HgCdTe	1-11	3-11	5-25	12-25

Table 2-6. Diffraction Limited Telescope Apertures

Ch.	$[\lambda]$ (μm)	$[\theta]$ (rad)	D (cm)
1	0.75	14/28	12.3/6.1
2	4.0	56	16.4
3	7.0	112	14.3
4	11.2	112	22.9
5	12.5	112	25.6

Table 2-7. Integration Times, TDI Dwells, and Attenuation

Ch. Factor	Integration Time per Pixel (usec)	Mechanical Dwell per Pixel (usec)	Attenuation
1	3.7	289	0.013
2	19,000.0 (InSb)		
	26,000.0 (PtSi)	1156	1.0
3	500.0	2312	0.216
4 & 5	165.0	2312	0.071

**Table 2-8. Background-Limited Detectivities (cm^{1/2}Hz/W)
with f/2 Cold Shield**

Ch. 300 degrees K	Material	T = 200 degrees K	240 degrees K
2	InSb or HgCdTe PtSi --	7.1 x 10 ⁽¹²⁾ 6.2 x 10 ⁽¹¹⁾	1.5 x 10 ⁽¹²⁾ 1.3 x 10 ⁽¹¹⁾
3	HgCdTe	2.2 x 10 ⁽¹²⁾ 9.3 x 10 ⁽¹¹⁾	--
4 & 5	HgCdTe	8.8 x 10 ⁽¹¹⁾ 5.3 x 10 ⁽¹¹⁾	3.2 x 10 ⁽¹¹⁾

Table 2-9. NEdT with Step-Stare Scan

(50% BLIP for channels 2 and 3, 10% for 4 and 5)

Ch.	Material		T = 200 degrees K	240 degrees K
300 degrees K				
2	InSb or HgCdTe	--	(1.24 degrees)	(0.416 degrees)
	PtSi		(13.5 degrees)	(4.54 degrees)
3	HgCdTe	0.14 degrees	0.08 degrees	--
4 & 5	HgCdTe	0.44 degrees	(0.39 degrees)	(0.36 degrees)

Table 2-10. NEdT with TDI Scan

(50% BLIP for channels 2 and 3, 10% for 4 and 5)

Ch.	Material		T = 200 degrees K	240 degrees K
300 degrees K				
2	InSb or HgCdTe	--	0.22 degrees	0.07 degrees
	PtSi		(2.4 degrees)	(0.80 degrees)
3	HgCdTe	0.03 degrees	0.02 degrees	--
4 & 5	HgCdTe	0.11 degrees	0.10 degrees	0.10 degrees

Table 2-11. Maximum Array Variations (percent)

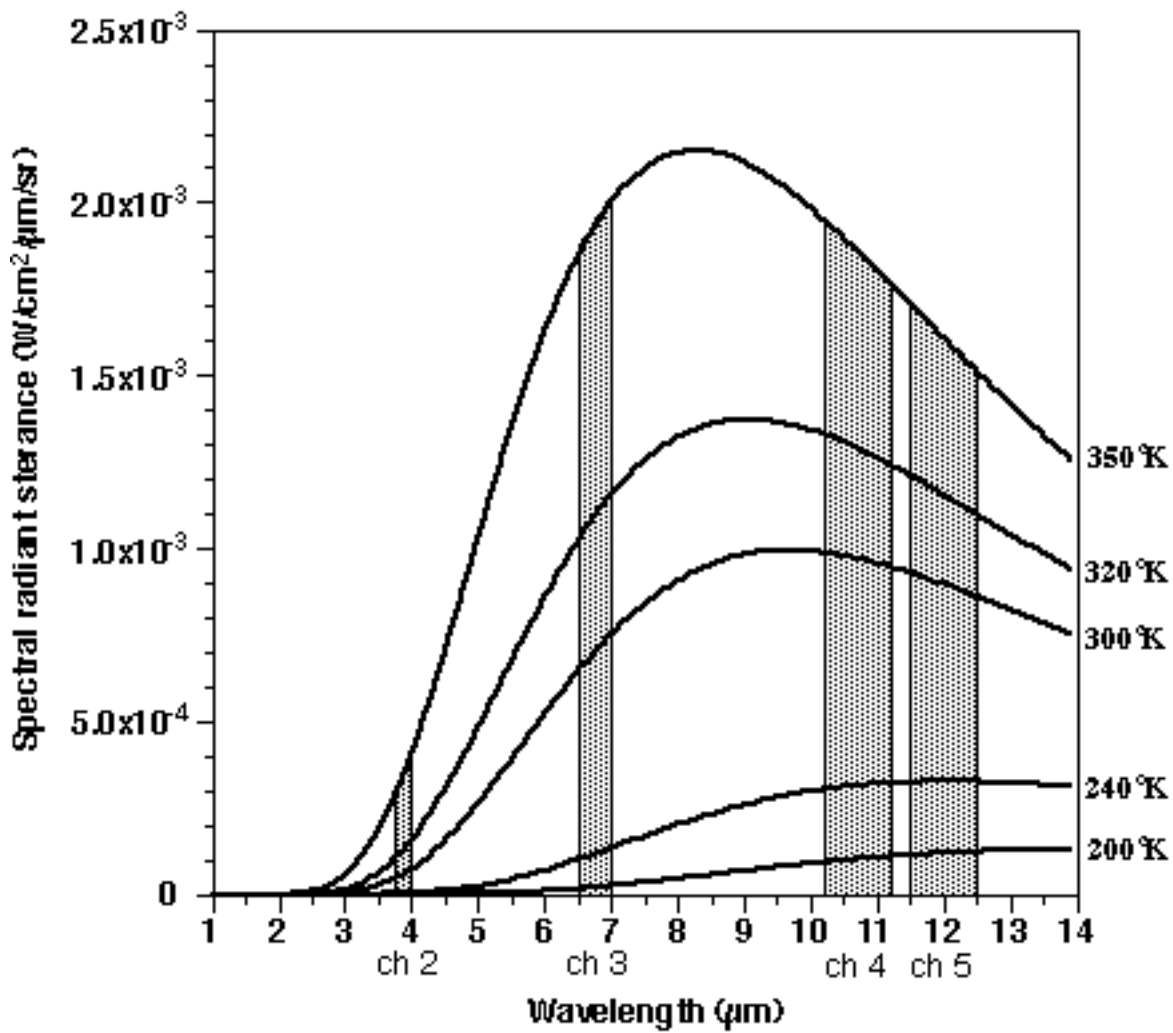
Ch.	T = 200 degrees K	T = 240 degrees K	T = 300 degrees K
-----	-------------------	-------------------	-------------------

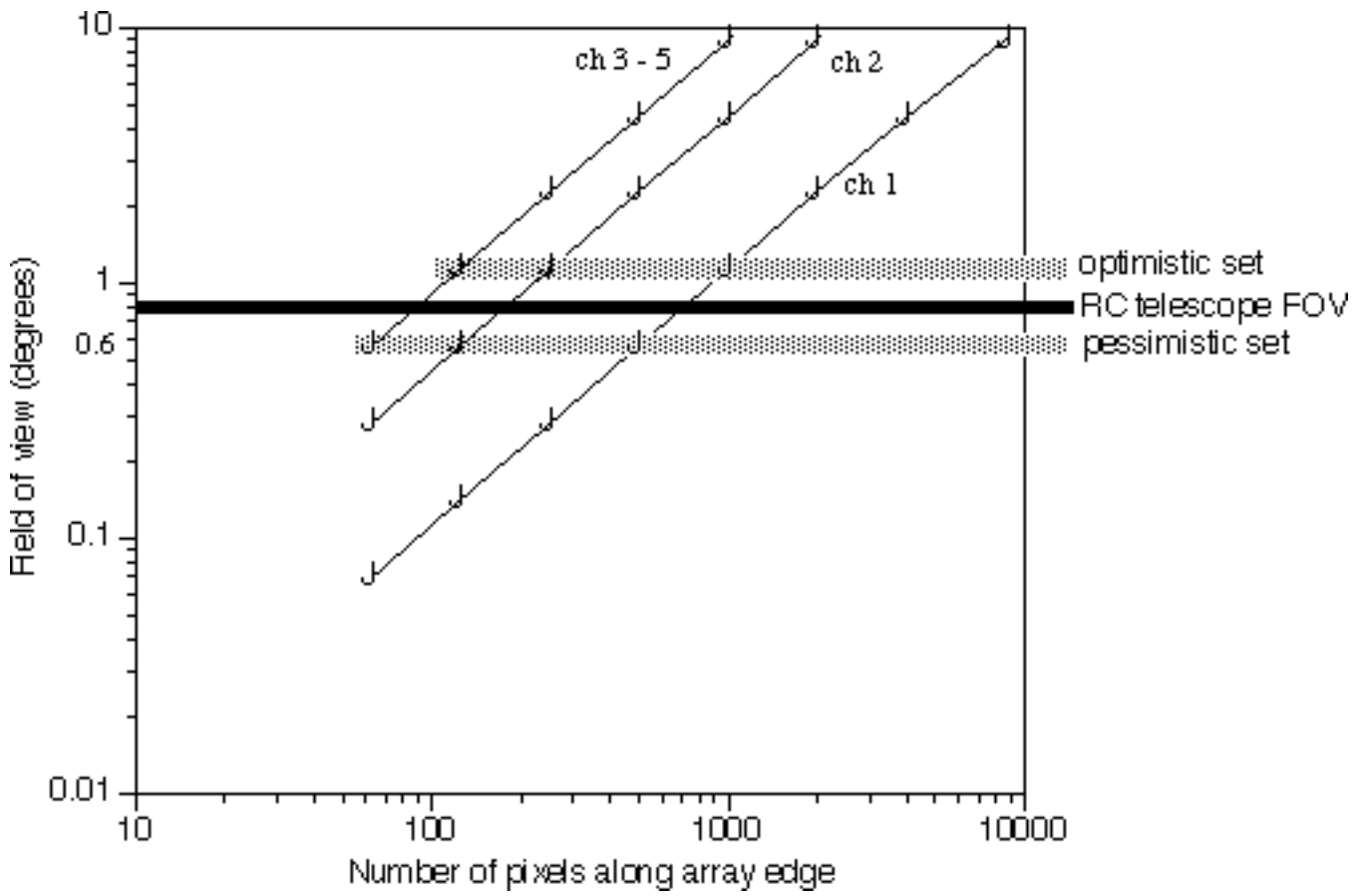
2	--	6.4	0.4
3	3.7	1.1	--
4	1.7	0.7	0.1
5	1.5	0.2	0.1

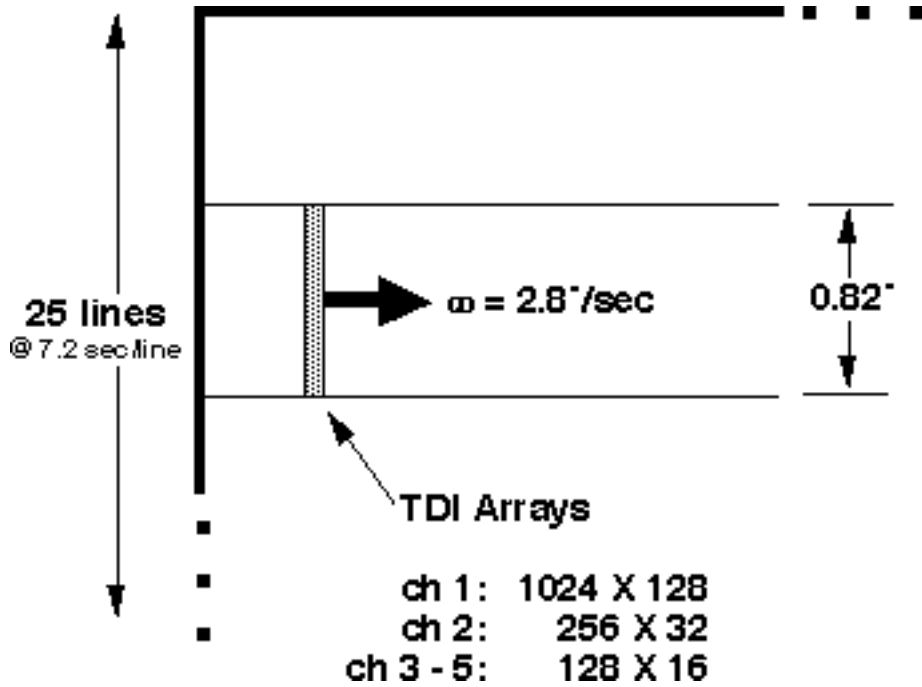
Table 2-12. System Focal Lengths

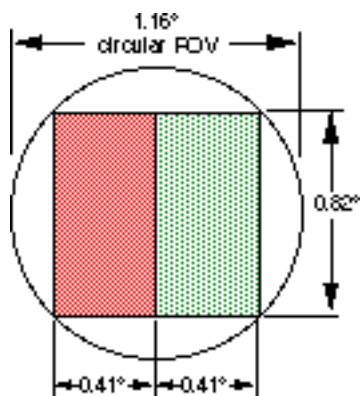
Ch.	I FOV (urad)	Pixel Edge, h (um)	System Focal Length, f (cm)
1	14	15	107.0
2	56	30	53.6
3-5	112	40	35.7

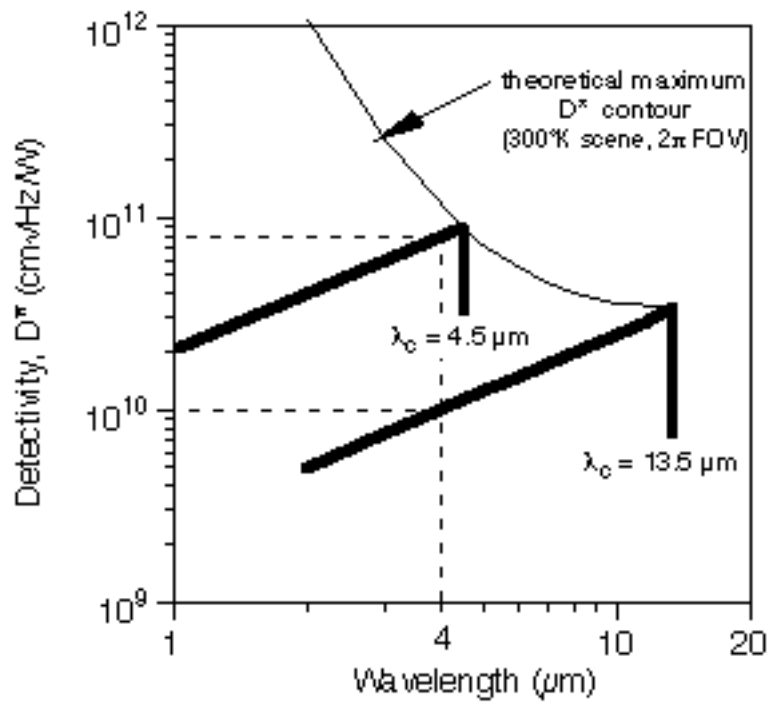
[Return to the text](#)

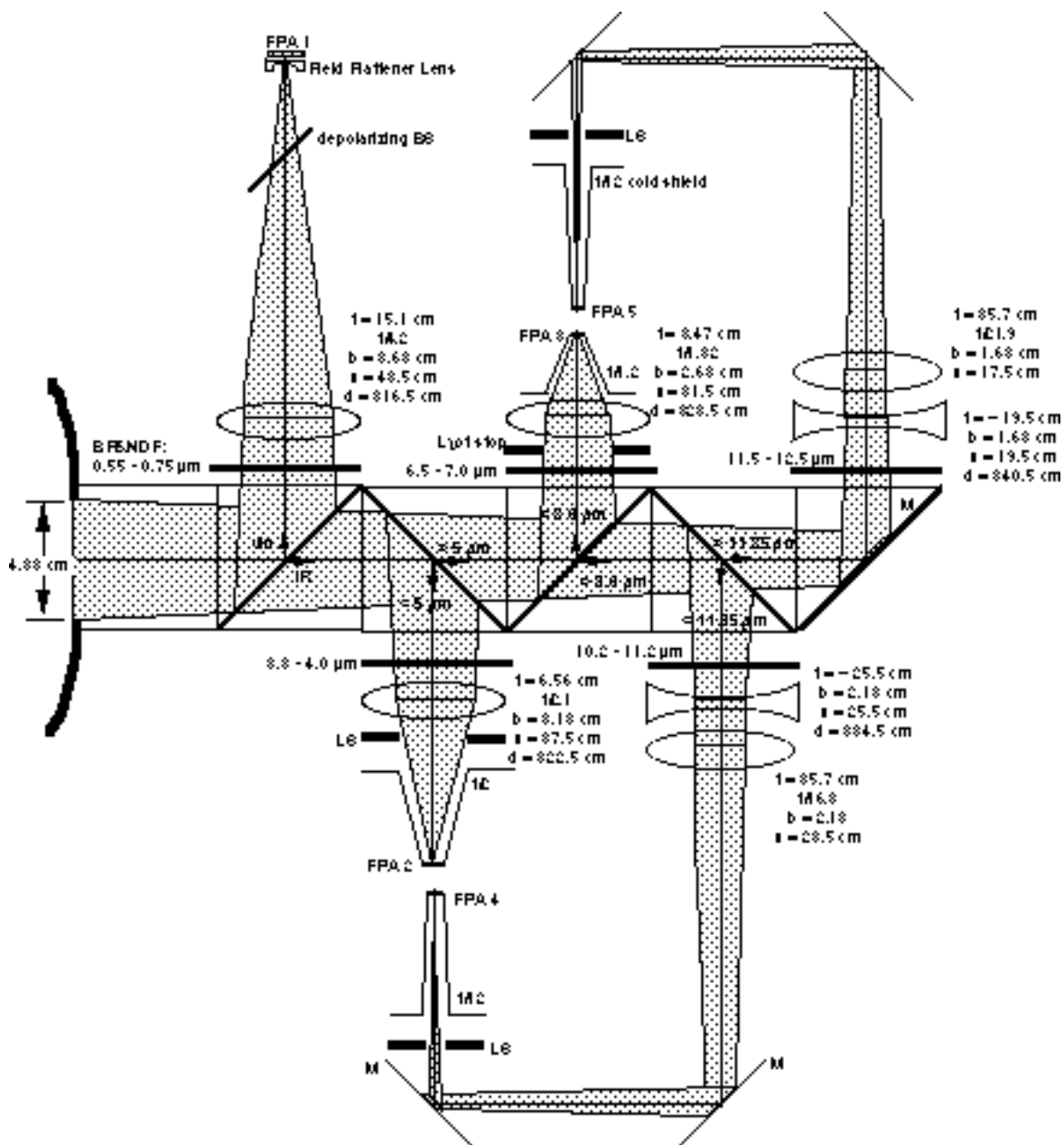


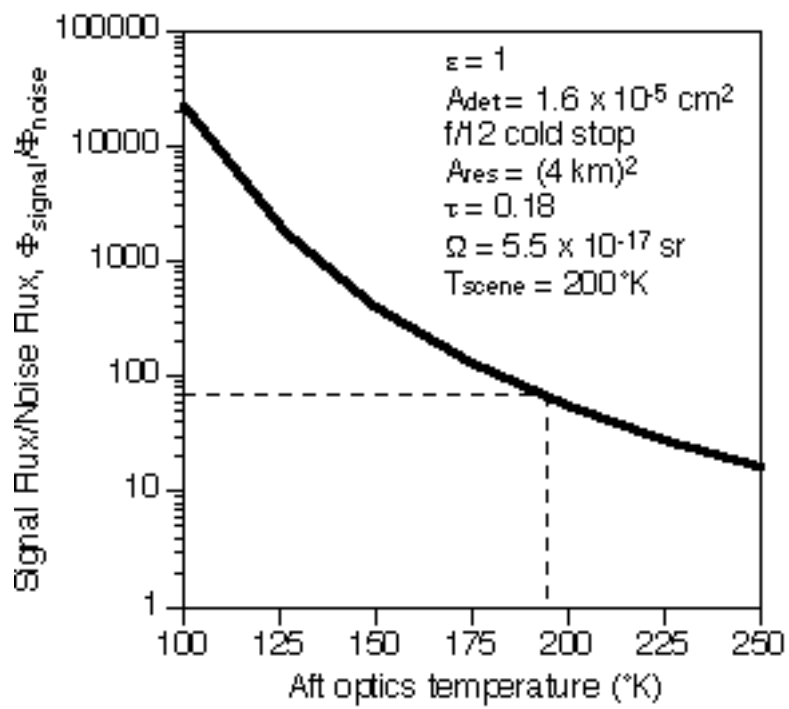












SECTION 3

IMAGE NAVIGATION AND REGISTRATION

3.1 INTRODUCTION

Geostationary imagery products are used mainly for storm surveillance, cloud drift wind calculation, and water vapor observation. In the future, closer observations to support operational mesoscale forecasting and observation will become part of the geostationary imaging mission. In all these cases, and especially for mesoscale operations, accurate location of atmospheric phenomena and measurement of their motions and positions over time (e.g., satellite-based photogrammetry) are underlying requirements for the imaging instrument that appear to transcend other requirements. To perform these missions, the imaging instrument must offer higher-quality images with higher resolution of terrestrial atmospheric and surface features, and improved accuracy in measuring spatial relationships relative to conventional imaging technology.

The desired resolution of the visible-spectrum images to be produced by the focal plane array (FPA) detector instrument being studied here is 0.5 kilometer (km) pixel dimension. There would be about half a billion pixels in such an image of the full earth disk. A high-quality image is one that has the needed resolution, and in which all pixels retain their spatial relationships with respect to the target (i.e., the earth) and to every other pixel. These spatial relationships are known as image registration and the process of maintaining the relationships is called image navigation and registration (INR).

Image navigation is the process of assigning the latitude and longitude values for each pixel of an image. Image registration is the process of maintaining pixel latitude and longitude accuracy within and among images, independently of time. A high quality of registration is required to provide high-quality images. Classically, doing this well has required the ability to know the orbit and attitude of the spacecraft bearing the imager, and to translate those parameters into the desired pixel coordinates. In addition, a spacecraft responds noticeably to the smallest disturbances, whether they are torque imbalances produced by the solar wind, stepping forces and motions of the solar array, reactions to propulsion jet firings, or reactions to changes in instrument mirror positions. Compared with the large-magnitude low-rate shifts and rapid motions that will be exhibited by spacecraft not tailored to the high-resolution remote sensing mission, the pointing resolution needs to be fine and the accuracy needs to be high to obtain the desired image quality.

Consider that geostationary spacecraft orbit at an altitude of 22,300 miles (mi) and have optical instruments that resolve 1 km on the earth in the case of current imaging systems. The FPA instrument concept is directed toward resolving half a kilometer. From an altitude of 22,300 mi, half a kilometer at the subsatellite point represents an angle of about 14 microradians (urad) or about 0.0008[ring]. Slow spacecraft motions that might be expected in a host spacecraft such as used for commercial geostationary communications platforms are of the order of 0.2[ring] [Interav92] long-term or more than 250 times larger than required if motions are to be held to the same order of magnitude as resolution. Short-term

disturbances, however, are not so well characterized.

In our FPA imager concept, large groups of pixels are captured simultaneously, thereby capturing their relative positions. It is well known that motions of a geostationary spacecraft over long and short periods of time will introduce distortions in the resulting images and sequences of images that could impair their usefulness for purposes of locating and tracking atmospheric phenomena such as cloud motion. It is important, therefore, that motions of the spacecraft be considered in the design of the remote sensing instruments we propose.

We use the GOES I imager as a point of reference. We compare FPA detector approaches using step-stare and time delay and integration (TDI) scanning strategies with GOES and with each other to explore several methods and image quality issues. This section reviews the problem and presents some ideas for future study. Section 3.2 examines the GOES I implementation of geosynchronous imaging instruments, section 3.3 presents INR approaches, section 3.4 offers some observations on image spatial relationships and ways in which they can be less than perfect, section 3.5 addresses an error budget for INR, and section 3.6 presents a summary and conclusions.

3.2 GOES I INSTRUMENTS

The GOES I imager is a flying spot scanner wherein the desired images of the earth are scanned by the instrument's small instantaneous geometric field of view (IGFOV). The imager's multidetector spectral channels simultaneously view the IGFOV, which amounts to about an 8 km field of view on earth through the optical system at the subsatellite or nadir point. The area is larger away from nadir because of the earth's curvature. The optical system provides simultaneous viewing coverage for two redundant sets of detectors for a total field of view of 16 km (a circular area 17.9 km in diameter). The IGFOV is swept along east-west and west-east (latitudinal) paths at a rate of 20[ring]/sec by means of a two-axis gimballed mirror scan system. At the end of each scan, the scan mirror moves the IGFOV in the north-south (longitudinal) direction to be ready for the next latitudinal scan.

The GOES I sounder has operational principles similar to those of the imager. It positions its IGFOV through use of a gimballed mirror which produces mechanical disturbances in the spacecraft, due to mirror motions, similar to those produced by the imager. Each instrument is disturbed by the same spacecraft- and instrument-produced motion factors.

The imager's mirror scan system is able to position the center of the IGFOV at any point in a rectangular field of regard (FOR) with respect to the spacecraft consisting of a rectilinear array of positions measuring about 25,000 (latitudinal) by 46,000 (longitudinal) positions. This corresponds with an angular FOR of 23[ring] by 21[ring] which is the imager's full viewing range. The positioning resolution is about 8 urad in the longitudinal direction and 16 urad in the latitudinal direction. The resulting visible spectrum image has 1 km pixel resolution, with about 0.29 km positioning resolution in the longitudinal direction and about 0.57 km in the latitudinal direction. The GOES imager provides an oversampled image in the latitudinal dimension with 1 km square pixels on 16 urad (0.57 km) centers for the visible

channel, and 4 and 8 km square pixels on 64 urad (2.29 km) centers for the IR channels. Scan lines are separated nominally by 8 km center-to-center without oversampling (in the longitudinal direction).

Variations in the spacecraft's motions and orbit that would alter the resulting image in undesirable ways are compensated through use of image motion compensation (IMC) and mirror motion compensation (MMC). For a rectilinear scan, the longitudinal position of the IGFOV stays at a constant latitudinal coordinate value in its FOR for the entire latitudinal motion of the scan mirror. For a motion-compensated scan, the system alters the mirror coordinates during the course of scanning, departing from the rectilinear mirror positioning to track and counteract undesirable motions, position, and attitude of the spacecraft in addition to scanner and other instrument errors. INR for the GOES I system is very complex and we have chosen to represent it here in a greatly simplified way to avoid very detailed and lengthy descriptions which would not contribute to the presentation of FPA INR.

For slower, predictable spacecraft displacements, IMC corrective mirror motions are predetermined by the GOES ground system; they are communicated to the spacecraft by way of the telemetry and command system and then to the imager through the attitude and orbit control system (AOCS), where departures from a strictly rectilinear scan are programmed into the mirror motion. Orbit inclinations and latitudinal drifts may be compensated in this way, as may thermal distortions of the spacecraft and instrument and drifts due to solar wind-induced torques on the solar array panels.

For motions of the imager and sounder instrument mirrors, which also cause predictable spacecraft disturbances, the AOCS calculates MMC corrections onboard and provides them in real time directly to the imager, along with IMC corrections.

For the GOES spacecraft, part of the spectrum of motions to be compensated is indicated in figure 3-1. Note that the figure does not include long-term orbital effects or the effects of propulsion system firings. The orbit inclinations of $\pm 0.5^\circ$ are off the scale of the figure to the left, and propulsion system firings produce such large disturbances as to render dynamic correction impossible. Fortunately, IMC can compensate for orbital effects. Propulsion system firings are used infrequently to perform orbit adjustments. Instrument performance requirements may be suspended during and for a period immediately after those maneuvers.

Figure 3-2 shows, for reference, definitions used to describe geostationary communications spacecraft motions. With respect to image motions, yaw produces latitudinal shifts of the image in the instrument FOR, pitch produces longitudinal shifts, and roll produces image rotation about the earth-spacecraft line.

3.3 APPROACHES TO IMAGE NAVIGATION AND REGISTRATION

For GOES I, INR is intended to produce images having a fixed earth-projection, that is, images that appear to have been captured from a zero-inclination geostationary orbit at all times. This is done through the IMC feature, whereby pixel shifts due to orbit inclination and other slow factors can be compensated by driving the flying spot through nonrectilinear scans, thereby straightening the equator and adjusting

for apparent rotation of the earth in the instrument's FOR.

In the FPA imaging concept, IMC cannot be performed the same way because large blocks of pixels will be captured simultaneously, and individual pixel locations and scan line trajectories cannot be altered. Images, therefore, must be captured without the beneficial distortion afforded by a GOES-like IMC system. This is one of the prices paid for the simultaneity offered by the FPA detector approach. Another price paid is that of having longer image pixel exposure times, which is discussed below.

However, it must be noted that there is no more information offered by the GOES IMC-based instrument than by the FPA concept, other than the possible benefits of oversampling. This is the case since both images will have been made from the exact same orbital position with the exact same field of regard and the exact same ability to "see" the features and extent of the target, the earth. The major differences are the amount of time taken to capture the image--about 30 minutes for GOES versus about 3 minutes projected for the FPA concept--and the enhanced coregistration, hence spatial accuracy, offered by an image composed of large blocks of perfectly coregistered pixels.

The approach to INR for the FPA instrument includes features that, taken together, would provide an accurate image set capable of fulfilling the accuracy requirements needed to support present and future primary image uses. Note that the approach outlined in the following addresses mainly the step-stare imaging method; time did not permit development of an approach for the TDI imaging method. The step-stare approach, here termed the "overlap" approach, requires three features to provide accurately registered and located images:

- * Acquisition of overlapping image blocks or frames
- * Application of image processing to creating a mosaic of adjacent frames
- * Creation of a collateral data set consisting of information that links together all visible landmarks, and provides a basis for spatial location and measurements in the image

Acquisition of overlapping frames is discussed below. The creation of mosaics of frames and of collateral data sets are discussed in [section 4](#) on ground-based processing.

3.3.1 Acquisition of Overlapping Image Frames

The FPA imaging instrument produces an image of the earth or a segment of the earth using a FPA detector as described in [section 2](#) of this report. An image frame is produced by the array detector instrument using the step-stare method in a single exposure time; that is, all pixels in the frame are exposed simultaneously.

An image of an area larger than an image frame is a mosaic of adjacent image frames "stitched together" through ground-based image processing, as in figure 3-3. Spacecraft motions will not permit accurate

enough positioning of the IGFOV of the instrument to abut adjacent frames such that pixel relationships between the two frames are maintained. The effects of motions on the use and content of the image frame are shown in figure 3-4.

Consequently, it is better to overlap adjacent frames and allow the spacecraft motions to expand and contract the overlap. In this way, the relationship between adjacent frames can be retained despite spacecraft motion, and spacecraft motion bounds need only be understood and not mitigated to retain spatial relationships. The adjacent frame relationship is retained by virtue of the fact that both frames will capture an image of the same area, the overlap. This feature obviates the need for the predictor-corrector approach to INR, as used in the GOES system, or for a real-time feedback system.¹ This is done at the expense of collecting and carrying redundant image information.

Table 3-1 shows the results of a calculation of overlap for the case of a variety of motions of the spacecraft. In these cases, the basic FOR covered was 17.4 degrees latitudinally and longitudinally. This is the minimum angle measured at the spacecraft subtended by a full earth disk across the equator.

Given a detector array having 512 x 1024 pixels for the visible channel at 0.5 km resolution, as in the FPA instrument design, 43 frames would be required to cover the 17.4 degree FOR in the latitudinal direction using the 512 pixel dimension. Likewise, it would require 22 frames in the longitudinal direction using the 1024 pixel dimension. In this case, there would be no overlap and since a discrete number of frames must be used, the FOR would be somewhat bigger than 17.4 degrees.

The table shows the number of pixels overlapped around the edges of each interior frame, given the addition of one or more frames to each FOR image dimension and overlapping them to yield the FOR angle indicated in the five center table columns. The FOR angle dimension of the table indicates the displacement of the spacecraft added to the 17.4 degrees. That is, the 17.6 degrees column implies that the spacecraft displacement is 0.2 degrees (or +/-0.1 degrees) and the imager FOR is increased by the displacement amount to accomodate the pointing error and still record the entire earth disk in the FOR. That number of frames is given in the first column of the table.

The overlap length (the last column of the table) is the other dimension of the overlap region; together with the overlap width, it forms an overlap or "stitching" vector that appears in both adjacent frames. For example, the table entry for a latitudinal direction of 45 frames and a 17.6 degrees FOR angle indicates a stitching vector with dimensions of 24 x 1024 pixels.

Although the stitching vector sizes are substantial in terms of the size of the pixel array available for image matching, the added frames represent no more than about 21 percent overhead in terms of data volume for a full earth disk in any of the cases in the table. A description of stitching vector processing is given in section 4.

Most commercial communications spacecraft attitude control systems can point the spacecraft toward the earth and at the subsatellite point within a half-cone angle of 0.2 degrees. The table and the column for a

FOR angle of 17.8 degrees then describe the instrument overlap parameters. An image composed of 45 latitudinal frames x 23 longitudinal frames would be able to capture the full earth disk under all normal circumstances of attitude and orbit shift.

The preceding, however, does not account for pointing errors within the instrument, such as effects due to the diurnal heating cycle. Nor does it account for more dynamic factors, such as vibrations due to other subsystems on the spacecraft. See figure 3-1 for several examples of the types of disturbances that can occur.

If we view these other disturbances as being additive to the spacecraft pointing error in the worst case, it is conceivable that overlap permitting relative frame displacement would be one of the solutions. For the 17.8 degree column and 45 latitudinal frames, the table shows an overlap of 18 pixels. Each pixel represents 0.5 km on earth or 14 urad at the spacecraft; 18 pixels represents 252 urad for these additional phenomena. Using an additional latitudinal frame (46 total) would permit increasing overlap to 29 pixels, giving 406 urad in the latitudinal direction and retaining the 23 frames in the longitudinal direction, which gives 59 pixels or 826 urad. Based upon the preceding discussion, this is about 9 percent data volume overhead.

The discussion of scanning in section 2 of this report notes that overlap might be a good way to compensate for dead pixels, and that doing so might require that each earth pixel be viewed by four detector pixels. The subject of scanning strategy could take considerable time and yet not be treated exhaustively. Perhaps the best approach is to make it possible to take any or all approaches and to make overlap a dynamically programmable feature, a dynamically programmed overlap method for INR.

FOR Angle

Latitudinal

Direction 17.4 degrees 17.5 degrees 17.6 degrees 17.7 degrees 17.8 degrees Overlap

Length

(frames) Overlap Width (pixels) (pixels)

44 19 16 13 (a) (a) 1024

45 29 27 24 21 18 1024

46 40 37 35 32 29 1024

47 42 39 1024

Longitudinal Direction

(frames)

23 80 75 70 64 59 512

24 120 115 109 104 99 512

25 156 151 146 141 136 512

(a) Indicates that more than 44 frames are required to cover the FOR angle with overlap.

Step-stare scanning could be implemented as it is for the GOES I sounder. The sounder scan mechanism has a gimbaled mirror similar to that of the GOES I imager. The scanner is capable of stepping the IGFOV 17.5 urad in the longitudinal direction and 35 urad in the latitudinal direction within a total FOR of 21 degrees longitudinally x 23 degrees latitudinally. Latitudinal mirror scan motions of 280 urad require 25 milliseconds (msec) to accelerate, step in 35 urad steps at 10,000 steps/sec, and settle prior to beginning a detector exposure. The sounder then performs a 75 msec detector exposure cycle prior to repeating the mirror stepping operation for a total cycle time of 0.1 sec.

Using these performance parameters as a guide, the FPA imager needs to step about $17.8 \text{ degrees}/46 = 0.387 \text{ degrees per step}$ (about 6755 urad). At 7.2 sec per 20 degrees latitudinal scan, the time allotted for 17.8 degrees is 6.4 sec or 139 msec for each frame. The exposure cycle would require 19 msec to finish considering the longest required exposure time (channel 2). This would leave 120 msec for scanner motion. A GOES-like scanner stepping rate is fast enough to move the IGFOV 6755 urad latitudinally in about 20 msec, leaving 100 msec for acceleration and settling.

3.4 IMAGE SPATIAL RELATIONSHIPS

The quality of an image produced from geostationary orbit is related to the spatial and temporal synopticity² of the image components (i.e., pixels, frames, and/or lines), and the ability to maintain spatial relationships between and within images. In the FPA imaging concept, synopticity is improved over current technology by having the same viewing range and an order-of-magnitude improved temporal performance.

Spatial relationship effects examined include pixel location, spread, smear, and rotation. Location refers to the ability to determine in absolute terms the earth latitude and longitude of an image pixel, and is addressed in [section 4](#). Spread is the enlargement in scene dimension represented by a detector pixel due to spacecraft motions during pixel exposure; smear is distortion of the representation of objects in the image due to their motion during image exposure; and rotation is image distortion due to scan mirror effects.

The current, GOES I, technology differs significantly from FPA detector technology. The approaches are discussed below.

3.4.1 GOES I Technology

In the GOES I imager instrument, single image pixels are formed predominantly independently of other image pixels.³ The spatial relationship between any two nonsimultaneous pixels is largely indeterminate because there are no inherent physical properties fixing the location of one pixel relative to another as with FPA detectors, where multiple detectors share the same rigid mechanical mounting surface. In addition, detector pixel exposures are made at different times since the instrument needs to point the IGFOV at the next target after each image pixel exposure. Although the spatial relationships among image pixels can be bounded by carefully controlling the motions of the spacecraft and of the imaging instrument, those relationships are statistical in nature because the spacecraft motions that occur between exposures are somewhat indeterminate.

GOES I technology has pixels formed during a more or less continuous scan of the instrument IGFOV across the earth. The instrument uses single- and double-pixel imaging for IR channels and an array of eight detectors for the visible channel. The visible channel is sampled every 45.7 usec, corresponding to 0.57 km scan movement of the IGFOV at nadir. The IR channels are sampled every 183.4usec, corresponding to 2.28 km movement of the IGFOV at nadir. Sampling durations are small (estimated at about 1 usec) to form a pixel.

Over tenths of seconds to seconds, the GOES I AOCS and the instrument servo systems can respond to correct for the spacecraft motions of concern. The net result is the predicted performance of the instrument as shown in table 3-2.

3.4.2 Array Detector Instruments

The array detectors employed in the FPA concept use the same materials as in the GOES I imager, but are constructed and operated differently. The GOES I instrument detectors are operated as light energy rate-sensitive devices, in which the instantaneous detector output corresponds with the rate of arrival of photons. Array detector devices are integrators in which electrons freed by arriving photons are collected and retained for a period of time, until the total number of photons for a detector pixel is read by the device and external circuits.

Image formation times (time between start and finish of exposure) for the step-stare approach, stated in section 2 of this report extend from 160 microseconds (usec) to 19 msec, orders of magnitude larger than the formation time needed by the GOES I technology. One detector pixel exposure is made for each image pixel. TDI image pixel formation time, as defined in section 2 of this report, is 37 msec.

3.4.2.1 Time Delay and Integration (TDI)

With the TDI method, image pixel exposures are the sum of a number of detector pixel exposures. While TDI has an advantage radiometrically because of superior noise levels (see the discussion of instrument design in [section 2](#)), from the standpoint of immunity to motion, TDI image pixel exposure times can be of concern since they are so long. Detector pixel exposure intensity for the TDI approach is adjusted to make all image pixel exposure times the same.

The TDI approach improves spatial relationships with respect to current technology in one dimension because of the columnar nature of the TDI array detectors. The visible channel detector array would be 1024 pixels long, compared with 8 pixels in the GOES I instrument, and IR channels would be composed of 128 and 256 pixels compared with 1 or 2 for the GOES I. Exposure time per image pixel would be the same for all channels, and incoming light energy in some channels would have to be attenuated to make this possible.

The simultaneous image formation of the entire column of TDI detectors preserves the spatial relationships among all the target pixels in the column since no spacecraft or image motion can take place between the times of capture of the individual pixels in the column. The motions that can reduce image quality in this case are motions that can take place during column image formations, that is, during exposure of a single image pixel, which is the same as the period between the start of the first detector pixel column exposure and the end of the last.

Performance Parameter 3 $[[\sigma]]$ Performance Prediction

Image navigation accuracy 22 km at nadir

Registration within an image 74 urad in 25 minutes

Registration between repeated images 37 urad in 15 minutes

Source: [GOES91].

Compared with the flying spot, the TDI approach might offer a quality improvement related to the number of pixels captured simultaneously and related inversely to the image formation times. Image pixel formation times for the TDI approach, as described earlier, are the longest of those for all the approaches, rendering this approach the most sensitive to mechanical noise (i.e., unwanted mechanical perturbations).

3.4.2.2 Step-Stare

The step-stare approach offers an advantage over the other approaches in retention of spatial relationships. First, a large area of pixels is exposed simultaneously, compared with single pixels or one-dimensional arrays of pixels. Thus, quality improvement is related not only to the linear dimension or number of coregistered pixels, as with the TDI array, but also to the area of pixels. The exposure time is

longer than that of the GOES I technology and shorter than that of the TDI approach.

The step-stare approach offers an added feature. Since it produces two-dimensional frames of pixels that are formed simultaneously, the spatial relationships among all image pixels in the scene area represented by the frame are perfectly, deterministically defined. This means any recognizable detail in the frame image can be located on earth to at least pixel-size accuracy.

Adjacent frames can be overlapped, thereby providing added features. Since image detail can be recognized in the overlapped region common to both frames, the adjacent frames can be accurately registered to one another through image processing after image formation. Without remapping of pixels, registration within about half a pixel dimension should be possible; with remapping, it may be possible to do better. See section 4 of this report for a discussion of the processing needed to register adjacent frames.

3.4.3 Pixel Spread

A detector pixel views a scene area on the earth (e.g., at nadir) that is the same shape and size as the detector pixel transformed (i.e., magnified, rotated, and perhaps distorted in other ways) by the optical system in a perfectly noise-free environment. Scene area coverage by the detector pixel increases because of the effects of mechanical noise or motions of the spacecraft during the time period of image pixel formation (i.e., exposure time).

If the motion of the spacecraft relative to the target earth were predictable and always the same, one could reduce the size of the detector pixel relative to the intended image pixel and, allowing for the detector (i.e., IGFOV) motion, represent the result as an image pixel. If the motion were random or not always the same, or not conveniently predictable, the coverage represented by the resulting image pixel would be somewhat larger than that of the desired image pixel. This excess size is referred to here as "spread." Spread is the enlargement in the coverage of an image pixel relative to that of the corresponding detector pixel, both referred to the same side of the optical system to account for optical transformations.

Spread is related to both the rate of motion and the time of exposure, and is a measure of the distance the pixel moves (rate multiplied by time = distance). In addition, spread brings with it the problem of adjacent pixel overlap, in which a pixel value is influenced by an area that contains all or part of adjacent scene pixel areas. This also can result in an apparent loss of resolution due to inadvertent exposure of more than one adjacent pixel to the same target area. The effective resolution of the step-stare FPA imager was investigated; the analysis is presented in appendix B, and shows that the RMS value of the imager-spacecraft system's effective resolution is given by the root sum square (RSS) of the full-half-width-maximum values of the point spread functions of the instrument and the spacecraft. These terms are defined in the appendix.

For a perfect spacecraft exhibiting no extraneous motions, spread would be equal to zero, and the image

pixel would have the same coverage as the detector pixel. For present purposes, spread and coverage have a linear dimension, but a similar argument could be made using an area dimension.

Figure 3-5 is a display of linear spread value incurred over image pixel exposure time. Spread is produced by spacecraft rotational rates about any axis that produce image displacements during exposure, and by finite frame exposure times. Points for GOES, TDI, and step-stare approaches are displayed for spread limited to 0.1 pixel size. The figure shows spacecraft angular rates relative to earth that would incur the 0.1 pixel spread, spreads that would result because of scanning rates, and spacecraft rates that could be tolerated without exceeding 0.1 pixel spread.

For step-stare imaging, the maximum exposure time needed for the 3.8-4.0 micron near IR channel is about 19 msec and the visible channel requires 200 usec. Allowing 0.1 pixel dimension or 0.2 km movement in the near IR (channel 2) during exposure, spacecraft rates of up to 295 urad/sec could be tolerated. If Step-Stare imaging required continuous exposure during scanning, the spreads would range from about 0.3 km to 33 km as shown along the TDI/Step-Stare scan line.

TDI-based imaging, as described earlier, could tolerate only 38 urad/sec without exceeding 0.1 pixel spread. TDI imaging exposes continuously while scanning. Each detector pixel contributing to an image pixel views the same scene pixel. The spreads associated with TDI scanning operation are shown in figure 3-5 along the TDI/step-stare scan line, and are, by definition of the TDI scan, equal to the scene pixel dimensions of 0.5, 2, and 4 km.

Published GOES I simulation results [GOES91] imply rates of 50 urad/sec for more than 80 msec and lower rates for a wide range of durations. This is shown in figure 3-5. We have no data at this time on commercial spacecraft dynamic environments.

3.4.4 Image Smear

Pixel spread, discussed above, relates image pixel enlargement for given spacecraft motions. Smear is defined as image object distortion due to object motion. To illustrate, consider that the FPA imager (TDI or step-stare) requires about 7.2 sec to complete a latitudinal 20 degree scan. From the left edge of the FOR, it requires about 14.4 sec to scan to the opposite edge of the FOR and return (neglecting turnaround, which would only increase the effect) to capture the frame below the starting frame.

This is a worst case, although there is not much moving detail of interest at the earth edge. A bad case might be farther in toward nadir longitude, at which the return time would be 7.2 sec, a median value. The shortest interval occurs between the last frame in the scan and the first frame on the return scan. For a step-stare step interval, as discussed in [section 3.3.1](#) above, the return time is 0.139 sec. A scan need not cover the width of the FOR. Figure 3-6 shows translational smear effects for a 16-frame wide scan.

The GOES I imager scans about 7 times faster than the FPA imager. Consequently, smeared images of moving scene objects that span more than one sampling period will appear smoother in GOES I images

because of the higher scan rate and sampling frequency.

In assembling the total image, frames are stitched together around all edges. As the scan returns from the far edge to a point just below the starting frame, the starting frame must be stitched to the scan frame below it through the overlap on their lower and upper edges. A moving image object lying in both frames will undergo translation during the return time, with the part lying in the last frame displaced in the direction of motion and the part lying in the starting frame occupying its starting position. Displacements are shown for the FPA imager in figure 3-7. The figure accounts for a 52-frame FOR to cover the full 20 degrees. Object speeds range from 10 to 300 miles per hour (mph). The shaded area indicates displacements of half a pixel that would affect frame overlap matches.

3.4.5 Field Rotation

With a single-scan mirror, image field rotations will occur as a result of the rotation of the mirror in the longitudinal and latitudinal directions. The distortions will be manifested in apparent rotation of the image focal plane, with accompanying changes in the transform of earth dimensions to image dimensions.

The scan mirror has two axes about which it can rotate, as shown in figure 3-8: One, the latitudinal scan axis, call it V, about a line perpendicular to the orbit plane; the other, the longitudinal scan axis, call it H, about a line parallel to the orbit plane. The mirror is nominally at a 45 degree angle with respect to the orbit plane, and the V-axis is perpendicular to the earth-spacecraft line through the nadir point. In this position, the imager is viewing a frame centered on the nadir point or the TDI array is centered on the nadir point, and is viewing along a longitude meridian. In either case, the detector is located in a plane parallel to the orbit plane.

If the detector is located northward of the scan mirror, and if the scan mirror is made to rotate about its H-axis toward either pole, there will be a maximum foreshortening of features in the longitudinal dimension of about 1.3 percent at the Poles. The phenomenon is a cosine function in between the extremes.

Likewise, scanning about the V-axis will produce a rotation of the image field, with scans toward the east producing clockwise rotation and those to the left producing counterclockwise rotation for the detector located northward of the scan mirror. Equal but opposite rotations will occur if the detector is located southward of the scan mirror. This is illustrated in figure 3-9, which shows how frames in the northeast quadrant would have to be rotated in order to be stitched together for a scanner having a detector located south of the scan mirror. In addition, the figure shows rotation about the detector's center. If the optical rotation center of the frame image field were located, say, at the detector edge, rotation would be about that point, thereby altering the frame assembly stitching pattern. Scan adjustments may be required to ensure that overlap occurs at all frame edges.

For scans about the V-axis with the mirror positioned to view along a line through the nadir point, the extremes of rotation will be equal to the mirror rotation angle, since the detector does not rotate along

with the mirror. Rotation of the detector is precluded by the need to attach it rigidly to its heat sink.

For compound mirror deflections about the H-axis, there also will be a foreshortening or lengthening of the field as described above, so as to alter the apparent rotation angle, as well as distort feature dimensions.

While these distortions can be accommodated and compensated with a flying spot imager, they are not so easily accommodated with a two-dimensional detector. One approach to be investigated would be to use a two-element scanner, such as a mirror-based equivalent of a Risley prism. Analysis of this option was beyond the scope of the present investigation.

3.5 ERROR BUDGET

In view of the lack of design details, an error budget cannot be stated conclusively at this time, although a rough order of magnitude (ROM) estimate for some of the error parameters is interesting to consider. Note that time dependency is not apparent in these estimates. This is due largely to the pixel spatial relationship inherent in the focal plane detector array.

For image navigation accuracy, we need to know the error implicit in the collateral data set. However, knowing the locations of landmarks with great accuracy and being able to recognize them in an image frame, it should be possible for that frame to provide a level of error well below that to be expected at the level of an integrated whole image. Allow one-third of a pixel error in locating any pixel within a landmark-bearing frame as an initial estimate, or 4.67 urad. This should be due largely to error in assigning the landmark location to specific pixels. No allocation is made for errors in pixel distribution in a FPA.

The error in assembling non-landmark-bearing frames having some image structure (see [section 4](#)) into an image is about half a pixel or 7 urad. If the typical distance to be measured from an image is assumed to be in the range of 1000-3000 km, then assume that knowledge of pixel location is required over that distance. This is a span of as many as 12 frames. In the worst case, only one frame contains any landmarks, and the potential error in locating a pixel 12 frames away from a landmark-bearing frame would be the RSS of 11 frame errors.

Additional error is incurred as a result of frame rotation; pixel spread; and other, as yet unconsidered parameters that cannot be assessed with the information on hand. Allow one-third of a pixel per frame for error due to compensation for rotation and for spread. The total error would be the RSS of 11 frame errors.

Total ROM navigation error due to the above factors would be 28.3 urad RSS. This is the error to be expected in measuring distances of the order of 3000 km from a known landmark in a two-dimensional image.

For registration within an image, there are two errors to assign--error within a frame and interframe errors. Registration error within a frame is negligible since all frame pixels are fixed with respect to one another. Interframe errors between any two adjacent frames would consist of translational and rotational errors, or about 8.4 μ rad RSS. Over the 3000 km range, errors would result from translation and rotation errors for 11 frame assemblies, or a ROM error of about 27.9 μ rad RSS so far, with changes to come as we learn more about the errors in this system.

Registration error between repeated images should not be greater than the navigation error within an image, or 28.3 μ rad RSS, with the understanding that there are more factors to be defined and evaluated.

3.6 SUMMARY AND CONCLUSIONS

The above discussion can be summarized in the following conclusions:

- * The use of FPA detectors precludes the use of image motion compensation and mirror motion compensation as defined for the GOES I system. This is due to the rigid spatial relationships among the pixels within a single frame of an image, and the consequent inability to alter the positions of individual pixels during image creation.
- * There is as much information in the FPA-based image of the earth as there is in the GOES I image, except for the possible benefits of oversampling as achieved in the GOES I imager.
- * There is greater simultaneity, hence temporal synopticity in a FPA-based image relative to a GOES I image as a result of an order-of-magnitude shorter total image formation time.
- * Use of overlapping image frames in the step-stare method offers deterministic spatial relationships within and among image frames.
- * The creation of overlapping image frames by the imager is necessary to provide well-coregistered images, with ground-based processing after image creation responsible for assembling the frames into a whole image. This is contrasted with the predictor-corrector approach to motion compensation used in the GOES I imaging system.
- * The predictor-corrector and feedback approaches to INR place the burden of image spatial relationships on the spacecraft and the imager scan system, whereas the overlap approach uses data redundancy and image processing.
- * The overlap INR approach and the feedback approach allow the imager to operate more independently of the spacecraft as compared with the GOES I predictor-corrector approach, whereas the overlap approach results in the simplest of the three space segments.
- * Whole image assembly from overlapped frames after image frame exposure permits compensation for

all spacecraft-earth relative motions as compared with the predictor-corrector approach, which can correct only as well as it can model the motions.

- * The step-stare approach to image creation has the advantage over the TDI approach of shorter image pixel exposure times, which result in greater immunity to pixel spread due to spacecraft motion, while the GOES I/flying spot approach has still better immunity to pixel spread due to shorter effective image pixel exposure times.

- * The slower frame scan rates of the proposed FPA imager would result in lower sampling rates for moving scene objects. Such objects would thereby be rendered less smoothly in scan-to-scan transitions than would be the case for the GOES I or other imager having greater scan rates, despite the FPA imager's smaller overall scan time.

- * Rotational distortion of the image focal plane due to rotation from single mirror scanning could amount to as much as 1.3 percent foreshortening of earth dimensions at the earth poles, and apparent rotation of image frame fields of about 8.9[[ring]] at latitudinal scan extremes. This is not peculiar to the FPA concept.

- * Scanning strategy and image frame assembly will be affected by rotational distortion, optical centering, and detector and scan optics design.

Several areas require further analysis to support design decisions and performance issues. Time and resources prevented us from examining the following areas further:

- * Resolution of the TDI-step-stare tradeoff or adoption of an appropriate combination is needed to obtain the best possible radiometric vs. mechanical noise rate immunity and spatial relationship performance.

- * Oversampling needs to be considered in the context of the FPA.

- * Optical scanning systems need to be investigated to eliminate, or reduce to acceptable levels, the effects of image field rotation due to scanning.

- * Scanner design, scan strategy, and scanning parameters need to be studied for impacts on image processing and image frame assembly.

- * A comprehensive error budget needs to be developed for navigation and registration performance.

1 Hughes Information Technology Co., together with a government-industry-university team, has proposed a geostationary imager onboard a commercial communications satellite. It has proposed use of a miniature solid-state gyroscope mounted on the scanner mirror and a feedback configuration to stabilize the IGFOV.

2 Synopticity here refers to the degree or faithfulness of representation by an image of an entire original scene of a wide area at a given time or over a short span of time. The notion is that an image of a very large area could be faulty and not represent meteorological events happening simultaneously. Spatial synopticity refers to the breadth of coverage at a given time, and temporal synopticity refers to the time needed to obtain a given breadth of coverage.

3 Strictly speaking, the GOES I imager creates eight simultaneous visible channel 1 image pixels and two simultaneous IR image pixels for each of channels 2, 4, and 5. Therefore, there is a degree of simultaneity. However, compared with the FPAs of 2000 to more than 500,000 detector pixels, this number of simultaneous pixels is small and offers small benefit as regards spatial relationships.

[Return to the text](#)

SECTION 4 GROUND-BASED PROCESSING OF FPA INSTRUMENT OUTPUT DATA

4.1 INTRODUCTION

Since 1974, environmental data have been collected using geostationary satellites. Over the years, a large user community with diverse interests has developed a variety of applications and conducted research using these data. These differing interests impose a variety of demands on the data providers. These demands are not restricted only to timely distribution of the data, but extend also to ensuring the continuity of the data. NOAA is responsible for stewardship of this valuable resource, and is committed to preserving both the quality and continuity of environmental data.

As NOAA improves environmental sensors and their supporting systems, continuity of services becomes increasingly important in protecting the investments of the diverse user community. Meeting this objective requires an evolutionary process for incorporation of improvements using modular services. With such a process, improvements do not require adjustments on the user's part to continue existing operations, but only to take full advantage of those improvements.

With the need for continuity of service in mind, this section addresses ground processing considerations for the proposed FPA imager in context of a NOAA ground processing system. This reference ground processing system is described in section 4.2. To support the proposed imager, sections 4.3 through 4.6 describe modifications of the functions of data reception, calibration and normalization, earth location and gridding, preparation for distribution, and sector distribution. Section 4.7 presents several scenarios of operation exploiting rapid image formation by the proposed imager and the earth location capabilities of the proposed ground processing system. Section 4.8 presents a summary and conclusions.

4.2 REFERENCE GROUND PROCESSING SYSTEM

Presently, NOAA operates geostationary satellites via a distributed network of ground systems at the Command and Data Acquisition Station (CDA) at Wallops Island, Virginia and the Satellite Operations and Control Center (SOCC) in Suitland, Maryland. At these facilities, data are received, processed, and distributed to government users in the various forms required. Outboard systems distribute data and products to external users such as the military, private industry, and educational institutions. For real-time data, these systems include GOES-TAP; Satellite Field Service Stations (SFSSs); and, in the future, NOAAPORT. The Data and Product Archives support both government and external users. This operation will continue into the future, with upgrades to support the enhanced capabilities of GOES I-M spacecraft.

Allowing time for development and production, the proposed imager would be ready for deployment well after GOES I-M series spacecraft and their ground processing system are due to begin operation; thus, GOES I-M ground processing is used as the reference system for the following discussion. GOES I-M ground processing will service all of the data streams communicated to and from the spacecraft. These data streams include those generated by meteorological sensors (imager and sounder), space environment

and monitoring sensors, search and rescue relays, and Data Collection System (DCS) observations. Also, the ground processing systems receive and transmit telemetry to monitor and supervise spacecraft operation. The discussion that follows considers the imager data stream and addresses other data streams only to the extent that they support processing the imager data.

4.2.1 GOES I-M Ground Processing System

GOES I-M ground processing is accomplished by subsystems grouped as follows:

- * The GOES I-M Spacecraft Support Subsystem, including the Operations Ground Equipment (OGE), the Telemetry and Control (T&C) Subsystem, the RF transmit/receive subsystems, and ground communications
- * The Product Generation and Distribution (PG&D) Subsystem, including the Central Meteorological Satellite Computer System (CEMSCS), the Multi-Discipline Data Analysis System (MIDAS), the GOES Sectorizer System, and the GOES Ingest and NOAAPORT Interface (GINI).

GOES I-M Spacecraft Support Subsystems reside at both the CDA and at the SOCC. PG&D Subsystems are at Federal Building #4 in Suitland, Maryland, and the NOAA Science Center in Camp Springs, Maryland. System components performing the real-time operations of processing and retransmitting raw instrument data are at the CDA; system components dealing with refined data and less time-critical operation are in Maryland.

4.2.2 Spacecraft Support Subsystems

Figure 4-1, adapted from [GOES91], shows the data flow among the geographically distributed GOES I-M Spacecraft Support Subsystems. Wideband raw instrument data are received by RF equipment at the CDA and routed by the OGE Data Acquisition and Patching Subsystem (ODAPS) to a Sensor Processing System (SPS), where the data are demodulated and processed.

Each SPS (one per spacecraft) ingests imager data and instrument telemetry, and then processes the imager data based on the telemetry and historical data. The SPS calibrates and normalizes imager data, computes and stores calibration statistics, applies reference grids to the image, locates the data samples with respect to earth coordinates, derives data to support orbit and attitude determination, applies time tags, and formats the data for GOES VARIABLE (GVAR) transmission.

Developed for the new capabilities of GOES I-M, the GVAR format was designed to maintain as much commonality as possible with the formats acceptable to existing Direct Readout earth stations. The largest data fields of this format are reserved for the meteorological data measured by the Imager and Sounder instruments. Also included are parameters associated with the measuring instruments, and provision for auxiliary products. After SPS processing, the GVAR-formatted data are transmitted from the CDA to the spacecraft that relays these data to Direct Readout earth stations, among them the SOCC.

Following the spacecraft relay, the GVAR-formatted data are received by RF equipment at the SOCC, resynchronized, and converted to an intermediate frequency (IF) signal. This signal is relayed to PG&D subsystems at Federal Building #4 and the NOAA Science Center, and to the other Spacecraft Support Subsystems in the SOCC, including the Product Monitors (PMs) and the Orbit and Attitude Tracking System (OATS).

Under normal operating conditions, the SOCC PMs identify and register landmarks in sectors of the imager data. The PMs support the OATS by providing, on request, the earth location coordinates of the landmark data, and Image Motion Compensation (IMC) and servo error data extracted from the GVAR-formatted data. PMs at both the CDA and the SOCC monitor the quality of GVAR-formatted imager and sounder data; display nonimage data contained in the GVAR-formatted data stream; and monitor the performance of calibration and normalization functions, accumulating statistics to support tuning of these functions. Under backup operating conditions, the CDA PM assumes the role of the SOCC PMs to support the OATS.

The principal function of the OATS is to produce the IMC coefficients used by spacecraft systems to meet the sensing systems' image navigation and registration (INR) requirements (as discussed in [section 4.5](#)). This process begins when the OATS ingests data forwarded by the GOES I-M Telemetry and Command System (GIMTACS), extracted from the Multi-purpose Data Link (MDL), and requested from the PM. From the star, range, and landmark observations of these data, the OATS determines the orbit and imager and sounder attitudes. On a daily schedule, the OATS produces IMC coefficients by predicting orbit and attitude perturbations following housekeeping operations or repositioning maneuvers. In addition, the OATS produces a schedule of commands to acquire needed data for the next day's processing and to satisfy other requests, including verification and tuning of Mirror Motion Compensation (MMC).

4.2.3 PG&D Subsystems

Each of the PG&D subsystems, whatever its location, shares a common architecture. This architecture includes VAS Interface Electronics (VIE) adapted from earlier GOES systems, a GVAR Ingestor, a GOES Real-Time Database (GRT), and applications. The VIE receives GVAR data and forwards them to a GVAR Ingestor that places the data in the GRT for access by PG&D applications. Located at Federal Building #4, the CEMSCS generates most of the automated products. These are image subsets for Weather Facsimile (WEFAX) distribution by the spacecraft, estimation of low-level winds from cloud motion, and data and product archives.

The remaining PG&D subsystems--MIDAS, the GOES Sectorizer System, and GINI--are at the NOAA Science Center. Most interactive products are generated by meteorologists using the display, processing, and database services of MIDAS. MIDAS maintains a comprehensive database of meteorological data from polar orbiting satellites, National Meteorological Center (NMC) guidance products, conventional observations, and weather radars. Using MIDAS, the interactive products generated are global winds

products, cloud top temperatures, atmospheric moisture distributions, rainfall estimates, sounding products (temperature and moisture profiles sampled at different altitudes), and derived imagery products (combined data from several imaging channels). The GOES Sectorizer System selects subsets (known as sectors) from the full earth disk GVAR data, enhances them, and distributes them in facsimile format (GOESFAX) to SFSSs. From the SFSSs these sectors are distributed to NWS Forecast Offices and other government and educational users. Currently in development, GINI remaps imagery into the three map projections required by AWIPS, and forwards these images to the AWIPS contractor for distribution via NOAAPORT.

4.3 DATA RECEPTION

For the proposed imager, ground processing begins with reception of a baseband digital data stream. Forming this digital data stream requires RF reception, detection, and bit synchronization equivalent to that performed by the ODAPS for NOAA-operated spacecraft.

Regardless of the origin of the baseband digital data stream, the next step in its processing is frame synchronization. This is the process of isolating and extracting data blocks by detecting synchronization patterns and headers in the data stream that represent the start of a data block and by accumulating the data a bit at a time. This processing is similar to that performed by the SPS, as is the remainder of the data reception processing required by the proposed imager.

Following frame synchronization, the SPS extracts nonimage data from the data stream and decommutates, or separates, the incoming data stream into separate data streams, one for each of the sensor channels. Nonimage data include instrument status and calibration measurements taken on board the spacecraft; these data are required for statistical analysis and subsequent ground processing steps.

Because of differences in scanning technique, the proposed imager data stream requires less data processing for decommutation than does the GOES I-M imager. While scanning latitudinally, the GOES I-M imager simultaneously acquires radiometric data for five channels, one visible and four IR. These data are accumulated in 480-bit data blocks, each corresponding to 64 microradians (urad) of latitudinal scan, and transmitted at a rate of 5460 blocks per second. By sorting these composite data based on their offset locations in the data block, decommutation performs time division demultiplexing to produce a synchronized set of individual sensor data streams.

Like the GOES I-M imager, the proposed imager acquires its five channels of radiometric data simultaneously. However, for a given scan position, the proposed imager arrays capture many more samples for each channel (as many as half a million for the visible channel and 32,000 for the IR channels). This allows forming transmission blocks that exclusively contain data for separate channels, with channel identification included in the block header. As with GOES I-M, time division multiplexing is performed, but requires less frequent computation to produce the individual sensor data streams.

Compared with GOES I-M, the proposed imager requires additional processing during data reception. As

discussed in [section 2.5](#), for a 3 minute transmission time from the proposed imager, the raw data rate is 50 Mbps and would require data compression to reduce the transmission channel rate if that was deemed to be desirable. As a consequence, decompression would have to be applied to transmitted data during ground processing to recover the original data.

A low-loss data compression technique that preserves the integrity of the original data while minimizing the encoding and transmission of redundant data would be required. Traditional compression techniques minimize redundancy by examining linear strings of data or scan lines and then replacing substrings that occur frequently with compact codes. Decompression is a process of copying data and replacing the codes with their corresponding substrings.

The array detectors of the proposed imager form two-dimensional images, a format that offers more opportunities for detecting and minimizing redundancy than a linear string. For example, the standard compression technique used in facsimile (FAX) coding is a two-dimensional extension of run length coding (RLC), a linear technique. FAX is a more efficient coding technique than RLC, when applied to a variety of images.

Selecting a suitable compression technique requires additional analysis and investigation of the redundancy in both GOES images and in high resolution images as produced by the proposed imager. The acceptable amount of information loss must be identified and weighed against the transmission rate reduction benefits of the various techniques.

Lossless, or error-free compression techniques can produce compression ratios in a range from 2:1 to 10:1, although generally they yield a maximum compression ratio of 3:1. Lossy techniques introduce distortion, but can produce compression ratios as high as 30:1 with some techniques offering extremely high fidelity at compression ratios ranging from 10:1 to 20:1. Also, the selected technique must be robust, providing the required compression ratio under the variety of diurnal and seasonal variations that are anticipated in the imager scenes. The required analysis is beyond the scope of the present investigation.

4.4 CALIBRATION AND NORMALIZATION

Following reception, these data are available: individual data sets for each of the imager channels, and non-image data including control and timing information from the imager and calibration measurements taken onboard the spacecraft. Calibration and Normalization, the next stage in processing, will use the non-image data to produce radiance estimates from the raw digital counts in the imager channel data sets. Calibration and normalization required for the proposed imager data is similar to that performed by the SPS for GOES I-M imager data, except for visible channel processing, where calibration is required instead of normalization.

Referring to SPS processing, radiance estimates for IR channels are produced from GOES I-M imager data using hardware look-up tables. A sensor's raw digital count is used as a table index to locate and

extract a radiance estimate from the look-up table. For GOES I-M, different tables are provided for each of the imager sensors. These tables are generated by a quadratic polynomial defined with calibration coefficients.

The polynomial's basic coefficients, adjusting the function's gain and bias, are derived from space look and blackbody calibration measurements taken on board the spacecraft. Space look is accomplished by exposing the IR detectors to a view of space beyond the edge of the earth, providing a cold reference. Blackbody measurement is accomplished by exposing the IR detectors to a view of an internal blackbody source, providing a 350 degree K reference. Second-order coefficients for the polynomial are developed from the factory-measured response characteristics of the IR sensors. Optionally, additional coefficients may be included; these are based on temperatures measured on the instrument's baseplate.

The process outlined here for calibration of GOES I-M IR imager data is essentially that required for calibration of the proposed imager's IR channel data sets. However, since a calibration table containing 2^{11} entries would be required for each pixel of the sensor arrays, direct computation of the radiance estimate from the calibration polynomial is a more suitable approach than table look-up.

Again referring to SPS processing, radiance estimates for visible channels are produced from GOES I-M imager data using normalization look-up tables (NLUTs). These tables are loaded with values that are periodically adjusted to incorporate current calibration and normalization information. Table values for the eight visible sensors are generated by an analyst at the PM, a non-real-time operation. From the GVAR data stream, the analyst chooses a full-resolution sector of maximum dynamic range, i.e., one containing cloud cover, ocean, and land masses. Then one of the visible sensors known to have long-term stability is selected as a reference and compared with the remaining seven visible channels. From this comparison, table values may be adjusted, if necessary, to provide uniform radiance estimates. The objective of this process is to ensure that uniform radiance estimates are produced from the raw digital counts of all eight visible sensors when viewing a scene of uniform brightness. If this process does not correct nonuniform visible detector response, striping will be observed in the visible images.

As discussed in sections [3.3.1](#) and [4.5](#), our approach to the problem of geographically locating pixels in a proposed imager frame begins with a process of "stitching together" overlapping frames. This process requires detecting features (based on contrast gradients) that are common to the overlap regions of overlapping frames and computing shifts to maximize the coincidence of the features in the overlap region.

Overlap regions for successive frames are viewed by different elements of the sensor array: the eastern overlap region of one frame is compared with the western overlap region of its successor. Any nonuniformities in the performance of the sensor elements across the array would degrade this process; consequently, a calibration process is required for the proposed imager's visible channel data sets. We propose the same as that used for IR calibration, discussed above, based on calibration measurements taken on board the spacecraft by scanning dark (no illumination) and light (evenly illuminated) line targets. In addition to improving visible image quality, this approach eliminates the labor-intensive

analytical operation of producing NLUTs using the PM. Deciding the allowable level of array sensitivity nonuniformity that will support our proposed image navigation technique will require evaluation of a variety of visible scenes. This evaluation is beyond the scope of the current investigation.

4.5 EARTH LOCATION AND GRIDDING

Longitude and latitude grid lines and geopolitical boundaries are referenced to imager data using a process known as gridding. Similarly, earth location is a process that associates longitude and latitude coordinates with identified pixels of the imager data. Both gridding and earth location information are annotations to the imager data. For GOES I-M data users, these annotations are transmitted in the GVAR data stream, gridding information in Block 0, and earth location information interleaved in the data blocks for every 196th pixel of the first visible line of every 14th scan.

As discussed in sections [3.2](#) and [3.3](#), the objective of the GOES I-M Image Navigation and Registration (INR) system is for all images to be consistently produced with the same fixed earth projection. Earth location and gridding for images produced with the GOES I-M INR is a straightforward transformation of the longitude and latitude grids and geopolitical boundaries, taking into account the spacecraft's orbit and attitude. For GOES I-M, this is performed by the SPS using either actual orbit and attitude data from the spacecraft, or reference orbit and attitude data provided by the OATS. As discussed in [section 3](#), there are significant differences between the scanning technique of the GOES I-M flying spot scanner and the techniques described for the proposed imager. These differences require a different approach to INR for the proposed imager than for GOES I-M INR and, consequently, a different approach to earth location and gridding.

For the proposed imager, we consider ground data processing that provides the INR function of locating imager array pixels with respect to earth coordinates as part of the process that produces gridding and earth location annotations. Our approach produces only these annotations and does not alter the pixels in imager frames. This approach is only outlined herein, since the details of its implementation depend on the information content of imager frames under a variety of diurnal and seasonal variations. As previously discussed in sections [4.3](#) and [4.4](#), the required analysis is beyond the scope of the current investigation. Also, we limit discussion to the step-stare imaging method, since time did not allow developing an approach for the time delay and integration (TDI) imaging method.

Our approach takes advantage of the proposed imager's principal benefit: a well-correlated sequence of overlapping "snapshot" images, each containing a consistently sampled set of pixels. Working with the collection of snapshot images provides a significant benefit to be realized during implementation of our approach. Many of the processing steps proposed operate within single image frames or localized regions of image frames; they do not depend on data outside their current frame or region. With no dependencies on other data, these operations can be performed in parallel; thus an implementation of our approach can provide high performance through parallel processing. The remainder of this section describes the required data processing, generally outlined as follows:

- * For a given channel, each frame of the imager data set is related to its neighbors; a mosaic of these frames is created based on redundant image information in overlap regions common to neighboring frames.
- * Landmarks are located in the mosaic image. The landmark locations are interconnected with a network of lines; each landmark location is connected to at least two other landmark locations, each in a different frame.
- * Distances between landmarks in the mosaic image are iteratively revised by adjusting the landmark locations within the mosaic until the distances agree with their known values, which are a function of actual spacecraft orbit, attitude, and time of day.
- * Landmark location adjustment values are apportioned among the frames of the data set.
- * Gridding and earth location annotations are developed for each frame based on its location in the frame sequence (e.g., scan mirror coordinates, frame image exposure event time) and the landmark location adjustment values.

With respect to a complete scene, each frame captured by the proposed imager includes redundant information. As discussed in section 3.3.1, this takes the form of an "overlap" or margin of additional rows and columns of pixels surrounding the targeted frame area. We propose using the redundant image information in these overlap regions for two purposes: first, to control our construction of a mosaic image, representing the entire scene viewed by the imager; and second, to support computation of the relative shifts and rotation of the imager frames that occurred while the imager scan was advanced from frame to frame.

Our mosaic is constructed with a coordinate system of subpixels. Subpixel dimensions are selected to limit any error introduced by the contrast gradient operation (discussed below) to less than one-fourth of a frame image pixel. This requires that the linear dimensions of a subpixel each be selected to be one-eighth the size of the linear dimensions of pixels of the imager frames. The validity of this selection of subpixel dimensions requires evaluation of the information content of imager frames with a variety of diurnal and seasonal variations.

Subpixels are used in the mosaic for two reasons: first, to allow determination of small relative rotations between frames, and second, to enhance the performance of the contrast gradient operation. As discussed in [section 3.3.1](#), for the visible channel, a full earth image is captured with a scan of 46 latitudinal frames and 23 longitudinal frames using a frame of 512 x 1024 pixels. In our mosaic, this region is represented using 8 x 46 x 512 or 188,416 latitudinal subpixels and 8 x 23 x 1024 or 188,416 longitudinal subpixels.

We begin the process by tentatively placing each frame in the mosaic at a nominal position based on its location in the frame sequence. We proceed, examining each frame in the order of the scan sequence, with the frame being shifted and rotated as needed to bring features in its portions of the overlap regions

into coincidence with the corresponding features in the overlap regions of its neighbors. As we proceed through the scan sequence, we record the shifts and rotations required for the addition of each frame.

Image processing offers a variety of approaches to detecting features in the overlap region and determining coincidence of features. The processes we require are similar to, but simpler than, those for matching cloud images when tracking their motion to produce estimates of winds aloft. Cloud motion winds are computed by tracking matched images selected from successive GOES images. The matching process is difficult since, during the 30 minute interval between GOES images, scene illumination variations and image deformations are common. For the proposed imager, the corresponding interval is generally not less than 200 milliseconds and never more than 14.4 seconds, so these variations and distortions are less likely.

Selection of optimal techniques requires an analysis of image data that is beyond the scope of the current investigation. For the sake of discussion, we offer a sample technique for detecting features and establishing coincidence in the overlap region at the east-west boundaries of two neighboring frames. Each frame's overlap region (one from the eastern frame and one from the western frame) is supersampled into mosaic subpixels, i.e., each subpixel is assigned the value of the frame image data at its location. A contrast gradient is derived for each supersampled sub-pixel. This is the magnitude of the vector sum of central differences in radiance taken north-south and east-west. This technique operates on the image's contrast gradients instead of image pixel values to minimize bias along preferred north-south or east-west axes, and to eliminate sensitivities to contrast and mean gray levels.

To construct a feature, we remove low-contrast gradient values, contracting the image, until a skeleton remains. A skeleton feature from one frame's overlap region is used as a mask and compared with the corresponding skeleton feature from the other frame's overlap region. The first frame's feature is shifted and rotated until the differences are minimized. These shift and rotation operations are recorded for each frame. Frames are added to the mosaic in scan sequence; for a given frame, the feature coincidence operation is performed only for overlap regions of the frame's predecessors. In general, the operation is performed once for each frame at the northern and eastern scan limits and twice for each of the other frames.

Matching of features in the east-west overlap regions is accomplished with a high degree of confidence, since the exposure event times of corresponding frames have an interval of less than 200 milliseconds. However, for north-south overlap regions, this interval could be as much as 14.4 seconds for north-south overlaps at the latitudinal extremes of the scan. Image motion during this interval can produce apparent shifting of a feature in one frame's overlap region with respect to the equivalent feature in a neighboring frame. This apparent shifting or "image smear" is defined and discussed in [section 3.4.4](#). We use the landmark locations and known relationships among the landmarks both to earth locate the image and to mitigate errors due to image smear.

To restrict the domain for landmark recognition, approximate landmark locations in the mosaic are determined from the frames' scan coordinates. These locations provide initial estimates for the

recognition processes. Considering the proposed imager's rapid scan rate (3 minutes for a full earth image), and its potential for frequently updated imaging (20 full earth images per hour, assuming continuous operation), automated landmark recognition is required. Details of an automated landmark recognition technique are dependent on image characteristics and require further analysis.

Using the focal plane arrays (FPAs) of the proposed imager in the step-stare mode simplifies the task of automated landmark recognition. As discussed in section 3.4.2.2, compared with single-pixel sensors or one-dimensional array sensors, the step-stare approach produces a large area of simultaneously exposed pixels. A two-dimensional frame produced by the step-stare approach is a "snapshot," preserving the topological relationships among all image pixels in the exposed scene (the frame image is subject to geometric distortions, as discussed in [section 3.4](#), besides those resulting from orbit and attitude variations). This frame is large enough to completely contain a landmark image.

With landmark images completely contained in frames, there is no need to assemble target images for landmark recognition as is required for single-pixel sensors or one-dimensional array sensors; thus a common source of errors is eliminated. We suggest automated landmark recognition is practical, given the proposed imager's high resolution and "snapshot" method of image formation. Also, we suggest that the enhanced resolution of the proposed imager's IR channels supports practical automated landmark recognition using IR. As with visible automated landmark recognition techniques, the details of an IR technique are dependent on image characteristics.

With landmarks located in the mosaic image, a network of lines interconnecting the landmark locations is formed so that each landmark location is connected to at least two other landmark locations. In the mosaic, these lines represent projections of great-circle arcs interconnecting the image landmark locations. Our objective is to adjust the landmark locations in the image so that the lengths of their interconnecting lines agree with known values. These known values are derived from the actual great circle arcs interconnecting the real landmarks. Landmark projections on a reference plane oriented by the spacecraft's orbit and attitude coordinates provide the needed values.

Adjusting the image landmark locations to bring their interconnecting lengths into agreement with known values is an application of well-known relaxation techniques. The required landmark location adjustments are recorded for each landmark-bearing frame as vectors encoding the required north-south and east-west shift operations. A significant benefit of the image landmark location adjustment process is that the earth location of an image landmark not only is a function of the landmark recognition process, but also is related to the known distances between the image landmark and its neighbors. Adjusting the interconnected network of image landmarks by matching a known reference takes advantage of the relationships among landmarks to minimize the impact of inaccuracies in the recognition of single landmarks. Using the additional information provided by the known lengths of interconnecting lines, we expect that the pixels of image landmarks can be reliably located to within a pixel of their true earth locations. This provides resolution of 0.5 km for visible landmark recognition and 4.0 km for IR landmark recognition using channels 4 and 5. Precise determination of the resolution limits of this technique requires evaluating the performance of the recognition technique when applied to imager

frames with a variety of diurnal and seasonal variations.

Image landmark location adjustments are apportioned among non-landmark-bearing frames using weighted averages. For a non-landmark-bearing frame, apportioned landmark adjustments are a weighted vector average of landmark adjustments from landmark-bearing frames using weights that are an inverse function of the distances between frames. In [section 3.4.4](#), image smear limits are described by a function of scan sequence width, a spatial measure of scan sequence timing. This is a sound basis for an alternative for apportioning landmark adjustments.

Since the latitudes and longitudes of the landmarks are known, the earth locations of the adjusted image landmark locations in the mosaic are similarly known. Consequently, the earth locations of all frame pixels in the mosaic can be found. For any frame pixel, this requires computation based on the enclosing frame's scan mirror coordinates, the shifts and rotations noted when the frame was incorporated in the mosaic, the recorded or apportioned landmark adjustments, and the orbit and attitude of the spacecraft. Image field rotation, as discussed in [section 3.4.5](#), is a function of the scan mirror coordinates, and is readily corrected as part of this computation. Similarly, channel-to-channel coregistration is accommodated by this computation, based on factory measures of optical system performance.

With earth locations established, geophysical boundaries and gridding lines can be associated with frame pixels. For each frame, annotations are produced conveying the gridding and earth location information. Gridding information is conveyed using a bitmap with an entry set for each frame pixel covered by a geophysical boundary or gridding line. Earth location information is conveyed by providing precise earth coordinates for the frame's most northwestern and most southeastern pixels, and parameters for a function that derives earth location for the remaining frame pixels. These parameters are computed from those listed above as required to determine earth location for any frame pixel. Also included in the frame's annotation are nonimage data, including frame exposure event time, mirror scan coordinates, and scan sequence coordinates.

4.6 PREPARATION FOR DISTRIBUTION AND SECTOR DISTRIBUTION

The NWS Modernization Program has set a goal of improving the forecasting and warning of locally severe weather events. This goal will be achieved by developing and fielding the AWIPS. AWIPS systems at Weather Forecast Offices (WFOs) will produce timely, high-resolution forecasts and warnings for their areas of responsibility from a database containing a detailed description of the state of the atmosphere in their local areas. This description of the state of the atmosphere will be formed as a gridded database integrating numerical guidance products, observations, weather radar products, and satellite imagery. Key to this operation is high resolution of mesoscale events, i.e., those with a time scale of less than 1 hour and a distance scale of less than 200 km.

Broadcast transmission of the annotated frames of proposed imager data is a suitable source of satellite imagery data for AWIPS, or other systems that select satellite imagery data and resample using specialized coordinate systems. Each frame's earth location annotations describe a bounding box for the

frame in earth coordinates, simplifying selection of frames that cover a region of interest. Also, these annotations support rapid and precise calculation of earth locations for the frame pixels. Resampling to local or specialized coordinate systems can be rapidly accomplished with a nearest-neighbor technique. This technique sets a pixel value in a resampled image from the value of the frame pixel with the closest earth coordinates to those of the resampled pixel. In overlap regions, where frame pixels are available from two frames, the frame pixel with the most recent exposure time is used.

Broadcast of the annotated frames, with resampling performed locally for specific uses, will provide improvements in image quality. This approach eliminates the cascade of errors that result from resampling generic products that are already resampled during their production. Detection and analysis of mesoscale events are enhanced by improved image quality and the rapid update rate of the proposed imager, which can produce a full earth image every 3 minutes.

With broadcast of annotated imager frames on this schedule, a WFO could revise its description of the state of the atmosphere for some region of interest every three minutes, a suitable rate for detecting and tracking mesoscale events. Also, an operational benefit derives from the broadcast; from the same broadcast transmission, frames can be selected to form either a full earth image or a multiplicity of images for regions of interest. This means the proposed imager can be operated in a free-running mode, with no special scanning modes or schedule interruptions for special events such as increased surveillance of locally severe weather conditions.

Broadcast of annotated frames, as outlined above, is suitable for advanced systems such as AWIPS and sector-generating systems capable of resampling data, but we must address the requirements of near-term product-generation systems. As discussed in [section 4.2.3](#), imager data are transmitted from the CDA in GVAR format, and processed by GVAR Ingestors to populate the GRT database. All product generation is performed by applications that operate either on this database or on the GVAR data stream. We propose that, over time, the GVAR Ingestors be modified to ingest the annotated frames, and that additional GRT access subroutines be developed for the proposed imager data. For continuity of service during this transition, the formatted imager frames would be resampled using the GOES Standard Projection, reformatted as GVAR, and transmitted to the PG&D systems for the normal course of product generation and distribution.

4.7 OPERATING SCENARIOS

With GOES I-M, NOAA plans to support three basic modes of operation:

- * Normal mode--the routine mode of operation. Full earth or near full earth images are provided every half hour.
- * Watch mode--enacted when the onset of severe weather is suspected. A sector covering the northern hemisphere and part of the southern hemisphere is provided every 15 minutes.

* Warning mode--enacted when the onset of severe weather is imminent. Regional sectors covering severe storm areas are provided; any or all sectors can be in a warning mode independently.

In addition, NOAA has international commitments for a full earth image once every 3 hours. As discussed in section 4.6 above, the proposed imager does not require special scheduling considerations to support all of these operating modes.

The enhanced resolution and rapid update rate of the proposed imager provide for early detection and accurate forecasting of mesoscale events, an objective of the NWS Modernization Program. NESDIS Office of Research and Applications Staff have researched and developed techniques supporting this endeavor. These techniques either require or benefit from data of high spatial and temporal resolution, like that of the proposed imager.

Applying these techniques to data of this quality, operational meteorologists can detect and better understand phenomena such as the following:

- * Triggering mechanisms important in thunderstorm genesis
- * Thunderstorm intensity (estimated through measurement of cloud top temperatures)
- * Atmospheric motion (cloud drift winds, water vapor gradient changes, and thermal gradient winds)
- * Atmospheric cloudiness (cloud cover emissivity, and height)
- * Tropical cyclone tracks (steering currents approximated by deep layer mean wind vectors)
- * Clear air turbulence
- * Fog detection and dissipation at airport locations
- * Potential thunderstorm development (determined from early morning cloud cover)

4.8 SUMMARY AND CONCLUSIONS

The above discussion can be summarized in the following conclusions:

- * During data reception, demultiplexing of the data stream from the proposed imager requires less frequent computation than is required for GOES I-M; decompression requires additional processing beyond that required for GOES I-M.
- * Automated landmark recognition, in both visible and IR channels, is feasible for the proposed imager's

frames.

- * The landmark location adjustment process can provide reliable earth location while accommodating image smear. As for GOES I-M, gridding is a straightforward process.
- * The frames produced by the proposed ground processing contain imager pixel data that have been radiometrically calibrated, but not altered in any other way. Earth location and gridding information is provided as annotations for these frames.
- * The proposed imager does not require special scheduling considerations to support all of the operating modes required by NOAA for GOES I-M imaging. From the same broadcast transmission, frames can be selected to form either a full earth image or a multiplicity of images for regions of interest. This means the proposed imager can be operated in a free-running mode, with no special scanning modes or schedule interruptions for special events.
- * The enhanced resolution and rapid update rate of the proposed imager provide for early detection and accurate forecasting of mesoscale events, an objective of the NWS Modernization Program. With broadcast of annotated imager frames on a 3 minute schedule, a WFO could revise its description of the state of the atmosphere for some region of interest every 3 minutes, a suitable rate for detecting and tracking mesoscale events.
- * Broadcast transmission of the annotated frames of proposed imager data is a suitable source of satellite imagery data for AWIPS, or other systems that select satellite imagery data and resample using specialized coordinate systems.
- * Broadcast of the annotated frames, with resampling performed locally for specific uses, will provide improvements in image quality by eliminating the cascade of errors that result from resampling generic products produced with resampling.

We identified several areas requiring further analysis, which time and resources did not permit us to address:

- * Selecting a suitable compression technique requires additional analysis and investigation of the redundancy in both existing GOES images and modeled high-resolution images as might be produced by the proposed imager. The acceptable amount of information loss must be identified and weighed against the transmission rate reduction benefits of the various techniques. Also, the selected technique must be robust, providing the required compression ratio under the variety of diurnal and seasonal variations that is anticipated in the imager scenes.
- * Deciding the allowable level of visible channel array sensitivity nonuniformity that will support our proposed image navigation technique will require evaluation of a variety of visible scenes.

- * Selecting suitable techniques for detecting features in the overlap region and determining coincidence of features will require an analysis of image data.
- * Determining details of automated landmark recognition, in both visible and IR channels, will require additional analysis of image characteristics

[Return to the text](#)

SECTION 5

DEPLOYMENT

5.1 CONTEXT

NOAA's GOES spacecraft carries three remote-sensing instrument packages, along with supporting communications subsystems, to serve its mission needs. An imaging radiometer, as described in [Section 1](#) of this report, is accompanied by a sounding radiometer that measures radiance's from the earth's surface to the upper stratosphere; from these measurements vertical temperature profiles can be derived. A Space Environment Monitor (SEM) consists of four instruments that monitor magnetic fields, solar x-ray flux, and charged particle fluxes.

Deploying a focal plane array (FPA) imager on a dedicated spacecraft is possible, as is deployment on a non-dedicated spacecraft as proposed in this project. To fulfill the rest of the GOES remote sensing mission, deployment of a sounder and the SEM must be considered. Both of these were beyond the scope of this project, although the following discussion applies.

The GOES I-M sounder is a flying spot scanner, about the same size and mass as the GOES I-M imager. It collects radiance data for 18 narrowband infrared (IR) channels and a visible channel. A filter wheel is used to discriminate among and shape the IR channels. In missions prior to GOES I, the imaging scanning radiometer was adapted to perform both imaging and sounding. If the FPA imager detectors can have the same extended IR sensitivity and perform their intended imaging function, it is conceivable that the step-stare imager could perform both imaging and sounding functions. The increased speed of the instrument may make it possible to perform both of these functions while maintaining the current 30 minute imaging/sounding schedule. An increase in mass and complexity would be expected to account for the added functionality for a combined instrument.

The imager or combined imager/sounder instrument package must be located on the earth-facing surface of the spacecraft and must have an unobstructed view to space for thermal control and detector calibration purposes.

The GOES I SEM consists of ten assemblies, including sensors mounted on the external structure of the spacecraft. As a consequence of the need to deploy sensors external to the spacecraft body and, in the case of the x-ray sensor, on a movable platform that faces the sun at all times (e.g., attached to the GOES I solar array positioning mechanism), the degree of integration with the host spacecraft is quite high.

The GOES I imager weighs 267 pounds (lb), the Sounder weighs 283 lb, and the SEM 72.8 lb as of April 1, 1993. In this project, we considered integration of the FPA imager only, at a weight of 235 lb.

5.2 PROGRAM PLAN

To determine a time frame in which an FPA imaging instrument could be available for integration with a nondedicated satellite, we projected the initiation of a National Oceanic and Atmospheric Administration (NOAA) development program. Given a decision to proceed, NOAA would have to initiate actions to have a program authorized through Department of Commerce management channels, the Office of Management and Budget (OMB), and funded by congressional action.

The National Aeronautic and Space Administration (NASA) serves as the satellite engineering, procurement, and launch agency for NOAA meteorological satellites. The NASA Management Instruction "Planning and Approval of Major Research and Development Projects" (NMI 7121.1) defines a four-phase program that would be undertaken for development of a NOAA imager. These instructions define a NASA in-house Phase A Study to identify requirements and develop implementation concepts, in this case for an FPA imager. This is followed by Phase B Studies, conducted by multiple contractors, to further develop design specifications. After a procurement action, a Phase C begins during which a selected contractor produces a final design, and manufactures and delivers the required end item. The final Phase, D, is for test and integration of the FPA imager with the host space platform. These phases are detailed below:

*** Phase A--Study:** The initial action under the instructions for R&D projects is an in-house study effort by which requirements are defined and concepts are developed to meet these requirements. Included in the study is a Government management plan and projected resource requirements, documented in a Phase A Study Report.

Based upon preliminary studies conducted for the NOAA N report, augmented by material developed by MITRE, the duration of a Phase A Study for the FPA imager is projected to be 1 year after a second quarter calendar year 1994 (CY94) start. Formal documentation, presentation, and review of a Phase A Study Report incorporating technical and management factors is projected to require 3 months, through third quarter CY95.

*** Program Initiation:** With a successful outcome from the Phase A Study effort, results would be available to NOAA to determine whether the potential benefits of the FPA imager warrant a new program start for a development program. It is expected that internal review by NOAA, coordination with NASA, and consultation with the meteorological data user community would occur prior to a decision to proceed. The documentation requirements and review process for program initiation is expected to require 6 months to accomplish, with funding for a new program start included in the 1996 budget submission.

*** Phase B--Study:** With authorization for a new program start and appropriation of funds in the first quarter CY97, the next program action would be contracting with industry for Phase B design studies. Multiple studies to develop design specifications for alternative approaches to producing the required end item would be contracted with qualified bidders. Internal review of the Phase A Study Report would refine requirements to the point where a Request for Proposals (RFP) for competitive procurement could be released to industry in third quarter CY96, 3 months after program authorization.

Submission of proposals from multiple qualified bidders, a period for questions and responses, proposal

evaluation, and contract negotiations would require an additional 12 months before contracts can be awarded in third quarter CY97. Completion of the Phase B Study activity and submission of final reports is expected to require twelve months, projecting the conclusion of the Phase B effort to occur in the third quarter CY98.

*** Phase C--Final Design/Production:** Under a modified A109 procurement plan, direct selection of a Phase B Study contractor for a Phase C contract award can occur after a cost competition. Phase C of the program plan is the activity to select a design from the Phase B study results which best meets cost and performance requirements with the least risk, and proceed with a Phase C contract for final design and manufacture of the instrument. The Phase B contractor selected can be expected to be awarded the Phase C contract after 6 months for Phase B Study evaluation and contract negotiation, with contract award in the second quarter CY99.

Based on government experience with developmental contracts of this nature, 3 years are projected until first instrument delivery in CY02.

*** Phase D--Integration and Launch:** Phase D of the development cycle would be the integration of the payload instrument with the host space platform. The actual time required for integration and test prior to launch is projected to be 1 year, with CY03 projected as the first launch opportunity.

The 1 year period for integration and test does not include the time required to identify and negotiate arrangements with a satellite operator on whose spacecraft the instrument would be carried. Nor does it include the time required for the spacecraft manufacturer to adapt the spacecraft design to accommodate an imager in the spacecraft payload. It is expected that these actions would be taken concurrently with Phase C, and that the spacecraft manufacturer would be under contract for Phase D integration and test.

5.3 LAUNCH OPPORTUNITIES

With the year 2003 as a launch target, we studied the current and planned US geostationary satellites to identify potential space platforms on which the proposed imaging instrument could be carried. [Table 5-1](#) lists all commercial communications satellites in orbit in United Nations International Telecommunications Union (ITU) Region 2 as of January 1, 1993.

5.3.1 Commercial Communications Satellite Systems

All commercial communications satellites, as of 1993, have been in an equatorial geostationary orbit of 22,300 miles over the equator, rotating at the same rate as the earth, such that they appear stationary to an observer antenna on the earth's surface. In 1964, SYNCOM III, produced by the Hughes Aircraft Corp. (HAC), El Segundo, California, demonstrated that a satellite at geostationary altitude, with the stability to maintain an antenna pattern consistently pointing to the same location on earth, could provide point-to-multipoint communications to ground stations on nearly one third the earth's surface. The required stability for antenna pointing was initially achieved by the gyroscopic effect of spinning the drum-like

body of the satellite containing spacecraft bus components in one direction at 50 revolutions per minute (RPM), and motor driving a despun communications payload platform at the same rate in the opposite direction. This technique, "spin stabilization," was employed in the majority of early geostationary satellites.

The first commercial communications satellite, "Early Bird" (INTELSAT I), was a derivative of SYNCOM, and was placed into orbit in the spring of 1965 by a consortium of the United States, Canada, and ten European nations--the International Telecommunications Satellite organization, INTELSAT.

Management of the radio frequencies used and the orbital spacing required to avoid mutual radio interference between satellites is the responsibility of the ITU. The ITU has established the International Frequency Registration Board (IFRB) which manages the allocation of frequencies to the three ITU Regions into which the world has been divided. Frequency management and authorization for orbital location assignments for US operators of communications satellites in ITU Region 2, nominally 61 degrees-W to 148 degrees-W longitude, in which the United States (US) are located, are vested in the US Federal Communications Commission (FCC). In compliance with a 1988 trilateral agreement between the United States, Canada, and Mexico, new US domestic satellites are authorized to occupy the eastern segment of the arc from 61 degrees-W to 105 degrees-W longitude, and the western segment from 121 degrees-W to 148 degrees-W longitude.

The FCC grants authorization for construction of a spacecraft for domestic communications purposes only after frequency allocations and orbital slots have been approved and are uncontested. Once authorized, the orbital slot and frequency assignments become extremely valuable assets of the satellite operators, and satellites are regularly replaced at the end of their useful life at the same location, with the same operating frequencies. As of 1 January 1993, 43 commercial communications satellites were in orbit and operational in ITU Region 2, with a total of 110 geostationary commercial communications satellites deployed worldwide.

In 1973 the Nixon administration announced an "open skies" policy whereby any financially and technically qualified organization could apply for and have authorized a domestic communications satellite system. Initial applicants included American Telephone and Telegraph (AT&T), Western Union, Radio Corporation of America (RCA), COMSAT, Lockheed/Microwave Communications, Inc. (MCI), Continental Telephone (CONTEL)/Fairchild American Satellite, Hughes, Southern Pacific Railroad, and General Telephone and Electronics (GTE). All of the initial applicants were eventually authorized construction and have operated satellites in orbit.

The first generation of communications satellites is relevant to identifying future candidate carriers for the FPA imager under study. They are being replaced in orbit by second- generation satellites, whose subsequent replacement will occur in the time frame during which the proposed FPA imager is projected to be available for operation.

First generation satellites have a nominal 5-7 year in orbit life, limited by the amount of station-keeping fuel, deterioration of the solar cell power-generation arrays, and cathode emission deterioration and

failure of traveling wave tube (TWT) transponders on board. These spacecraft are characterized as being either "spinner"-type descendants of SYCOM III, or "body stabilized" with three-axis stabilization produced by internally contained spinning momentum wheels providing gyroscopic stability. All domestic US geostationary communications satellites, and virtually all the first-generation commercial communications satellites in the world, are either the Hughes HS376 spin stabilized spacecraft, with 34 in orbit, or the RCA or GE Astro 3000 three-axis stabilized spacecraft.

Since its inception, the commercial communications satellite industry has gone through a dramatic evolution, during which satellite ownership, network operation, and satellite manufacturing have been in a state of change. These changes are reflected in the current status of the initial domestic satellite applicants.

5.3.1.1 First-Generation Systems

American Telephone and Telegraph (AT&T): AT&T was a pioneer in satellite communications, having built and, in 1962 launched the experimental series of inclined orbit (nonsynchronous) TELSTAR communication satellites. The TELSTAR satellites were "active repeaters," whereby a signal transmitted from a ground station was received by the satellite, frequency translated, amplified, and retransmitted to the ground by on-board transponders. AT&T's initial application to the FCC was for a constellation of geostationary satellites to augment the capacity of its Long Lines Department's network of long-haul terrestrial cable and microwave wideband transmission facilities. This application was subsequently withdrawn after AT&T contracted for these services with COMSAT Corp. through use of a COMSAT-owned and-operated COMSTAR constellation of four satellites, first launched in 1976. AT&T traffic was moved to the GTE SPACENET system of satellites in 1984. In July 1983, AT&T launched TELSTAR 301, the first of a three geostationary satellite network providing service to link television networks with their affiliated stations throughout the country. TELSTAR 301 was the first commercial communications satellite to use solid state power amplifiers in orbit, as well as TWTs.

Western Union: In July 1974, Western Union launched the first of its six WESTAR satellites, establishing the first US commercial communications satellite system. The launch of WESTAR VI, in 1982, completed the constellation. In November, 1988 the FCC approved Western Union's application for construction of replacements for its WESTAR IV and V. In 1989, upon the departure of Western Union from the industry, the FCC approved assignment of Western Union's authorization to Hughes Communications Galaxy, Inc., which renamed the satellites Galaxy IV-H and Galaxy V-W.

In 1976, NASA awarded a contract to Western Union to construct and operate a hybrid satellite that would serve the commercial needs of Western Union, and also provide NASA with an in-orbit geostationary communications satellite using frequencies assigned to the government to serve as a data relay for low-orbit NASA space missions, primarily the Space Shuttle. Delays in construction and cost over runs for these Advanced WESTAR satellites being produced by TRW, resulted in termination of the contract with Western Union. In 1981, the construction permits and contract were transferred to the Space Communications Co. (Spacecom) of CONTEL, which has leased the 24 C-band domestic satellite transponders to Columbia Communications Corp. of Honolulu, while providing Tracking and Data Relay

Satellite System (TDRSS) capacity for NASA. The Columbia commercial satellite network, using the TDRSS satellites, is the only global, commercial communication satellite system other than Intelsat.

Radio Corporation of America (RCA): RCA was both a manufacturer of three axis stabilized spacecraft and operator of the RCA Americom satellite system. It also was the operator of RCA Alaskcom and the Aurora satellites, as the communications provider for Alaska after it purchased the Alaskan Communication System franchise from the US Army in 1974. The SATCOM constellation of satellites through SATCOM VII included SATCOM VI, the first completely solid state communications satellite, launched in April 1983. RCA's satellite manufacturing and Americom's communications satellite constellation were sold to General Electric in 1987.

Comsat Corporation: Comsat had initially filed for a constellation of large, multi-user C-band satellites to provide services for other communications companies. This application was rejected and replaced by an application for and approval of a four satellite COMSTAR system providing voice, data, and TV services exclusively for AT&T under a seven year contract. COMSTAR D4, launched in February 1981 reached the end of its operational life in 1988. Through use of a proprietary "Comsat Maneuver" whereby its antennas are continually repointed by ground command, the satellite is in an inclined instead of geostationary orbit and its communications capability has been extended.

Lockheed/(MCI): The initial application by Lockheed/MCI was for authority for construction and launch of all-digital communications satellites operating at Ku-band (11-14 GHz) to service private networks with customer premises earth stations. After initial studies, Lockheed withdrew from the partnership and was replaced by COMSAT Corp., and IBM who, along with MCI, created Satellite Business Systems (SBS). The FCC authorized construction and assigned orbital slots for six SBS Ku-band satellites, all of which have been successfully launched and operated. SBS-1 was launched in November 1980. In 1984, SBS was dissolved as a company with its assets distributed among its three partners. COMSAT took ownership of the satellites then in orbit, while IBM, through a subsidiary Satellite Transponder Leasing Corp. (STLC), acquired the orbital slot assignments and the satellites then under construction. In 1990, the Hughes Communications Co., a subsidiary of Hughes Aircraft Co. (HAC), acquired the assets of STLC including SBS 4, SBS 5, and SBS 6, the last of the series, which was launched in October 1990.

Continental Telephone(CONTEL)/American Satellite: CONTEL acquired the American Satellite Corp. from Fairchild Corp., which as a domestic communications satellite operator launched two spacecraft: ASC-1 in August 1988, and ASC-2 in April 1991. These satellites are hybrids, operating both at C-band (4 and 6 Ghz) and at Ku-band (11 and 14 Ghz) and were the first commercial satellites to introduce uplink command encryption. In 1991, CONTEL ASC merged with GTE SPACENET; ASC-2 now designated SPACENET IV, while ASC-1 remains under CONTEL's control.

Hughes: HAC, originally a subsidiary of the Hughes Tool Co. and now part of General Motors Corp., is the manufacturer of the highly successful HS 376 spin-stabilized spacecraft. It is also the largest domestic commercial communications operator through its Hughes Communications, Inc. and Hughes Communications Galaxy Inc. subsidiaries. Hughes Communication Inc. operates SBS-4,-5,-6 Ku-band only satellites which it acquired in 1990. The Hughes Galaxy system is a six satellite constellation

operating at C-band, first launched in June 1983. Replacement Galaxy satellites will be both C-band only and hybrids operating at both C and Ku-bands, to incorporate the functions of the Hughes- owned SBS Ku-band satellites into the Galaxy system. The Hughes Galaxy network provides services to customers who collectively have over 25,000 ground station dishes.

Hughes Communications is also the operator of the LEASAT constellation of eight global satellites. LEASAT 1 (SYNCOM 4-2) launched August 1984, providing leased communications services exclusively for the US. Navy.

Southern Pacific Railroad: Southern Pacific Railroad, an initial applicant for domestic satellite authorization, received FCC approval of its SPACENET system in 1980. Southern Pacific became a communications company as a result of its railroad rights of way, which served as sites for pole lines and microwave towers. The planned SPACENET system was intended to provide communications services for its SPRINT voice and data network. In June 1983, GTE Satellite Corp. acquired the SPACENET authorizations and spacecraft under construction, the first of which was launched as SPACENET I in June of 1984.

General Telephone Electronics (GTE): GTE Satellite Corporation, which became the GTE SPACENET Corporation after the 1983 acquisition of Southern Pacific Railroad's SPACENET, operates two satellite systems--the SPACENET hybrid C-band/Ku-band system and the all Ku-band GSTAR system. SPACENET I, launched in June 1984, was the first of the four satellite SPACENET constellation. GSTAR I, launched in May 1985, was the first of the four satellite GSTAR constellation.

GE Americom: The acquisition of RCA Corp. by General Electric Co. in 1986 established GE Americom as the operator of the RCA Americom SATCOM and the RCA Alaskom Aurora satellites then in orbit. SATCOM 1R was launched in April 1983 and is the oldest of the six GE Americom C-band only satellites in orbit. SATCOM K1, which serves as a medium power direct broadcast satellite (DBS), was launched in November 1985 and is the oldest of the two GE Americom Ku-band only satellites in-orbit. The acquisition of the GE Astrospace Division by Martin Marietta in 1992 left the Americom satellite system with GE.

At present there remain four operators of US commercial communications satellites:

- * Hughes Communications, Inc. Galaxy Network
- * GTE SPACENET and GSTAR Networks
- * GE Americom Network and Alaskom
- * AT&T TELSTAR Network.

5.3.1.2 Second-Generation Systems

On November 17, 1988, the FCC authorized construction and launch of 10 replacement satellites and the construction of 13 new domestic communications satellites. Second- generation satellites now under construction or on order for replacement of operational satellites approaching the end of their life, are three axis stabilized, large spacecraft, with a projected 10 to 12 year mission life. Compared with early geostationary satellites they will have a launch weight of up to 7500 lbs, contrasted with 2500 lb weight of the first- generation satellites. They will have over twice the in orbit dry weight (3250 lb vs. 1300 lb), greater electrical power (4700 vs. 1000 W), and higher-power transponders (up to 240 W contrasted with the early 5.5 W transponders). Galaxy VII, launched October 27, 1992, is the first US replacement second-generation satellite in orbit, replacing SBS-4. [Table 5-2](#) lists projected replacements for commercial satellites.

In addition to authorizing replacement satellites for those currently in orbit, the 1988 action approved new domestic DBS and mobile satellite service (MSS) systems. Economic viability of DBS operation in the United States has not as yet been demonstrated, and this has resulted in two approaches to DBS service. One is medium-power DBS service, such as that presently being provided by SATCOM K-1, with 47 W Ku-band transponders, requiring the use of 3 ft diameter dish receiving antennas. The other approach is high-power DBS service with up to 240 W Ku-band transponders, permitting use of antennas as small as a 10 inch conical horn, or an 18 inch flat planar array receiving antenna.

The 1983 Regional Administrative Radio Conference (1983 RARC) of the ITU allocated eight orbital slots from 61.5- W to 175- W. longitude., for DBS service, with only 101-, 110-, and 119- locations, about in the middle of the GOES 75- and 135- positions, capable of providing coverage to the entire continental United States (CONUS).

Hughes Communications/US Satellite Broadcast, Inc.: The FCC has authorized construction, assigned orbital slots, and authorized use of frequencies for two high power DBS satellites manufactured by Hughes Space and Communications Group, scheduled for launch in December 1993 and July 1994. The communications package design supports these "Direct TV" satellites' direct broadcast operation exclusively, and does not provide typical communications downlink services envisioned for use with an FPA imager. In 1989, Hughes was authorized construction of two additional high power DBS spacecraft.

EchoStar Satellite Corp.: A 1988 FCC Opinion and Order authorized the EchoStar Satellite Corp. to have constructed and operate a constellation of ECHOSTAR satellites to provide DBS service to CONUS, Puerto Rico, Alaska, and Hawaii. The preferred orbital locations for ECHOSTAR are 61.5-W serving the eastern half of the United States, and 148-W, serving the western half. EchoStar has contracted for one GE 7000 spacecraft, with options for six additional spacecraft.

Advanced Communications: Advanced Communications has contracted with GE Astrospace (now Martin Marietta) for a high-power GE 7000 spacecraft for DBS services, with completion of its DBS facilities scheduled for December 1994.

5.3.1.3 Mobile Satellite Service (MSS)

Eleven applications were filed with the FCC in the mid-1980s to provide a first-generation MSS system. MSS is a satellite-based alternative to terrestrial cellular telephone and radio services that will provide telephone, radio, and data communications throughout its area of coverage, including sparsely populated areas. In 1986, the FCC determined that only one MSS first-generation system was feasible and directed all qualified applicants to form a consortium that it would license to construct, launch, and operate an MSS system. Eight of the applicants, including Hughes Communications Mobile Satellite, Inc., formed the American Mobile Satellite Corp. (AMSC) of Washington, DC.

American Mobile Satellite Corp. (AMSC): The AMSC authorization for MSS service projects a constellation of three geostationary satellites, the first of which is a Hughes HS601 second-generation satellite now under construction, with a planned launch as AMSC-1 in 1994.

Telesat Mobile Inc. (TMI) of Canada: Under a Joint Operating Agreement signed in 1990, TMI's M-SAT satellites and AMSC's satellites will provide complementary mobile telephone, radio, and data services to land, aviation, and maritime users, providing back-up and restoration capacity for each other. As a result, both systems will deploy the same spacecraft design, with Hughes providing the spacecraft bus and SPAR Aerospace Limited of Canada providing the communications payload package.

5.3.1.4 Spacecraft Manufacturers

The concept for imaging from nondedicated satellites includes an arrangement whereby domestic geostationary commercial communications satellite operators would provide a platform for the imager and provide communications and operational support services to NOAA under contract. It anticipates NOAA's providing the imager as Government Furnished Equipment (GFE) and bearing the full cost of the necessary modification to the operator's spacecraft bus. It recognizes the requirement for integration and test of the imager with the communications payload of the spacecraft, which would be done by the spacecraft manufacturer, either by direct contract with NOAA or through contractual arrangements with the satellite operator.

The following U.S. companies produce spacecraft for commercial geostationary satellite communications.

GE Astro Space/Martin Marietta: GE Astro Space of East Windsor, New Jersey, acquired RCA in 1986 and was itself purchased by Martin Marietta of Bethesda, Maryland in April 1993. GE/RCA was a major supplier of three axis stabilized first-generation communication satellites for both foreign and domestic operators. It currently has on order eight of its GE 7000 series of second-generation communications satellites and is developing an advanced spacecraft designated, GE 2100, for delivery in 1996.

Hughes Space and Communications Group: Hughes is the leading builder of commercial communications satellites, both for domestic and international operators. It currently has contracts for construction of 30 of its second-generation HS 601 spacecraft, and continues to deliver upgraded HS 376 spacecraft for operators with modest capacity requirements.

Space Systems/Loral: Loral entered the spacecraft manufacturing business by acquiring Ford Aerospace Western Development Laboratories (WDL) and its manufacturing facility at Palo Alto, California. Ford manufactured communications satellites, including INTELSAT V and VA, and INTELSAT 7 and 7A. For India it produced the INSAT constellation of four hybrid domestic communications and meteorological satellites, using the very high resolution radiometer (VHRR) imager, precursor to the advanced AVHRR currently flown on US polar orbiting (ATN) satellites. Ford Aerospace, now Space Systems/Loral, also produced the SUPERBIRD DBS satellites for Japan, based on its FS-1300 spacecraft platform, comparable to the GE 7000 or HS601, of which 3 are in orbit and 12 are on order. It has not delivered a communications satellite for US domestic operation.

In 1992, a 49 percent interest in Space Systems/Loral was sold to the European aerospace companies of Aerospacial, Alcatel, Alenia, and Deutsches Aerospace, each with a 12.25 percent interest, to form the Space Systems/Alliance.

5.3.2 Government Geostationary Satellite Systems

In addition to commercial communications satellites, the US government operates a number of global geostationary communications satellites in support of defense activities. The following is a brief summary of such government systems, based on unclassified information contained in the open press.

MILSTAR: The US Air Force managed MILSTAR program, formerly the Military Strategic and Tactical Relay system, is a \$32 billion communications satellite system currently under construction. An eight satellite constellation with an in orbit spare is planned. The system comprises two series of spacecraft: a three satellite MILSTAR I system, with first launch scheduled for summer 1993, and at least a four satellite MILSTAR II system, with first delivery projected for 1999. Lockheed Missiles and Space Co., Sunnyvale, California, is the prime contractor for MILSTAR, with TRW, Hughes, and GE as major subcontractors. The MILSTAR program is presently being reevaluated and is subject to modification.

The MILSTAR I system provides relatively low-data-rate communications links, intended primarily for secure dissemination of orders to US nuclear forces. The MILSTAR II system will have the low-data-rate capability of MILSTAR I, but will also provide a medium-data-rate capability to support commanders with tactical communications to forces in the field. The MILSTAR systems are designed to be jamming resistant, utilizing extremely high frequencies (EHF) above 30 Ghz, with spectrum spreading and frequency hopping, and with nuclear hardening to protect against electromagnetic pulse (EMP) impairment. The MILSTAR II satellites will have an intersatellite link at EHF to avoid the transmission delays encountered when two earth terminals are not in view of the same satellite, and multiple ground-to-spacecraft-to-ground hops are required to establish a communications link.

LEASAT: In September 1978, Hughes Communications Services entered into a contract with the US Navy to establish and operate a global network providing ultrahigh frequency (UHF) transponder service to US Department of Defense (DoD) users. Hughes has provided a five satellite Space Shuttle (STS)-launched constellation, with flight F-1 launched in August 1984, and flight F-5 in November 1989.

FLTSATCOM: The Fleet Satellite Communications System (FLTSATCOM) is a six- satellite constellation providing 23 UHF (244-400 megahertz [MHz]) communications channels serving land based US Navy and US Air Force facilities, shipborne and AFSATCOM airborne terminals, and an antijam fleet broadcast channel uplinked at S-band. FLTSATCOM spacecraft were produced by TRW, with the launch of F-1 in 1978 and the launch of F-8, last in the eight spacecraft series, in September 1989.

UHF Follow-on Program (UFO): A satellite program to continue the UHF satellite services to DoD users currently provided by the LEASESAT and FLTSATCOMM systems has been undertaken by the Navy. It is planned to be a ten satellite program with two satellites located over CONUS, and two satellites each over the Atlantic, Pacific, and Indian Ocean regions. When fully implemented it will have an in-orbit spare and one on-the-ground spare. Hughes was awarded a contract in mid-1988 for its commercial HS601 spacecraft bus.

DSCS III: The global Defense Communication Satellite System (DSCS) became operational in July 1967 with the first of the 26 Phase I satellites. A 16-satellite Phase II followed, with first launch in 1972, and has progressed to the current Phase III system, first launched in October 1982. The DSCS III spacecraft are produced by GE, which is under contract for a total of 11 spacecraft.

5.4 OPERATIONAL CONSIDERATIONS

Deploying an FPA imager on a suitable domestic communications satellite offers opportunity for satellite operation not heretofore available.

The FPA imager described in [Section 2](#), can capture a full earth disc image in 3 minutes. Using appropriate modulation methods, and possible data compression techniques, the basic 50 megabits per second (Mbps) data rate can be accommodated easily by the 36 MHz C-band or a 72 MHz Ku-band transponder of a commercial communications satellite.

Each communications satellite operator has established Telemetry and Command (T&C) operations centers for control of its in-orbit satellites, eliminating the need for NOAA to provide those functions. It is envisioned that the host spacecraft operator would expect some compensation from NOAA for conducting these operations supporting a NOAA payload.

5.5 COST CONSIDERATIONS

The cost of placing a commercial communications satellite in orbit consists of the cost of the spacecraft; the cost of the launch vehicle; the cost of ground handling; and, where applicable, the cost of spacecraft in-orbit insurance. Spacecraft costs vary according to customer requirements and the number of spacecraft over which one-time development costs are spread. Launch vehicle costs are dependent on the launch weight of the satellite to be orbited. At present, the French firm Aerospatial, with the Ariane family of launch vehicles, supplies about 60 percent of the world's launch vehicles. The recent entry into the market

of China's Long March, Russia's Proton, and the imminent entry of Japan's H-2 launcher introduced some instability in launch costs. Insurance costs for the spacecraft vary according to the value of the spacecraft and the particular launch vehicle selected. Recent launch failures have established a range of 16 to 20 percent of the spacecraft value for launch insurance. Rough order of magnitude (ROM) estimates for in-orbit, nonrecurring, and recurring costs are summarized in [Table 5-3](#).

5.5.1 Projected In-Orbit Costs

We did not solicit cost estimates from the spacecraft manufactures or the satellite operators. Discussions with spacecraft manufacturers, however, confirmed that the concept of carrying a piggyback instrument for NOAA on a commercial communications satellite was technically feasible and has been considered previously, as in the case of Loral's delivery of India's INSAT. The cost to NOAA would include the cost of the FPA instrument, including development and production costs; a proportionate share of the launch and spacecraft costs; spacecraft-imager adaptation and integration costs; and the recurring costs for the communications or other services the satellite operator would provide.

The share of launch and spacecraft costs can be estimated on the basis of the mass of the FPA imager as compared with the mass of the commercial payload. The payload is defined as the collection of equipment; including antennas, antenna structures, transponders, electronics, RF plumbing, cables, etc. onboard exclusively for the generation of revenue. All expenses incurred are for the sole purpose of having a payload in orbit to generate revenue.

The mass of the payload for a typical second-generation communications satellite is in the range of 20-25 percent of the total beginning of life (BOL) weight of the satellite after orbit insertion, including station keeping fuel. This estimate is based on a spacecraft under construction with a projected launch mass of 6500 lb, an in-orbit dry weight of 3100 lb, and a BOL station keeping fuel mass of 800 lb, or a total BOL mass of 3900 lb. A projected payload mass of 900 lb represents 23 percent of the total BOL mass.

A recent PanAmSat contract with Hughes for \$92.3 million per spacecraft, and \$82.5 million for the Ariane launch vehicle, for a \$174.8 million total without costs for launch insurance, can be considered at the high end of the range. A more modest cost of \$65 million to \$70 million for the spacecraft, a similar cost for a launch vehicle or a total cost of \$135 million is more typical of second generation satellites. With the payload representing, for example, 25 percent of a 3900 lb total BOL mass, or 975 lbs, a \$135 million combined launch and spacecraft cost would equate to \$138,000/lb of revenue producing payload.

As detailed in [Section 2](#), a preliminary estimate of the mass of the proposed FPA imager, using lightweight materials and redundant mechanical cryocoolers, in a best-case scenario, is 235 lb. At \$138,000 a lb, this would result in a cost to NOAA in the \$32 million range.

In actually negotiating a contract with a communications satellite operator, many additional factors would have to be entered into the cost calculation. For example, some of the larger second-generation spacecraft have a peak power rating of 4.7 kilowatts (kW), whereas the FPA instrument is projected to require about

300 W. Some cost offset for the mass of the solar array and battery mass would have to be considered. Additionally, spacecraft contracts normally provide for progress payments during the manufacturing period. NOAA's contribution to progress payments from the start of contract would offset the cost of money to the operator and help reduce projected costs.

5.5.1.1 Spacecraft Costs

The following are examples of non-recurring costs for recently contracted spacecraft:

- * PanAmSat: PanAmSat is a US-based international carrier that has contracted for three Hughes HS 601 spacecraft at a cost of \$276.9 million, or \$92.3 million each.

- * Intelsat: Intelsat is a 126 member international consortium providing global communications services. It has the largest constellation of in-orbit satellites (19) with a total of 1200 transponders available.

- Intelsat 7: Two FS1300 spacecraft are on order from Loral at a unit cost of \$90.0 million.

- Intelsat 8: Two Series 7000 spacecraft are on order with Martin Marietta Astrospace at a unit cost of \$82.5 million.

- * AT&T: AT&T has contracted with Martin Marietta for three Series 7000 TELSTAR satellites for domestic service, with a unit cost of \$66.6 million.

5.5.1.2 Launch Vehicle Costs

The following are examples of nonrecurring costs for recently contracted launch vehicles.

Atlas--General Dynamics: The General Dynamics family of launch vehicles, Atlas I, II, IIA, and IIAS, has a payload weight for geostationary transfer orbit ranging from 4,000 to 8,000 lbs. Atlas II, the vehicle for moderate spacecraft payloads, was the vehicle for a first generation spacecraft launched July 1993, at a cost of \$54 million.

Ariane--Aerospatial: The Ariane family of launch vehicles, with 6 models of the Ariane 4 version is to be joined by an Ariane 5 heavy lifter with capability of 7.5 tons to geostationary transfer orbit. Ariane launches from the Kourou site in French Guiana.

- * Ariane 4, the contracted vehicle for the PanAmSat second generation spacecraft launches at a unit price of \$82.5 million.

- * Ariane 5 estimated cost of \$100 million with a first launch planned for 1995.

Proton--Russia: The first contract for launch of a western commercial communications satellite for a

Russian Proton launch vehicle was by the 64-member INMARSAT international maritime satellite consortium. The launch vehicle cost is \$36 Million, with an additional \$12 Million to modify the launch site at Biakonur Cosmodrome in Kazakhstan. Lockheed Corp. has entered into an agreement with the Proton manufacturer, Krunichev Enterprises, to market the launch vehicle internationally.

5.5.1.3 Ground Segment Costs

Commercial communications satellite operators each conduct telemetry collection and command of their spacecraft through their own telemetry and command (T&C) stations. These facilities control the station-keeping, power management, and other necessary housekeeping functions for the in-orbit satellites. The proposed FPA imager, carried as part of a commercial satellite payload, would require no special control activities once activated after launch. Telemetry of instrument performance would be contained in the downlink instrument output data for monitoring by instrument controllers, with only a brief list of contingency commands maintained at the T&C station. These commands would be invoked, if necessary, by a phone call from the instrument controllers.

Downlink instrument and telemetry data would require a dedicated receive-only ground terminal as is required for GOES operation. The current market price for a C-band or

X-band terminal, including antenna and receiving equipment, is estimated to be in the range of \$200 thousand to \$350 thousand including site preparation and installation.

A ground processing system for the instrument data, comparable in function to the GOES Sensor Processing Subsystem (SPS), would require software development and hardware acquisition efforts. A ROM estimate for these efforts is estimated to be in the range of \$2.25 million to \$4 million. This does not include the cost of end-user processing systems.

5.5.1.4 Instrument Costs

We analyzed instrument development and production costs for two instruments currently under contract for the Earth Observing System (EOS), to be deployed starting in 2000: the Moderate-resolution Imaging Spectrometer (MODIS) and the Atmospheric Infrared Sounder (AIRS).

The MODIS is a large 250 kilogram (kg) instrument combining a conventional imaging radiometer and a cross-track scanning mirror with a set of linear focal plane detector arrays with spectral interference filters. The \$180 million contract is for development and delivery of a prototype unit at \$130 million, and delivery of two production flight units at \$25 million each.

The AIRS is a high-resolution FPA covering the spectral range between 0.4 and 15.4 microns, measuring simultaneously in over 2,300 spectral channels. The AIRS contract provides \$122 million for development and delivery of a prototype instrument, with the first production unit delivered for \$24 million, and the second unit for \$18.1 million.

It is recognized that these two instruments are only representative of the contract cost for instrument development. However, they are a reasonable basis for projecting a ROM cost for the proposed FPA imager.

5.5.2 Operating Costs

5.5.2.1 Downlink Services

An FPA imager in the payload of a commercial communications satellite offers the opportunity to utilize the commercial communications downlinks of the satellite. A customer for satellite communications can lease either partial or full transponders, or can have the system operator provide ground stations and communications services. With either arrangement, the cost to the customers is proportionate to the power and bandwidth provided.

In the case of an FPA imager in the payload of a commercial satellite, a configuration could be established whereby NOAA would lease a transponder for its imager downlink and receive data directly at the NOAA premises in Suitland, Maryland as is currently done with its dedicated geostationary satellites. Transponder lease costs are in a transitional state at present, depending on the remaining operational lifetime of a particular satellite, and bandwidth, and downlink power requirements. Present rates range from \$50 thousand to \$280 thousand per month. Using a figure of \$200 thousand for moderate-power, 36 Mhz transponder on a new CY 2003 launched spacecraft, results in a ROM cost to NOAA per spacecraft, of \$2.4 million per year in 1993 dollars, for downlink services.

5.5.2.2 Telemetry and Command Services

Each communications satellite operator has established T&C ground stations for maintaining the health and safety of its satellites. The T&C function provides capabilities to monitor performance of satellite subsystems and to command on-board subsystem configurations to maintain subsystem operation. The system operator's requirements for performing station keeping and for battery management, for example, would relieve NOAA of this responsibility, which it has for its dedicated geostationary satellites. Where a commercial communications satellite user purchases rather than leases a transponder, the satellite operator can apply a service charge for a proportionate share of T&C expenses. Such charges are estimated to be on the order of \$0.1 million per year for the proposed FPA imager.

In the case of telemetry monitoring, the limited amount of data required to characterize instrument performance could be incorporated into the imager data stream without an appreciable increase in output data rate. In the case of commanding the FPA imager, very few functions can be foreseen as requiring uplink commands, with perhaps the management of the mechanical cryocoolers as an example. An arrangement whereby NOAA would establish procedures to have any required uplink commands prestored on the system operator's command facility and initiated by a phone call from NOAA. Such an arrangement would have virtually no cost impact on system operation.

5.6 SUMMARY AND CONCLUSIONS

The above discussions can be summarized in the following conclusions:

- * There are no technical restrictions to having a meteorological instrument integrated with the payload of a nondedicated geostationary satellite.
- * No Public Law or Federal Regulation can be identified to preclude including a NOAA meteorological instrument in the payload of a commercial geostationary communications satellite.
- * Given a development program for an FPA imager, an availability date of 2003 is projected for a flight ready instrument. This projection is based on authorization of a new program start in 1996.
- * Based on current instrument development contracts, the cost for development of a FPA imager is estimated to be in the range of \$72 to \$78 million, in 1993 dollars.
- * The cost of orbiting an FPA imager on a commercial communications satellite is estimated to range from \$53.3 to \$73.3 million, including the cost of the instrument.
- * First-generation 5-7 year lifetime commercial communications satellites in orbit are at present being replaced by larger, three axis stabilized spacecraft with a 10-12 year mission life. Launch opportunities will be available for a piggyback FPA imager on replacements for the second-generation spacecraft in the year 2003 and beyond.
- * Projected launch dates for new DBS and MSS satellites and their subsequent replacements provide additional opportunities for a piggyback FPA imager.
- * Currently programmed government geostationary satellite systems offer no opportunity for serving as a host for a NOAA FPA imager.
- * There are presently four major US commercial communications satellite operators whose future spacecraft could serve as host for a NOAA FPA imager.
- * There are two manufacturers of US domestic communications satellites that would integrate a NOAA FPA imager with a domestic communications satellite operator's spacecraft.

[Return to the text](#)

SECTION 6

SUMMARY OF CONCLUSIONS

An objective of this project was to determine if an imager using FPA detector technology could be designed to provide performance that would meet the NWS requirements for imaging from geostationary orbit for the year 2000 and beyond. We also examined the potential for including such an imager in the payload of a commercial geostationary communications satellite. The limited pointing accuracy of communications satellites compared with that for satellites such as the GOES I, which are dedicated to the imaging mission, led us to explore means to compensate for pointing inaccuracies and for spacecraft motion by exploiting the imaging capabilities of the FPA instrument. We postulated ground processing concepts to achieve required INR performance given the 3 minute full-earth images provided by the FPA instrument. While many tradeoffs and options still exist, we can present our conclusions based on our work to-date. We summarize the detailed conclusions presented in sections 2 through 5 of this report as follows:

- * Second-generation FPA detector technology is the key to improved imaging from nondedicated satellites. We believe that a rapid imager is feasible and can provide the resolution and radiometric performance sought by the NWS as expressed in the NWS' GOES-N requirements [GOESN89].
- * A number of technologies now under development are important to FPA imager development. For example: IR detector arrays should be cooled to 70 degrees K or less. A passive radiative cooler to do this would be too large for an imager on a nondedicated satellite. The reverse turbo Brayton mechanical refrigerator is preferred. Mechanical refrigerator developments are well underway with lifetime goals of 10 years.
- * For step-stare scanning, the most demanding NEdT requirement is to be able to detect a 0.1 degrees K temperature change in a 300 degrees K scene in channels 4 and 5. This puts a 0.1 percent limit on residual FPA detector nonuniformities, which is within the state-of-the-art for FPA technology. TDI scanning offers superior radiometric performance and reduced requirements for detector production yield compared with step-stare scanning.
- * The use of FPA detectors precludes the use of image motion compensation and mirror motion compensation as defined for the GOES I system. This is due to the rigid spatial relationships among the pixels within a single frame of an image, and the consequent inability to alter the positions of individual pixels during image creation.
- * The use of overlapping image frames in the step-stare scanning method offers deterministic spatial relationships within and among image frames to a greater degree than TDI scanning. This provides well-coregistered images using ground-based processing for assembling the frames into a whole image. While the predictor-corrector and feedback approaches to INR place the burden of image spatial relationships on the spacecraft and the imager scan system, the overlap approach uses data redundancy and ground-

based image processing and results in the simplest space segment. Whole-image assembly from overlapped frames permits compensation for all spacecraft-earth relative motions.

* The proposed instrument can be operated in a free-running mode thereby precluding the need for scheduling special scanning modes or scenarios. The high resolution, improved image quality, and rapid 3 minute update rate for full-earth coverage make the resulting imagery suitable for AWIPS use and for the mesoscale observation objectives of the NWS Modernization program.

* It appears programmatically and legally feasible to deploy FPA instruments on nondedicated commercial communications spacecraft. Costs for such deployment may be sufficiently less than deployment on a dedicated spacecraft. Deployment of an instrument on a non-dedicated satellite could be done as a primary mission or as an adjunct to a primary mission. It also is possible to deploy a developmental instrument in this way to avoid risk to an operational system. Opportunities for deployment on commercial geostationary communications satellites including several Direct Broadcast Service and Mobile Subscriber Service satellites will be available in the post-2000 time frame. There appears to be little opportunity for sharing satellites with currently programmed government geostationary systems.

In the post-2000 time frame, NOAA will need advanced remote sensing technology that includes imaging from geostationary orbit. FPA technology can meet and, in some cases, exceed the performance anticipated in the GOES-N requirements for that era. Technical, programmatic, and legal issues do not appear to present barriers to lower-cost, high-quality imaging instruments to satisfy anticipated needs.

[Return to the text](#)

List of References

- [Bradley88] Bradley, C., November 1988, *The GOES I-M System Functional Description*, NOAA Technical Report NESDIS 40, Washington, D.C.
- [DeWames92] DeWames, R. E. et al., 1992, "An Assessment of HgCdTe and GaAs/GaAlAs Technologies for LWIR Infrared Imagers," Infrared Detectors: State of the Art, *SPIE* , V. 1735, pp. 2-16.
- [Gibson84] Gibson, J., November 1984, *GOES Data User's Guide*, Washington, D.C.
- [GOESN89] Statement of Guidelines and Requirements: GOES-N Phase-A Study, Department of Commerce, NOAA/NESDIS, Office of Systems Development, Advanced Systems Planning Division, May 22, 1989.
- [GOESN91] *GOES-N Report*, December 1991, Advanced Missions Analysis Office, Goddard Space Flight Center.
- [GOES91] Space Systems/Loral, May 1991, *GOES Spacecraft Operations Handbook, Vol, III, Spacecraft Description*, DRL 503-02.
- [GOES92] Space Systems/Loral, December 1992, *GOES I-M Operations Ground Equipment (OGE) Interface Specification* , DRL-504-02.
- [Gonzalez92] Gonzalez, R. and R. Woods, 1992, *Digital Image Processing*, Addison-Wesley Publishing Company, New York, N.Y.
- [Komajda87] Komajda, R., October 1987, *An Introduction to the GOES I-M Imager and Sounder Instruments and the GVAR Retransmission Format*, NOAA Technical Report NESDIS 33, Washington, D.C.
- [Long92] *The 1992/1993 World Satellite Almanac*, M. Long, MLE Inc.
- [Martin92] *Communications Satellites 1958-1992*, D. H. Martin, The Aerospace Corp.
- [Merrill91] Merrill, R. T., W. Menzel, W. Baker, J. Lynch, and E. Legg, March 1991, *A Report on the Recent Demonstration of NOAA's Upgraded Capability to Derive Cloud Motion Satellite Winds*, Bulletin of the American Meteorological Society, Vol. 72, No. 3.
- [NESDIS89] NESDIS Standard S24.808, 1989, "Application Software Access to the GOES Real-Time Database (GRT)."

[Norton91] Norton, P. R., November 1991, "Infrared Image Sensors," *Optical Engineering*, V. 30, pp. 1649-1663.

[ORA89] Office of Research and Applications Staff, National Environmental Satellite, Data, and Information Service Office of Research and Applications Research Programs, October 1989, Washington, D.C.

[Rao90] *Weather Satellites*, , Rao, P. K. et al., 1990, American Meteorological Society.

[Vincent90] Vincent, J. D., 1990, *Fundamentals of Infrared Detector Operation and Testing*, John Wiley and Sons.

[Walter86] Walter, G. A. and E. L. Dereniak, April 1986, "Photodetectors for Focal Plane Arrays, Part 2: HgCdTe," *Laser Focus/Electro-Optics*, pp. 86-96.

[Wilson92] *Interavia Space Directory 1992-93*, A. Wilson, Jane's Information Group.

[Wolberg90] Wolberg, G., Digital Image Warping, 1990, IEEE Computer Society Press, Washington, D.C.

[Wolfe89] Wolfe, W. L. and G. J. Zissis, *The Infrared Handbook*, 1989, Environmental Research Institute of Michigan.

1991 TRW Space Log, TRW Space and Technology Group.

Space News, The Army Times Publishing Company.

[Return to the text](#)

APPENDIX A

BLACKBODY RADIATION

Blackbody radiation physics is used extensively in infrared imaging system design and performance analyses. Blackbody radiation formalism is used often in this document. Blackbody radiation units and terminology can be confusing. When dealing with the blackbody radiation laws, care must be taken to avoid common errors by factors of 2, $[\pi]$, or 10. This appendix provides a brief review of Planck's radiation laws and terminology. The terminology has been adopted from Vincent [VINCENT90].

What is a blackbody? A blackbody is defined as an ideal body that completely absorbs all radiant energy striking it and, therefore, appears perfectly black at all wavelengths. A blackbody is also a perfect emitter of radiation; one that, for a given temperature, radiates the maximum number of photons possible per unit time per unit area in a specific spectral interval.

From the temperature T of a blackbody, Planck's radiation law determines the quantity of radiation $M_q([\lambda], T)$ emitted by a blackbody, per cm^2 of blackbody area, as a function of wavelength $[\lambda]$ according to:

$$M_q(\lambda, T) = \frac{2\pi c}{\lambda^4 \left(e^{\frac{hc}{\lambda T}} - 1 \right)} \text{ photons}/(\text{cm}^2 \cdot \text{sec} \cdot \mu\text{m}) \quad (\text{A-1})$$

where $c = 3 \times 10^{10}$ cm/sec (speed of light), $h = 6.626 \times 10^{-34}$ J*sec (Planck's constant), $k = 1.381 \times 10^{-23}$ J/degrees K (Boltzmann's constant), $[\lambda]$ = wavelength in cm, T = temperature in degrees K.

M_q is called *spectral photon exitance*. (Exitance is the ANSI standard name. Others refer to this quantity as emittance.) The word *spectral* indicates that the quantity is expressed per unit wavelength. If an integration is performed over a wavelength band, or over all wavelengths, the term spectral is dropped and we obtain *photon exitance*.

Spectral radiant exitance $M_e([\lambda], T)$ has units of $\text{W}/(\text{cm}^2 \cdot \mu\text{m})$ and is related to the spectral photon exitance M_q by:

$$M_e(\lambda, T) = \frac{hc}{\lambda} M_q(\lambda, T) \quad \text{W}/(\text{cm}^2 \cdot \mu\text{m}). \quad (\text{A-2})$$

We are oftentimes interested in the amount of radiation emitted in a certain direction per unit solid angle. *Photon sterance*, L_q , or *radiant sterance*, L_e , are the terms and symbols used for quantities normalized to unit solid angle. [Figure A-1](#) (Solid Angle from Blackbody to Detector Aperture) illustrates a detector observing a blackbody from a distance. The aperture of the detector subtends a solid angle $[\Omega]$ at

the differential area dA of the blackbody.

Spectral photon sterance is obtained by dividing the spectral photon exitance by $[\pi]$:

$$L_q(\lambda, T) = \frac{1}{\pi} M_q(\lambda, T) \quad \text{photons}/(\text{cm}^2 \cdot \text{sec} \cdot \mu\text{m} \cdot \text{sr}) \quad (\text{A-3})$$

It is tempting to divide by $2[\pi]$, but the correct factor is $[\pi]$. If the detector views the differential area at an angle, $[\theta]$, the differential area will appear reduced by a factor of $\cos([\theta])$. The factor of $[\pi]$ accounts for this $\cos([\theta])$ area reduction averaged over a hemisphere. Spectral photon sterance is the rate at which photons are emitted per unit area, per unit wavelength, per unit solid angle.

Spectral radiant sterance curves for several temperatures are shown in [Figure A-2](#) (Blackbody Spectral Radiant Sterance). For a fixed wavelength, as the temperature increases the spectral radiant sterance increases. Also, as the temperature increases, the peak of the curves shift toward shorter wavelengths. The wavelength of the maximum $[\lambda]_m$ (in μm) is determined from Wien's displacement law:

$$\lambda_m = \frac{2897.8}{T} \quad \mu\text{m} \quad (\text{A-4})$$

If the spectral radiant exitance is integrated over all wavelengths, the result is the power per unit area (called *radiant exitance* M_e [with no arguments $[\lambda], T$]). This is the area under the spectral radiant exitance curve (or $[\pi]$ times the area under a spectral radiant sterance curve of [Figure A-2](#)). This is the classic Stefan-Boltzmann law:

$$M_e = \int_0^\infty d\lambda M_e(\lambda, T) = \sigma T^4 \quad \text{W}/\text{cm}^2 \quad (\text{A-5})$$

where $s = 5.670 \times 10^{-12} \text{ W}/(\text{cm}^2 \cdot \text{K}^4)$; the Stefan-Boltzmann constant. (If M_q were integrated over all wavelengths the result would be in $\text{photons}/\text{sec}/\text{cm}^2$ and the Stefan-Boltzmann constant is $1.52 \times 10^{11} \text{ photons}/(\text{sec} \cdot \text{cm}^2 \cdot \text{K}^3)$).

When only a wavelength band, from $[\lambda]_1$ to $[\lambda]_2$ is integrated, we will use the notation:

$$L_{e, \lambda_1, \lambda_2} = \int_{\lambda_1}^{\lambda_2} d\lambda L_e(\lambda, T)$$

$$\text{or} \quad L_{q, \lambda_1, \lambda_2} = \int_{\lambda_1}^{\lambda_2} d\lambda L_q(\lambda, T) \quad (\text{A-6})$$

We also will have occasion to use the temperature derivative $\frac{dL_{q,\lambda,\lambda_e}}{dT}$.

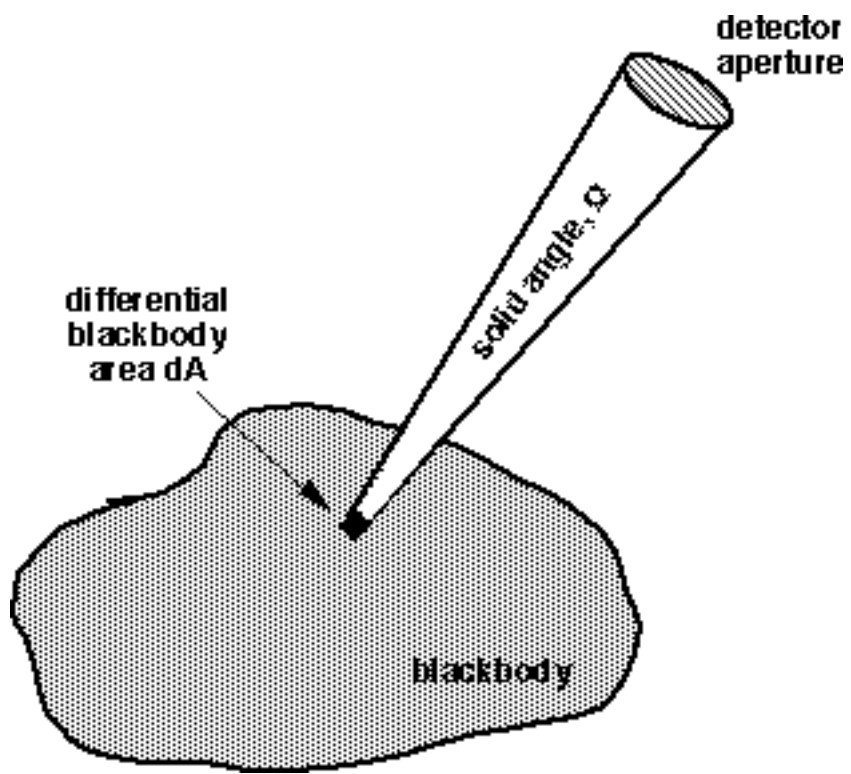
A blackbody is an ideal radiator. The spectral emissivity $\epsilon(\lambda)$ of a graybody is defined as the ratio of the spectral photon (or radiant) exitance of the graybody to that of a blackbody:

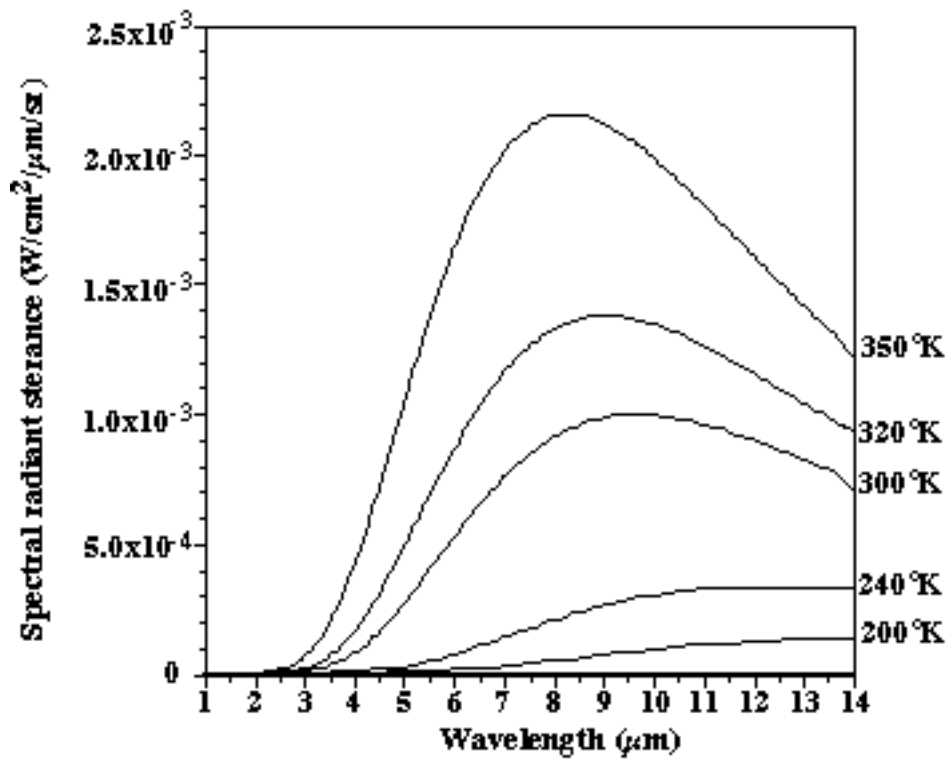
$$\epsilon(\lambda) = \frac{M_q^{GB}(\lambda, T)}{M_q^{BB}(\lambda, T)} \quad (A-7)$$

The inverse Planck function is used to derive the temperature of a blackbody from its *measured* photon exitance M . Solving equation A-1 for T gives:

figure. (A-8)

[Return to the text](#)





APPENDIX B

STEP-STARE FPA IMAGER SYSTEM EFFECTIVE RESOLUTION

B-1 INTRODUCTION

Image errors result due to spacecraft-induced quiescent and dynamic disturbances that cause the imaging instrument's Line of Sight (LOS) motion. These errors are characterized by the low frequency component called "drift" and the high frequency component called "Jitter". Drift is a consequence of motion between frame dwells. The drift errors can be accommodated by over scanning the frame sample area in an overlap region that ensures that the frame contains the intended image region. Jitter consists of motions that have predominant effects during the pixel exposure time. Jitter causes a blurring effect in the image and results in degradation of image resolution. MITRE's proposed enhancements in the technology and concept design of the imaging instrument are aimed at achieving a high resolution. In order to achieve the desired resolution, a technique for precise estimation for the jitter component of the LOS errors is needed. Thus our main focus is to determine the jitter component of the LOS error and to compute its effect on the image resolution; that is, to determine the imager's effective resolution.

B-2 DRIFT AND JITTER COMPONENTS

B-2.1 Evaluation of Drift and Jitter Components of LOS Motion

The total LOS motion has two components, namely, the drift and the jitter. The drift causes displacement of the scene whereas the jitter causes distortion of the scene. Let the total error in the LOS motion, at any time during the picture taking interval, T , be denoted by $e(t)$. Then the mean value of LOS error in the scene represents the actual drift of the LOS. As the drift occurs due to low frequency disturbances, the drift component may be considered constant during the picture taking interval T . The error component, $d(t)$, due to jitter effect is a time-dependent component as it occurs during the picture taking interval. The total jitter, D , is the RMS value of $d(t)$ over the time T and its mean square value is of interest to us in computing its effect on the image quality.

The expressions for drift and jitter could be computed simply if $e(t)$ were a known function, which is usually not the case. In general, $e(t)$ is a stationary random process, and the quantities of interest are the expected values of mean square drift and of mean square jitter.

In order to compute these quantities, we proceed as follows:

* We Compute the auto correlation function of $e(t)$:

$$R_e(\tau) = E[e(t)e(t + \tau)] \quad (B-2.1)$$

* The Fourier Transform of $R_e(\tau)$ and its inverse function are given by

$$S_e(\omega) = \frac{1}{2\pi} \int_{-\infty}^{\infty} R_e(\tau) e^{-i\omega\tau} d\tau \quad (B-2.2)$$

$$R_e(\tau) = \int_{-\infty}^{\infty} S_e(\omega) e^{i\omega\tau} d\omega \quad (B-2.3)$$

where $S_e(\omega)$ is the spectral density, also called the power spectral density, of the process $e(t)$, and is a function of ω [rad/sec], where ω [rad/sec] is the frequency in radians/sec.

* Setting $\tau=0$ in the above relation yields

$$R_e(\tau=0) = \int_{-\infty}^{\infty} S_e(\omega) d\omega \quad (B-2.4)$$

which, from the fundamental definition of $R_e(\tau)$, gives

$$E[e^2] = \int_{-\infty}^{\infty} S_e(\omega) d\omega \quad (B-2.5)$$

$$= \int_{-\infty}^{\infty} S_e(f) df \quad (B-2.6)$$

where f is the frequency in Hz.

Thus the area under the curve, $S_e(f)$ vs. f , # gives the expected value of the mean square LOS error. The units of $S_e(f)$ are those of mean square quantity, in this case e^2 , per unit of frequency, Hz. In physical sense, the plot of $|S_e(f)|$ vs. f [Hz] is the spacecraft's Point Spread Distribution of the LOS to nadir and is the counterpart of the spacecraft's Point Spread Function (PSF), which is a plot of the spatial distribution of the LOS error. A diagrammatic representation of the spacecraft PSF and Point Spread Distribution are shown in figures [B-1](#) (A Typical Spacecraft Line-of-Sight Error PSF) and [B-2](#) (Typical Frequency Spectrum of LOS Point Spread Distribution).

The concept of the point spread distribution of the LOS error is of interest to us because it allows us to perform the analysis in the frequency domain. It may be noted that the Point Spread distribution ranges for values of f from $-\infty$ [Hz] to $+\infty$ [Hz]. The mean square spectral density of a stationary random process, $e(t)$, is a real, even and nonnegative function of frequency, f . Let Power Spectral Density (PSD) equivalent of $|S_e(f)|$ for values of f between 0 and $+\infty$ [Hz] be denoted by $B^2(f)$. The equivalent expression for mean square of the LOS error, E^2 , can be written as:

Mean Square Error:

$$E^2 = \int_0^{\infty} 2B^2(f) df \quad (B-2.7)$$

We introduce here a weighting function for Jitter and denote it by $W_d(C)$, where $C = 2\pi fT$ is a function of the picture exposure time T . The expected value of the mean square drift and jitter can now be computed by multiplying the area under the PSD curve by the appropriate weighting function. Thus,

Mean Square Drift:

$$S^2 = \int_0^\infty 2B^2(f) [1 - W_d(2\pi fT)] df \quad (\text{B-2.8})$$

and the mean square jitter can be expressed as:

Mean Square Jitter:

$$D^2 = \int_0^\infty 2B^2(f) W_d(2\pi fT) df \quad (\text{B-2.9})$$

where,

$$W_d(2\pi fT) = 1 - 2[1 - \cos(2\pi ft)] / (2\pi fT)^2 \quad (\text{B-2.10})$$

is the weighting function for jitter and $[1 - W_d(2\pi fT)]$ is the weighting function for Drift. Derivation of the expressions for the weighting functions is shown in Appendix C.

B-2.2 Crossover Frequency Between Drift and Jitter

We notice that the weighting functions for Jitter and Drift are a function of the parameter C which represents the total angular shift of the LOS motion during the picture taking time interval, T . A plot of the weighting functions $W_d(C)$ and $1 - W_d(C)$ vs. C is shown in [Figure B-3](#) (Weighting Function for Jitter and Drift).

At the point of intersection of the two curves the value of the weighting function for jitter and drift are equal ($= 0.5$). The value of C corresponding to this point is 2.78. It may be noted that for values of C higher than 2.78, the values for the Jitter weighting function is considerably high whereas the Drift weighting function values are negligible. For values of C lower than 2.78, the reverse is the case. The value of C corresponding to the intersection point justifiably can be considered as the crossover point for Drift and Jitter. The frequency corresponding to this is called the crossover frequency. Thus we define

$$F_{\text{cross}} = \frac{C_{\text{cross}}}{2\pi T} = \frac{2.78}{2\pi T} = \frac{1}{2.3T} \quad (\text{B-2.11})$$

The crossover frequency, which is dependent on the picture taking interval, T, of the Imaging instrument, plays a significant role in separating the frequencies which contribute to Jitter from those that contribute primarily to drift errors of the LOS disturbance spectrum.

B-2.3 Typical LOS Disturbance Power Spectral density (PSD) Curves

Equations for straight line envelopes of typical LOS disturbance PSD curves may be written as a function of frequencies, f, f_r , and f_s as:

$$B^2(f) = \frac{B_0^2}{\left[1 + \left(\frac{f}{f_r}\right)^2\right] \left[1 + \left(\frac{f}{f_s}\right)^2\right]} \quad (\text{B-2.12})$$

where f represents all frequencies in the spectrum below the rollover frequency f_r , and f_s are all the frequencies in the spectrum above f_r . B_0^2 is the constant value of the Power Spectrum between $f = 0$ to $f = f_r$. Setting the dimensionless frequency ratios as:

$$X = \frac{f}{f_r} \quad b = \frac{f_r}{f_s} \quad (\text{B-2.13}) \quad (\text{B-2.14})$$

the equation for a typical spectrum curves can be written in terms of the dimensionless parameters b and X as:

$$B^2(f) = \frac{B_0^2}{[1 + X^2][1 + b^2 X^2]} \quad (\text{B-2.15})$$

Thus we can draw envelopes of disturbance, PSD, for the range of all spectrum frequencies normalized to the rollover frequency, f_r , and for various values of b from $b=0$ to $b=1$. Plots of various typical PSD curves for $b=0$, $b=0.2$, $b=0.5$ and $b=1$, are shown in [figure B-4](#) (Normalized LOS PSD Curves).

B-2.4 MODIFIED DRIFT AND JITTER WEIGHTING FUNCTIONS FOR TYPICAL PSD CURVES

Expressions for weighting functions, $W_d(C)$ and $1-W_d(C)$, for Jitter and Drift respectively, were derived earlier in equations B-2.8 through B-2.10. By substituting the analytical expression for the typical PSD spectrum, $B^2(f)$, equation B-2.15, in the integral for the mean square LOS Error, equation B-2.7, we can express the mean square error for each of the typical PSD curves in terms of the parameters b and C. A very insightful simplification results if we introduce a new normalized frequency parameter $a = f_r/f_{\text{cross}}$, where f_{cross} is the crossover frequency between drift and jitter components of the error spectrum, as determined in section B-2.2. We define C1 at the crossover frequency pertinent for each typical spacecraft, i.e., $C1 = 2\pi \cdot f_{\text{cross}} \cdot T$. We can now express the weighting functions for drift and

Jitter as a function of the parameters a , b , and C_1 . The resulting expression for the modified weighting function, $G_1(a,b)$, for drift is given by:

$$G_1(a, b) = \frac{2}{C_1^2 a^2 (1-b)} \times \left\{ C_1 a (1-b^2) - [1 - \exp(-C_1 a)] + b^3 [1 - \exp(-C_1 \frac{a}{b})] \right\} \quad (B-2.16)$$

Accordingly, the modified Jitter weighting function is given by $1-G_1(a,b)$. A plot of the drift and jitter weighting functions for $b=0$, $b=0.2$, $b=0.5$ and $b=1$ for parameter, a , ranging from 0.1 to 10.0 is shown in figures [B-5](#) (Modified Drift Weighting Function: $G_1(a,b)$) and [B-6](#) (Modified Jitter Weighting Function $[1-G_1(a,b)]$).

It can be seen from these plots that the value of jitter weighting function increases exponentially as the rollover frequency, F_{roll} , of a specific PSD curve for LOS disturbance is closer to or greater than the crossover frequency, F_{cross} , whereas the drift weighting function shows exponential drop in value. The LOS disturbance PSD curve of a specific spacecraft has a flat plateau for frequencies up to the rollover frequency. For frequencies above the rollover frequency, the PSD curve slopes down as per the equation for the power spectrum. The spacecraft attitude control system effectively controls the low frequency contents of the disturbance spectrum and keeps the power spectrum at a constant B_0^2 power level. Above the rollover frequencies, the control system is no more effective and the power spectrum contributes primarily to the jitter content in the LOS error.

B-2.5 Evaluation of Drift and Jitter Components for Typical Spacecraft

The area under the PSD curves gives the total mean square value of the LOS error. That is, the total scene shift is given by

$$E^2 = \int_0^\infty 2B^2(f) df \quad (B-2.17)$$

which, for values of spectrum frequencies, f_s , greater than f_r , the value of the integral for the typical PSD curves can be expressed as

$$\text{Mean Square Error: } E^2 = \frac{\pi}{2} \frac{f_r}{(1+b)} B_0^2 \quad (B-2.18)$$

The drift and jitter components can be computed by multiplying the mean square error value by the respective weighting functions, i.e.,

$$\text{Mean Square Drift: } S^2 = E^2 \times G_1(a, b) \quad (B-2.19)$$

$$\text{Mean Square Jitter: } D^2 = E^2 \times [1 - G_1(a, b)] \quad (B-2.20)$$

B-3 IMAGE RESOLUTION

B-3.1 Algorithm to Compute Jitter Component of LOS Error

A step by step procedure to compute the Jitter component of the LOS error is summarized below:

Step 1: Given the exposure time, T , we use Eqn. (2.11) to compute F_{cross} : $F_{\text{cross}} = 1/(2.3 T)$

Step 2: From the PSD curve of the LOS spectra, obtain the following Characteristic data:

- i) Roll-over Frequency, F_r
- ii) B_0^2 in units of $\text{Arcsec}^2/\text{Hz}$.
- iii) Slope of the section of the PSD curve from F_r to F_s
- iv) Highest frequency of the PSD, F_s

Step 3: From the above, compute the dimensionless quantities a and b :

$$a = F_r / F_{\text{cross}}$$

$$b = F_r / F_s$$

Step 4: Compute the LOS mean square error, E^2 , using Eqn. (B-2.18)

$E^2 = \text{Area under the PSD Curve}$

$$= \int_0^{\infty} 2 B^2(f) df = \frac{\pi}{2} \frac{F_r}{(1+b)} B_0^2$$

Step 5: Compute modified Weighting Function for Jitter and Drift using Plots of $G_1(a,b)$ and $[1 - G_1(a,b)]$ shown in Figures [B-5](#) and [B-6](#), section B-2.4.

The Jitter weighting function, $G_1(a,b)$, and the Drift Weighting function, $[1 - G_1(a,b)]$, can be extrapolated for the appropriate b value of the LOS power spectral density curve.

Step 6: From step 4 and 5, we compute the Jitter component of mean square error, Eqns. (B-2.19) and (B-2.20), section B-2.5.

Mean Square Drift: $S^2 = E^2 \times G_1(a, b)$

Mean Square Jitter: $D^2 = E^2 \times [1 - G_1(a, b)]$

The RMS value for Jitter = D

B-3.2 Effect of Jitter on Image Resolution

We assume that the disturbance Power Spectrum, $B^{(2)}(f)$, is known for the particular spacecraft and that the crossover frequency, F_{cross} , between drift and jitter of the spectrum have been computed following the procedure outlined in the previous section.

Step 1: INR System's Point Spread Function , PSF(INR):

* Assuming a Gaussian distribution of the LOS error $e(t)$, we denote the Probability Distribution Function, PDF, of $e(t)$ as $GD(e)$.

* If $x(t)$ is the actual spatial position of the Imager's LOS at time, t , then the real position without LOS error would be $(x(t)-e(t))$.

* The effective Point Spread Function, PSF(INR), of the Image Navigation and Registration (INR) system is obtained from the convolution of the imager's PSF, PSF(INST), with $GD(e)$, i.e.,

$$PSF_{(INR)}(x) = \int_{-\infty}^{\infty} PSF_{(INST)}(x-e) G_D(e) de \quad (B-3.1)$$

Step 2: INR System Resolution:

* The most commonly used measure of image resolution is the Full-Width-Half-Maximum (FWHM) of the PSF. Assuming a Gaussian PDF of the Jitter component of LOS error, the FWHM value is 2.35 times

the standard deviation

$$PSF_{(INR)}(x) = \int_{-\infty}^{\infty} PSF_{(INST)}(x-e) G_D(e) de \quad 2.35 D$$

* Then the RMS value of the INR system's effective Resolution is given by the RSS of the FWHM values for the imaging instrument, itself, and the spacecraft:

$$RES_{(INR)} = \left[FWHM_{(INST)}^2 + (2.35D)^2 \right]^{1/2} \quad (B-3.2)$$

B-4 APPLICATION

The computational techniques discussed in the foregoing were applied to assumed data for HIRIS, a NASA project, and MITRE's concepts as shown in examples 1 and 2 below:

B-4.1 Example - 1. The High Resolution Imaging Spectrometer (HIRIS)

Following data was assumed for the HIRIS instrument and the spacecraft disturbance spectrum:

$$T = 0.1 \text{ sec}$$

$$F_r = 15 \text{ Hz.}$$

$$B_0^2 = 1.0 \text{ Arcsec}^2 / \text{Hz.}$$

$$F_s = 1000 \text{ Hz.}$$

Following step 1 through 6 of section B-3.1, we compute the RMS value of the Jitter, D:

$$F_{\text{cross}} = 1/(2.3 T) = 4.34 \text{ Hz.}$$

$$a = F_r/F_{\text{cross}} = 3.46$$

$$b = F_r/F_s = \text{approximately zero.}$$

$$\text{Mean Square Error: } E^2 = \frac{\pi}{2} \frac{f_1}{(1+b)} B_0^2 = 23.56 \text{ Arcsec}^2$$

Using the figures in section 2.4, we get the values of the weighting functions for drift and jitter as follows:

For $\log(a) = \log(3.46) = 0.54$, and using the curve, $b=0$, the values obtained from the plots are:

$$\text{Drift Weighting Function: } G_1(a,b) = 0.18$$

$$\text{Jitter Weighting Function: } [1-G_1(a,b)] = 0.82$$

$$\text{Mean Square Drift: } S^2 = E^2 \times G_1(a,b) = 4.24 \text{ Arcsec}^2$$

$$\text{Mean Square Jitter: } D^2 = E^2 \times [1-G_1(a,b)] = 19.32 \text{ Arcsec}^2$$

$$\text{RMS value of Jitter: } D = 4.395 \text{ Arcsec} = 2.13 \text{ Microrads.}$$

HIRIS INR System Resolution:

We make the assumption that the HIRIS instrument's FWHM = 10 microrads.

Then using Eqn. (B-3.2) of section B-3.2, we get $RES_{(INR)} = [FWHM_{(Imaging)}^2 + (2.35D)^2]^{1/2} = 11.18 \text{ microrads}$

B-4.2 Example - 2. Comparison with MITRE's Concept

Using the same disturbance characteristics as used in example-1, we compute the INR system resolution.

$$T = 0.0005 \text{ sec}$$

$$Fr = 15 \text{ Hz.}$$

$$B_0^2 = 1.0 \text{ Arcsec}^2 / \text{Hz.}$$

$$Fs = 1000 \text{ Hz.}$$

Following steps 1 through 6 of section B-3.1, we compute the RMS value of the Jitter, D:

$$F_{cross} = 1/(2.3 T) = 869.56 \text{ Hz.}$$

$$a = Fr/F_{cross} = 0.01725$$

$$b = Fr/Fs = 0$$

$$\text{Mean Square Error: } E^2 = \frac{\pi}{2} \frac{f_1}{(1+b)} B_0^2 = 23.56 \text{ Arcsec}^2$$

Using Figures [B-5](#) and [B-6](#) of section B-2.4, we get the values of the weighting functions for drift and jitter as follows:

For $\log(a) = \log(0.01725) = -1.763$, and using the curve $b=0$, the values obtained from the plots are:

$$\text{Drift Weighting Function: } G_1(a,b) = \blacksquare 0.9$$

$$\text{Jitter Weighting Function: } [1-G_1(a,b)] = \blacksquare 0.1$$

$$\text{Mean Square Drift: } S^2 = E^2 \times G_1(a,b) = 21.2 \text{ Arcsec}^2$$

Mean Square Jitter: $D^2 = E^2 \times [1 - G_1(a, b)] = 2.356 \text{ Arcsec}^2$

RMS value of Jitter: $D = 1.535 \text{ Arcsec} = 0.744 \text{ Microrads}$.

MITRE's INR System Resolution:

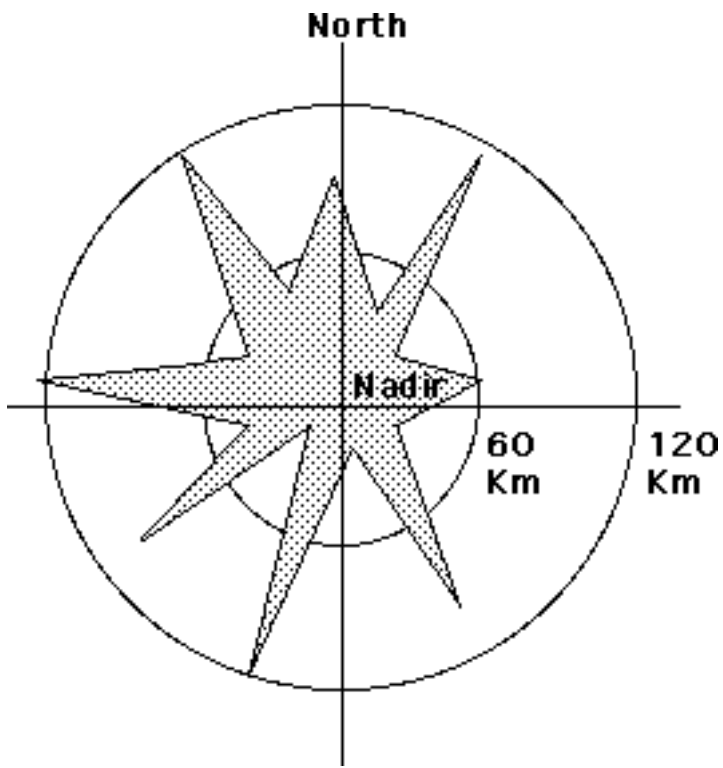
We make the assumption that the instrument's FWHM = 10 microrads, (same as for HIRIS instrument in Example 1). Then using equation B-3.2 of section B-3.2, we get

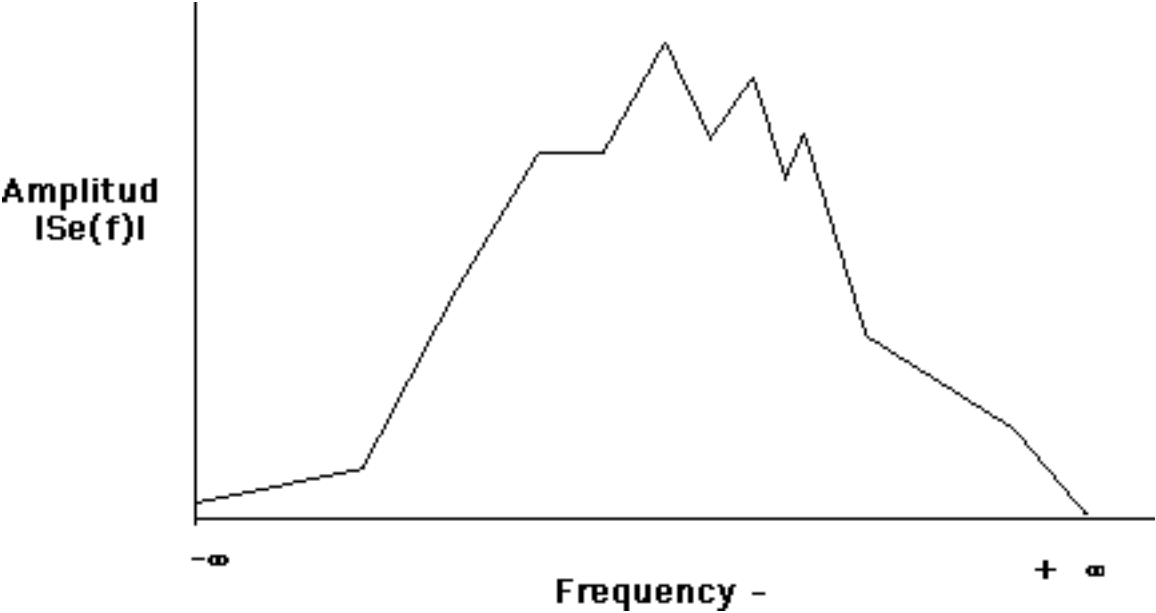
$$RES_{(INR)} = [FWHM_{(microrads)}^2 + (2.35D)^2]^{1/2} = 10.15 \text{ microrads}$$

Thus in using a staring sensor the instrument's FWHM is not modified significantly by the effect of spacecraft jitter.

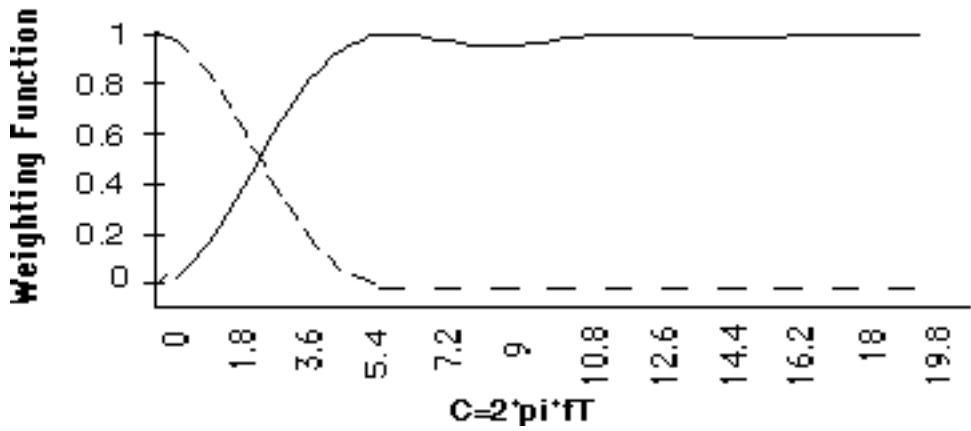
It may be noted that the data used in the above two examples is only for illustrating the technique. The procedure can be used easily to validate the INR system performance once the real instrument's data and the real platform disturbance spectrum are available.

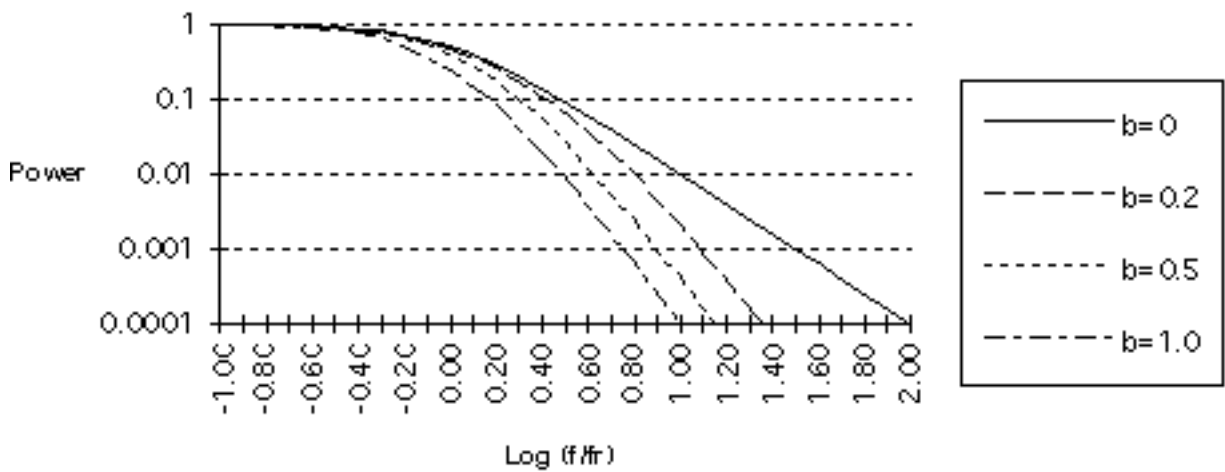
[Return to the text](#)

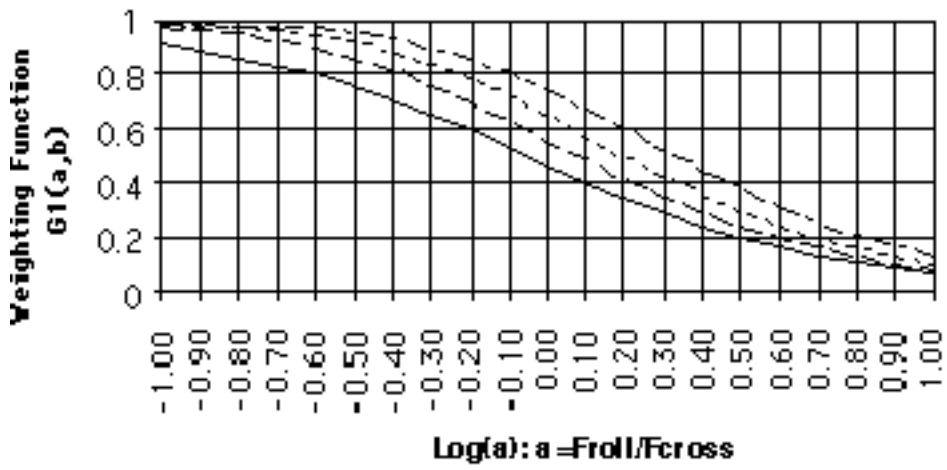


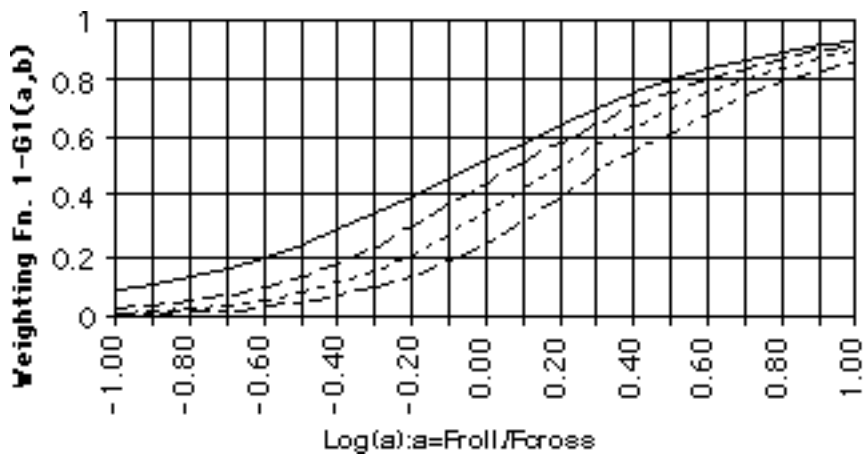


Plot of $W_d(C)$ & $1 - W_d(C)$ vs. $C=2\pi fT$









Appendix C

WEIGHTING FUNCTION FOR DRIFT AND JITTER

Let the error in the Imaging instrument's Line of sight (LOS) due to drift and jitter at any time during the picture taking interval, T , be $e(t)$. Then, assuming a zero-mean Gaussian distribution, the mean value of the LOS pointing error of a particular scene is given by

$$\bar{S}(t_1, T) = \frac{1}{T} \int_{t_1}^{T+t_1} e(t) dt$$

The mean value of LOS error in the scene represents the actual drift of the LOS. As the drift occurs due to low frequency disturbances, the drift component may be considered constant during the picture taking interval, T .

The error component, $d(t)$, of the particular picture due to jitter effect is then given by

$$d(t) = e(t) - \bar{S}(t_1, T)$$

The total jitter, D , is the RMS value of $d(t)$ over the time, T , and its mean square value is given by

$$\begin{aligned} D^2(t_1, T) &= \frac{1}{T} \int_{t_1}^{t_1+T} d^2(t) dt \\ &= \frac{1}{T} \int_{t_1}^{t_1+T} e^2(t) dt - S^2(t_1, T) \end{aligned}$$

The above expressions for drift and jitter could be used directly, only if $e(t)$ were a known function, which is usually not the case. In general, $e(t)$ is a stationary random process, and the quantities of interest are the expected values of mean square drift and of mean square jitter. In order to compute these quantities, we proceed as follows:

We compute the autocorrelation function of $e(t)$:

$$R_e(\tau) = E[e(t)e(t+\tau)]$$

The Fourier Transform of $R_e(\tau)$ and its inverse function are given by

$$S_e(\omega) = \frac{1}{2\pi} \int_{-\infty}^{\infty} R_e(\tau) e^{-i\omega\tau} d\tau$$

$$R_e(\tau) = \int_{-\infty}^{\infty} S_e(\omega) e^{j\omega\tau} d\omega$$

where $S_e(\omega)$ is the spectral density, also called the power spectral density, of the process $e(t)$, and is a function of the angular frequency $\omega = 2\pi f$. Setting $\tau = 0$ in the above relation yields

$$R_e(\tau = 0) = \int_{-\infty}^{\infty} S_e(\omega) d\omega$$

which, from the fundamental definition of $R_e(\tau)$, gives

$$E[e^2] = \int_{-\infty}^{\infty} S_e(\omega) d\omega$$

$$E[S^2(t_1, T)] = E\left[\frac{1}{T^2} \int_{t_1}^{t_1+T} \int_{t_1}^{t_1+T} e(\rho)e(\nu) d\rho d\nu\right]$$

$$= \frac{1}{T^2} \int_{t_1}^{t_1+T} \int_{t_1}^{t_1+T} R(\rho - \nu) d\rho d\nu$$

$$= \frac{1}{T^2} \int_{t_1}^{t_1+T} \int_{t_1}^{t_1+T} \int_{-\infty}^{\infty} S_e(f) e^{j2\pi f(\rho - \nu)} df d\rho d\nu$$

$$= \int_{-\infty}^{\infty} 2S_e(f) [1 - \cos(2\pi fT)] / (2\pi fT)^2 df$$

Simplifying the expression, we can write mean square drift as

$$S^2 = \int_0^{\infty} 2S_e(f) [1 - W_d(2\pi fT)] df$$

where,

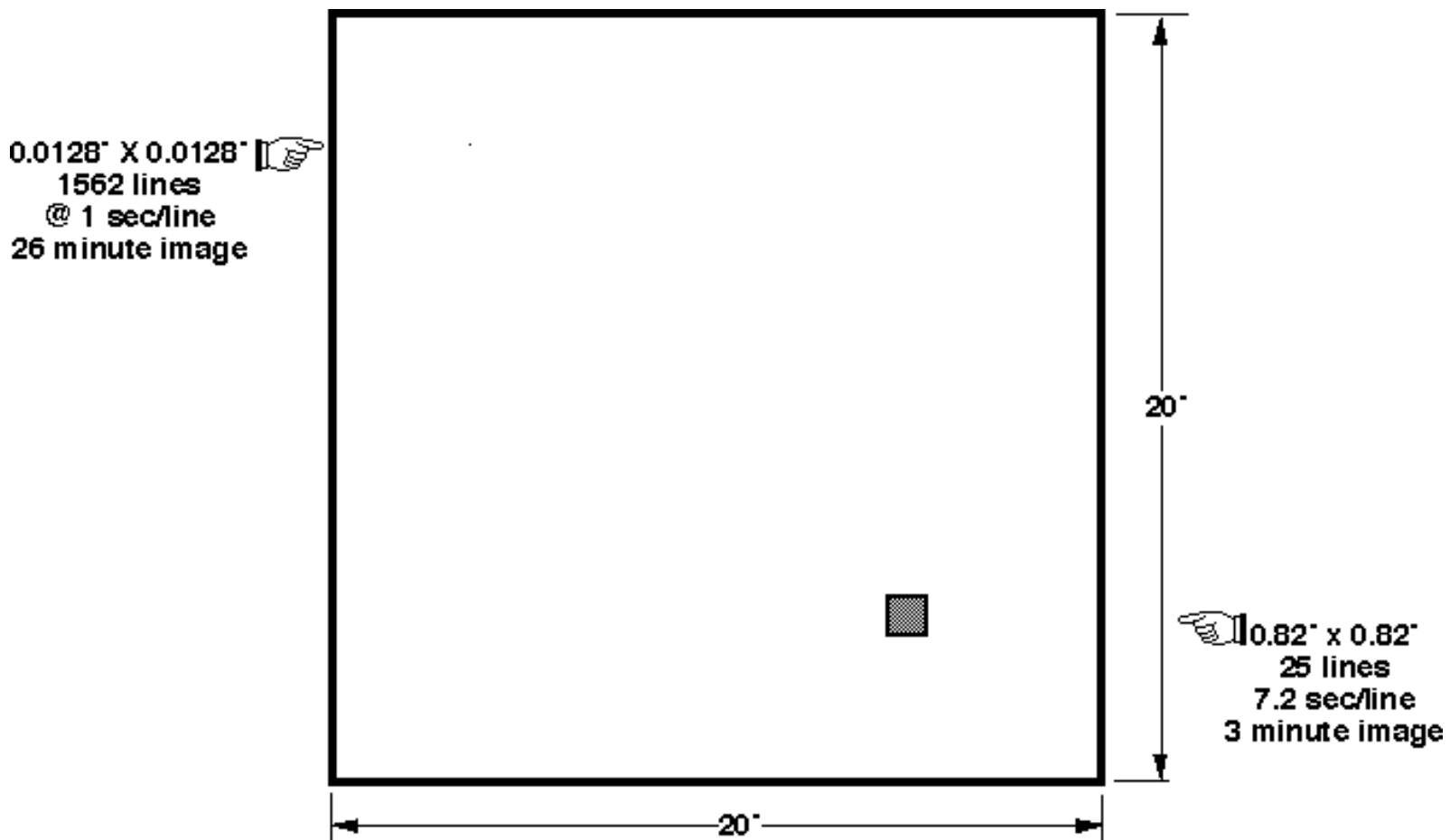
$$W_d(2\pi fT) = 1 - 2[1 - \cos(2\pi fT)] / (2\pi fT)^2$$

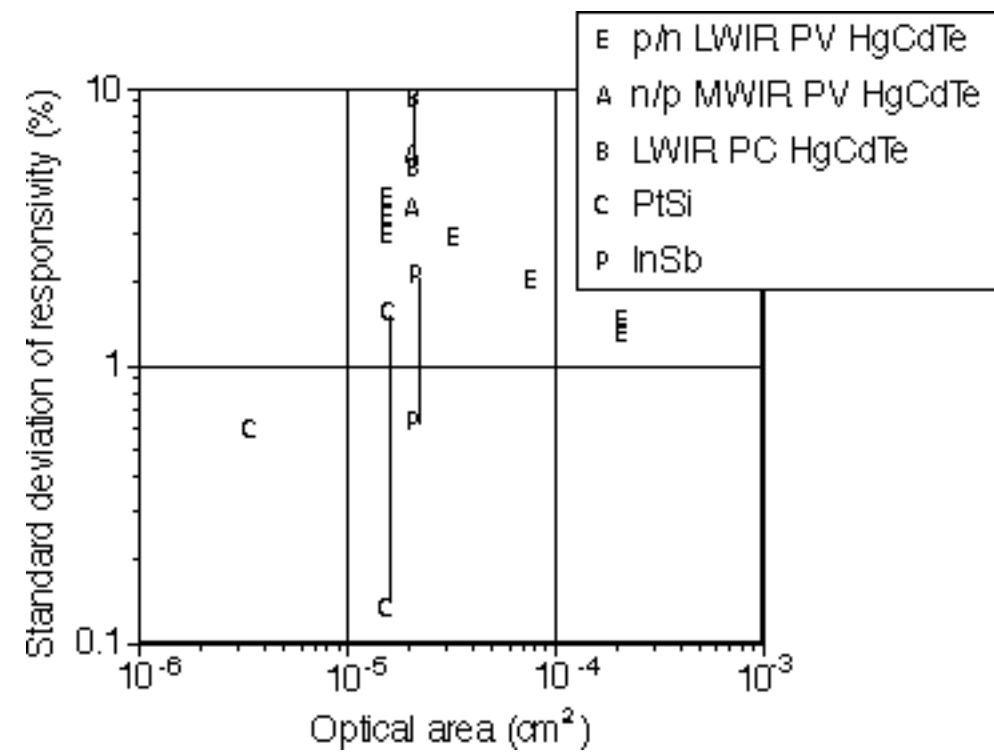
Similarly, the mean square value of the jitter can be expressed as:

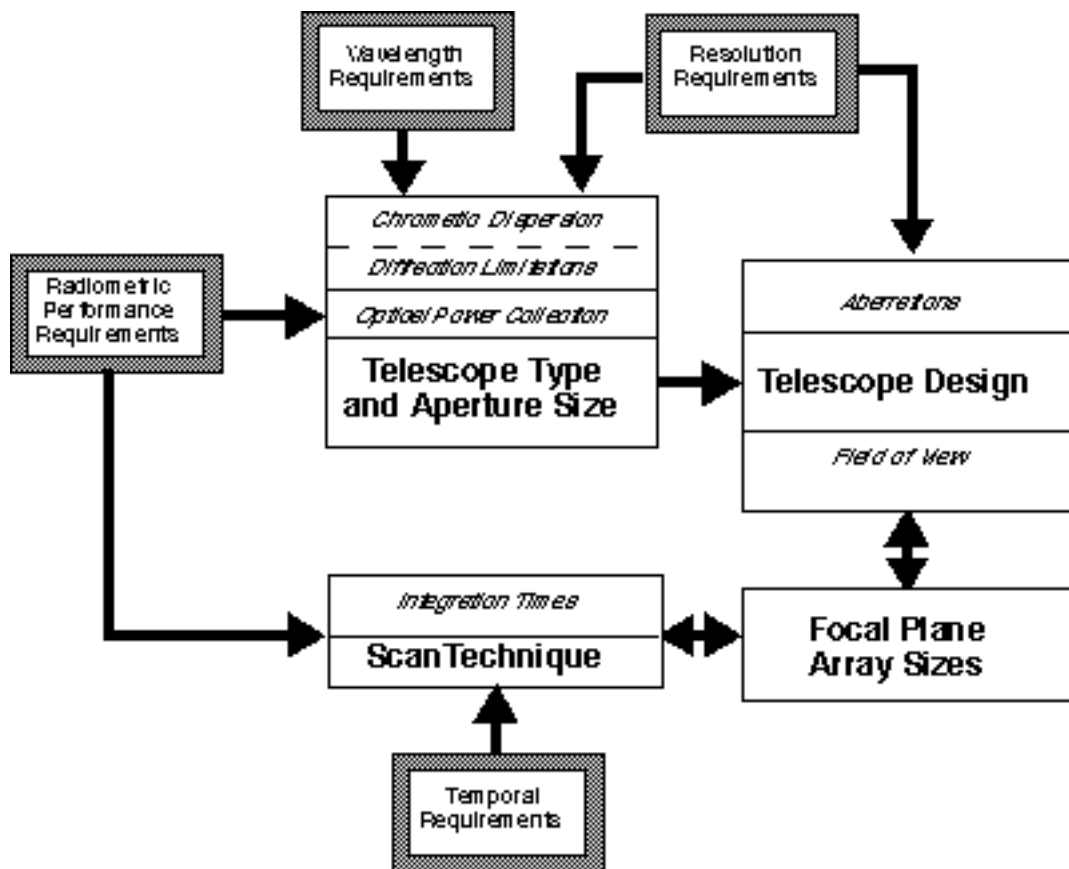
$$D^2 = \int_0^{\infty} 2S_e(f) W_d(2\pi fT) df$$

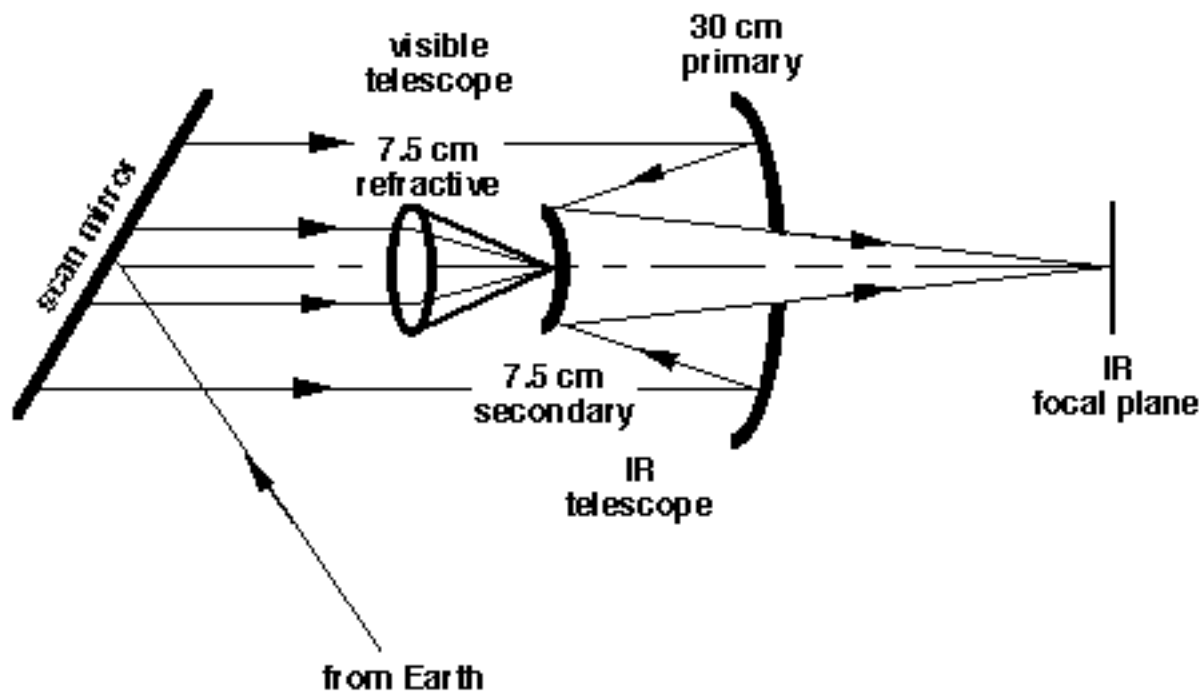
[Return to the text](#)

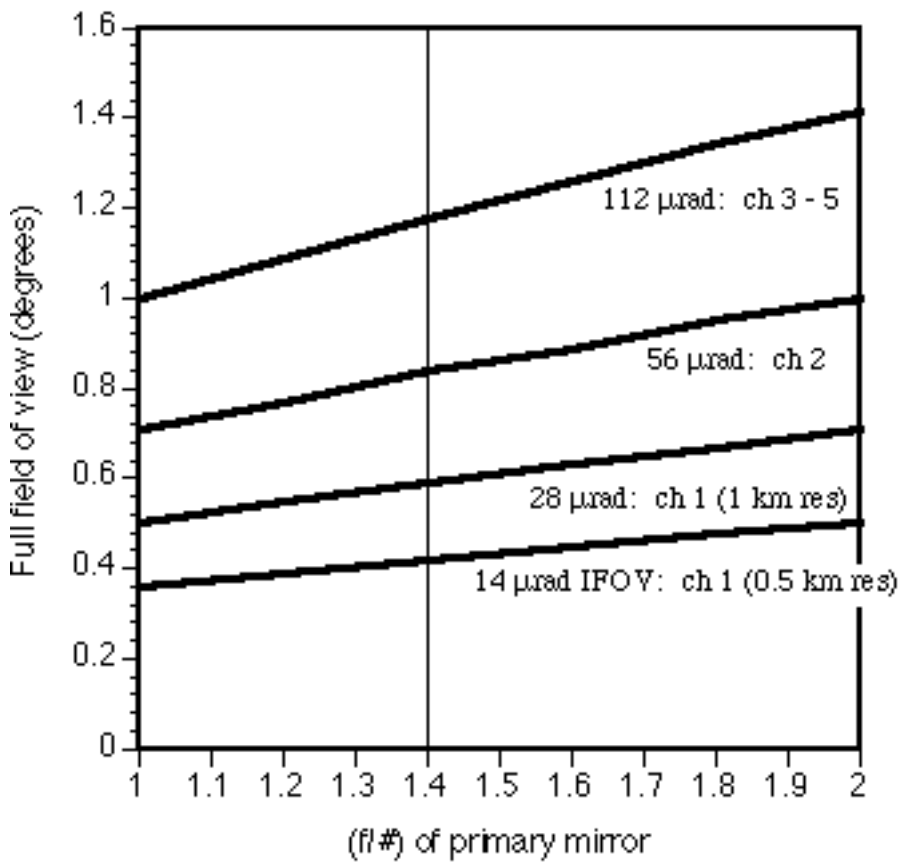
GLOSSARY AIRS Advanced Infrared Sounder AMSC American Mobile Satellite Corp. AOCS Attitude and Orbit Control System ATN Advanced TIROS-N Spacecraft AVHRR Advanced Very High-Resolution Radiometer AWIPS Advanced Weather Interactive Processing System BLIP Background Limited Performance BOL Beginning of Life CCD Charged Coupled Device CDA Command and Data Acquisition Station CEMSCS Central Environmental Satellite Computer Center CID Charge Injection Device DBS Direct Broadcast Satellite DCS Data Collection System DoC Department of Commerce DoD Department of Defense DSCS Defense Satellite Communications System EDM Engineering Development Model EHF Extremely High Frequency EMP Electromagnetic Pulse EOL End of Life EOS Earth Observing System ERS European Research Satellite FOR Field of Regard FOV Field of View FPA Focal Plane Array GE General Electric GHz Gigahertz GIMTACS GOES I-M Telemetry and Control Subsystem GOES Geostationary Environmental Operational Satellite GRT GOES Real Time Database GSFC Goddard Space Flight Center GTE General Telephone and Electronics GVAR GOES Variable Format HAC Hughes Aircraft Co. HIRS High-Resolution Infrared Sounder IF Intermediate Frequency IFOV Instantaneous Field of View IFRB International Frequency Registration Board IGFOV Instantaneous Geometric Field of View IMC Image Motion Compensation INR Image Navigation and Registration IR Infrared ISAMS Improved Stratospheric and Mesoscale Sounder ITU International Telecommunications Union km Kilometer kW Kilowatt LRIP Low Rate Initial Production Mbps Megabits per second MCI Microwave Communications, Inc. MDL Multipurpose Data Link MHz Megahertz mi Statute Mile MMC Mirror Motion Compensation mrad milliradian MODIS Moderate-resolution Imaging Spectrometer MSR MITRE Sponsored Research MSS Mobile Satellite Service MIDAS Multi-discipline Data Analysis System NASA National Aeronautics and Space Administration NEdT Noise Equivalent Temperature Difference NESDIS National Environmental Satellite, Data, and Information Service NMC National Meteorological Center NMI Nautical Miles NOAA National Oceanic and Atmospheric Administration NWS National Weather Service OATS Orbit and Attitude Tracking ODAPS Operational OGE Data Acquisition and Patch Subsystem OGE Operational Ground Equipment OIS OGE Input Simulator OMB Office of Management and Budget PACS Polar Acquisition and Control Subsystem PC Photo Conductive PG&D Product Generation and Distribution PM Product Monitor POES Polar-orbiting Environmental Operational Satellite R&D Research and Development RARC Regional Administrative Radio Conference RCA Radio Corporation of America RF Radio Frequency RFP Request for Proposal ROM Rough Order of Magnitude RMS Root Mean Square RSS Root Sum Square RPM Revolutions per minute SBS Satellite Business Systems SEM Space Environment Monitor SFSS Satellite Field Service Center SOCC Satellite Operations Control Center SPS Sensor Processing Subsystem STLC Satellite Transponder Leasing Corp. STS Space Transportation System T&C Telemetry and Command TDI Time Delay Integration TDRSS Tracking Data Relay Satellite System TIROS Television and Infrared Observation Satellite TMI Telsat Mobile, Inc. TRW Thompson Ramo Woolridge TWT Traveling Wave Tube UARS Upper Atmosphere Research Satellite UHF Ultra High Frequency USAF United States Air Force USN United State Navy VAS VISSR Atmospheric Sounder VHF Very High Frequency VHRR Very High-Resolution Radiometer VIE VAS Interface Electronics VIS Visible VISSR Visible Infrared Spin Scan Radiometer WDL Western Development Laboratories -----
----- Return to the text Back to the CAASD Home Page

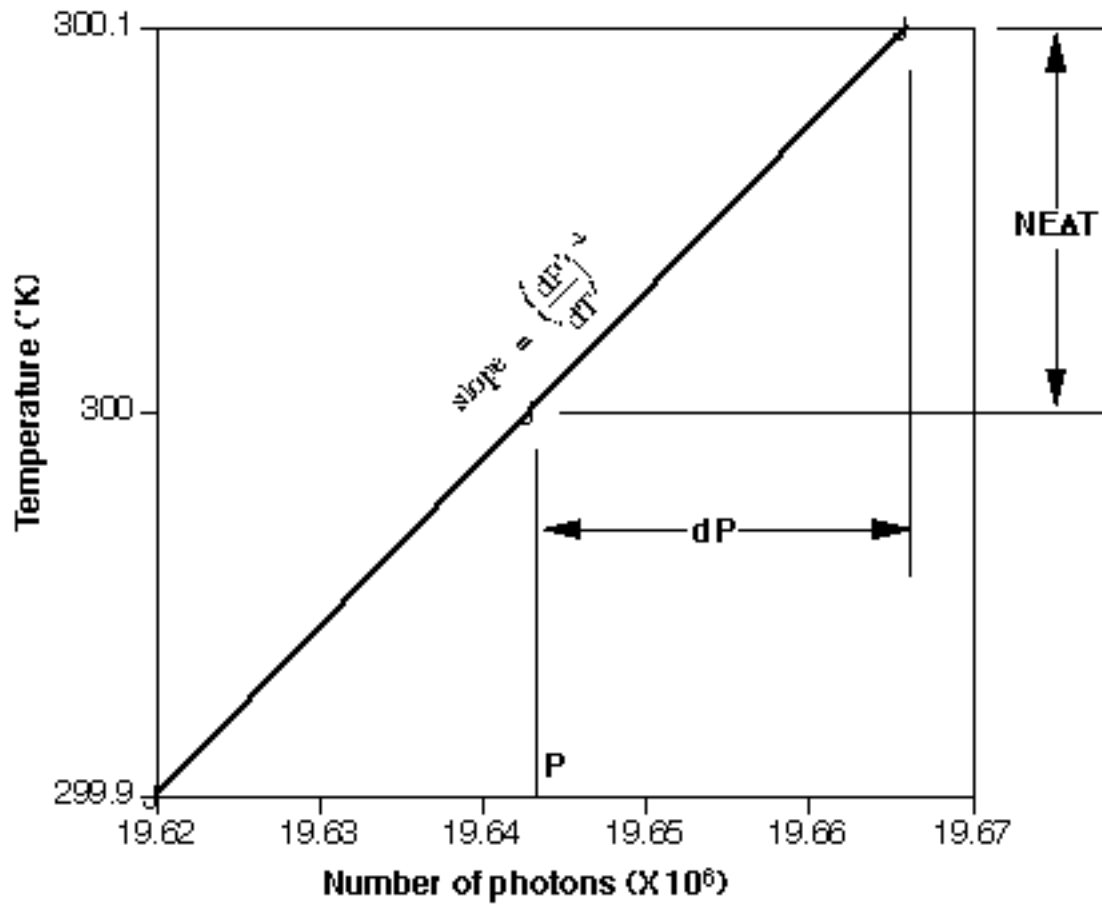


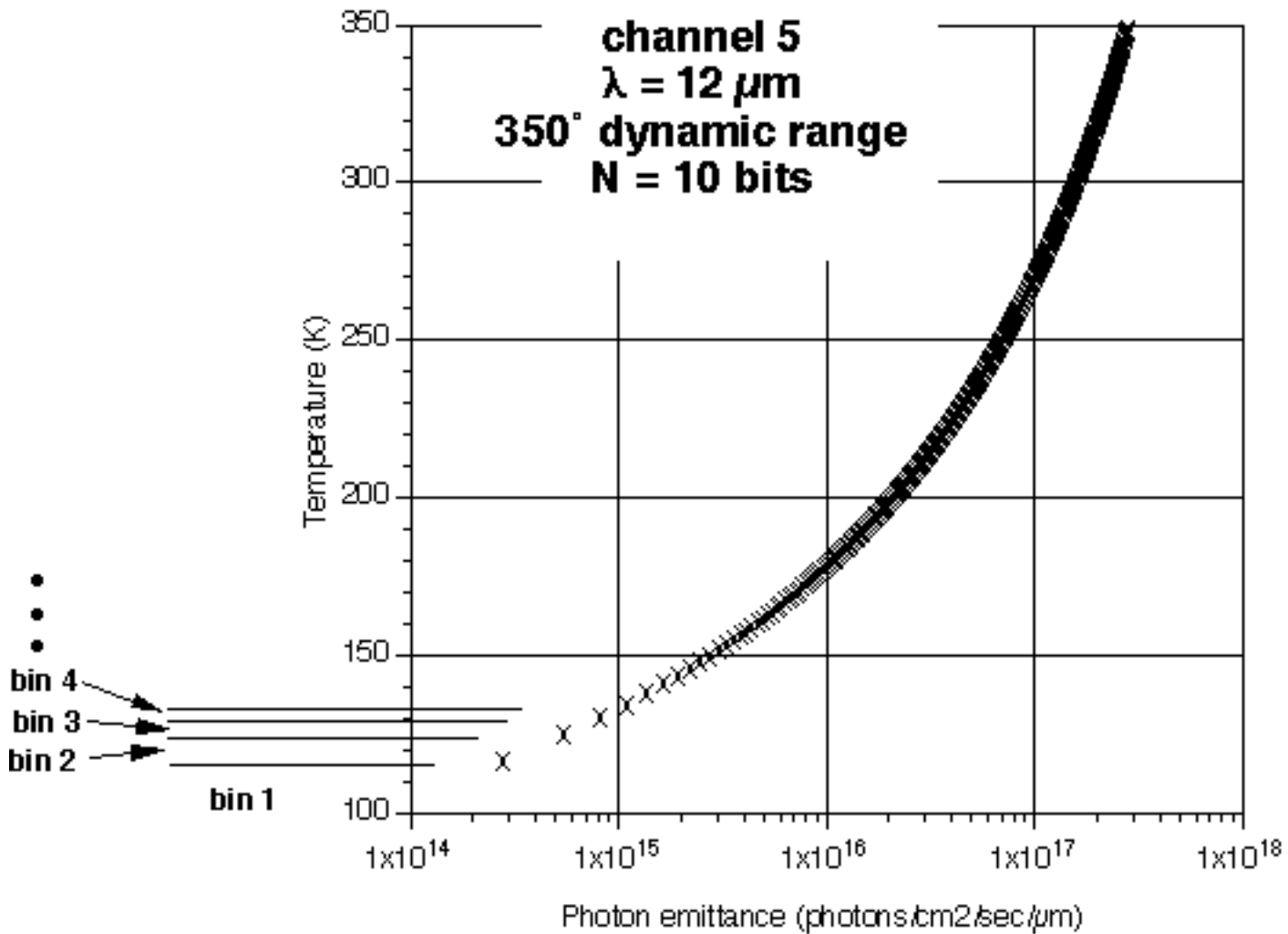


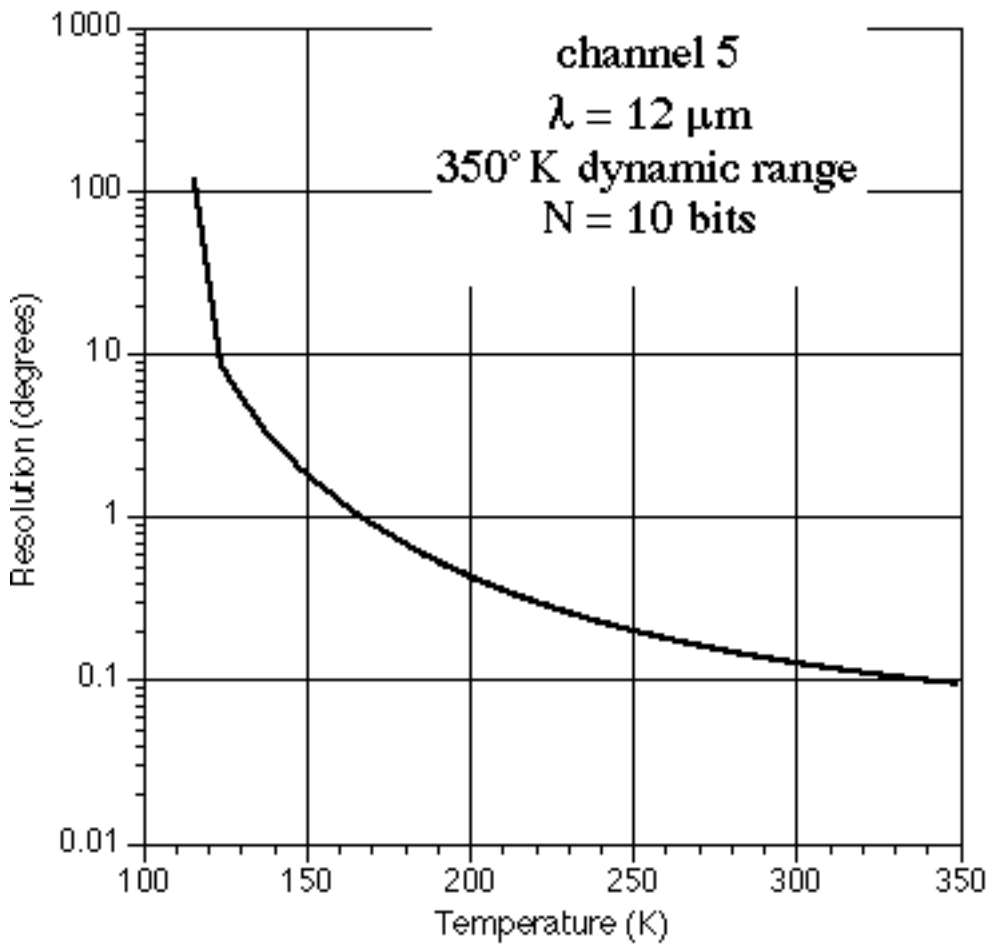


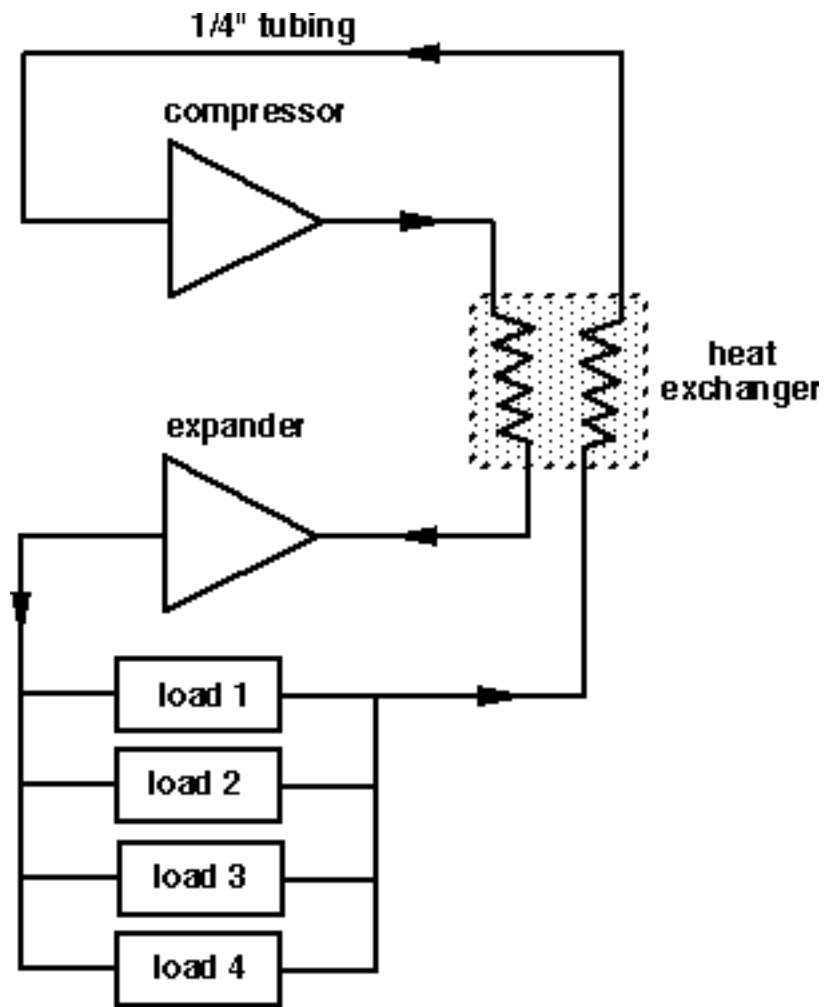


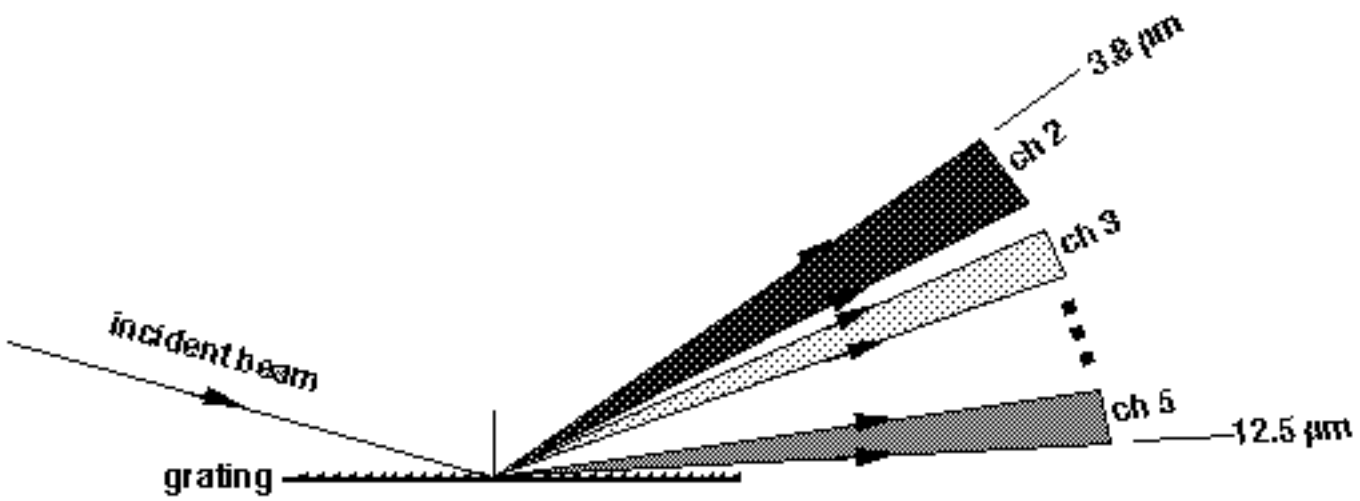


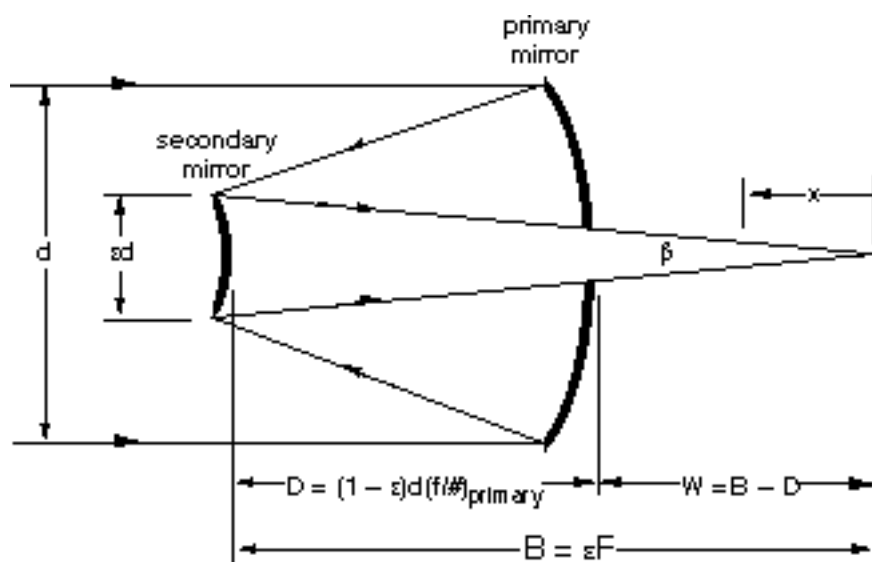


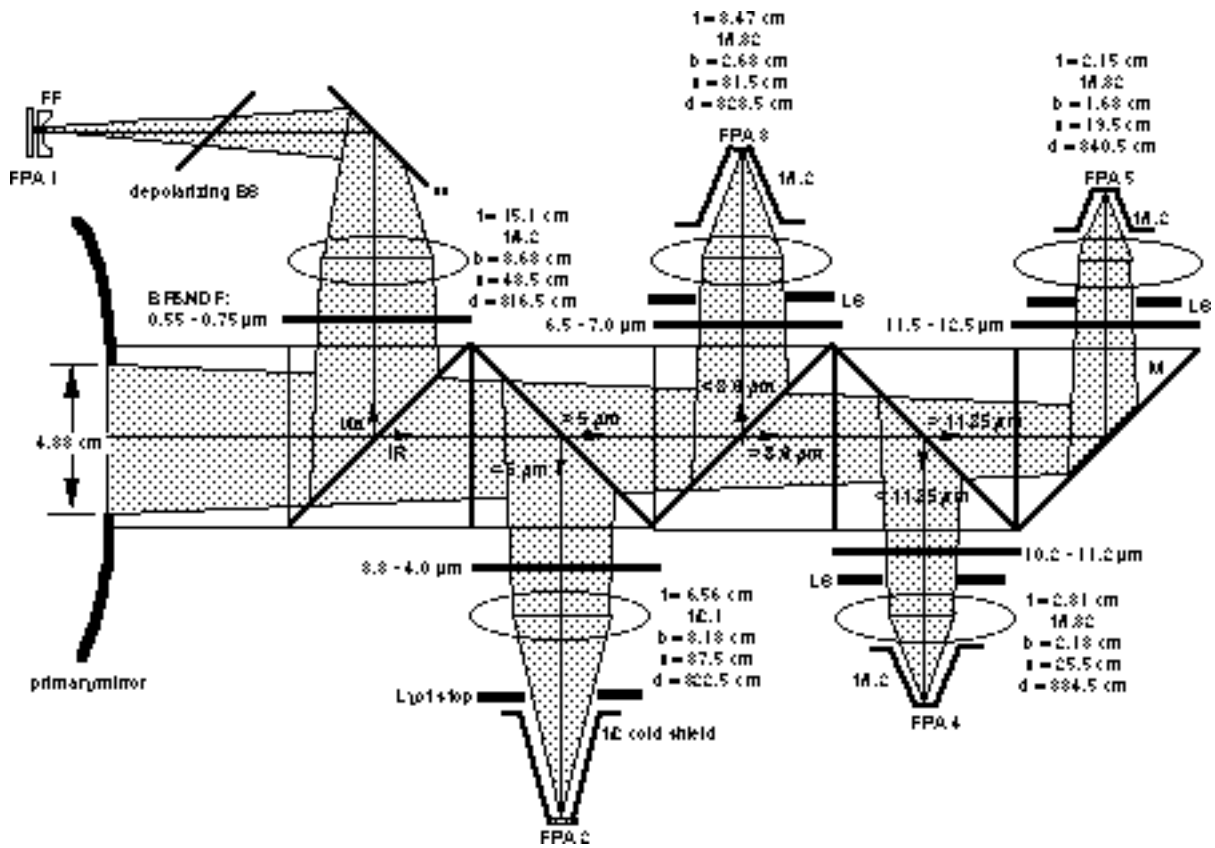


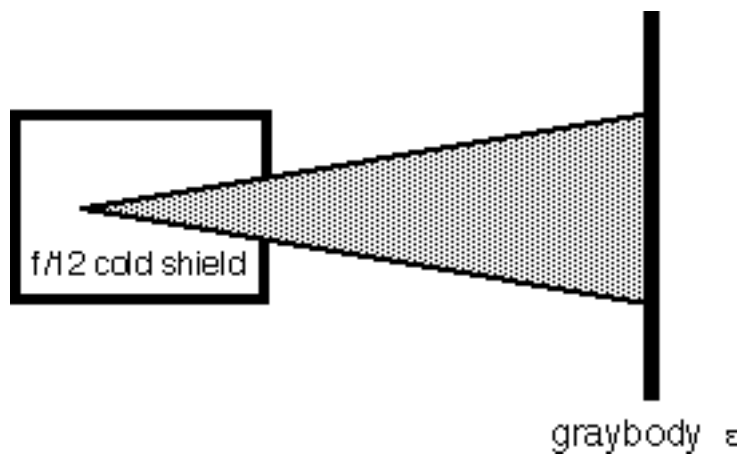












SECTION 2

IMAGER TECHNOLOGY AND DESIGN CONSIDERATIONS

2.1 INTRODUCTION

A geostationary weather satellite orbits at an altitude of 35,800 km. The Earth's radius is 6378.4 km. The Earth disk subtends an angle of 17.3 degrees at the satellite. For scanning purposes, the field of regard (FOR) for a full disk scan is defined as 20 degrees (N/S) x 20 degrees (W/E). A 1 km length on the Earth's surface at nadir subtends an angle of 28 urad ($= 1 \text{ km}/35,800 \text{ km}$) or 1.6×10^{-3} degrees.

GOES I-M weather satellites are currently under development. The GOES I imager is based on a flying-spot-scanning technique whereby, via motion of a two-axis scan mirror, the scene's resolution areas are optically imaged onto a single pixel (or a relatively small number of pixels). The GOES I instrument images five wavelength bands with resolutions ranging from 1 km to 8 km. The 8-km-resolution channel is scanned by a single detector pixel.

The GOES I pixel is illustrated in the upper left portion of the FOR in [figure](#) Figure 2-1 (Scanning the Field of Regard). The GOES I flying spot has an angular extent of 0.0128 degrees x 0.0128 degrees. There are 1562 horizontal scan lines over the FOR. The scan mirror moves horizontally at a rate of 20 degrees/sec. Therefore, a full disk image requires 1562 sec, or 26 minutes.

Imaging with detector arrays offers significant advantages over flying spot scanning. Depending on the detector material system appropriate for the desired wavelength, these arrays consist of many thousands to millions of detector pixels, along with a multiplexing and readout system. An array imager, with appropriate optics, would allow redundant arrays with a large 0.82 degree x 0.41 degree angular view. With 25 horizontal scan lines, an image can be formed in 3 minutes with a scan rate of 7.2 sec/line.

Since the scan rate is slower, the dwell time per pixel is longer, and the detectors in the array can collect more energy from the scene. This improves signal-to-noise ratio (SNR) and noise equivalent temperature difference (NEdT) performance. Of course, detector saturation must be prevented. Alternatively, the longer dwell time can allow us to shrink (improve) the resolution area somewhat and still collect sufficient energy to meet baseline SNR and NEdT requirements. The motivation for exploring an array imager is based on faster image formation and improved resolution and radiometric performance.

We begin this section by defining performance goals for an array imager and a brief review of focal plane array technology. We then examine the impacts from wavelength, resolution, and radiometric performance requirements on telescope design and focal plane array size. Tradeoffs associated with different scanning techniques are examined. Radiometric performance estimates are made for each channel. For cooling the detector array, the size of a passive radiative cooler is estimated and the state of the art in mechanical coolers is discussed. Design issues regarding spectral separation and common focal planes are considered. A preliminary instrument design is developed.

2.2 IMAGER PERFORMANCE GOALS

Performance goals for the proposed imager are based on documented NOAA meteorological requirements [GOESN89]. There are five channels to be imaged: one visible and four infrared (IR). Wavelengths, resolution goals, and principal applications are given in [Table 2-1](#). Resolution goals for channels 1, 2, and 3 represent improvements by a factor of 2 over GOES I-M. Enhanced resolution, especially in channels 2 and 3, is considered very desirable in the requirements document.

For the visible channel (1), performance is specified in terms of SNR. An SNR of 3 is required at 0.5 percent albedo. Albedo is the ratio of solar energy reflected from a rough surface to that incident on it. The dynamic range for the visible channel extends up to 100 percent albedo.

For the IR channels, the upper end of the dynamic range for GOES I-M is 320 degrees K. An increase in dynamic range to 350 degrees K is desired. This would allow more detailed observation of extremes in surface temperatures and differential heating, and would improve the monitoring of forest fires, volcanic eruptions, and other hot spots on the Earth.

Radiometric performance for the IR channels is specified in terms of NEdT. NEdTs are specified at three scene temperatures: 200 degrees K, a typical cloud top temperature; 240 degrees K, a mid-level cloud temperature; and 300 degrees K for surface scenes. A matrix of desirable NEdTs is given in [Table 2-2](#). Core requirements, specified for GOES I-M, are shown in parentheses in Table 2-2.

Numerous benefits could be gained from the improved NEdTs. These benefits relate to the following: more accurate corrections for Earth atmosphere absorption, detection of diurnal temperature fluctuations over land and shallow waters, better tracking of the Gulf Stream, determination of coastal upwelling in response to wind changes (all of the preceding from improvements at $T = 300$ degrees K), improved mid-tropospheric moisture estimates (240 degrees K), and cloud parameter estimates for improved indicators of severe convection intensity (200 degrees K).

Blackbody spectra and the IR channels are shown in [figure](#) Figure 2-2 (Blackbody Spectra and IR Channels). For the interested reader, Planck's radiation law is reviewed in Appendix A. A dynamic range increase from 320 degrees to 350 degrees K results in a thermal radiation increase of 169 percent for channel 2 (from 1.3×10^{-4} to 3.5×10^{-4} W/cm²/um/sr). The impact from increasing dynamic range is less for the other channels. Because channel 2 lies farthest from the peak spectral wavelengths, and because it has the narrowest spectral band ($d[\lambda] = 0.2$ um), it will require the longest integration time. [Figure 2-2](#) also shows that channels 4 and 5 will have similar performance since their radiation levels are close to each other.

For each channel and temperature, we can determine the rate at which photons are emitted per unit area (of blackbody source) per unit solid angle (subtended by the detecting aperture). This normalized emission rate is called the photon sterance and has units of photons/(sec*cm²*sr). Our radiometric nomenclature is adopted from Vincent [VINCENT90]. Further discussion of this nomenclature is found in Appendix A. Photon sterance levels will be used later in our radiometric performance calculations.

For a given scene temperature, photon sterance levels for the IR channels are computed by integrating the spectral photon sterance $L_q([\lambda], T)$ over the channel wavelength bands ($[\lambda]_1$ to $[\lambda]_2$):

[figure](#) photons/(sec*cm²*sr)

Photon sterance levels, are given in [Table 2-3](#). Also shown in parentheses in Table 2-3 is the relative temperature derivative of the photon sterance [figure](#). This derivative will come into play when characterizing the radiometric (NEdT) performance of the imager.

For the visible channel, we are interested in optical power levels in the range from 0.5 to 100 percent albedo. The required optical dynamic range is a factor of 200. The solar constant at the mean distance of the Earth from the sun is 0.1353 W/cm². Of this flux, 22.3 percent falls in the channel 1 wavelength band between 0.55 and 0.75 um. At a fractional albedo, A , the radiant sterance is $9.60 \times 10^{-3} A$ W/(cm²*sr). With $A = 0.005$ and 1.0, the radiant and photon sterance levels are given in [Table 2-4](#).

There are temporal requirements for synoptic (full disk) and mesoscale (U.S. sectors) applications. The core requirement is for a full disk image within 30 minutes. Any 3000 km x 3000 km area must be imaged within five minutes, and a 1000 km x 1000 km area must be imaged within 2 minutes. For an array imager, these temporal requirements are very liberal. Our temporal goal is for a full disk image within 3 minutes.

2.3 FOCAL PLANE ARRAY (FPA) TECHNOLOGY

Silicon image sensor arrays are appropriate for the wavelength band of channel 1. Silicon devices respond out to 1 μm . Silicon arrays have been made with up to 4096 x 4096 pixels (e.g., Loral Fairchild CCD481 or Ford Aerospace FA4096S). Pixel sizes range from 6.8 μm on edge (e.g., Kodak KAF 1400 image sensor) to more than 30 μm square.

Silicon image sensor arrays employ either charge-coupled device (CCD) or charge-injection device (CID) technology. In a CCD, each photoelement has a capacitor for accumulating and storing optically generated electrons. A clocking operation shifts the charges sequentially across the capacitors. The efficiency of charge transfer can be 99.999 percent. The charges appear at an output gate at the edge of the device. In a CID, the charge under each photoelement is measured, and there is no shifting of charge. Since the charges remain stationary, a selective or random readout of individual pixels is possible. The CIDs are resistant to blooming (charge spillover from an overexposed pixel to neighboring pixels) and smearing (transfer of the overexposure effect along the array).

Image sensor array architectures may be full-frame, frame-transfer, interline, or time delay and integration:

- * With the full-frame architecture, rows of scene information (pixel charges) are shifted in parallel to a serial shift register, which subsequently shifts the row of information to the output as a serial stream of data. The process repeats until all the rows are transferred off the array.
- * In a frame-transfer architecture, there is a parallel storage array that is not light sensitive. The captured scene from the photosensitive array is rapidly transferred to the storage array. Readout from the storage array is then performed as for the full-frame architecture while the photosensitive array is integrating the next frame.
- * In an interline architecture, the photodetecting and readout functions are separated by forming isolated photosensitive regions between lines of nonsensitive (or light-shielded) parallel readout CCDs. After a scene has been integrated, the signal collected in every pixel is transferred, all at once, into the light-shielded parallel CCD.
- * Time delay and integration is a mode of processing the signal charge from the detector array that enables the integration of charge from multiple detector elements. Multiple pixel-sized images of an object are added to obtain an enhanced SNR. TDI is discussed further in connection with scene scanning tradeoffs.

There are several detector material systems for IR detection. The cutoff wavelength $[\lambda]_c$, where the spectral response on the long wavelength side is at 50 percent of peak, depends on the temperature of the detector. [Table 2-5](#), from [Norton91], shows the cutoff wavelength for several material systems at various detector temperatures.

A temperature of 190 degrees K can be achieved with a four-stage thermoelectric (TE) cooler. A temperature of 80 degrees K requires liquid nitrogen, a Joule-Thompson cryostat, or a single-stage mechanical cooler. Temperatures between 1.5 degrees K and 60 degrees K require multiple-stage mechanical coolers, or liquid neon, hydrogen, or helium.


Indium antimonide (InSb), platinum silicide (PtSi), and mercury cadmium telluride (HgCdTe) are all candidates for the wavelength range of channel 2 (3.8-4.0 μm), but only HgCdTe is possible for the longer-wavelength channels. The relative concentrations of HgTe molecules with CdTe molecules can be adjusted in the growth process to form $\text{Hg}_{1-x}\text{Cd}_x\text{Te}$ and obtain a desired cutoff wavelength, larger x resulting in shorter $[\lambda]_c$. Typical uncertainties in production of long-wavelength $\text{Hg}_{1-x}\text{Cd}_x\text{Te}$ arrays are $dx \sim \pm 0.2$ percent, corresponding to a cutoff wavelength uncertainty of $d[\lambda]_c \sim 0.5 \mu\text{m}$.

In a photovoltaic (PV) detector, there is a p-n junction. Photoelectrons created near the junction are separated by the junction and produce a voltage in proportion to the incident number of photons. With photoconductive (PC) detectors, incident photons are absorbed and produce free charge carriers. The carriers increase the electrical conductivity of the element and therefore


decrease its resistivity. A bias circuit must be used with PC detectors. Advantages of PV over PC detectors include a better theoretical limit to the SNR, no biasing and therefore low power dissipation on the focal plane, high impedance for matching into a silicon CCD, and more accurately predictable responsivity ([Vincent90] and [Walter86]). PC HgCdTe technology is presently limited to linear arrays. So-called first-generation IR focal plane arrays were photoconductive and had a pair of electrical leads for every pixel; no multiplexing was involved. Second-generation PV arrays multiplex pixel signals to output ports on the readout integrated circuit (ROIC).

For IR imaging, PtSi offers the largest array sizes. Two-dimensional PtSi arrays have been made with 480 x 640 elements. EG&G is currently developing a monolithic-structure 512 x 512 PtSi array for the U.S. Air Force. Both monolithic (photodetection and readout on same substrate) and hybrid (PtSi photodetection silicon readout) arrays have been fabricated. As compared with other IR detectors, PtSi offers the advantages of large formats and excellent uniformity of response from pixel to pixel. However, the quantum efficiency of PtSi is very low--in the range of 0.1 to 1 percent. Quantum efficiency is the number of electrons generated per incident photon. Low quantum efficiencies require long integration times for low level incident radiation.

There is continuing debate in the industry on tradeoffs for selection of InSb versus HgCdTe for channel 2. The arguments center on detectivity, detector temperature, cutoff, cost, and uniformity. Some of this debate is reviewed by DeWames [DeWames92]. The detectivity of InSb is much better at 65 degrees K than at 80 degrees K; its performance is very poor above 80 degrees K. At 65 degrees K, InSb offers better (precorrected) uniformity and operability than HgCdTe. Operability is a term used to characterize the percent of pixels with detectivity and quantum efficiency greater than some acceptable level. An argument in favor of HgCdTe is that the cutoff wavelength of InSb cannot be tailored to the channel 2 application, whereas the chemistry of HgCdTe can tailor the cutoff to around 4.3 μm . This would reduce noise and allow operating margin. Large array size and cost favor InSb technology. InSb arrays of 256 x 256 pixels have been produced, and those of 512 x 512 are in development. HgCdTe array sizes of 128 x 128 are common.

As we will see later, pixel-to-pixel uniformity is an important aspect for an imager using FPAs. Pixel-to-pixel nonuniformity is usually characterized in terms of the standard deviation of responsivity over the pixels of the array.  Figure 2-3 (Responsivity Nonuniformity of IR Sensor Arrays) [Norton91] shows response nonuniformity of IR detector material systems. PtSi is seen to approach a nonuniformity of 0.1 percent, whereas HgCdTe nonuniformity can be as high as 10 percent. InSb's nonuniformity falls in the 0.7 to 2 percent range. To reduce the effects of responsivity variations, an array must be characterized pixel-by-pixel. Correction coefficients are determined and gain values for each pixel are stored. However, even after this correction process, there are still residual variations. The residual variations result from pixel response nonlinearities. Residual variations have been reported as low as 0.01 percent.

2.4 TELESCOPE AND ARRAY SIZES

The imager requires a telescope to collect and focus energy from the Earth scene. Our study of an array imager begins with telescope considerations.  Figure 2-4 (System Considerations) illustrates the flow of imager requirements and interaction among system aspects. The wavelength requirements impact the telescope type and aperture size through considerations of chromatic dispersion and diffraction limitations. Aperture size is also driven by radiometric performance requirements. In addition to wavelength, resolution requirements enter into determining aperture size. In the telescope design, resolution requirements set an upper limit on aberrations. This establishes the telescope's field of view (FOV), which in turn determines the maximum array sizes for the channels. Dimensions of the detector array pixels, along with resolution requirements, determine the required system focal lengths. Scan techniques are driven by temporal and radiometric performance requirements, and interact with array sizes.

Telescopes fall into the categories of reflective, refractive, and catadioptric designs. Because of the wide wavelength range required for the imager (0.55-12.5 μm), a common refractive telescope cannot be considered; chromatic aberrations would be too great. Some catadioptric telescopes, such as the Mangin mirror, Bouwers-Maksutov, and Schmidt systems, use mirrors with a refracting element to correct for spherical aberrations. Once again, the refractive element would result in severe

chromatic distortion over the wide wavelength range. Other catadioptric designs use a shaped refractive meniscus to reduce chromatic aberration; however, the resulting focal plane is a curved surface.

The imager's wide wavelength requirements lead us to reflective telescope designs. The most common of the reflective designs are the two-mirror telescopes. These include the classical Cassegrain and Ritchey-Chrétien (RC) designs. In these two-mirror systems, the secondary mirror presents an obscuration to the collection of light by the primary. For our analysis, we assume a linear obscuration of $[\epsilon] = 0.25$ (0.0625 by area).

If an angular resolution $[\theta]$ is to be met with an obscured aperture, then the minimum diameter D , determined from diffraction limitations, is:

figure

where x is a root of $J_1(x) - [\epsilon]J_1([\epsilon]x) = 0$, and $J_1(x)$ is an ordinary Bessel function.

For $[\epsilon] = 0.25$, we found that $x = 3.59$, and the diffraction law becomes:

figure

Diffraction-limited apertures for the five imager channels are given in [Table 2-6](#). Channel 5 requires the largest aperture, and we henceforth assume a telescope with a 30 cm diameter aperture. Presenting an $[\epsilon] = 0.25$ obscuration, the diameter of the secondary mirror is 7.5 cm.

We see from [Table 2-6](#) that the diffraction-limited aperture for channel 1 is 12.3 cm for an enhanced resolution of 14 urad (0.5 km). However, if we accept the standard 28 urad (1 km) resolution, the minimum diameter is 6.1 cm. Since this diameter is smaller than the 7.5 cm obscuration of the 30 cm telescope, it allows for an interesting design of a two-telescope imager; a 30-cm reflective telescope for the IR channels and a 7.5 cm refractive telescope for the visible channel, positioned within the obscuration of the IR telescope. This design concept is illustrated in [figure](#) Figure 2-5 (Two-Telescope Imager). Time did not allow us to pursue the two-telescope design, but we mention it here as a design alternative to the single-telescope system, which we analyze in detail.

Aberrations distort the focused image in a telescope. Aberrations include spherical, coma, astigmatism, and Petzval curvature. The Cassegrain telescope, with paraboloidal primary and hyperboloidal secondary mirrors, corrects for spherical aberration. The RC design has aspheric surfaces chosen to correct for both spherical and coma aberrations. Both designs have been built and flown in space. The visible and infrared spin scan radiometer (VISSR) and Hubble telescopes are RC designs. Since the RC corrects for more aberrations, and since we desire the largest FOV, we analyze the RC design.

The RC telescope suffers from astigmatism and Petzval field curvature. Aberrations are a function of the $f/\#$ of the primary mirror; the lower the $f/\#$, the worse the aberrations. However, lower primary mirror $f/\#$ s are desirable because mirror spacings are closer, the telescope is more compact, and there is more working distance behind the primary mirror before the beam comes to focus. Extra working distance for the aft optics (beamsplitters, filters, lenses, stops, etc.) is important since there are five channels to process.

The maximum full FOV is defined as twice the angle at which aberrations result in a spot diameter equal to the required instantaneous field of view (IFOV). Astigmatism and Petzval aberrations were computed for the RC telescope according to [Wolfe89]. The magnitudes of the aberrations were added to determine a blur radius. The blur diameter divided by the focal length is the blur angle. The blur angle increases with the off-axis angle of incidence. The off-axis incidence angle was increased, and the blur angle was allowed to increase up to the IFOV for each channel. The analysis was performed as a function of primary mirror $f/\#$. The results of this analysis are shown in [figure](#) Figure 2-6 (Field of View for 30 cm $f/12$

Ritchey-Chrétien Telescope). For an f/1.4 primary, the 14 urad IFOV of channel 1 limits the maximum FOV to approximately 0.42 degrees. A 28 urad IFOV, corresponding to 1 km resolution, allows a 0.59 degree FOV. The 56 urad IFOV of channel 2 allows a 0.84 degree FOV, and channels 3-5, with 112 urad resolution, allow a 1.18 degree FOV.

Channel 1 restricts the telescope FOV. Further analysis of RC telescope aberrations shows that the dominant aberration is Petzval field curvature. In effect, the focal plane is curved. A field corrector lens may be used to reduce Petzval aberration, and it is not unreasonable to assume that the correction will double the FOV from 0.42 degrees to 0.84 degrees. The field corrector lens would be required only for the optics of channel 1, not the other channels.

A square array has $N \times N$ pixels. The required FOV for an $N \times N$ array is $N(\text{IFOV})^{1/2}$. The factor $^{1/2}$ increases the diameter of the circular FOV so that it encompasses a square array (i.e., the array diagonal is the diameter of the telescope's FOV). In [figure](#) Figure 2-7 (Field of View and Array Size), FOV is plotted against array size for the three resolutions.

For channel-to-channel coregistration, all channels must have a common FOV. The 0.84 $^{\circ}$ FOV of the 30 cm f/12 RC telescope, indicated by a dark line in [Figure 2-7](#), falls between two sets of array sizes. The optimistic set consists of a 1024 x 1024 array for channel 1, a 256 x 256 array for channel 2, and 128 x 128 arrays for channels 3-5. The optimistic set would require a telescope FOV of 1.16 degrees. The pessimistic family of array sizes is 512 x 512 for channel 1, 128 x 128 for channel 2, and 64 x 64 for channels 3-5. In our aberration analysis of the RC telescope, we added the magnitudes of the astigmatism and Petzval contributions. This is known to be a worst-case situation, so there is some justification for optimism. Furthermore, preliminary results of ray tracing analyses on an optimized RC telescope are encouraging. We are optimistic.

Redundancy is desired in spacecraft systems to avoid single points of failure. In our array size arguments, we assumed a square array. However, for redundancy, we will place two identical arrays within the FOV. Redundant rectangular arrays are illustrated in [figure](#) Figure 2-8 (Redundant Arrays in the Field of View). Redundancy reduces the array width by a factor of 2. The optimistic family of redundant array sizes is 1024 x 512 for channel 1, 256 x 128 for channel 2, and 128 x 64 for channels 3-5.

We assume square pixels in the array. For a channel 1 silicon array, we assume a 15 μm pixel edge. For InSb (channel 2), we assume 30 μm , and for HgCdTe (channels 3, 4, 5), 40 μm . These dimensions are typical of commercial products. The corresponding physical dimensions of the optimistic array family are 15.4 x 7.7 mm (channel 1), 7.7 x 3.8 mm (channel 2), and 5.1 x 2.6 mm (channels 3-5).

2.5 SCANNING

Before discussing scanning techniques, we need to distinguish between *scene pixels* and *detector pixels*. Scene pixels are characteristic of the object (the Earth) and are characterized by the nadir resolution or equivalent angle (IFOV). For the visible channel, the entire 20 degree x 20 degree field of regard (FOR) is divided into 6.2×10^8 scene pixels. Each of these scene pixels represents an angular IFOV of $(14 \text{ urad})^2$, corresponding to an area of $(0.5 \text{ km})^2$ at the subsatellite point (nadir). The detector array comprises a number of detector pixels. A detector pixel is a very small square area of detector material, measuring $(15 \text{ } \mu\text{m})^2$ in the case of the visible channel. The system optics image scene pixels onto detector pixels in the focal plane.

Two methods of scanning are addressed: step-stare and time delay and integration (TDI). We first address the step-stare scan technique. The 20 degree x 20 degree FOR is to be scanned in 3 minutes. With the optimistic array set, all five arrays see the same 0.82 degree x 0.41 degree FOV. There are 1190 FOVs in the FOR. To accomplish a 180 sec scan, the FOV may dwell up to $180/1190 = 151$ milliseconds (msec). We will see later that this time interval is very long in comparison with maximum integration (exposure) times for detector arrays.

In a step-stare scan, it is desirable to overlap the FOV steps. Overlap allows consecutive FOV registration and partially

compensates for any dead pixels in the detector array. Dead pixels are programmed out of the final sum. Consider the FOV of the array oriented to view 0.82 degree in the North-South direction and 0.41 degree in the West-East direction. If we require that every scene pixel (e.g., 0.5 km x 0.5 km Earth region) be viewed by four different detector pixels and their results averaged, then the 0.82 degree x 0.41 degree FOV will advance by 0.205 degrees in a west/east scan line. After completion of a scan line, the FOV will step downward (north/south direction) by 0.41 degrees. This is equivalent to a FOV measuring 0.41 degrees x 0.205 degrees stepping through the FOR. The maximum dwell in this case is 38 msec--still relatively long compared with detector saturation exposure times. Thus, even with a four-fold FOV overlap, step-stare dwell times are not limiting.

TDI is an alternative scanning technique. To illustrate TDI, we look at figure Figure 2-9 (TDI Scanning) and suppose that the 20 degree x 20 degree FOR is divided into 25 horizontal scan lines (20 degrees/0.82 degrees ~ 25). For channel 1, we use a 1024 vertical x 128 horizontal array. This array, as well as the other coregistered arrays, scans horizontally at a rate of 2.8 degrees/sec to form a 3 minute full disk image. As the array scans horizontally, each channel 1 scene pixel is seen by 128 detector pixels. The accumulated photoelectrons from the 128 pixels are added, and the final sum is read out.

As long as the detector pixels do not fill to saturation, there is an SNR performance benefit provided by the TDI scan over the step-stare approach. Essentially, this benefit arises from the coherent linear addition of signal photoelectrons to the incoherent root mean square (rms) addition of noise electrons. If there are m pixels in TDI, the SNR is improved by a factor of $[\text{radical}]m$. Measurements have shown this improvement is valid and precise. With 128 pixels in TDI, channel 1 will have an improvement of 11.3 over the step-stare scan.

Our choice of 128 pixels in TDI for channel 1 is arbitrary. Silicon arrays have been made with 96 pixels in TDI, and 128 is not unreasonable. [Figure 2-9](#) shows a family of TDI array sizes for all five channels. These arrays would be coregistered, simultaneously viewing the same scene area. At an angular velocity of 2.8 degrees/sec (7.2 sec/line), the maximum dwell time *per detector pixel* is 0.289 msec for channel 1, 1.156 msec for channel 2, and 2.312 msec for channels 3-5. Figure 2-9 shows the TDI array scanning from left to right. At the end of this scan line, the array moves to the next scan line and moves right to left, with reversal of the charge addition process. This feature is referred to as a bidirectional TDI array. Redundant TDI arrays are easily fit within the telescope's FOV since, the TDI arrays are thinner than those portrayed in [Figure 2-8](#).

In addition to the SNR enhancement, TDI offers several other advantages over the step-stare scan. The adding/averaging process of TDI results in better pixel-to-pixel response uniformity. As will be discussed later, uniformity is very important for array imagers. Inoperable or dead pixels may be deselected in a TDI array. Furthermore, the redundancy inherent in the TDI array lessens production yield requirements, and therefore reduces development risk and cost. All focal plane vendors and sensor system developers contacted during the course of this effort were advocates of TDI. Further arguments on the TDI/step-stare tradeoff, from a navigation/registration perspective, are found elsewhere in this document.

Whether a TDI or step-stare scan is employed, we can estimate the downlink data rate from the satellite to a ground station. The data rate is found by determining the total number of scene pixels, encoding each pixel in a data word, and then transmitting the resulting data load within a specified (3 minute) interval. The total number of scene pixels is 1.69×10^8 . Later, we will see that radiometric goals require encoding with 11 bits/pixel, and on top of this we allow a 20 percent overhead. The resulting data load is 9.1×10^9 bits (b). If this data load is sent within 3 minutes, the data rate is on the order of 50 megabits per second (Mbps). However, data compression could result in a reduced data rate. Therefore, with compression the downlink would require a data rate well within transponder capability that would be employed on a nondedicated communications satellite.

2.6 RADIOMETRIC PERFORMANCE

The dwell times determined in the previous section are an upper bound on detector integration times. The integration time is determined by the upper end of the instrument's dynamic range, and detector characteristics such as quantum efficiency and electron well capacity. These parameters depend on the detector material system, pixel size, and maximum radiation level from the scene. Integration times will vary considerably over the five channels.

Maximum IR radiation levels are at a scene temperature of 350 degrees K. [Table 2-3](#) provides the 350 degrees K photon sterance levels, [figure](#). The resolution areas, Ares, of the blackbody sources are $(2 \text{ km})^2$ for channel 2 and $(4 \text{ km})^2$ for channels 3-5. The 30 cm optical aperture of the telescope subtends a solid angle of $[\Omega] = 5.5 \times 10^{-17} \text{ sr}$, and we assume that the transmission of the optical system (fore and aft optics) is $[\tau] = 0.25$. The integration time is often defined as the time to fill the electron well to half capacity (0.5w). This leaves a little reserve to prevent the possibility of saturation. The integration time is:

[figure](#)

The quantum efficiency of the detector is $[\eta]$. We use $[\eta] = 0.55$ for both InSb and HgCdTe, but $[\eta] = 0.0042$ for the PtSi channel 2 alternative. Well capacities, taken from the technical literature on commercial array products, are $w = 1.6 \times 10^7 \text{ e-}$ for InSb, $4.0 \times 10^7 \text{ e-}$ for HgCdTe, and $1.7 \times 10^5 \text{ e-}$ for PtSi.

The integration times work out to 19 msec for channel 2 with InSb, 0.5 msec for channel 3, and 0.165 msec for channels 4 and 5. If PtSi were used for channel 2, the integration time would increase to 26 msec. Clearly, channel 2 paces the system because of its longer integration time. The other channels must be shuttered or attenuated to balance the integration times.

The integration times all fall well within the maximum dwell times for the overlapping step-stare scan with optimistic array sizes. However, for the TDI scan, we previously found that the maximum dwell times *per detector pixel* were 1.16 msec for channel 2, and 2.32 msec for channels 3-5. The implication is that with a 3 minute TDI scan, the integration time of channel 2 will be limited by the mechanics of the scan. This may be offset by the SNR enhancement provided by TDI. The impact on channel 2's radiometric performance from this limited integration time is examined later.

The per pixel integration time for the visible channel 1 is based on the characteristics of a commercially available 1024×96 TDI array. In this array, the TDI process works on the bucket brigade principle. Each pixel in TDI accepts the accumulated charge from the previous pixels and adds to this charge during its own integration time. The charge is then passed along to the next pixel. The specified saturation exposure pertains to the total integration time (i.e., the sum of all the TDI exposures).

The saturation exposure for channel 1 is determined at 100 percent albedo, which is $9.60 \times 10^{-3} \text{ W}/(\text{cm}^2 \cdot \text{sr})$ (see [Table 2-4](#)). With the previous assumptions for solid angle, transmission, and with a resolution area of $(0.5 \text{ km})^2$, the maximum incident optical power level is 330 pW. The channel 1 integration time is determined from the specified saturation exposure and pixel area as:

[figure](#)

This per pixel integration time is for each of the 96 pixels in TDI. The total time for all 96 integrations is 470 usec. Scaling the integration time to our case of 128 pixels in TDI, the channel 1 per pixel integration time is $t_{\text{int}} = 3.7 \text{ usec}$.

Except for channel 2, the mechanical dwell times exceed the pixel integration times. To avoid saturation of the other channels, they may be attenuated to balance the exposures. An appropriate attenuation factor is found from the ratio of integration time to dwell time. Attenuation factors for exposure balancing are given in [Table 2-7](#). With exposure balancing, all detectors integrate for their full mechanical TDI dwell time. For all channels, the total TDI integration time is 37 msec ($= 128 \times 289 \text{ usec} = 32 \times 1156 \text{ usec} = 16 \times 2312 \text{ usec}$).

At 0.5 percent albedo, the optical power collected by the telescope aperture for channel 1 is 6.4 pW. With an aft optics transmission of $[\tau]_o = 0.25$ and a neutral density filter with $[\tau]_{\text{nd}} = 0.013$ for exposure balancing, the detector collects $P_{\text{min}} = 21 \text{ nW}$. With 128 pixels in TDI, the SNR is:

figure

where the responsivity is $400 \text{ V} \cdot \text{cm}^2 / \text{uJ}$, and the specified rms noise voltage is $V_{\text{noise}} = 0.2 \text{ mV}$. A SNR of 1200 at 0.5 percent albedo greatly exceeds the required value.

For IR photon detectors, a well-known figure of merit is the detectivity, D^* . D^* is the reciprocal of the detector's noise equivalent power. It is used in determining the detector's NEdT performance. There is a theoretical limit to D^* based on the detector's cutoff wavelength, $[\lambda]_c$ and quantum efficiency, $[\eta]$, and the background photon flux, Q , seen by the detector. For a photovoltaic detector, the theoretical limit is:

figure

where $[\lambda]_c$ is in microns, and Q is in photons/($\text{sec} \cdot \text{cm}^2$). This is called the background-limited (BLIP) D^* . Depending on the cutoff wavelength and detector temperature, state-of-the-art IR detectors can approach the theoretical limit to D^* .

The smaller the background flux Q , the better the detectivity. For our application, Q is limited spectrally by channel bandpass filters. Additionally, Q can be limited spatially with a cold shield or cold stop. The cold shield, specified by its $f/\#$ or cone angle, prevents radiation from IR sources at angles greater than the cone angle. For our computations, we use an $f/2$ cold shield. The cold cone has a 29 degree full angle and reduces background flux by a factor of 16, thereby improving D^* by a factor of 4.

Theoretical D^* values were computed for each material system ($[\eta] = 0.55$ for InSb and HgCdTe; $[\eta] = 0.0042$ for PtSi) and each channel at the scene temperatures of interest. The resulting BLIP D^* s are given in [Table 2-8](#).

Several FPA vendors claimed that for the lower-wavelength channels (2 and 3), a 50 percent BLIP D^* could be expected; however, for the longer-wavelength channels (4 and 5) only 10 percent BLIP could be expected. We followed their suggestions for the computation of NEdT performance. NEdT can be evaluated in terms of system parameters as:

figure


[Table 2-9](#) shows NEdTs computed for the step-stare scan with 50 percent BLIP detection assumed for channels 3 and 4, and 10 percent BLIP for channels 4 and 5. Values in parentheses do not meet the GOES N desired NEdT performance levels of [Table 2-2](#); the majority of cases fall in this category.

Improvements in NEdT performance are attained with TDI scanning. The improvement reduces the NEdT by a factor of $[\sqrt[m]]{m}$, where $m = 32$ for channel 2, and $m = 16$ for channels 3-5. NEdTs for a TDI scan are shown in [Table 2-10](#). It is important to note that we have not assumed bucket-brigade-style charge-passing pixels as we did for the visible channel. Rather, we have assumed here that the charge is removed from each pixel after it is exposed. The charges are then added in a higher electron-well capacity CCD. This assumption means that the *per pixel* integration time for TDI is the same as the step-stare integration time tint. The total TDI integration time is therefore $m \text{ tint}$. This assumption allows us to divide the step-stare NEdT values by $[\sqrt[m]]{m}$ without worrying about overexposure.² We discussed this assumption with array developers, they considered it to be a reasonable assumption.


The TDI calculations show that all desired NEdT performance goals are met or exceeded except for the case of using a PtSi detector array. Its low quantum efficiency and detectivity result in very poor performance. PtSi is therefore considered no further.

The NEdT calculations were performed under the tacit assumption of perfect response uniformity from pixel to pixel in the

array. Of course, nothing is perfect, and there will be some level of nonuniformity. Nonuniformities take the form of variations in quantum efficiency from pixel to pixel, response nonlinearities, and variations in offset (response under conditions of no light). In attempting to measure small temperature differences over the array, response nonuniformities will appear as noise. Characterization and correction of the array and frequent calibration will help. However, there will still be *residual* nonuniformity. Our next step is to determine a bound for residual nonuniformity. This bound depends on the NEdT.

The inverse Planck function is used in ground processing to determine the temperature from the estimated number of photons collected by the imager from the scene resolution area.  Figure 2-10 (Temperature Resolution) shows the inverse Planck function for channel 5 around 300 degrees K. The abscissa is the number of photons, P, collected during the 165 usec integration time, and the ordinate is the corresponding temperature as determined by the inverse Planck function. The desired 0.1 degree NEdT is indicated. If residual nonuniformities result in a pixel-to-pixel variation, dP, in the estimated received number of photons, then to achieve a specified NEdT, the relative variation must be bounded by:



P and  are the Plank function and its derivative. Thus the NEdT sets a bound on residual array nonuniformities. We determined the maximum residual nonuniformities for all channels and their specified scene temperatures. The results are given in [Table 2-11](#). The most demanding requirements are imposed by channels 4 and 5 at the scene temperature of 300 degrees K. To achieve the GOES N desired 0.1 degree NEdT, a residual array nonuniformity of less than 0.1 percent is required. Experimental residual nonuniformities as low as 0.012 percent [GOESN91] have been reported. Other developers have reported TDI arrays with 0.1 percent nonuniformity. The requirement is therefore within the state of the art.


The TDI scan provides a better uniformity characteristic than the step-stare scan. By summing m pixels in TDI, the standard deviation is reduced by a factor of \sqrt{m} . This further amplifies the arguments favoring the TDI scan.


Another impact levied by the NEdT requirement, along with the extended dynamic range, lies in encoding of the pixel samples. Specifically, the number of bits used to encode each sample is determined from these performance requirements. An insufficient number of bits will result in quantization noise greater than the desired NEdT. We use the worst case of channel 5 for this analysis.

At the maximum temperature of 350 degrees K, the spectral photon exitance (see Appendix A) from a blackbody at $\lambda = 12 \mu\text{m}$ is $Q_{\text{max}} = 3 \times 10^{17}$ photons/(sec*cm²*μm). The electrical output of an ideal photodetector is proportional to the input photon flux. If there are N bits for encoding, there are 2^N levels (bins) into which the detector's output is quantized. If the flux range from 0 to Q_{max} is divided equally into 2^N levels, then the flux increment dQ is:



With N = 10 bits for encoding (as is used in GOES I-M), the flux increment is $dQ = 2.9 \times 10^{14}$ photons/(sec*cm²*μm).

A plot of the inverse Planck function for channel 5 in increments of dQ is given in  Figure 2-11 (Inverse Planck Function for Channel 5). Detection of flux values in the range of 0 to dQ is in the first bin. The corresponding temperature is 116 degrees K. Any scene temperatures up to 116 degrees K are quantized to this first bin. The next dot up the curve is at T = 124.3 degrees K at twice the unit flux 2dQ. Any scene temperature between 116 degrees K and 124.3 degrees K is quantized in the second bin. The resolution rapidly improves with temperature since the inverse Planck function becomes very steep. Resolution is defined here as the difference in temperature levels separated by unit flux steps dQ.

Resolution as a function of temperature is seen in  Figure 2-12 (Quantization Noise Resolution for Channel 5). At 200 degrees K, the resolution is 0.44 degrees, which is within the desired 0.5 degree specification. Similarly, at 240 degrees K, the resolution is 0.23 degrees, which is within the 0.3 degree specification. However, at 300 degrees K, the resolution is 0.13

degrees and is worse than the desired 0.1 degree specification. In this case, quantization noise is larger than the desired NEdT. Encoding with more than 10 bits will decrease quantization noise and improve resolution. We found that with 11 bits, the quantization noise allows a resolution of less than 0.07 degrees on a 300 degree K scene, and 12 bits are necessary to resolve better than 0.05 degrees.

2.7 DETECTOR COOLING

To approach background limited detection, the IR detector arrays must be cooled. The maximum detector temperature for BLIP operation is a function of cutoff wavelength and background flux levels: the longer the cutoff wavelength, the colder the detector must be. The cutoff wavelength for channel 5 is at 13.5 μm , one micron above the upper end of its optical passband. With an f/2 cold stop, a scene at 200 degrees K gives a background flux of 5.7×10^{15} photons/(sec*cm²). Using IR Handbook nomographs, [WOLFE89] we found the maximum detector temperature for BLIP operation to be 80-85 degrees K. However, this is a theoretical maximum, and all focal plane array developers we contacted emphasized the importance of operating at 65-70 degrees K. In addition to cooling the IR detector arrays, the cold shields and aft optics of the imager system must be cooled, though not necessarily to the temperature of the detector arrays.

A passive radiative cooler radiates heat into cold space. The *ideal* radiative cooler radiates a flux, Q, from its area, A, at temperature T according to Stefan-Boltzmann's law:

figure

with $[\sigma] = 5.67 \times 10^{-8} \text{ W}/(\text{m}^2 \cdot \text{K}^4)$. If we estimate a minimum heat load of $Q = 1 \text{ W}$ for array dissipation and parasitic heat creeping through support structures, and require the radiative cooler surface at a temperature of $T = 60$ to provide a temperature difference between the arrays and the radiator for heat to flow through a reasonably sized thermal link, then the minimum area of the radiator is found to be $A = 1.4 \text{ m}^2$ or 1.2 m on edge. This is a large radiator and would, in practice, probably be larger because of less-than-ideal conditions. In fact, a doubling of the radiator area might be expected in practice. This large radiating surface must be thermally isolated from the platform on which it is mounted, and shielded from sunshine and Earthshine. Shielding of such a large surface may be very difficult to achieve on a nondedicated spacecraft. We therefore turn our attention to mechanical coolers.

Two mechanical coolers that show promise of long-lifetime operation are the Stirling engine and the reverse turbo-Brayton refrigerator. Both of these refrigerators have been designed for 10-year operating lifetimes. The Stirling engine for British Aerospace was originally designed by Oxford University and Rutherford Appleton Laboratory. The Stirling cooler consists of three components: a compressor, a displacer, and electronics. The detector is cooled by thermal contact with a *cold finger*. This cooler can supply 0.8 W of cooling capacity at 80 degrees K with a power consumption of 35 W. The mass of the refrigerator is 8.4 kilograms (kg) (18.5 pounds). In 1992, the Stirling cooler was flying on the Improved Stratospheric and Mesospheric Sounder (ISAMS) experiment on the NASA Upper Atmosphere Research Satellite (UARS), and on the European Remote Sensing (ERS-1) Satellite. Stirling coolers are being built in the United States by TRW, Creare Inc., Hughes, Lockheed, and Ball Aerospace. TRW has developed and tested a miniature Stirling engine capable of 0.25 milliwatt (mW) cooling at 65 degrees K with a power input of 18 W.

Creare Inc. is developing a 65 degree K Stirling cooler with a 2 W capacity, with a 60 W input power and a target mass of 14 kg (31 pounds). The cooler is designed for a 10 year lifetime with 95 percent reliability. The Ball Aerospace Stirling cooler can provide 0.8 to 3 W of cooling capacity at 80 degrees K, with a power consumption of 60 W. Its mass is 12 kg (26.4 pounds), and is also designed for a 10 year lifetime.

The reverse turbo-Brayton refrigerator, also under development by Creare, works by compressing and expanding neon gas through tiny turbines. The compressor turbine rotates at 300,000 revolutions per minute (rpm), and the turbo-expander spins at 600,000 rpm. After the refrigerator starts and the turbines lift off, the turbine rotor is suspended on gas bearings, and there are no touching parts to wear out. The most likely failure mechanism is the three-phase motor that spins the turbines. Other factors that could affect reliability are particle jamming (e.g., impurities in the neon gas) and material mismatches. The lifetime goal is

10 years. The cooler is being designed to deliver 5 W of cooling at 65 degrees K, with a power consumption of 200 W (specific power = 40W/W). The mass of the cooler is 13.7 kg (30 pounds).

The reverse turbo-Brayton refrigerator is preferred over the Stirling engine for our imager application. One reason is that piston movements of the Stirling engine impart some level of vibration to the host spacecraft, whereas with the Brayton, virtually no vibration is imparted to the mounting structure. The second reason is that the Stirling refrigerator is basically designed to handle only a single load at the end of its cold finger. In our multiple-array application, several Stirling engines would be required, and several more when redundancy is considered. The turbo-Brayton, however, can service multiple loads at multiple locations. Our imager will have as many as four IR arrays, cold shields, and optics to be cooled, and the turbo-Brayton is best suited to this application. **figure** Figure 2-13 (Reverse Turbo-Brayton Refrigerator with Multiple Heat Loads) is a schematic of the components of a turbo-Brayton refrigerator, with multiple loads being cooled in parallel. The neon gas flows through 1/4" tubing. Refrigerator plumbing lines may be routed to various array and aft optics locations.

A typical lifetime design goal specification is a 95 percent chance of operation after a period of 10 years. Thus the probability of failure of a single refrigerator is $p = 0.05$ after 10 years of operation. With a redundant compressor, expander, and motor, the probability of failure is $p^4 = 0.0025$ or 0.25 percent. A redundant compressor and expander system would be valved into the plumbing of the primary system.

Technical risk lies in the lifetime of the mechanical coolers. Design goal lifetimes may be quoted at 10 years, but there are no flight test data over this long period of time. The turbo-Brayton refrigerator is still under development. A brassboard model now exists, and an engineering development model (EDM) is to be completed by the end of the third quarter 1993. The EDM will then be subjected to laboratory testing and parametric mapping. The current development schedule calls for protoflight hardware to be constructed by early 1995. Low-rate initial production (LRIP) refrigerators, if funded, would be available in the 1996/7 time frame.

2.8 DESIGN CONSIDERATIONS

The fore optics consist of the scan mirror and telescope. The aft optics reside behind the primary mirror of the telescope. The functions of the aft optics are to separate the collected radiation into the spectral channels, prevent stray radiation by stopping and filtering the beams, and focus the beams on the focal plane detector arrays.

Approaches to spectral separation of the beam include dispersion by a prism, diffraction with a grating, and optical filtering. The benefit of spectral separation with a prism or grating is less loss than an approach using beamsplitters. Several filters (dichroic beamsplitters) in series add to the loss of the system. Another advantage of a prism/grating separation over the full IR band of interest (3.8-12.5 μm) is that it would provide the hook for adding additional spectral channels desired for GOES N. With the series beamsplitter approach, adding extra channels would radically alter the optical layout and add to insertion losses. With a grating or prism, the separation is done over the full band, and it is a matter of component spacings to collect and focus the wavelengths of interest. The concept of spectral separation with a grating over the full IR band of the imager is illustrated in **figure** Figure 2-14 (Spectral Separation with a Grating). The concept is similar with a prism.

A recent study [GOESN91] suggests an approach that avoids beamsplitters. It describes a common extended focal plane providing enhanced channel-to-channel co-registration. However, no method is suggested as to how the beam is to be spectrally separated.

A potential problem with the grating or prism is that the passband of both channels 4 and 5 is 1 μm wide, and the upper edge of channel 4 (11.2 μm) is only 0.3 μm from the lower edge of channel 5 (11.5 μm). The diffraction (or dispersion) required to separate these channel edges and also to work over the full 3.8 μm -12.5 μm spectrum could result in a very complicated aft optics system, possibly more complex than that of the beamsplitter approach. The grating/prism approach needs further analysis.

Another imager instrument design issue is the use of a common FPA for multiple channels. Let us examine the radiometric performance penalty for a common array. Suppose that all four IR channels are to be detected with a common focal plane detector array. The only possible material system is HgCdTe, and the cutoff wavelength must be around 13.5 μm , 1 μm above the upper band edge of channel 5. The thin-line curve in [figure](#) Figure 2-15 (Detectivity Tradeoff (300 degrees K Scene, 2[[pi]] sr FOV)) shows the well-known contour for the theoretical maximum detectivity with a 300 degree K background flux. The detector FOV is 2[[pi]] sr. For a cutoff wavelength [[lambda]], the contour gives the maximum achievable D^* for an HgCdTe detector ([[eta]] = 0.55). The theoretical detectivity curves for two detector arrays are shown with thick lines--one with the required 13.5 μm cutoff and the other for an array with a 4.5 μm cutoff.

We wish to compare the degraded performance of channel 2 detected with a 13.5- μm -cutoff common array against the performance of a system with an array optimized for channel 2 (i.e., with [[lambda]]_c = 4.5 μm). The penalty at 4.0 μm , projected with dashed lines in [Figure 2-15](#), is a factor of 8 in detectivity. The detectivity of the optimized 4.5 μm cutoff detector at 4 μm is $8 \times 10^{(10)} \text{ cm}[[\text{radical}]]\text{Hz/W}$, whereas if the 13.5- μm -cutoff common array is used, the detectivity is $1 \times 10^{(10)} \text{ cm}[[\text{radical}]]\text{Hz/W}$. Furthermore, since array developers were consistent in estimating 10 percent BLIP for long-wavelength IR detectors and 50 percent BLIP for short-wavelength IR detectors, the degradation factor is multiplied by a factor of 5. The estimated D^* degradation is therefore on the order of a factor of 40. It follows that NEdT performance will suffer by a factor of 40. The feasibility of a common array for all four IR channels is therefore questionable.

In our discussions with detector array developers and imaging system houses, the possibility of using a single HgCdTe array for channels 4 and 5 was suggested. The possibility of using an InSb array for both the visible channel and the 3.8-4.0 μm IR channel was also discussed. A tradeoff similar to that illustrated in [Figure 2-15](#) may be performed on the case of combining channels 4 and 5; only a small penalty is expected. These two-channel combination cases need further analysis. Here we proceed under the assumption of four separate IR detector arrays.

We now focus on a specific optical implementation for the imager. It is a preliminary design and is not optimized. Its purpose is to identify optical parameters (lens spacings, surface curvatures, focal lengths, etc.) to a point where analysis of optical performance (e.g. spot size, transmission) can be carried out by ray-trace simulation. This analysis would be used to determine problems and optimize performance. Such analysis was beyond the resources available for this effort, but should be performed in the event of a follow-on effort. We assume a system with five FPAs, and therefore five separate optical paths.

If a detector pixel is square with an edge length h , and an IFOV is to be focused within the pixel, then the required system focal length, f , is:

[figure](#),

where the system consists of the combination of fore and aft optics.

The required IFOVs and assumed pixel sizes, shown in [Table 2-12](#), determine the necessary focal lengths for the various optical paths of the system.

The focal length of the RC telescope is $f_T = 360 \text{ cm}$. For each channel, a lens system must be placed between the telescope and the detector array. The system focal length, f , is approximated from the thin lens equation:

[figure](#),

where x is the location of the principal point of the lens system measured from the focal point of the telescope. To determine the appropriate lens focal lengths, we solve this expression for f_L in terms of f_T and f . The required lens focal lengths are determined from:

figure

(x, f in cm).

Telescope geometry is illustrated in **figure** Figure 2-16 (Telescope Geometry), and the coordinate x is shown. For the f/12, d = 30 cm, f/1.4 primary RC telescope under consideration, the telescope parameters are:

focal length $f_T = 360$ cm

obscuration $[\epsilon] = 0.25$

beam angle $[\beta] = 4.77$ degrees

mirror spacing $D = 31.5$ cm

back focal length $B = 90$ cm

working distance $W = 58.5$ cm (behind primary, before focus).

The range of the coordinate x is up to $W = 58.5$ cm.

Our design uses a series of dichroic beamsplitters for spectral separation of the five channels. The diameter of the telescope beam as it just emerges behind the primary mirror is 4.88 cm. We use a series of 45 degree-oriented beamsplitters, each being the diagonal of a 6 cm x 6 cm x 6 cm cube. Our first aft optics design is illustrated in **figure** Figure 2-17 (First Aft Optics Design). Lens positions, beam diameters, focal lengths, and operating f/numbers are shown for each lens.

The first dichroic beamsplitter in the optics train splits the visible from the IR channels. The visible channel 1 is filtered and attenuated by an optical bandpass filter and neutral density filter (BP&NDF). The total attenuation of the BP&NDF was given in [Table 2-7](#). The visible beam is then focused by an f/4.2, 15.1 cm lens onto the visible detector array. The beam is depolarized by a beamsplitter and corrected for the telescope's Petzval curvature by a field flattener lens.

The second beamsplitter in line separates the IR spectrum at 5 μ m. Channel 2 is split off, filtered and attenuated, and focused by an f/2.1, 6.56 cm lens. The FOV of the channel 2 detector array is limited by an f/2 cold shield. A Lyot stop images the entrance pupil and prevents stray light from reaching the detector array.

Channels 3, 4, and 5 are split off in sequence and then focused with f/1.32 lenses. Their cold shields have been set at f/1.2. We previously computed detectivities and NEdTs based on an f/2 cold shield; however, this optics design requires a wider-angle f/1.2 cold cone. The improvement factor at f/2 was a factor of 4, whereas with an f/1.2, we only obtain an improvement of 2.6. The net result is that the D^* s and NEdTs are degraded by a factor of 1.5 from the values we computed earlier.

Notice that the focal lengths of channel 3, 4, and 5 relay lenses are short. Each beam focuses quickly after its lens. This is undesirable because these infrared beams cannot be folded, with mirrors, to a common location for cooling. Cooling would be more efficient if the detectors were in close proximity. The beamsplitter orientations could be rotated to get the detector arrays closer together. Imagine, for example, that the beamsplitters and following optics for channels 2 and 4 were rotated 90 degrees, so that the detector arrays came out of the page. Still, the short focal lengths prevent a common cold area.

A second aft optics design is illustrated in **figure** Figure 2-18 (Second Aft Optics Design). Here we have altered the optics of channels 4 and 5. These beams are collimated by negative lenses and then focused by a positive lens with the proper focal length. This allows long high f/number beams, which can be redirected by folding mirrors. Channels 3 and 5 are in close

proximity, as are channels 2 and 4. The beams of channels 4 and 5 have f/numbers of f/16.8 and f/21.9, respectively, allowing a smaller-angle cold cones. [Figure 2-18](#) shows an f/12 cold stop. An f/12 cold stop has a theoretical improvement factor of 24; however, in practice the factor is typically limited to less than 4.

The design of [Figure 2-18](#) could be further modified to bring all IR arrays in close proximity. For example, a third aft optics design could collimate and refocus channels 3, 4, and 5. These beams could then be manipulated in three-dimensional space and all brought close to the focus of channel 2.

With any of these aft optics designs, a detailed ray trace simulation of the optics should be performed. In particular, the impact from the required wide FOV should be examined. A potential aberration problem in any of these designs relates to angular magnification resulting from Lagrange's optical invariant. The beam diameter at the lenses for channel 5 is on the order of $b = 1.6$ cm. The system demagnification is $m = -30 \text{ cm} / 1.6 \text{ cm} = -18.75$. The magnitude 18.75 is also the angular magnification. Incident angles as great as 0.6 degrees (i.e., half the FOV for an optimistic array set) will be multiplied to 11.25 degrees. These large angles could cause problems since aberrations increase as angles depart from paraxial.

In previous calculations, we made an assumption of an aft optics transmission of $[\tau] = 0.25$. Let us now estimate the transmission for the design of [Figure 2-18](#). We base this estimate on the worst case with channel 5. Not shown in [Figure 2-18](#) are the scan mirror and the secondary mirrors of the RC telescope. Desired radiation from the Earth first reflects from the scan mirror, then from the two mirrors of the telescope. The telescope's secondary mirror presents a 6.25 percent area (25 percent linear) obscuration of the primary mirror aperture. The radiation then passes through four dichroic beamsplitters, reflects from a mirror, passes through the 11.5-12.5 μm bandpass filter and two lenses, reflects from two folding mirrors, and comes to focus on the detector array.

The following terms and assumed values are defined:

r_m = mirror reflectivity = 0.98

t_o = transmission through 6.25 percent area obscured aperture = 0.94

t_1 = transmission at air/lens interface of lens = 0.90 (antireflection coatings are assumed [3](#) [figure](#))

t_2 = transmission through dichroic beamsplitter/bandpass filter = 0.8

In total, the beam passes through the obscuration, 6 mirrors, 5 dichroic beamsplitters/filters, and 4 air/lens material interfaces--16 events in total. The optical transmission of the system is then:

[figure](#)

The sum of the exponents in the above expression totals 16. This 18 percent transmission is somewhat less than the 25 percent value assumed in earlier radiometric performance computations.

The optics in front of the IR detector arrays may be considered as a graybody with some emissivity, $[\epsilon]$. Depending on their temperature, these optical elements (filters, lenses, mirrors) will radiate, and some amount of this radiation will find its way to the detector array and introduce noise. If these optics are cooled, the noise will be reduced.

A simplified model for estimating the required aft optics temperature is illustrated in [figure](#) [Figure 2-19](#) (Cold Shield). The detector's FOV is limited by an f/12 cold stop. The aft optics are represented by a graybody of emissivity $[\epsilon]$. We will compute the photon flux emitted from the aft optics graybody (within the f/12 cone) and compare it with the flux collected from the Earth scene.


On the detector, the noise flux from the graybody is:

 (photons/sec),

where M_q is at the temperature T of the aft optics. The signal flux collected from the Earth scene is given by:

.

For a worst case, we have taken the Earth scene at 200 degrees K.

We now examine the flux ratio $[\Phi]_{\text{signal}}/[\Phi]_{\text{noise}}$ in terms of the aft optics temperature. This is plotted in  Figure 2-20 (Flux Ratio and Optics Temperature) for a worst-case aft optics emissivity of unity ($[\epsilon] = 1$).

An operating point on this curve can be established from NEdT requirements. We define:

.

For a $T = 200$ degree K scene, [Table 2-3](#) gives the ratio:

.

With a required NEdT of 0.5 degrees, a minimum flux ratio of 67 is found from:

.

In other words, for a 200 degree K scene, the signal level L is 67 times the differential signal dL corresponding to a scene temperature change of $\text{NEdT} = 0.5$ degrees. If the noise flux from aft optics radiation is greater than $1/67$ th of the signal flux level, a 0.5 degree scene temperature change will be hidden. The flux ratio must be greater than 67. This operating point is indicated in the graph of [Figure 2-20](#). The optics temperature must be less than 190 degrees K. However, this may be too stringent since Figure 2-20 is based on the assumption of an emissivity of unity. If the emissivity of the optics were $[\epsilon] = 0.5$, the flux ratio would double and the aft optics temperature would be between 200 and 225 degrees K.

2.9 Instrument weight and power

The total weight of the GOES I imager is 267 pounds. This represents the combined weight for the sensor assembly, electronics module, and power supply module. An itemized component weight breakdown for the GOES I subsystems was not available. Our best estimate for the weight of our array imager is 80 to 100 percent of the GOES I imager: 214 to 267 pounds, including the mechanical cooler. Because of the long-wavelength resolution requirement, the telescope size and the weight of the array imager will be comparable to those of the GOES I telescope. The weight of the turbo-Brayton refrigerator, discussed earlier, is 30 pounds. With redundant compressor/expander turbines and motors, the cooling system would weigh 40-45 pounds. We believe this would be heavier than the three-stage aluminum-beryllium radiative cooler used on GOES I.

Weight savings might be achieved with new mirror materials such as silicon carbide instead of the ultra low expansion (ULE) glass used on the GOES I telescope. Furthermore, weight reduction might be achieved with graphite epoxy as a lighter weight structural alternative to INVAR. Another area where weight savings might be realized is in the use of application-specific integrated circuits (ASICs) for the electronics and control modules.

Because of the mechanical cooler, the electrical power requirement for our array imager will undoubtedly exceed that of the GOES I instrument. The GOES I average power consumption is 120.5 W. The specific power of the turbo-Brayton cooler is 40 W/W. For an estimated heat load of 1-2 W to cool the detector and aft optics, an additional 40 - 80 W of power would be required. The required power estimate is therefore in the range of 160 - 200 W.

2.10 SUMMARY AND CONCLUSIONS

The above discussion can be summarized in the following conclusions:

- * Second-generation FPA technology is the key to rapid imaging from a nondedicated satellite. We believe a rapid imager is feasible and can provide the enhanced resolution and radiometric performance sought by the National Weather Service.
- * The wavelength and resolution requirements for the long-wavelength channel 5 dictate the size of the imager. Diffraction limitations require an optical aperture 30 cm in diameter.
- * The wide wavelength range of the imager leads to reflective telescope designs.
- * Rapid imaging with a large FPA requires a telescope with a wide FOV. Of the common two-mirror telescope designs, the RC system offers the widest FOV.
- * The resolution of channel 1 limits the telescope's FOV, which in turn limits usable array sizes. We found that redundant TDI-architecture arrays of sizes 1024 x 128 (channel 1), 256 x 32 (channel 2), and 128 x 16 (channels 3-5) require an FOV of 1.16 degrees. The RC telescope cannot provide this wide FOV for channel 1 because of Petzval field curvature aberrations. A field flattener lens may be used to counter the Petzval aberrations.
- * To meet the desired requirements for a 350 degree K dynamic range and 0.1 degree NEdT at 300 degreesK, 11-bit encoding is required.
- * The low flux from imaging channel 2 temporally paces the system. The other channels must be attenuated to balance integration times.
- * The material PtSi does not meet the desired NEdT performance level within the 3 minute scan time. There is continuing debate on the use of InSb versus HgCdTe for the 3.8-4.0 um band.
- * TDI scanning offers certain advantages over step-stare scanning. These advantages include superior radiometric performance and reduced yield requirements which translate to lower production risk and cost.
- * The most demanding NEdT requirement is to be able to detect a 0.1 degree temperature change in a 300 degree K scene in the wavelength bands of channels 4 and 5. This requirement puts a 0.1 percent limit on residual array nonuniformities. This level of uniformity is within the state of the art.
- * The IR detector arrays should be cooled to 70 degrees K or less. The aft optics should be cooled to less than 225 degrees K.
- * A passive radiative cooler will be too large for an imager on a nondedicated satellite. The reverse turbo-Brayton mechanical refrigerator is preferred over the Stirling refrigerator because of the multipoint and multiload nature of the imager. Mechanical refrigerator developments are well under way, with lifetime goals of 10 years.
- * The concept of imaging all four IR channels with a single detector array would compromise NEdT performance by a factor of 40. However, combining two channels on a common array appears feasible.

* We developed a preliminary optical instrument design. This design is conservative in the sense that it uses an array per channel instead of common arrays for multiple channels, and it uses a train of beamsplitters to spectrally separate the channels instead of a single optical element (prism or grating). The design defines basic optical parameters for input to an optical ray tracing program. Ray tracing could reveal problems that would suggest design modifications. This process would be used to verify the feasibility of rapid imaging with second-generation FPA technology.

* We estimate that the weight of the imager will be in the range of 210 to 270 pounds. Weight savings, relative to the 267 pound GOES I imager, might be realized by use of ASICs for the electronics module, silicon carbide for the telescope, and graphite epoxy for structural supports. The power requirement is estimated in the range of 160 - 200 W. This is more than the 120.5 W GOES I power requirement because of our use of mechanical, rather than radiative, cooling.

We identified several areas where further analysis would be required to arrive at an optimum instrument design. Time and resources prevented us from delving into the following areas:

* A two-telescope design with a refractive telescope for the visible channel residing in the obscuration of a reflective IR telescope. The field-of-view constraint could be reduced, and larger arrays (faster imaging) might be possible. The resolution of the visible channel would be 1 km.

* Ray tracing, discussed earlier, to verify the feasibility of the optimistic versus pessimistic families of array sizes. Aberrations of the total system would be modeled.

* The issue of calibrating the detector arrays, which we did not examine in our preliminary design. Calibration at two or more temperatures would be required to meet the desired radiometric performance.

* Performance tradeoffs of InSb versus HgCdTe for the channel 2 array.

* Spectral separation with a grating or prism instead of beamsplitters. Using diffraction/dispersion to spectrally separate the channels offers the potential advantage of superior channel-to-channel coregistration. It also provides the hook for adding additional spectral channels.

* Combining channels on a common FPA, for example, combining channels 1 and 2 on a single InSb array, and combining channels 4 and 5 on a single HgCdTe array. Coregistration benefits may result.

1 The 20 degrees x 20 degrees FOR contains 6.2×10^8 channel 1 pixels (14 urad square); 3.9×10^7 channel 2 pixels (56 urad square); and 9.7×10^6 pixels (112 urad square) each for channels 3-5. The total number of pixels is 6.9×10^8 ; 90 percent of the pixels are for channel 1.

2 To alleviate the well capacity saturation problem in bucket-brigade TDI, one array developer suggested the possibility of grading the well capacities so that they become progressively larger in the direction of the bucket brigade. However, there may be a problem with graded well capacities in a bidirectional TDI array, where the brigade must pass electrons in both directions.

3 Note that antireflection coating of germanium lenses is very important. For a wavelength of 12 μm , the index of refraction of germanium is $n = 4$. Transmission at an air/material interface at normal incidence is:

$$t = 1 - [(n-1)/(n+1)]^2.$$

For an uncoated air/germanium interface, the transmission is only 0.64. This would reduce the system transmission to $[\tau] = 0.046$.

Table 2-1. Imager Resolution Goals

Ch.	Spectral Range	Spatial/Angular Resolution	Applications
1	0.55-0.75 um	0.5 km/14 urad	Weather monitoring, severe storm detection, cloud mapping, snow cover
2	3.8-4.0 um	2 km/56 urad	Nighttime cloud detection, water vapor estimates
3	6.5-7.0 um	4 km/112 urad	Jet stream location, mid-tropospheric circulations
4	10.2-11.2 um	4 km/112 urad	Surveillance of convective storms, low-level moisture, surface temperatures, winds, soil moisture
5	11.5-12.5 um	4 km/112 urad	Low-level water vapor, surface temperature

Table 2-2. Desired (and GOES I-M) NEdT Performance Goals

Ch.	200 degrees K Cloud Tops	240 degrees K Mid-level Cloud	300 degrees K Surface
2	--	< 1.00 degrees 0.1 degrees (1.4 degrees)	

3	0.7 degrees	0.3 degrees (1.0 degrees)	--
4	0.5 degrees	0.3 degrees	0.1 degrees
5	(1.4 degrees) 0.5 degrees	0.3 degrees	(0.35 degrees) 0.1 degrees (0.35 degrees)

Table 2-3. Photon Sterance Levels (photons/(sec*cm^(2)*sr)) and Relative Temperature Derivatives (K^(-1)) for the IR Channels

Ch.	T = 200 degrees K	240 degrees K	300 degrees K	350
degrees K				
2	--	1.11 x 10^(13) (0.064)	2.39 x 10^(14) (0.041)	1.38 x 10^(15) (0.030)
3	3.42 x 10^(14) (0.053)	2.02 x 10^(15) (0.037)	3.28 x 10^(16) (0.017)	--
4	5.50 x 10^(15) (0.034)	1.69 x 10^(16) (0.023)	5.22 x 10^(16) (0.015)	1.00 x 10^(17) (0.011)
5	7.21 x 10^(15) (0.030)	1.97 x 10^(16) (0.021)	5.41 x 10^(16) (0.014)	9.71 x 10^(16) (0.010)

Table 2-4. Radiant and Photon Sterance Levels for Channel 1

Percent Albedo	Radiant Sterance	Photon Sterance @ [[lambda]] = 0.65 um
----------------	------------------	--

(W/(cm²*sr))

(photons/(sec*cm²*sr))

0.5%	4.8 x 10 ⁽⁻⁵⁾	1.57 x 10 ⁽¹⁴⁾
100%	9.60 x 10 ⁽⁻³⁾	3.14 x 10 ⁽¹⁶⁾

Table 2-5. IR Detector Cutoff Wavelengths (um)

Detector	300 degrees K Uncooled	190 degrees K TE Cooled	80 degrees K Mechanically Cooled	60-1.5 degrees K
InSb	--	6.1	5.5	5.0
PtSi	--	--	4.8	--
PV HgCdTe	1-3	1-5	3-12	10-16
PC HgCdTe	1-11	3-11	5-25	12-25

Table 2-6. Diffraction Limited Telescope Apertures

Ch.	[[lambda]] (um)	[[theta]] (rad)	D (cm)
1	0.75	14/28	12.3/6.1

2	4.0	56	16.4
3	7.0	112	14.3
4	11.2	112	22.9
5	12.5	112	25.6

Table 2-7. Integration Times, TDI Dwells, and Attenuation

Ch. Factor	Integration Time per Pixel (usec)	Mechanical Dwell per Pixel (usec)	Attenuation
---------------	--------------------------------------	--------------------------------------	-------------

1	3.7	289	0.013
2	19,000.0 (InSb)		
	26,000.0 (PtSi)	1156	1.0
3	500.0	2312	0.216
4 & 5	165.0	2312	0.071

**Table 2-8. Background-Limited Detectivities (cm^{1/2}Hz/W)
with f/2 Cold Shield**

Ch.	Material	T = 200 degrees K	240 degrees K
300 degrees K			

2	InSb or HgCdTe PtSi	--	7.1 x 10 ⁽¹²⁾ 6.2 x 10 ⁽¹¹⁾	1.5 x 10 ⁽¹²⁾ 1.3 x 10 ⁽¹¹⁾
---	---------------------	----	--	--

3	HgCdTe	2.2 x 10 ⁽¹²⁾	9.3 x 10 ⁽¹¹⁾	--
---	--------	--------------------------	--------------------------	----

4 & 5	HgCdTe	8.8 x 10 ⁽¹¹⁾	5.3 x 10 ⁽¹¹⁾	3.2 x 10 ⁽¹¹⁾
-------	--------	--------------------------	--------------------------	--------------------------

Table 2-9. NEdT with Step-Stare Scan

(50% BLIP for channels 2 and 3, 10% for 4 and 5)

Ch.	Material	T = 200 degrees K	240 degrees K
300 degrees K			

2	InSb or HgCdTe PtSi	--	(1.24 degrees) (13.5 degrees)	(0.416 degrees) (4.54 degrees)
---	------------------------	----	----------------------------------	-----------------------------------

3	HgCdTe	0.14 degrees	0.08 degrees	--
---	--------	--------------	--------------	----

4 & 5	HgCdTe	0.44 degrees	(0.39 degrees)	(0.36 degrees)
-------	--------	--------------	----------------	----------------

Table 2-10. NEdT with TDI Scan

(50% BLIP for channels 2 and 3, 10% for 4 and 5)

Ch.	Material	T = 200 degrees K	240 degrees K
300 degrees K			

2	InSb or HgCdTe	--	0.22 degrees	0.07 degrees
---	----------------	----	--------------	--------------

PtSi (2.4 degrees) (0.80 degrees)

3 HgCdTe 0.03 degrees 0.02 degrees --

4 & 5 HgCdTe 0.11 degrees 0.10 degrees 0.10 degrees

Table 2-11. Maximum Array Variations (percent)

Ch.	T = 200 degrees K	T = 240 degrees K	T = 300 degrees K
2	--	6.4	0.4
3	3.7	1.1	--
4	1.7	0.7	0.1
5	1.5	0.2	0.1

Table 2-12. System Focal Lengths

Ch.	IFOV (urad)	Pixel Edge, h (um)	System Focal Length, f (cm)
1	14	15	107.0
2	56	30	53.6

3-5 112 40 35.7

[Return to the text](#)

Table 3-2. GOES I Imager Predicted INR Performance

Performance Parameter	3 σ Performance Prediction
-----------------------	-----------------------------------

Image navigation accuracy	22 km at nadir
---------------------------	----------------

Registration within an image	74 urad in 25 minutes
------------------------------	-----------------------

Registration between repeated images	37 urad in 15 minutes
--------------------------------------	-----------------------

Source: [GOES91].

[Return to the text](#)

Table 5-1**ITU Region 2****1992 In-Orbit Communications Satellites**

W.Long MFG	NAME BAND	REPLACEMENT	LAUNCH LAUNCH	MFG	D/L	EOL	OWNER
65 BrazilSat B1	BrazilSat A1 1993	02/08/86 HS376	8	EMBRATEL		HS376	C
69 SPACENET II-R	SPACENET II 1994	11/09/84 GE3000	13	GTE		GE3000	C/K
70 BrazilSat B2	BRAZILSAT A2 1994	03/28/86 HS376	8	EMBRATEL		HS376	C
72 SATCOM C-3	SATCOM 2FR	09/08/83 GE7000 12	10	GE AMERICOM		RCA	C
74	GALAXY II	1983	9	HUGHES		HS376	C
74	GALAXY IV	1990		HUGHES			C
76 TELSTAR 303	COMSTAR D4	02/21/81	7	COMSAT		HS376	C/K
81	SATCOM K2	01/12/86	10	GE AMERICOM		GE3000	K
82 SATCOM C-4	SATCOM F4R 1992	11/09/84	10	GE AMERICOM		HS376	C
85 TELSTAR 402	TELSTAR 302 1994	08/30/84 GE7000 12	10	AT&T SKYNET		HS376	C/K
85	SATCOM K1	11/28/85	10	GE AMERICOM		GE3000	K

87	SPACENET IIIR	03/11/88	10	GTE	GE3000	C/K
91	SBS 4	08/30/84	9	HUGHES	HS376	K
GALAXY	VII-H	1992				
93	GSTAR III	09/08/88	5	GTE	GE3000	K/L
93	5 GALAXY III	09/24/84	9	HUGHES	HS376	C
95	SBS 3	11/11/82	7	COMSAT	HS376	K
96	TELSTAR 301	07/28/83	10	AT&T	HS376	C
TELSTAR	401 08/93	GE7000 12				
97	SBS 2	11/24/81	7	COMSAT	HS376	K
99	GALAXY VI	10/12/90	10	HUGHES	HS376	C
99	SBS 6	10/12/90	15	HUGHES	HS393	K
GALAXY	IV-H					
101	SPACENET IV	04/12/91	10	GTE	GE3000	C/K
103	GSTAR I	05/08/85	10	GTE	RCA	K
105	GSTAR II	03/28/86	10	GTE	RCA	K
106	MARISAT F1	1976		COMSAT	HS376	C/L
107	5 ANIK E2	04/04/91	10	TELSAT CANADA	GE	C/K
110	ANIK C1/C2	1985		TELSAT CANADA		K
111	ANIK E1	09/26/91	10	TELSAT CANADA	GE	C1/K1

113	5 MORELOS F1 SOLIDARIDES 1994	06/17/85 HS601	9	MEXICO	HS376	C1/K1
114	9 ANIK C3	1982		TELSAT CANADA		K
116	5 MORELOS F2 SOLIDARIDES 1994	11/28/85 HS601	9	MEXICO	HS376	C1/K1
120	SPACENET I	05/22/84	10	GTE	GE3000	C1/K
123	TELSTAR 303	06/19/85	10	AT&T	HS376	C
123	SBS 5	09/08/88	9	HUGHES	HS376	K
125	GALAXY V-W	05/28/92		HUGHES	HS376	C
125	GSTAR IV	11/20/90	10	GTE	GE3000	K
128	ASC 1	1985		CONTEL ASC		C/K
131	SATCOM F1R SATCOM C-3 12/92	04/11/83		GE AMERICOM	GE	C
134	GALAXY I GALAXY I R 1993	1983 HS376		HUGHES	HS376	C
135	SATCOM C-4	1992		GE AMERICOM		C
137	SATCOM C-1	11/20/90	12	GE AMERICOM	GE3000	C
139	AURORA II (SAT C-5)			ALASCOM/GE	GE3000	C

[Return to the text](#)

Table 5-2 PROJECTED REPLACEMENT SATELLITES The following tabulation identifies, by orbital location, those ITU Region 2 domestic communications satellites currently in operation. It provides the name, year of launch, and announced projected end of life. Replacement satellites of record are identified by name, projected launch date, project mission life (EOL), and whether a Hughes or GE second generation spacecraft. The requirements (RQ) listing projects the year the subsequent replacement will be required. W.Long 1st Generation Launch EOL Replacement Launch EOL GE HAC RQ -----

----- 96 TELSTAR 301 1983 TELSTAR 401 1993 12 X* 2005
 85 TELSTAR 302 1984 TELSTAR 402 1994 12 X* 2006 123 TELSTAR 303 1985 1995 120
 SPACENET I 1984 1995 12 2007 69 SPACENET II 1984 1995 87 SPACENET III 1986 1999 101
 SPACENET IV 1991 2001 103 GSTAR I 1985 1995 105 GSTAR II 1986 GSTAR II-R 1995 93 GSTAR
 III 1986 125 GSTAR IV 1990 133 GALAXY I 1983 GALAXY IR 1992 (Launch Failure replace in 1995)
 74 GALAXY II 1983 GALAXY VI-H 1993 9 X 2002 93.5 GALAXY III 1984 GALAXY III-H 1994 12
 X* 2006 101 GALAXY IV 1990 12 X 2002 125 GALAXY V-W 1992 12 X* 2004 99 GALAXY VI
 1990 GALAXY IV-H 1993 12 X* 2005 91 (SBS-4) 1984 GALAXY VII H 1992 12 X* 2002 131
 SATCOM F1R 1983 SATCOM C-1 1990 12 X 2002 72 SATCOM 2FR 1983 135 SATCOM 3FR 1984
 SATCOM C-3 1992 12 X 2004 82 SATCOM F4R 1984 SATCOM C-4 1993 12 X 2005 85 SATCOM K-
 1 1985 1995 12 2007 81 SATCOM K-2 1986 1996 12 2008 139 AURORA I 1983 SATCOM C-5 1991
 12 X 2006 97 SBS 2 1981 NONE PLANNED 95 SBS 3 1982 NONE PLANNED 91 SBS 4 1984
 GALAXY 123 SBS 5 1988 GALAXY 99 SBS 6 1990 GALAXY 110 ANIK C1 1985 110 ANIK C2
 1983 114.9 ANIK C3 1982 107.5 ANIK D1 1982 ANIK E2 1991 10 X* 2001 111 ANIK D2 1984 ANIK
 E1 1991 10 X* 2001 101 AMSC-1 1994 12 X* 2006 101 HC5-2 1994 12 X* 2006 -----

----- * Second Generation Spacecraft Bus 01/01/93 Return to the text
 Back to the CAASD Home Page

Table 5-3**ROM Cost Summary for Commercial Host Satellite**

IN-ORBIT COST		MEDIUM	HIGH
<hr/>			
* Spacecraft	\$70M	\$90.3	
* Launch Vehicle	\$65M	\$82.5	
* Mass Ratio	0.23	0.25	
Subtotal	\$31.1M	\$43.2M	
* FPA Instrument	\$22.	\$30.	
* Per Flight Total	\$53.1M	\$73.2M	
* Satellite Terminal	\$0.2	\$0.35	
	Per Flight Total	\$53.3	\$73.35M
NON-RECURRING COST		MEDIUM	HIGH
<hr/>			
* Development - Instrument	\$72M	\$78M	
* Engineering/Proto Flight	\$50M	\$52M	
* Pre-Processor Development	\$2.25M	\$4.0M	

Total	\$124.25	\$137.00
--------------	----------	----------

RECURRING OPERATING COSTS	MEDIUM	HIGH
----------------------------------	---------------	-------------

* Transponder Lease	\$1.2 M/Yr.	\$3.4 M/Yr.
* T&C - Share	\$0.1 M/Yr.	\$0.1 M/Yr.

[Return to the text](#)

age